M. Vinyas
Amelia Loja
Krishna R. Reddy *Editors*

Advances in Structures, Systems and Materials

Select Proceedings of ERCAM 2019

🐎 Springer

Lecture Notes on Multidisciplinary Industrial Engineering

Series Editor

J. Paulo Davim , Department of Mechanical Engineering, University of Aveiro, Aveiro, Portugal

"Lecture Notes on Multidisciplinary Industrial Engineering" publishes special volumes of conferences, workshops and symposia in interdisciplinary topics of interest. Disciplines such as materials science, nanosciences, sustainability science, management sciences, computational sciences, mechanical engineering, industrial engineering, manufacturing, mechatronics, electrical engineering, environmental and civil engineering, chemical engineering, systems engineering and biomedical engineering are covered. Selected and peer-reviewed papers from events in these fields can be considered for publication in this series.

More information about this series at http://www.springer.com/series/15734

M. Vinyas · Amelia Loja ·
Krishna R. Reddy

Editors

Advances in Structures, Systems and Materials

Select Proceedings of ERCAM 2019

🐎 Springer

Editors
M. Vinyas
Department of Mechanical Engineering
Nitte Meenakshi Institute of Technology
Bengaluru, Karnataka, India

Amelia Loja
Department of Mechanical Engineering
Instituto Superior de Engenharia de Lisboa
Lisbon, Portugal

Krishna R. Reddy
Department of Civil and Environmental
Engineering
University of Illinois at Chicago
Chicago, USA

Preface

The ERCAM proceedings includes the abstracts from selected manuscripts from peer-reviewed papers under various themes, namely Materials, Mechanics, Structures and Systems of the Second International Conference on "Emerging Research in Civil, Aeronautical and Mechanical Engineering" (ERCAM 2019), organized by Nitte Meenakshi Institute of Technology (NMIT), Bangalore, India, from 25 to 26 July 2019.

NMIT, established in 2001 under well-known NITTE Education Trust, is one of the renowned technical institutions of the country and known as the premier institution in Karnataka in particular. This institution is affiliated to the Visvesvaraya Technological University (VTU) and approved by UGC/AICTE/Government of Karnataka. Recognizing its performance in both teaching and research, University Grants Commission has granted autonomous status from the year 2007, accredited at the "A Grade" by the National Assessment and Accreditation Council (NAAC), and four UG programmes got accredited by the National Board of Accreditation under Tier 1 for three years from 2014 and again in 2017. It is the only unaided private engineering college in Karnataka state that was selected by the Government of India for World Bank funding under TEQIP Phase II Subcomponent 1.1.

Teaching, learning, research and development—the four major pillars—are sustaining the edifice of higher education. Multidisciplinary research has become an indispensable imperative in the development of a wide range of engineering materials, processes and systems.

Higher education is now in the process of a paradigm shift, with research gaining increasing attention from policy planners and educationists. Contribution to the research field is prioritized right from the undergraduate level in the universities, making teachers enthusiastic and involving student community. NMIT is conscious and cognizant of this phenomenon and is organizing ERCAM 2019 to create a platform of interaction to the researchers across the world to share/exchange their knowledge. ERCAM 2019 is therefore intended to bring together specialists and practitioners from industries, R&D institutes and academicians, providing a forum of exchange of knowledge on researches in recent trends in major sectors of

materials, processes and systems pertaining to various fields under civil, aeronautical and mechanical engineering.

The conference succeeded in providing a solid platform for researchers around the globe to share insights, experiences and various aspects of evolving technologies related to civil, aeronautical and mechanical engineering. Proceedings covers a wide range of topics which are relevant to the current needs of the industry. All the papers received for ERCAM 2019 conference on various aspects of focused areas were rigorously triple-reviewed by a pool of experts in respective fields from all over the world under Technical Review Committee, first-level review being plagiarism check limiting 20% including self-plagiarism. The committee selected the best 28 papers for oral and poster presentation in the conference to publish in association with Springer and AIP accordingly. The management of NMIT and Team-ERCAM 2019 express their sincere gratitude to the reviewers for their contribution of rigorous review and also authors for revising their papers to incorporate the comments and suggestions by the reviewers.

We are immensely grateful to all the organizers and members of the Program Committee for their diligent work, which ensured high-quality publications. We highly appreciate the guidance and continuous support provided by the management of NMIT and Advisory Committee being with us spending their valuable time for creating ERCAM 2019 a brand image. We recognize the involvement of faculty members of all three departments throughout.

We thank all our sponsors for their support, especially AICTE, Government of India; VTU, Belagavi; and The Supreme Industries Ltd. We are grateful to our fellow professionals from academia and industry who have volunteered to review papers and accepted our invitation to deliver plenary talk despite being of their preoccupied schedules. We would like to thank Springer Nature, AIP publications, JVC Printers and USB Printers for their fruitful collaboration during the preparation of the proceedings. The proceedings of ERCAM 2019 is organized in a single volume. We hope that the ERCAM 2019 proceedings will serve as an important intellectual resource for civil, aeronautical and mechanical engineering researchers, pushing forward the boundaries of these fields and enabling better collaboration and exchange of ideas. Our special thanks to all authors for their contributions, and we anticipate extended contributions in coming years of the flagship event of NMIT—ERCAM—an international conference.

Bengaluru, India	M. Vinyas
Lisbon, Portugal	Amelia Loja
Chicago, USA	Krishna R. Reddy

Contents

About the Editors

Dr. M. Vinyas is an Assistant Professor in the Department of Mechanical Engineering, Nitte Meenakshi Institute of Technology (NMIT), Bangalore, India. He received his Ph.D in Mechanical Engineering from the National Institute of Technology Karnataka, Surathkal in 2018. He received the university medal in his Masters of Technology at Visvesvaraya Technological University. He is also a visiting research faculty in foreign universities and founder of Composite Research: Experimentation, Analysis and Design (CREAM) lab, NMIT, Bangalore. He has published more than 70 articles in reputed international journals and is also serving as a reviewer for many refereed journals. Recently, considering his research achievements, Dr. Vinyas received the CV Raman post-doctoral award from the Indian Institute of Science, Bangalore. His research areas include finite element analysis, composite structures, coupled structural analysis, and vibration control.

Dr. Amelia Loja is presently Adjunct Professor at the Mechanical Engineering Department of the Engineering Institute of Lisbon (ISEL/IPL), and Senior Researcher of the Mechanical Engineering Institute (IDMEC/IST). Her academic background integrates a BSc with honours in Marine Engineering from the Portuguese Nautical School and a BSc in Computer Science. Her MSc degree in Mechanical Engineering was conferred by the Technical University of Lisbon, and later she obtained her PhD in Mechanical Engineering also from this University. Her major areas of interest include the scientific areas of Computational Solids Mechanics, Optimization and Reverse Engineering. Until now she published 41 papers in scientific international journals. Amelia Loja is also Chairperson of the ECCOMAS thematic conference SYMCOMP (International Conference on Numerical and Symbolic Computation: Developments and Applications) and since 2017, she has been invited by the European Commission to evaluate project proposals in different subjects related to her competences.

Dr. Krishna R. Reddy is a Professor of Civil and Environmental Engineering, the Director of Sustainable Engineering Research Laboratory, and also the Director of the Geotechnical and Geoenvironmental Engineering Laboratory in the

Department of Civil and Materials Engineering at the University of Illinois, Chicago, USA. Dr. Reddy received his Ph.D. in Civil Engineering from the Illinois Institute of Technology, Chicago, USA. He received gold medals for being first in his class of B.E. (Civil Engineering) at Osmania University and M.E. (Civil Engineering) at the Indian Institute of Technology, Roorkee.

Dr. Reddy has over 25 years of teaching, consulting and research experience within the fields of geotechnical engineering, environmental engineering, and sustainable engineering. Specifically, his expertise includes: (1) remediation of polluted soils, sediments, groundwater and stormwater, (2) waste management and landfill engineering; (3) life cycle assessment and sustainable engineering; and (4) geotechnical engineering (foundations, earth structures, etc.). His research is funded by the U.S. National Science Foundation, the United States Environmental Protection Agency, several prominent state and local government agencies, and industries. He has published 4 books, 206 journal papers, and 182 full conference papers (with h-index of 52). Dr. Reddy has given 185 invited presentations in the USA and 18 other countries (Brazil, Canada, China, Colombia, France, Germany, Greece, Hong Kong, India, Italy, Japan, Macedonia, Spain, Sri Lanka, South Korea, Turkey, Thailand, and U.K.). Dr. Reddy is an Associate Editor or Editorial Board Member of over 10 different journals. He has been an active member of various professional societies, including the ASCE.

Dr. Reddy has received several awards for excellence in research and teaching, including the ASTM Hogentogler Award, the University Distinguished Researcher Award, the University of Illinois Scholar Award, and the University of Illinois Award for Excellence in Teaching. He is a Fellow of the American Society of Civil Engineers and a Diplomate of Geotechnical Engineering.

Chapter 1
Cerium Oxide and Silicon Carbide Reinforced Al6063 Metal Matrix Composites Comparative Evaluation for Mechanical Properties and Fractography Studies

Check for
updates

Abdul Nazeer and Mir Safiulla

Abstract Aluminum matrix material is considered as advanced material because of its very good mechanical, tribological properties which have been used in automobile, aerospace industries at the larger end, and now aluminum matrix materials have been used in medical and electronics industries because of its good and high strength to weight ratio and low coefficient of thermal expansion. The present work is focused about the improvement in mechanical properties and fracture graphic studies of aluminum matrix reinforced with ceramic particulate silicon carbide and cerium oxide of laboratory grade size, respectively. Here, the reinforcement is varied in terms of weight percent ranging from 0 to 8% in the steps of 2%, and the composites were fabricated using a stir casting route. Prepared specimens were tested as per ASTM standard and performed tensile, compressive, impact and hardness test and fracture surfaces studies done under the scanning electron microscope (SEM) and X-ray diffraction (XRD). The results reveal that with increase in percentage of reinforcement, the mechanical properties of the composite system have increased, SEM images clearly reveal the modes of fracture, and XRD shows the presence of reinforcement.

Keywords Aluminum matrix composite · Stir casting · Mechanical testing · SEM · XRD

1.1 Introduction

The term "composites material" deals with mixing two different materials, where one is called as matrix and other as reinforcement. Composite materials are becoming increasingly popular because of its good mechanical, tribological properties and good resistance to wear, good fatigue life, prevention to corrosion and ability to the

A. Nazeer (✉) · M. Safiulla
Mechanical Engineering, Ghousia College of Engineering, Ramnagaram, Karnataka, India
e-mail: nazeer0301@gmail.com

coefficient of thermal expansion. Composite material is broadly classified on the basis of matrix and reinforcement. On the matrix, it is classified as polymer matrix composite (PMC), Metal matrix composite (MMC), and ceramic matrix composite (CMC), on reinforcement is classified as continuous fibers, discontinuous fibers, Whiskers and particulates. The function of reinforcement is to carry the load, and the matrix is used to transfer and distribute the applied load. These composite materials have been used in many industries mainly in automotive and aerospace industries due lightweight, high load carrying capacity and good resistance to wear, and metal matrix composite is gaining more importance because of easy processing and cost effectiveness. Other advantage of composite metal matrix is that it can be fabricated as hybrid composite in order to increase the properties for specific requirement, where in a single matrix two different reinforcements are introduced such as Al6061 as matrix and SiC and Al_2O_3 as reinforcement [1]. In order to increase tensile strength, hardness and toughness, hybrid composites are prepared by reinforcing fly ash and SiC [2]. Researchers have done work on aluminum alloy with alumina and boron carbide and found that tensile strength, flexural test, impact test and Brinell hardness test values have marginally increased.

Lightweight aluminum alloy matrix composites (AMCs) become increasingly popular due to great mechanical and tribological properties as compared to conventional aluminum alloys. Cast particle-reinforced composites show good results in the automobile sector due to inherent simplicity in fabrication combined with an advantage of mass production [3]. Silicon carbide (SiC)-reinforced aluminum matrices have been widely accepted as potential candidates for weight-critical automobile and aerospace applications.

1.2 Experimental Details

1.2.1 Matrix and Reinforcement Material

Aluminum 6063 is used as metal matrix, silicon carbide and cerium oxide as reinforcement in laboratory grade.

Silicon carbide of laboratory grade 10–20 μm size is chosen as reinforcement owing its high hardness, low coefficient of thermal expansion and highly wear resistant.

Cerium oxide of 5 μm size was considered as a reinforcement. It is an important commercial product and an intermediate in the purification of the element from the ores.
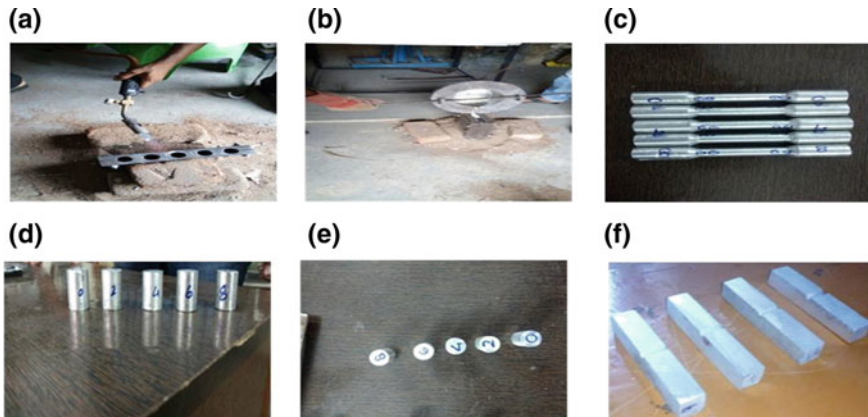
Fig. 1.1 Preparation of composite system with various reinforcements and testing for mechanical properties. **a** Preheating of mold, **b** pouring of molten material into mold, **c** tensile test specimen, **d** compression test specimen, **e** hardness test specimen, **f** Charpy impact specimen

1.2.2 Preparation of Composites

Aluminum 6063 alloy was melted utilizing a 6 kW electric heater. Hereliquid metallurgy route stir casting technique adopted where mechanical stirrer is turned to make a vortex, reinforcement SiC and CeO_2 powders is at first preheated and gradually mix in liquid metal with consistently stirred. The stirring time was 10 min. The molten composites maintained at a constant temperature of 740 °C. The reinforcement induced 0–8% in steps of 2%, and Fig. 1.1a, b shows the preparation of composite.

1.2.3 Scanning Electron Microscopy (SEM)

A scanning electron microscope (SEM) is a type of electron microscope that produces images of a sample by scanning the surface with a focused beam of electrons. The analysis was conducted on Hitachi SU 3500 make at Centre for Incubation Innovation Research and Consultancy (CIIRC) Jyothy Institute of Technology, Bangalore (INDIA). The fractured surfaces of tensile test specimen were studied under SEM.

1.2.4 X-Ray Diffraction

When the geometry of the incident X-rays impinging the sample satisfies the Bragg Equation, constructive interference occurs and a peak in intensity occurs. The powder
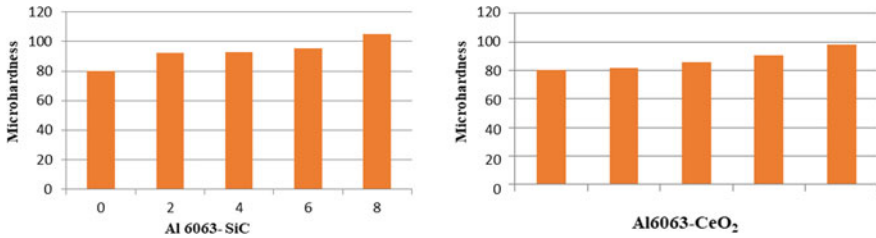
Fig. 1.2 Variation of micro hardness with increased content of SiC and CeO_2 for cast matrix alloy and its composite systems

was collected from the samples of Al6063–SiC and CeO_2 composites for all weight percentage of (0, 2, 4, 6, 8), and diffraction patterns were recorded to confirm the presence of SiC and CeO_2 in the composite. The sample is in powder form so that it can be easily placed in sample holder of dimension 24.6 mm × 1.0 mm.

1.3 Result and Discussion

1.3.1 Micro Hardness Test

Micro hardness tests were performed by applying load of 10 N for a period of 20 s. It can be observed from Fig. 1.2 that the hardness value of composite goes on increases with increase in reinforcement for all composites with different reinforcement which indicate that hardness of the base alloy can be increased with increase in reinforcement which clearly shows the effect of hard reinforcement. It also found that hardness value is more for reinforcement SiC as compared to CeO_2. Addition of 8 wt% of SiC increases hardness of matrix alloy 31.6%, while addition of CeO_2 is 22.25%.

1.3.2 Compression Strength

The results reveal that as percentage of reinforcement increased, the compressive strength also increases. This is because SiC and CeO_2 are strong and hard particulate added to aluminum alloy. The strength of composite systems increases which requires high energy to compress. The variation compressive strength for composite systems is very much similar to other researchers (Fig. 1.3).
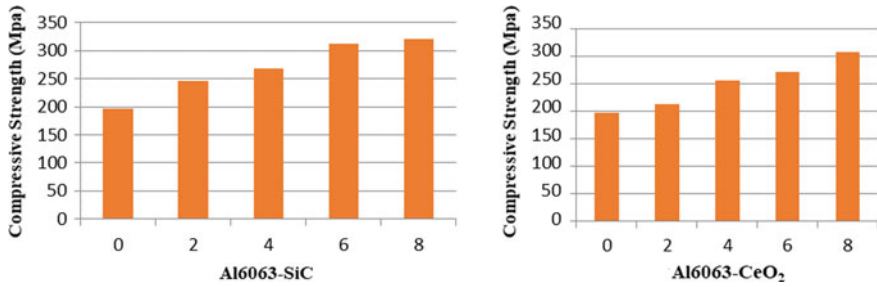
Fig. 1.3 Variation of compressive strength with increased content of SiC and CeO_2 for cast matrix alloy and its composite systems [2, 4]
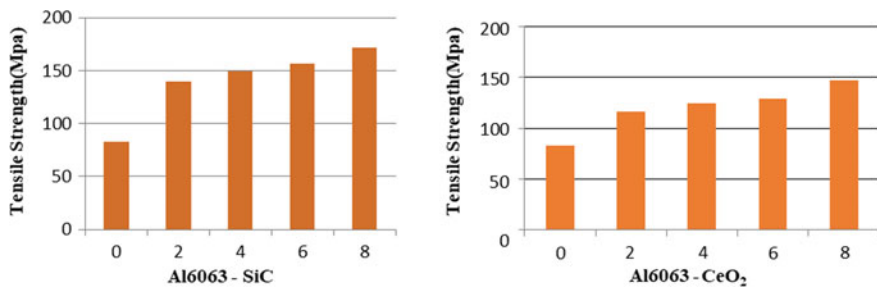
Fig. 1.4 Variation of tensile strength with increased content of reinforcement for cast matrix alloy and its composite systems

1.3.3 Tensile Test

Figure 1.4 summarizes the tensile strength of cast alloy and its composite systems and tries to identify which reinforcement will give the maximum ultimate tensile strength, and from Fig. 1.4 it clearly observed that the maximum tensile strength is for silicon carbide reinforcement, as silicon carbide is harder than cerium oxide. The maximum ultimate tensile strength at 8 wt% composites is found for Al6063–SiC in comparison with Al6063–CeO_2. It was found 51.9% of increase in tensile strength with reinforcing 8% of SiC and 43.6% increase in tensile strength with reinforcing 8% of CeO_2 as compared with base metal matrix alloy.

1.3.4 Charpy Impact Test

It is observed from Fig. 1.5 that as the percentage of reinforcement is increased, the ductility of the material is decreased and brittleness is increased, so due to the impact, the energy absorbed by the composite is decreased with increase in percentage of reinforcement, and similar results are obtained by other researchers [4, 5].
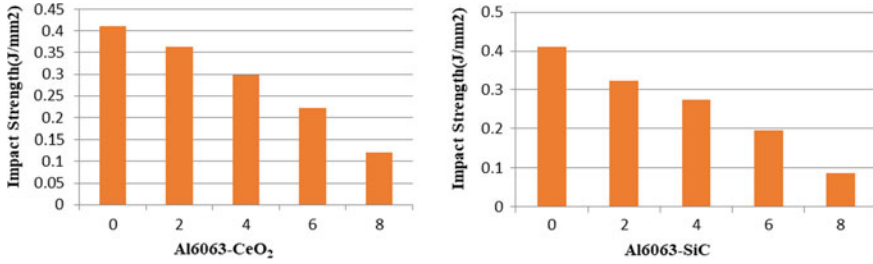
Fig. 1.5 Variation of impact strength with increased content of SiC and CeO_2 for cast matrix alloy and its composite systems

1.3.5 Fractography Studies

The study of fracture surfaces for different weight percentages of SiC and CeO_2 reinforcement under scanning electron microscope (SEM) technique is shown in Fig. 1.6 as the SEM photographs of the tensile test fractured surfaces of the cast Al6063 and its composite systems. It is evident that the base matrix alloy has got larger dimples when compared with different composite system studied for given content of reinforcement. Al6063 matrix alloy showing very large dimples indicates
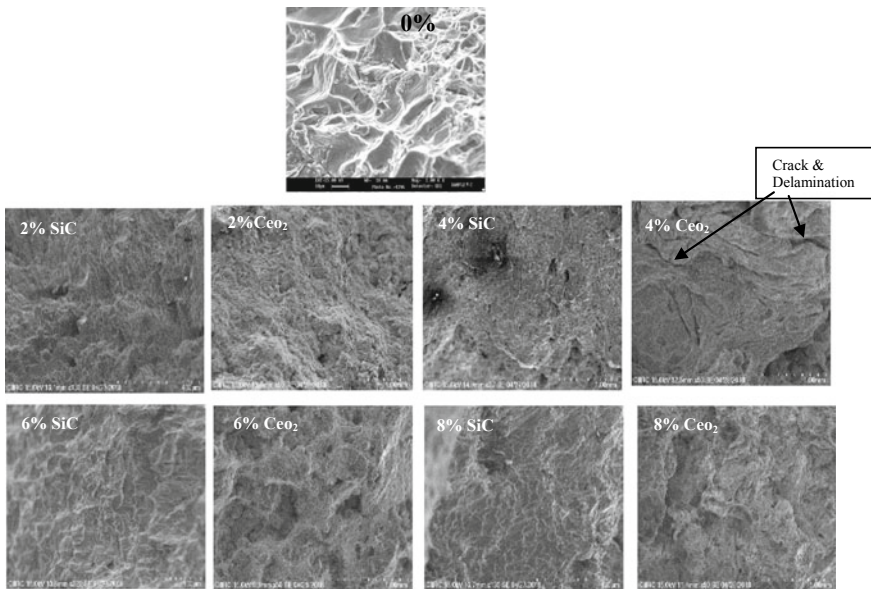
Fig. 1.6 SEM of tensile fractured surface of Al6063 0–8 wt% composites system

ductile fracture as shown in Fig. 1.6 for 0% reinforcement, whereas in case of Al6063-8 wt% composite, particles of reinforcement and medium-sized dimples are visible as evident from Fig. 1.6, and these observations are similar to other researchers [2].

1.3.6 X-Ray Diffraction Analysis

XRD graphs and results given below clearly indicate the presence of reinforcement in the matrix alloy with varying percentage, XRD result shows a variation in the amount of reinforcement embedded in matrix alloy, and this is because XRD samples in powder form in minute quantity from a particular region are taken.

In X-ray diffraction pattern (Fig. 1.7a–i), many peaks are obtained in the 2 span ranging from 5 to 90, but the common peaks at 2 of 38.44°, 44.7°, 65.32° and 77.2° belong to pure Al and the peaks at 2 of 28.5, 38.83°, 50.80°, 78.88° and 82.43° belong to CeO_2 and for SiC 35.1960, 38.370 and 38.31,83.0. With the help of Match software, graphs are compared with JCPDS card JCPDS file #04-0787 for SiC (Table 1.1).
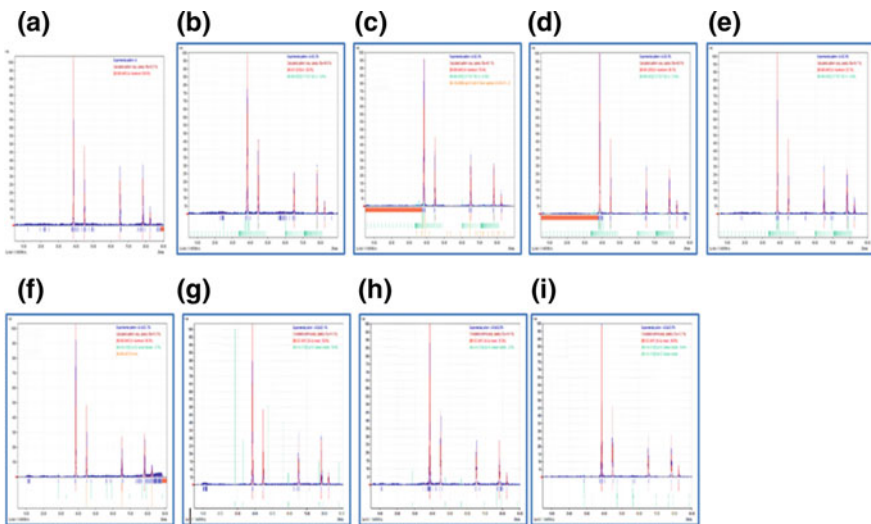
Fig. 1.7 XRD pattern for Al6063 matrix alloy and its composites

Table 1.1 Analysis of XRD data using Match software and identification of the presence of reinforcement with following percentage

Figure 1.7	a	b	c	d	e	f	g	h	i
Name	Al6063	Al6063-2 wt% SiC	Al6063-4 wt% SiC	Al6063-6 wt% SiC	Al6063-8 wt% SiC	Al6063-2 wt% CeO_2	Al6063-4 wt% CeO_2	Al6063-6 wt% CeO_2	Al6063-8 wt% CeO_2
Amount (%)	100%	92% Al 8% SiC	93.1% Al 6.9% SiC	86.1% Al 13.9% SiC	78.4% Al 21.6% SiC	99.3% Al 0.7% CeO_2	97.8% Al 2.2% CeO_2	99.6% Al 0.4% CeO_2	80.6% Al 19.4% CeO_2

1.4   Conclusion

- Successful synthesis and characterization of Al 6063-silicon carbide and cerium oxide composites are obtained.
- Tensile strength of composites increased significantly with increased content of SiC and CeO_2.
- Energy absorbed during the impact test on composites decreased with increased content of SiC and CeO_2 in matrix alloy under identical test condition.
- Micro hardness of composites increased significantly with increased content of SiC and CeO_2.
- It has been noted that the compressive strength of composite increased with increased content of reinforcement and is higher than base aluminum alloy, and Al6063 SiC composites have higher compressive strength than CeO_2 for identical test condition.
- SEM studies clearly show the modes of fractured occurred.
- XRD analysis confirms the presence of SiC and CeO_2 in Al6063 composite with varying percentage.

References

1. Chakraborty, A., Mitra, R., Kamat, S.V., Jain, M.K., Subramanyam, J.: Structure property relations for $MOSi_2$ and Nb particle reinforced Al_2O_3 matrix composite. In: Proceeding of the Third International Conference on Advances in Composites, pp. 547–558 (2013)
2. Ravi kumar, N.V., Pai, B.C., Dwarakadasa, E.S.: Effect of particle content and matrix stength on the mechanical properties of Al-ZN-MG/SiCp composites. In: ADCOMP, IISc, pp. 295–301 (1996)
3. Schwartz, M.M.: Composite Materials Handbook. McGraw-Hill Book Company, New York (1984)
4. Rajesh, P., Rana, R.S., Verma, C.S.: Fabrication of Al–SiCp composite through powder metallurgy process and testing of properties. Int. J. Eng. Res. Appl. **2**, 420–437 (2012)
5. Sekunowo, O.I., Adeosun, S.O., Lawal, G.I., Balogun, S.A.: Mechanical characterization of aluminium bronze-iron granules composite. Int. J. Sci. Technol. Res. **2**(4) (2013)
6. Surappa, M.K.: Metal matrix composites. Mater. Res.: Curr. Scenar. Futur. Proj. 301–318 (2003)
7. Hosamani, G.G., Manoji, V.B., Biradar, V.R., Kallappagol, V.N., Haragapure, L.I.: Characterization of silicon carbide reinforced aluminum matrix composite by using stir casting method. Int. J. Mech. Prod. Eng. (Special issue)
8. Ezatpour, H.R., Sajjadi, S.A., Sabzevar, M.H., Huang, Y.: Investigation of microstructure and mechanical properties of Al6061-nanocomposite fabricated by stir casting. Mater. Des. 921–928 (2016)
9. Ramnath, B.V., Elanchezhian, C., Jaivignesh, M., Rajesh, S., Parswajinan, C., Siddique Ahmed Ghias, A.: Evaluation of mechanical properties of aluminium alloy–alumina–boron carbide metal matrix composites. Mater. Des. **58**, 332–338 (2014)
10. Jagadish, B.S.: Synthesis and characterization of aluminium2024 and graphene metal matrix composites by powder metallurgy. Int. J. Mech. Eng. (SSRG-IJME) **2**(7) (2015)
11. Gupta, M., Surappa, M.K.: Effect of weight percentage of SiC particulates on the ageing behaviour of 6061/SiC metal matrix composites. J. Mater. Sci. Lett. 141283–141285 (1995)

12. Mohal, S.: Microstructural investigation of Aluminium–silicon carbide particulate metal matrix composite fabricated by stir casting. Int. J. Innov. Res. Sci. Technol. (IJIRST) **3**(11) (2017)
13. Ray, S.: Review synthesis of cast metal matrix particulate composites. Mater. Sci. **28**, 5397–5413 (1993)
14. Dewangan, S.K., Arora, A.: Mechanical properties of aluminum 6063 alloy based graphite particles reinforced metal matrix composite. Int. J. Sci. Res. Develop. (IJSRD) **3**(05), 2321-0613

Chapter 2
Feasibility Study of Detonation Wave Initiation by Multiple Structured Blockages in a Plain Tube

S. Srikrishnan, V. Jayakumar and P. K. Dash

Abstract Pulse detonation engines, due to its simplistic design, have gone through critical acclaim in recent years as a viable solution of high-speed propulsion in the aerospace industry. Through various experimental and theoretical methods, researchers are trying for the most explicit method for initiating a controlled detonation in a plain tube. Studies are being conducted on various types of cross sections and multiple forms of blockages to evolve detonation using several chemical and mechanical procedures. Previous study shows a rectangular blockage which blocks about 60% of the flow at 2/3rd distance from the origin produces best detonation wave initiating a sustained exit velocity and increment in pressure. The current paper studies the variation effect of placing multiple blockages in different permutations along the length of the plain tube and their effect on the onset of detonation. It has been observed that multiple blockages placed throughout the length inhibit the possibility of formation of the detonation wave. Further, it has been summarized that an ascending rectangular cascade produces the best onset of detonation wave with a proximal maximum velocity of 10,858 m/s at the outlet when a mixture of kerosene and air at a maximum pressure of 100 MPa is given at the inlet of the tube.

Keywords Detonation · Blockage · Pulse detonation engine

S. Srikrishnan (✉)
Institute of Aeronautical Engineering, Hyderabad, India
e-mail: krishnan.1987@gmail.com

V. Jayakumar
Amrita School of Engineering, Amrita Vishwa Vidyapeetham Chennai, Chennai, Tamil Nadu, India

P. K. Dash
NITTE Meenakshi Institute of Technology, Bangalore, India
e-mail: drpdash@gmail.com

2.1 Introduction

Detonation is normally signified by short pulses of combustion using hypergolic mixtures like hydrogen and oxygen, and however, any practical application of detonation requires a steady and constant flow of gases for the effective supply of thrust in any vehicle. Tubular combustion and transition to detonation is limited by the interval of feasible detonation. The detonation is possible only by completely filling the control volume with both fuel and oxidizer mixture and firing in supersonic speed, where each pulse will give a burst of thrust and the cycle can be repeated. But on the longer run, the downstream of such vehicles will experience both bursts of high-pressure waves and vacuum intermittently causing the loss of thrust. To reduce such a loss, the frequency of the detonation occurring in the tube has to be increased. The frequency of detonation is primarily dependent on the detonation transition time which in turn is dependent on internal geometry, fuel and oxidizer selection, initial spark energy and ambient conditions.

Georgina et al. [1] discussed the effects of orifice plates as a type of blockage in a tubular section and the propagation of detonation waves through experimental methods and high-speed photography to show the onset in transparent plastic tubes. A mixture of hydrogen and oxygen at an initial pressure of 60 kPa is fired in a 1.55 m plastic tube to try and predict the critical inlet pressure required for detonation initiation and transition. The experiment with 50% blockage ratio did have an increment of velocity and pressure, but the critical pressure required for the initiation of detonation could not solved in the experimental procedure.

Bo et al. [2] discussed the effect of spiral blockages on the detonation propagation of hydrogen–oxygen mixtures with an inclusion of a surface roughness factor for the blockages. It has concluded that higher the roughness fraction lower the chance of detonation initiation as the higher surface roughness acts as a detonation quencher and inhibits the flow. The spiral section initiates better detonation transition speeds, and the flow is more sensitive across the spiral due to which failure of detonation is mitigated. Sun et al. [3] studied extensively rotating detonation engines burning a mixture of hydrogen and oxygen under both premixed and non-premixed conditions. In a density-based solver across multiple inlet mass flow rates, the rotating detonation engine behaves similar to a single-wave engine at both premixed and non-premixed conditions. In case of a higher mass flow rate, the single-wave operation is only possible during premixed condition and in a non-premixed condition dual-wave flow occurs. It had been concluded that the thrust offered by the engine burning hydrogen–oxygen mixture is higher in premixed condition than the non-premixed condition.

Lu et al. [4] discussed the effects of back pressure wave propagation on valve-less two-phase air-breathing pulse detonation engine. A successful model of pulse detonation combustor and subsequent operations were performed under different firing patterns where all the tubes were fired in sequential and simultaneous order. It was found that the pressure peaking feasibility is higher during simultaneous firing of all the tubes in comparison to the sequential firing. Forlov et al. [5] performed experiments on continuous detonation of ternary hydrogen, liquid propane and air mixture

in a large-scale annular combustor. The introduction of hydrogen in propane liquid increases the possibility of detonation wave rather than enriching the air with oxygen and a continuously rotating detonation wave was achieved for a small duration.

Wenhu et al. [6] simulated an integrated process of flame acceleration and DDT resulting in detonation propagation in micro-scale and macro-scale channels. It is found that the viscosity and turbulent flame development play a significant role in determining the detonation propagation factor in both these channels and that the rate of detonation propagation across both is not similar. In macro-channels, strong detonation waves decay over the length and are transformed into quasi-detonation waves. Zhenhua et al. [7] studied the detonation propagation modes of ethylene–oxygen mixtures and initiated the fabrication of a helical detonation channel to aid in the onset of detonation. It has been found that for a stoichiometric mixture of ethylene and oxygen, a curved section increases the possibility of detonation wave initiation by morphing the detonation waves from steady to unsteady detonation waves across the helical section. Continuous failure, restart and regeneration occur in the helical tube by which a steady stream of detonation wave has been achieved.

Joshua and Deanna [8] studied the effects of nanosecond repetitive pulsed plasma discharge in the enhancement of detonation waves for a hydrogen–oxygen mixture. While the plasma pulse is not sufficient for ignition of the fuel oxidizer mixture, it has been observed that the plasma pulse can enhance the probability of detonation initiation and transition. Sergio et al. [9] studied the effect of a single blockage in a flow stream of hydrogen–oxygen enriched air mixture when passed through a tube. The tube constrained the flow through a convergent-divergent section acting as a blockage, and it has been found that detonation is initiated in short-run space which is useful for practical applications.

Pandey and Debnath [10] have reviewed the recent advances in pulse detonation engines and studied the phenomena of combustion in a PDE combustor through the effects of fuel–air mixture, combustion, blowdown and purging as a factor of efficiency. It was observed that detonation wave flow path, ejectors and Mach number are the main parameters responsible for improving the propulsion performance of PDE. Further scope of work was also discussed. Hu et al. [11] studied the numerical simulation of DDT of iso-octane vapor in an obstacle filled tube through a single-step reaction mechanism under Navier–Stokes equation. It has been found that the detonation initiation in an iso-octane environment is a function of both pressure and flame parameters. The temporal variation of total energy release rate and flame front location parameters were studied, and the flame was categorized into four stages.

In all the above literature, DDT is studied extensively by the variation of factors like choosing the correct fuel oxidizer mixture, selection of premixed or non-premixed combustion, position of block and blockage ratio, variation of flow parameters, etc. Most of the literature concentrates on hydrogen–oxygen enriched air mixture, but the disadvantage of such a mixture is that they tend to be hypergolic. A more stable fuel oxidizer mixture is required for sustained ignition and propagation of deflagration to detonation waves. Previous presented research have extensively studied the geometry of a blockage and blockage ratio, though not studied extensively the effect of placing multiple blockages throughout the flow stream and their

effect on detonation initiation and propagation [12]. This paper concentrates on the internal geometry of the tubular section and the effect of placing multiple blockages throughout the tubular section in relation to the detonation transition [13].

2.2   Methodology

2.2.1   Modeling

The analysis of a pulse detonation engine done in this paper is based on a shock tube design being a plain tube with multiple blockages at various intervals. A plain tube of 1 m length is considered for the design where for the purpose of analysis, and the inlet is designated to be a pressure inlet where a mixture of kerosene gas and air is supplied at various pressures simulating a diaphragm being blown and the pressure being expanded into the tube. The diameter of the tube is 1 inch or 2.53 cm, and the blockages that have been provided at various distances across the tube have a blockage ratio of 60% of the diameter. The blockage ratio is given by:

$$\text{Blockage Ratio} = \frac{\text{Diameter of Tube} - \text{Height of Blockage}}{\text{Diameter of Tube}}$$

The blockages are positioned throughout the length of the tube as a function of fraction of the tube length like 1/4th, 1/3rd, 1/2nd, 2/3rd and 3/4th of the length of the tube, which simplifies the distribution of blockages during modeling stages and capture of the properties across blockages during analysis stages. Figure 2.1 shows the various forms of models that have been considered for the analysis in this paper.

Model 'a' shows a rectangular spiral setup where three blockages are given at 1/3rd, 1/2nd and 2/3rd the distance of the plain tube. It is similar to a coil spring inserted in the mean of the tube and the blockage ratio of the rectangular element is 60% in each case. Model 'b' represents a cascade blockage where three rectangular blocks are set up in a cascade arrangement continuously at the 1/3rd, 1/2nd and 2/3rd position of the tube. Model 'c' shows a plain tube with multiple blockages which set different positions in the tube length where the blockage height is steadily
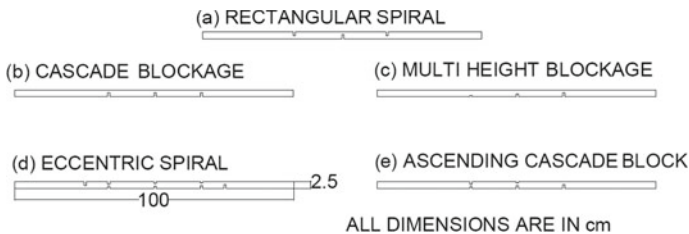
Fig. 2.1   Models considered for the analysis of DDT

increased from 20 to 60% of the diameter of the tube. Model 'd' shows an eccentric spiral arrangement. This is almost symmetric to the multi-height blockage stream and inverse of the same. But in this model, the number of blockages has been increased to study the effect of placing multiple blockages in the flow stream and determine the critical limit of blockages present across the tube. Model 'e' is the minimized version of model 'd' where the number of blockages is reduced so that a comparative study between both can conclude whether restricting the number of blockages in the flow field is a legitimate solution.

2.2.2 Numerical Analysis

The two-dimensional plain tube is modeled using 'GAMBIT' as the meshing tool which has a characteristic ease of usage in 2D meshing and import to any viable commercial software for analyzing fluid flow where an unstructured mesh is constructed to analyze the models in a computational fluid dynamic domain. The scaling factor is considered in meters for the modeling of the tube as shown in Fig. 2.1. The meshing has been done at an average rate of 1800–2000 nodes and 1500–1700 elements so that the analysis is simpler in CFD software tool used. The initial boundary conditions that were used are listed in Table 2.1.

The models are further analyzed in a computational fluid domain having a fluid mixture of kerosene vapor and air pass through the tube using the k–ε model. ANSYS 16.0 workbench is the selected solver and Fluent 16.0 standalone system is used to analyze the above boundary conditions and the results are tabulated and detailed graphical images have been recorded for the easy assimilation of the data. The standard equations of the model are given in Eqs. 1 and 2.

$$\frac{\partial \langle k \rangle}{\partial t} + \frac{\partial [\langle u_i \rangle \langle k \rangle]}{\partial x_i} = \frac{\partial}{\partial x_i}\left[\frac{\langle v_t \rangle}{\sigma_k}\frac{\partial \langle k \rangle}{\partial x_i}\right] + P_k - \langle \epsilon \rangle \tag{1}$$

$$\frac{\partial \langle \epsilon \rangle}{\partial t} + \frac{\partial [\langle u_i \rangle \langle \epsilon \rangle]}{\partial x_i} = \frac{\partial}{\partial x_i}\left[\frac{\langle v_t \rangle}{\sigma_\epsilon}\frac{\partial \langle \epsilon \rangle}{\partial x_i}\right] + C_{\epsilon 1} P_k \frac{\langle \epsilon \rangle}{\langle k \rangle} - C_{\epsilon 2}\frac{\langle \epsilon \rangle^2}{\langle k \rangle} \tag{2}$$

Table 2.1 Input parameters for analysis

S. no.	Description	Input
1	Fuel and oxidizer	Kerosene vapor and air
2	Volume fraction	0.5 for kerosene vapor
3	Inlet pressure	Range from 1 to 100 MPa
4	Inlet velocity	0.15 m/s
5	Back pressure	Vacuum condition
6	Wall function	Standard wall functions without slip or wall heating
7	Temperature	1500 K at the inlet for the mixture

where 'k' represents the energy present in eddies of various sizes which is governed by the transport equation with terms that are model of exact terms, and 'ε' represents the small actions of all eddies which aid in the dissipation of the kinetic energy. Turbulent boundary conditions are used near the wall to resolve steep gradients. The model is then analyzed in a transient boundary condition, and the time step is defined for 1 s divided into 1000 steps as the movement speed predicted through the analysis being very high, anything higher than the division may not be feasible for the capturing of the various properties of the flow at the exit during the process of the flow. It is made sure that the flow is controlled by controlling the residue frequencies and the residue is monitored such that divergence due to temperature increment and large Courant number does not occur.

2.3   Result and Discussions

The models are analyzed in a domain of fluid where the input is a mixture of kerosene vapor and air where the inlet pressures range from 1 to 100 MPa. Table 2.2 shows the increment of exit velocity of the burnt mixture of kerosene vapor and air for the various types of blockages as shown above.

For a minimum inlet velocity of 0.15 m/s inside the tube, the multi-height blockage and ascending cascade perform well by increasing the velocity at the exit across all pressure inputs. The maximum velocity at the exit is achieved by using an ascending cascade blockage ranging at 10,858 m/s when the input pressure is 100 MPa. Further, it can also be seen that during the comparison of ascending cascade blockage and eccentric spiral blockage, even though the blockage is similar in structure, the eccentric spiral blockage performance is inherently low at 7856 m/s for the same input pressure. It can be concluded that increasing the number of blockages throughout the length of the tube may inhibit the flow, and the exit velocity dissipation rate would increase causing an imminent loss. The graphical representation of the above result is shown in Fig. 2.2.

The variation of exit pressure with variable pressure input for different arrangements of blockages is shown in Table 2.3. The onset of detonation is marked by the

Table 2.2 Input pressure versus exit velocity

Input pressure (MPa)	Exit velocity in m/s				
	Multi-height blockage	Eccentric spiral blockage	Cascade blockage	Ascending cascade blockage	Rectangular spiral blockage
1	996	779	822	1065	677
10	3198	2470	2611	3378	2146
100	10,500	7856	8809	**10,858**	6780
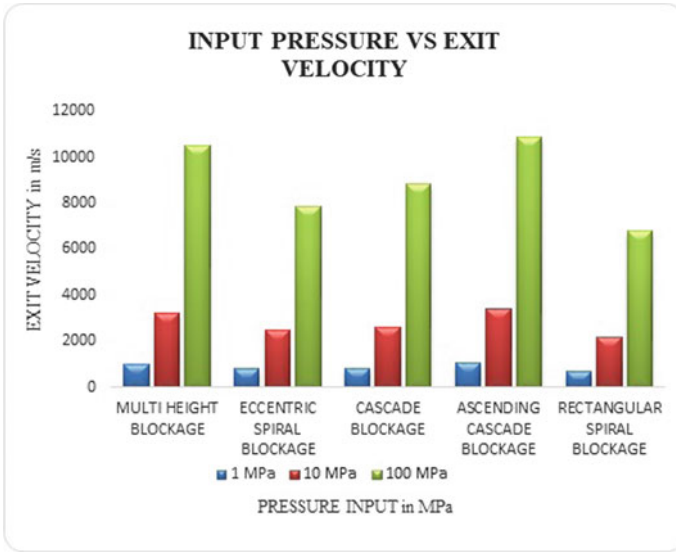
Fig. 2.2 Graphical representation of input pressure versus exit velocity

Table 2.3 Input pressure versus exit pressure

Input pressure (MPa)	Exit pressure in MPa				
	Multi-height blockage	Eccentric spiral blockage	Cascade blockage	Ascending cascade blockage	Rectangular spiral blockage
1	1.005	1.02	1.02	1.04	1.013
10	10.06	10.27	10.22	10.47	10.14
100	100.07	102.79	102.75	**104.96**	101.47

increment of both pressure and velocity at the exit due to the various stages of expansion across the structures of blockages in the flow stream. In the previous comparison, the multi-height blockage and the ascending cascade were analyzed stating that the performance of the two types of blockages is similar. But in case of exit pressure as a factor of detonation initiation and propagation, it is observed that the ascending cascade blockage performs better than that of the multi-height blockage. The other types of block pale in comparison with ascending cascade blockage and gross lower pressures at the exit than the ascending cascade blockage. Across the input pressure range, the multi-height blockage has the lowest possible exit pressures stating that the type of blockage may not be feasible for the onset of detonation where it only increases the exit velocity and not the exit pressure which is almost similar to that of the inlet pressure or close enough to consider that there is variation of pressure across the tubular flow. The above statement is contradictory to the jet flow function, but the placement of the blockages at the various positions with an incremental permutation
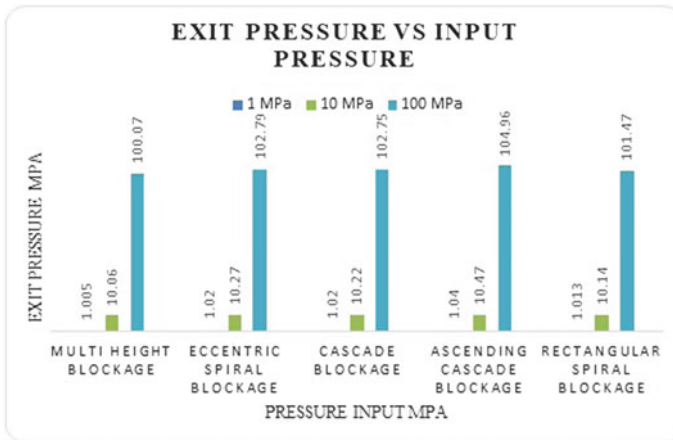
Fig. 2.3 Graphical representation of exit pressure versus input pressure

of the height of the blockage may happen to increase the pressure due to the jumping effect of the flow across the cascade of multiple height blockages.

Further comparing the eccentric spiral, cascade and rectangular spiral blockage, it is clearly stating that the pressure increment across the input of various pressure is significantly lesser compared to the ascending cascade blockage but fares well when compared to the multi-height blockage. Slight change in the placement and height of the blockage in the eccentric spiral and rectangular spiral blockage may mimic the results of the ascending cascade but said analysis has not been formulated as ascending cascade blockage have given the optimum result. The graphical representation of the comparison between exit pressure and inlet pressure of the mixture is shown in Fig. 2.3.

The variation of turbulence kinetic energy across the tube with various permutations of blockages is shown in Table 2.3. The turbulence kinetic energy is physically formulated from the root mean square of the velocities and is the kinetic energy associated with the eddies in the turbulent flow. The turbulent kinetic energy across the comparative data is the highest with the ascending cascade blockage. This shows that the ascending cascade blockage arrangement to the most suitable type of the blockage arrangement in a tubular pulse detonation engine design. Figure 2.4 shows the contour representation of turbulence kinetic energy through an ascending cascade blockage where the input pressure of the mixture is 1 bar (Table 2.4).

Characteristically, the flow remains almost steady till it reaches the imminent blockage and once it crosses the blockage, the flow kinetic energy rapidly increases due to the orifice effect. Subsequent blockages increase the turbulent kinetic energy due to the flow jumping and jet flow effect evolving a maximum of 54,311 m^2/s^2 at the exit of the tubular section. This value is comparatively lower than that of the multi-height blockage and a cascade blockage, but other significant properties like pressure and velocity at the exit for an ascending cascade blockage are higher in
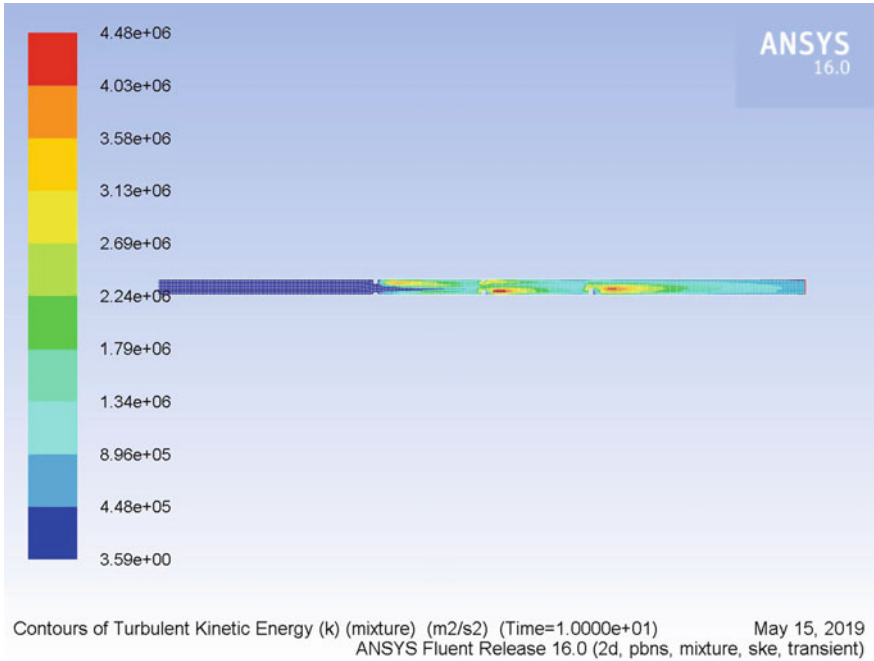
Fig. 2.4   Turbulent kinetic energy (100 MPa input pressure)

Table 2.4   Turbulence kinetic energy versus input pressure

Input pressure (MPa)	Turbulence kinetic energy in m^2/s^2				
	Multi-height blockage	Eccentric spiral blockage	Cascade blockage	Ascending cascade blockage	Rectangular spiral blockage
1	58,678	37,913	66,849	54,311	35,159
10	591,655	389,691	681,500	546,620	358,082
100	4,014,101	2,572,688	4,180,167	**4,478,380**	3,096,003

case of an ascending cascade blockage. It can also be seen that at 100 MPa pressure input the maximum value of turbulent kinetic energy occur when using an ascending cascade blockage having 4,478,380 m^2/s^2.

2.4   Conclusion

With reference to the above results and the detailed discussions, the following conclusion remarks can be achieved:

1. The ascending cascade blockage is the most viable type of flow restrictor and produces the ideal exit velocity of 10,858 m/s and exit pressure of 104.96 MPa for an inlet pressure of 100 MPa in a mixture of kerosene vapor and air jet.
2. The number of blockages across the flow stream must be restricted as 3 blocks per meter of the tube length. Exceeding this limit starts to inhibit the flow causing pressure and velocity loss at the exit as shown by the eccentric spiral blockage when compared to the multi-height or the ascending cascade blockage.
3. Turbulent kinetic energy plays a significant role in the onset of detonation but can be compromised when other salient properties like exit pressure and velocity are higher which aid in the initiation and propagation of detonation waves.

References

1. Georgina, R., Deepinder, J.S.A., Gaby, C.: Visualization of detonation propagation in a round tube equipped with repeating orifice plates. Combust. Flame **198**, 205–221 (2018)
2. Bo, Z., Hong, L., Cheng, W.: On the detonation propagation behavior in hydrogen-oxygen mixture under the effect of spiral obstacles. Int. J. Hydrogen Energy (2017)
3. Sun, J., Zhou, J., Liu, S., Lin, Z.: Numerical investigation of a rotating detonation engine under premixed/non-premixed conditions. Acta Astranautica (2018)
4. Lu, J., Zheng, L., Wang, Z., Peng, C., Chen, X.: Operating characteristics and propagation of back-pressure waves in a multi-tube two-phase valveless air-breathing pulse detonation combustor. Exp. Therm. Fluid Sci. **61**, 12–23 (2015)
5. Forlov, S.M., Aksenov, V.S., Ivanov, V.S., Shamshin, I.O.: Continuous detonation combustion of ternary "hydrogen-liquid propane-air" mixture in annular combustor. Int. J. Hydrogen Energy 1–13 (2017)
6. Wenhu, H., Yang, G., Chung, K.L.: Flame acceleration and deflagration-to-detonation transition in micro- and macro-channels: an integrated mechanistic study. Combust. Flame **176**, 285–298 (2017)
7. Zhenhua, P., Jun, Q., Jianfeng, P., Penggang, Z., Yuejin, Z., Mingyue, G.: Fabrication of a helical detonation channel: effect of initial pressure on the detonation propagation modes of ethylene/oxygen mixtures. Combust. Flame **192**, 1–9 (2018)
8. Joshua, A.T.G., Deanna, A.L.: Enhancement of the transition to detonation of a turbulent hydrogen–air flame by nanosecond repetitively pulsed plasma discharges. Combust. Flame. **199**, 258–266 (2019)
9. Sergio, B., Joshua, A.T.G., Julius, R., Jonas, P.M., Oliver, C.P., Jorn, S.: Detonation initiation in pipes with a single obstacle for mixtures of hydrogen and oxygen-enriched air. Combust. Flame **198**, 290–304 (2018)
10. Pandey, K.M., Debnath, P.: Review on recent advances in pulse detonation engines. J. Combust. 1–16 (2016)
11. Hu, M., Zhenjuan, X., Wei, G., Changfei, Z., Dong, W.: Numerical simulation of the deflagration to- detonation transition of iso-octane vapor in an obstacle-filled tube. Int. J. Spray Combust. Dyn. **10**(3), 244–259 (2018)
12. Srikrishnan, S., Dash, P.K., Jayakumar, V.: Evaluation of critical blockage ratio and pulse length in a pulse detonation engine using CFD and MATLAB. In: MATEC Web of Conferences, vol. 172, pp. 1–8 (2018)
13. Srikrishnan, S., Dash, P.K.: 2D CFD analysis of deflagration to detonation transition in closed pipe using different blockage. IJMET **8**(6), 447–454 (2017)

Chapter 3
Spectral Density at Roof of Setback Tall Building Due to Time Variant Wind Load

Amlan Kumar Bairagi and **Sujit Kumar Dalui**

Abstract Turbulence due to wind around conventional square shape bluff body creates the pressure difference of different planes of the body. Nevertheless, the unconventional bluff body creates a large amount of turbulence around its face and on the roof region. This paper highlights the pressure variation of top roof and setback roof of square and setback tall building with respect to different time domains. The frequency of the roof due to wind also affects the pressure fluctuation on neighbor faces. Most of the pressure fluctuation develops at 0.06 s which forms the initial time and maximum pressure difference occurred at the setback roof for along wind condition. The present study concentrated on the fluctuation of time-dependent pressure between top and setback roof to take special care during the design.

Keywords Spectral density · Setback tall building · Roof pressure

3.1 Introduction

Velocity of wind changes continuously with the building height. Similarly, the pressure around the building always fluctuates with respect to time, and therefore, the frequency and the spectral density change abruptly. The turbulence around the conventional tall building changes its vortex for the unconventional setback tall building. The turbulence, pressure, frequency and spectral density on the top roof of the building have some amount of difference in setback roof of the building. A number of past studies were highlighted the wind effect on different unconventional tall buildings. Kim et al. [1] studied the tapered tall building aeroelastic models with different taper ratios. Kim and Kanda [2] highlighted the static and dynamic wind pressure distribution on tapered and setback tall building. Tanaka et al. [3] presented the wind flow

A. K. Bairagi (✉) · S. K. Dalui
Department of Civil Engineering, Indian Institute of Engineering Science and Technology, Shibpur, Howrah, India
e-mail: bairagiak@gmail.com

S. K. Dalui
e-mail: sujit_dalui@rediffmail.com

characteristics on thirty-four number of tall buildings with analytical and experimental tools. Bairagi and Dalui [4, 5] estimated the optimum distance where interference effects nullify and principal building behave like isolate building. Mukherjee and Bairagi [6] focused the wind behavior around 'N' plan shape tall building by CFD analysis. Mendis et al. [7] developed the solution of different mistakes of CFD analysis. Xu and Xie [8] evaluated the optimization of aerodynamic effect on tall building and perfect fitted wind angle. Roy and Bairagi [9] presented the wind-induced pressure and force variation on setback tall building with different geometrical shapes. Tamura et al. [10] estimated the dynamic response on tall building for different configurations. Elshaer and Bitsuamlak [11] optimized the opening of tall building to reduce the wind-induced load. Bairagi and Dalui [12] compared the different aerodynamic parameters between various setback tall buildings. Namchu et al. [13] highlighted the pressure coefficients on tall chimney for different wind terrain conditions. Bairagi and Dalui [14] highlighted the aerodynamic effects and power spectral density on setback roof compared to the top roof of setback model. Mukherjee and Bairagi [15] studied the interference effect on square plan shape tall building due to setback model for different orientations. Rajasekarababu and Vinayagamurthy [16] studied the experimental analysis of sharp edge setback model of aspect ratio 1:5. The study described the hybrid turbulence models, which used delayed detached eddy simulation (DDES) and improved delayed detached eddy simulation (IDDES) and introduced the treatment of wall for roughness parameter combination.

The present study is based on computational fluid dynamics (CFD) simulation and highlights the variation of pressure on top roof and the setback roof on different time intervals and the spectral density of that particular region for along and across wind conditions. The considered models are square plan shape bluff body and a setback tall model of the setback roof on both sides and at half of the height from base of the model.

3.2   Model Detail

Two numbers of analytical models have been placed inside the domain and analyze the spectral density and pressure variations on the top surfaces of the models. The square (SQ) model has length (L): breath (B) which was 1 and height (H): length (L) which was 2. A setback (SB) model also considered with the same aspect ratio of SQ model. The setback distance used 20% of the length of the model and placed on both sides and half-height of model from base. As the setbacks are equally distributed, the total area of setback roof and top roof of the SB model compared it to SQ model. The wind incidence angels are considered from 0° to 90° at 15° intervals (see Fig. 3.1).
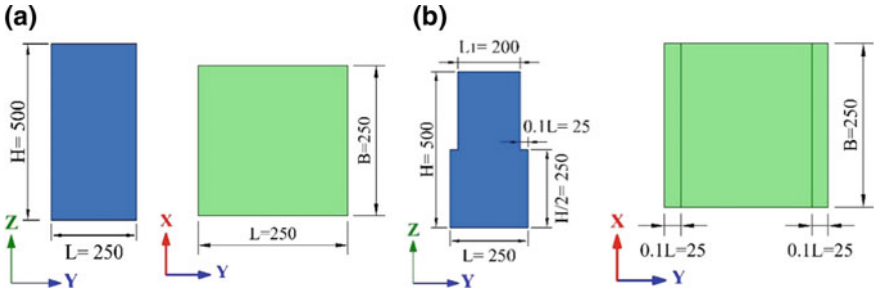
Fig. 3.1 Model details for **a** SQ and **b** SB

3.3   Analytical Domain and Mesh

The computational fluid dynamics (CFD) is a widely accepted method of for the analytical application of wind engineering. The present study based on this CFD simulation. The models are placed inside the analytical domain at 5H from the extreme edge of the model to the inlet and sidewalls of the domain and 15H and 6H for outlet and top of model, respectively, as stated by Frank et al. [17] (see Fig. 3.2a). The height of analytical model is presented by H. The boundary conditions are free slip for the sidewall of domain, i.e., $U_{wall} = 0$, $\tau_w = 0$ and no slip for model wall, i.e., $U_{wall} = 0$. Here, U_{wall} is velocity normal to the wall, and τ_w is the wall shear stress. The power law is introduced in this study to estimate the velocity around the experimental model as explained in SP:64 (S&T) [18] as shown in Eq. 3.1.

$$U/U_H = (Z/Z_H)^\alpha \tag{3.1}$$

where U represents the horizontal wind speed at an elevation Z; U_H represents the 10 m/s speed at the reference elevation Z_H; α represents the power law index 0.133 for terrain category 2; and Z_H is 1.0 m. The kinetic energy of turbulence and its
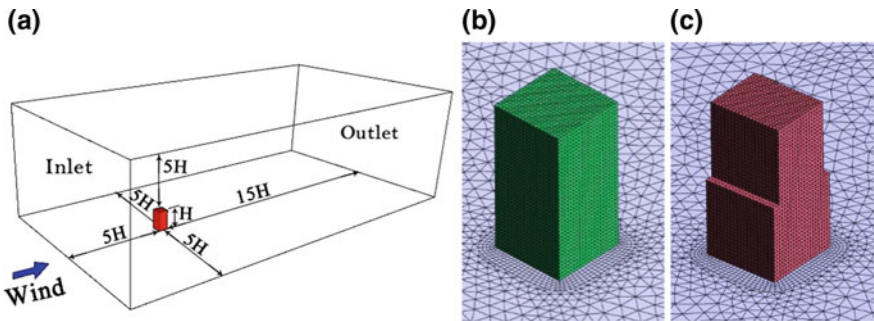
Fig. 3.2 **a** Computational domain for CFD simulation; **b** mesh detail of SQ model; and **c** mesh detail of SB model
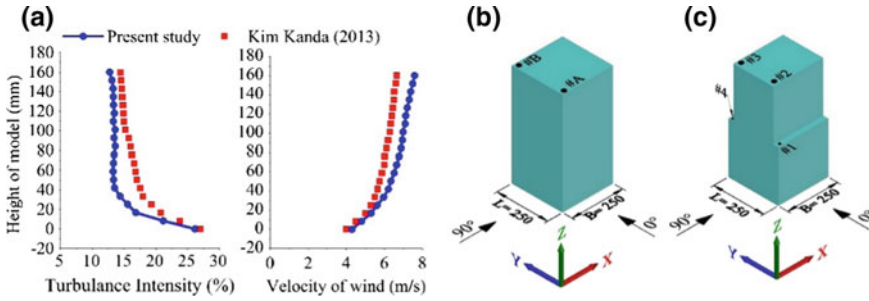
Fig. 3.3 **a** Validation of velocity and turbulence intensity of wind between present studies with Kim Kanda [2]; **b** pressure tapping points on the roof of SQ; and **c** for SB

dissipation rate at the inlet section are calculated according to Eq. 3.2.

$$k = 1.5\left(U_{avg} \times I\right)^2 \text{ and } \varepsilon = C_\mu^{0.75} \times \left[k^{1.5}/l\right] \tag{3.2}$$

where U_{avg} represents the mean velocity at the inlet; I represents the turbulence intensity; and l denotes the turbulence integral length scale. The $k - \varepsilon$ turbulence model has air temperature 25 °C with tetrahedron meshing (see Fig. 3.2a, b).

3.4 Comparison with Analytical Study

This analytical study also validated with the experimental study of setback model discussed by Kim and Kanda [2]. The experimental model was 40 m × 24 m × 160 m with 8 m setback in 1:400 scale was a study in 1.8 m × 1.8 m × 12.5 m wind tunnel at the University of Tokyo. The simulated model has the same aspect ratio with the same boundary conditions. The velocity profile and turbulence intensity of present study validated with Kim and Kanda [2] as shown in Fig. 3.3a.

3.5 Results and Discussion

Pressure variation of unconventional rooftop is quite different compared to the conventional rooftop of tall building. In this study, the setback model has three numbers of roof. One is top and another two are setback at half of the building height. The attacking wind creates a huge amount of turbulence near the setback roof and surrounding surface of the model. Bairagi and Dalui [19] conferred the variation of spectral density on the setback roof of tall model. The authors were considered an unconventional setback model which had setback on one side. This study is discussed the pressure variation, and the power spectral density calculation is carried out in

this study for along the wind and across the wind conditions. The pressure tapping points are considered at the edge of the roof of SQ and SB model (see Fig. 3.3b, c). The points #A and #B are located at 0.04 L from the edge of top roof of SQ model. Similarly, for the SB model has #1, #2, #3 and #4 are the pressure tapping points. The points #1 and #4 are situated at 0.15L from the edge and #2 and #3 are 0.24 L and 0.96 L, respectively, from the edge.

3.5.1 Pressure-Transient Analysis

The change of pressure over time is the pressure-transient analysis. This study high-lighted the pressure fluctuation at the rooftop of SQ and SB model followed by Eq. 3.3.

$$C_p(t) = [P(t) - P_0]/(0.5\rho V_z^2) \tag{3.3}$$

where $P(t)$ is the pressure at time t, P_0 is the reference static pressure of that particular point, ρ is the density of air and V_z is the mean velocity at the height of the roof. Here, negative sign denotes suction, and positive sign presents the pressure.

Pressure coefficient at top roof and setback roof with respect to time for along and across wind conditions has been plotted (see Fig. 3.4). From the figures, it is clear that the high amount of pressure fluctuation is developed at first 0.06 s. The maximum pressure coefficient (3.52) observed at the beginning of the flow of the SB model at the tapping point #3 and maximum suction (−1.8) noticed at 1.43 s at tapping point

Fig. 3.4 Comparison of pressure transient for SQ and SB model at **a**, **b** top roof along wind and across wind; **c**, **d** setback roof of SB model along wind and across wind

#A of SQ model for along wind condition as shown in Fig. 3.4a. The point #B and #3 has maximum pressure 1.38 for 2.85 s and 1.66 for 2.82 s and suction is −1.6 for 1.46 s and −1.25 for 1.2 s. For across wind condition, maximum pressure (1.38) is developed at #B for SQ model at 2.87 s and maximum suction −2.08 at #3 for 1.42 s (see Fig. 3.4b). After that, it may be said that the pressure coefficient of SB is greater than the SQ model. Again, the pressure in the setback zone at #1 and #4 has 1.55 and 1.87 for 2.82 s and 0.02 s for along wind condition (see Fig. 3.4c), where maximum suction is 1.44 in 1.28 s at #4 point. For across wind condition, pressure has 1.07 and 1.30 in 2.56 s and 2.79 s. The suction is −2.02 is same for #1 and #4 points for 1.34 s (see Fig. 3.4d). According to the above condition, it may be said that the pressure variation is maximum at setback region due to a large amount of turbulence due to setback for along wind condition.

3.5.2 Spectral Density on Top and Setback Roof

Power spectral density (PSD) is the process, which defines the strength of energy as a function of frequency variation of a particular point. In this connection, anyone can calculate the frequency and amplitude of a variable signal in a time series. Another non-dimensional part Strouhal number takes place in this oscillating flow mechanism. The equations of PSD and Strouhal number are described under Eqs. (3.4)–(3.5), respectively.

$$[S_p(f)]/\sigma^2 \qquad (3.4)$$

$$f B/U \qquad (3.5)$$

where S_p is the power spectral density in energy/frequency, f is the frequency in Hz, σ is the standard deviation of pressure variation with respect to time, U is the flow velocity in m/s and B is height of pressure tapping point marked as #.

Figure 3.5 represents the PSD of top roof and the setback roof of SQ and SB models for across and along wind conditions at the points as stated in the previous section. For along wind condition, the spectral density of farthest point #B has high value compared to the #A at the Strouhal number 0.1 (see Fig. 3.5a). Similarly, the farthest point #2 has high spectral density with respect to #1 and has Strouhal number 0.05. Again for across wind condition, the SB model has less spectral value compared to SQ model at the Strouhal number 0.07 in Fig. 3.5b. In the case of setback roof, the spectral value of #1 is 0.12 for the fB/U value 0.025, whereas at point #4 has spectral value 0.05 for fB/U value 0.038 (see Fig. 3.5c). From this graph, it may be said that the high amount of pressure fluctuation observed in the setback zone of SB model for along wind condition. Figure 3.5d presents the spectral density curve for across wind condition. Here, the spectral density fluctuation is minimum except the Strouhal number 0.076. In this zone, high amount of spectral density variation is
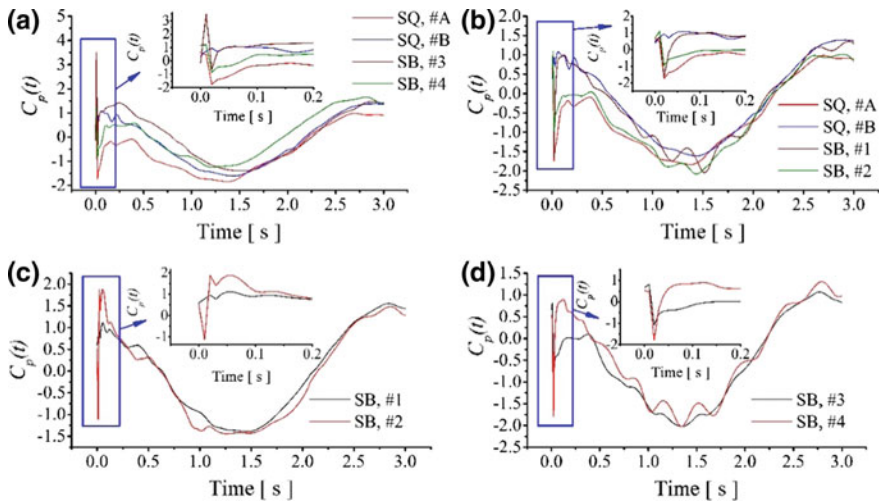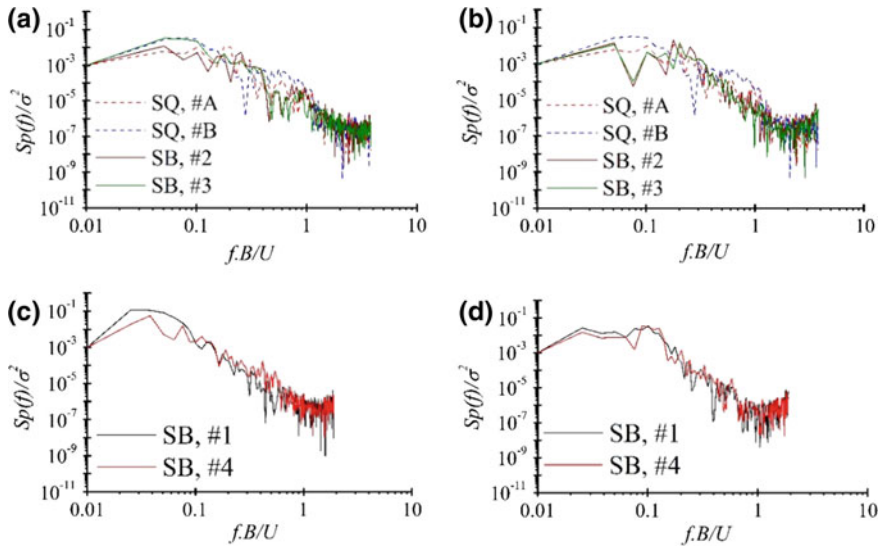
Fig. 3.5 Comparison of spectral density of SQ and SB model at **a**, **b** top roof along wind and across wind; **c**, **d** setback roof of SB model along wind and across wind

compared to #1 and #4. According to those graphs, it is clear that the SB model has higher spectral density variation in its setback region and affects the neighbor faces to change its frequency due to the high amount of turbulence. Therefore, special care should be adopted to design the setback roof and the neighbor face compared to the conventional roof of a tall building.

3.6   Conclusion

The CFD simulation has been studied in this paper for square and setback tall model to calculate the pressure transient and power spectral density at the top roof and setback roof. The number of simulations has been conducted in CFD analysis for along and across wind conditions. The results convey the message to the designer to consider special care to design the setback roof and adjacent wall of the setback tall building. The number of important features is observed in this study and stated as follows.

- High amount of pressure fluctuation is observed at first 0.06 s for both square and setback model.
- Maximum pressure (3.52) has been developed on the top roof of the setback model at the initial time for along wind condition. However, the square model has less pressure at the same time series.

- The maximum pressure variation has been observed for across wind condition on the setback model for 0.15 s.
- The farthest setback roof for along wind condition has maximum pressure coefficient 1.87 for 0.02 s and 1.30 for 2.77 s and has the same suction (-2.02) for 1.34 s.

References

1. Kim, Y.M., You, K.P., Ko, N.H.: Across-wind responses of an aeroelastic tapered tall building. J. Wind Eng. Ind. Aerodyn. **96**, 1307–1319 (2008)
2. Kim, Y.C., Kanda, J.: Wind pressures on tapered and set-back tall buildings. J. Fluids Struct. **39**, 306–321 (2013)
3. Tanaka, H., Tamura, Y., Ohtake, K., Nakai, M., Kim, Y.C., Bandi, E.K.: Aerodynamic and flow characteristics of all buildings with various unconventional configurations. Int. J. High-Rise Build. **2**, 213–228 (2013)
4. Bairagi, A.K., Dalui, S.K.: Evaluation of interference effects on parallel high-rise buildings for different orientation using CFD. In: 3rd World Conference on Applied Sciences, Engineering & Technology, pp. 764–774. Kathmandu, Nepal (2014)
5. Bairagi, A.K., Dalui, S.K.: Optimization of interference effects on high-rise building for different wind angle using CFD simulation. Electron. J. Struct. Eng. **14**, 39–49 (2014)
6. Mukherjee, A., Bairagi, A.K.: Wind pressure and velocity pattern around 'N' plan shape tall building—A case study. Asian J. Civil Eng. (BHRC) **18**, 1241–1258 (2017)
7. Mendis, P., Mohotti, D., Ngo, T.: Wind design of tall buildings, problems, mistakes and solutions. In: 1st International Conference on Infrastructure Failures and Consequences, Melbourne, Australia (2014)
8. Xu, Z., Xie, J.: Assessment of across-wind responses for aerodynamic optimization of tall buildings. Wind Struct. **21**, 505–521 (2015). (Techno-Press Ltd.)
9. Roy, K., Bairagi, A.K.: Wind pressure and velocity around stepped unsymmetrical plan shape tall building using CFD simulation—A case study. Asian J. Civil Eng. (BHRC) **17**, 1055–1075 (2016)
10. Tamura, Y., Xua, X., Tanakac, H., Kima, Y.C., Yoshidaa, A., Yangd, Q.: Aerodynamic and pedestrian-level wind characteristics of super-tall buildings with various configurations. In: 10th International Conference on Structural Dynamics, EURODYN, vol. 199, pp. 28–37. Procedia Engineering (2017)
11. Elshaer, A., Bitsuamlak, G.: Multiobjective aerodynamic optimization of tall building openings for wind-induced load reduction. American Society of Civil Engineers (2018)
12. Bairagi, A.K., Dalui, S.K.: Comparison of aerodynamic coefficients of setback tall buildings due to wind load. Asian J. Civil Eng. Build. Housing **19**, 205–221 (2018)
13. Namchu, A.D., Bairagi, A.K, Chakroborty, S.: Aerodynamic coefficients of steel stacks under different terrain category. In: Proceeding of International Conference on Frontier in Engineering Applied Science and Technology (FEAST'18), pp. 133–138. NIT Tiruchirappalli (2018)
14. Bairagi, A.K., Dalui, S.K.: Aerodynamic effects on setback tall building using CFD simulation. In: 2nd International Conference on Advances in Dynamics, Vibration and Control, pp. 381–388. NIT Durgapur (2018)
15. Mukherjee, S., Bairagi, A.K.: Interference effect on principal building due to setback tall building under wind excitation. In: SEC18, Proceedings of the 11th Structural Engineering Convention—2018. Jadavpur University, Kolkata, India (2018)
16. Rajasekarababu, K.B., Vinayagamurthy, G.: Experimental and computational simulation of an open terrain wind flow around a setback building using hybrid turbulence models. J. Appl. Fluid Mech. **12**, 145–154 (2019)

17. Franke, J., Hirsch, C., Jensen, A., Krüs, H., Schatzmann, M., Westbury, P., Miles, S., Wisse, J., Wright, N.G.: Recommendations on the use of CFD in wind engineering. COST Action C14. Impact of Wind and Storm on City Life and Built Environment. Von Karman Institute for Fluid Dynamics (2004)
18. SP 64 (S&T): Explanatory Hand Book on Indian Standard Code of Practice for the Design Loads (Other than Earthquake) for Buildings and Structures (Part-3. Wind Loads) [IS:875 (Part-3):1987]. Bureau of Indian Standards, New Delhi, India (2001)
19. Bairagi, A.K., Dalui, S.K.: Comparison of pressure coefficient between square and setback tall building due to wind load. In: SEC18, Proceedings of the 11th Structural Engineering Convention—2018. Jadavpur University, Kolkata, India (2018)

Chapter 4
Distribution of Wind Pressure Around Different Shape Tall Building

Amlan Kumar Bairagi and **Sujit Kumar Dalui**

Abstract Wind effect is the most interesting and important parameter for different structural elements like sidewall, roof and around the building also. A number of researchers were presented their thoughtful inspections on different, unconventional tall buildings due to wind issue. The present study focuses on the pressure distribution around the square and setback tall buildings due to wind load. The models have single and double type setback at different elevations. The pressure calculation was conducted by analytical study of plane and highlights the pressure fluctuation. Some amount of pressure bulb was observed on the leeward side of setback model, which mean the increase of suction on that particular region. The excessive amount of suction envelop recognized at the top roof of setback model compared to square model.

Keywords Setback model · Pressure coefficient · Tall building

4.1 Introduction

According to architectural point of view, setback tall building always robbed the feather of elegance. Environmental effects like wind also claim to reveal around the building and its surrounding region. Mendis et al. [1] enumerated simple quasi-static treatment of wind load on tall buildings. Irwin et al. [2] established the energy in tall building increased with the increase in the height of a tall building. Kim et al. [3] carried out for three aeroelastic, tapered, tall building models with taper ratios of 5, 10 and 15%. Kim and Kanda [4] focused the wind pressure on the setback and tapered shape tall buildings in both static and dynamic for different flow condition. Tanaka et al. [5] studied the aerodynamic response due to wind and

A. K. Bairagi (✉) · S. K. Dalui
Department of Civil Engineering, Indian Institute of Engineering Science and Technology, Shibpur, Howrah, India
e-mail: bairagiak@gmail.com

S. K. Dalui
e-mail: sujit_dalui@rediffmail.com

flow characteristics of tall buildings with thirty-four numbers unconventional shapes in wind tunnel test and CFD simulation. Bairagi and Dalui [6, 7] evaluated the interference effects, pressure coefficients and optimum distance on parallel high-rise buildings for different orientation using CFD. Mukherjee and Bairagi [8] studied the 'N' plan shape tall building and evaluated the pressure, force and velocity around the model. Mendis et al. [9] discussed a number of problems, mistakes and solutions for CFD wind analysis. Baby et al. [10] presented an overview of the optimal external shape and structural system for tall buildings subject to aerodynamic loads and the response of a structure through a comprehensive investigation of the building. Xu and Xie [11] focused the aerodynamic optimization of tall buildings and best compromise wind issues. Roy and Bairagi [12] discussed wind pressure and force coefficients on stepped tall building at different geometrical shape placed on above to each other like rectangular, square and triangular. Tamura et al. [13] conferred pedestrian level and aerodynamic wind characteristics of super-tall buildings with various configurations and conducted the dynamic wind response. Mittal H et al. [14] investigated the effect of building shape (square, tapered and setback) and wind direction on pedestrian level. Bairagi and Dalui [15] discussed comparison of aerodynamic coefficients between two setbacks tall buildings due to wind load. Namchu et al. [16] highlighted the pressure coefficients on tall chimney for different wind terrain condition. Bairagi and Dalui [17] highlighted the aerodynamic effects and power spectral density on setback roof compare to the top roof of setback model. Bairagi and Dalui [18] focussed on pressure coefficient on square and both side setback tall building and concluded the pressure coefficient of the setback roof was 205.4% more effective than the top roof. The present study discussed the pressure coefficient around the square and the setback tall building at different plane for along and across wind condition.

4.2 Description of Model

Different types of unconventional modes were analyzed by the wind tunnel test and the test is expensive. To overcome this situation, computational fluid dynamics (CFD) is a widely acceptable simulation process of wind analysis. This study based on this type of simulation. Three sets of models, namely S1, S2 and S3, are used in this study. All the models have l/b ratio is 1 and the h/b is 2. The S1 model has same plan area along height, but S2 and S3 changed their plan area $h/2$ and $h/3$ level from the ground. The S2 model has 20% setback at $h/2$ level and S3 has 10% setback at each $h/3$ and $2h/3$ level. The attacking wind angles are from 0° to 180° at 15° interval. The considered h, b and l are 500 mm, 250 mm and 250 mm, respectively (see Fig. 4.1).
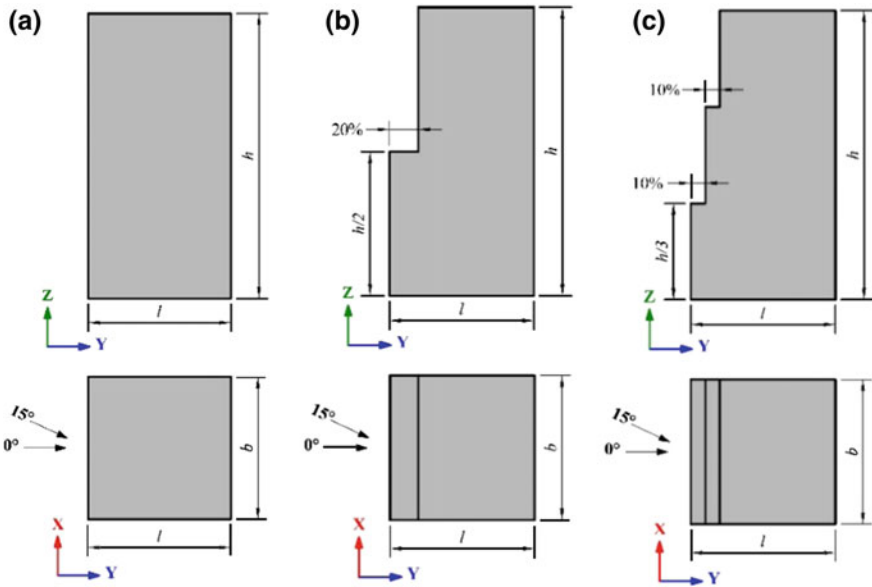
Fig. 4.1 Elevation and plan of model. **a** S1, **b** S2 and **c** S3

4.3   Analytical Domain and Mesh

The three models were placed inside the domain for CFD simulation. The boundary of domain has been set $5H$ from inlet and both sidewalls and $6H$ from the base of model as stated by Frank et al. [19], Revuz et al. [20] (see Fig. 4.2a). Here, H is the height of the analytical model. The boundary conditions for different walls and different non-dimensional parameters are stated in Table 4.1.
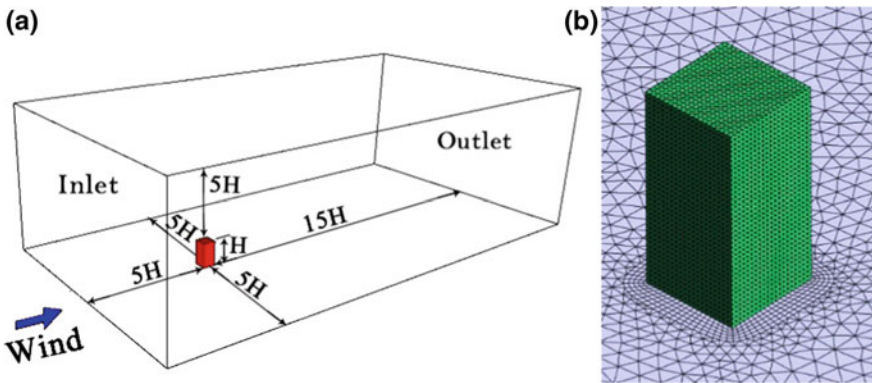
Fig. 4.2 **a** Computational domain for CFD simulation. **b** Mesh detail of square model

Table 4.1 Boundary conditions and non-dimensional parameters

Condition	Parameters
Flow regime	Subsonic
Turbulence intensity	Low (1%)
Method of mesh	Tetrahedron
Inlet	$U/U_H = (Z/Z_H)^\alpha$
Relative pressure of outlet	Zero
Sidewall	Free slip
Model wall	No slip
Air temperature	25 °C
Model wall roughness	Smooth wall
Velocity of wind	10 m/s
Ground roughness (α)	0.133
k	$3/2\,(U_{avg} \times I)^2$
ε	$C_\mu^{(3/4)} \times \left[k^{(3/2)}/l \right]$

Where U is the horizontal wind speed at an elevation Z; U_H is the speed at the reference elevation Z_H; which was 10 m/s; Z_H is 1.0 m; k is the kinetic energy of turbulence and ε is the dissipation rate; U_{avg} is the mean velocity at the inlet; I is the turbulence intensity; l is the turbulence length scale; C_μ is the turbulence model constant, i.e., 0.09. The mesh detail of the S1 model (see Fig. 4.2b).

4.4   Comparison with Analytical Study

The analytical study validated with the experimental study of square model discussed by Kim and Kanda [21]. The experimental study was conducted in Eiffel-type wind tunnel at the University of Tokyo. The experimental model had $L = 100$ mm, $B = 100$ mm, $H = 400$ mm and length scale 1/400 with $\alpha = 0.13$. The blockage ratio was 1.2% with wind flow at 6.5 m/s. The simulated square model has the same aspect ratio and has same non-dimensional parameters adopted by the author. The validation of turbulence intensity and mean wind speed as shown in Fig. 4.3.

4.5   Results and Discussion

Pressure contour around the models S1, S2 and S3 are presented in this study. The pressure distribution on *YZ* and *XZ* plane has been studied for along the wind and across wind conditions. Figure 4.4a shows the wind pressure contour at *YZ* plane and at the center of model for along wind condition for S1 model. For along wind
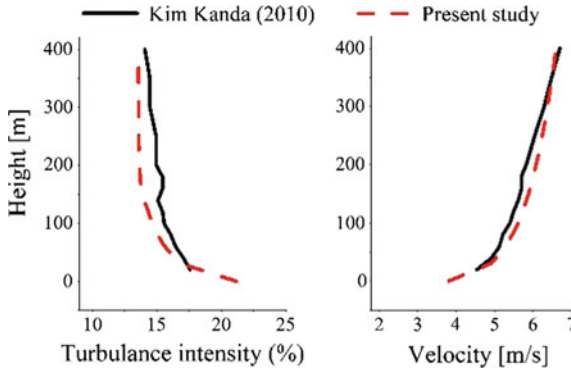
Fig. 4.3 Validation of turbulence intensity and mean wind speed of square model with Kim and Kanda [21] and present study
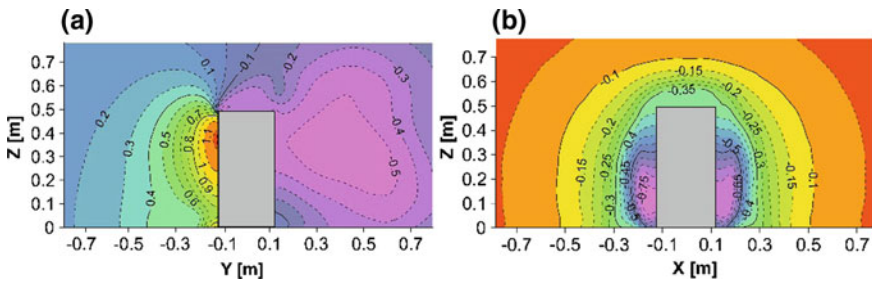
Fig. 4.4 Wind pressure coefficient around S1 model for **a** along wind condition, **b** across wind condition

condition, the windward face encircled by the ranged from 1.2 to 0.1 and the top and leeward faces ranged from −0.1 to −0.5. In this connection, the excessive amount of suction shown in purple color at −0.5 on leeward zone. Similarly, the pressure contour at the *XZ* plane and the center of the model for across wind conditions showcased in Fig. 4.4b. For this condition, the pressure envelope ranged from −0.1 to −0.75 and the values are high suction. A comparative study also carried out between S2 and S3 models on *YZ* and *XZ* plane for 0°, 90° and 180° wind incidence angles as shown in Table 4.2. Mou et al. [22] found the large amount of pressure difference on leeward surface further established the negative and positive pressure around the building depends upon the width of the building. No special change has been focused for along wind condition for 0° wind on *YZ* and *XZ* plane except the bulb region on the leeward face of S2 and S3 models compared to S1 model. However, large amounts of pressure variant take place on opposite sides of the setback face on the *YZ* plane for 90° wind angle. S2 model has line −0.85 near the top and bottom of setback zone. However, S3 model has the same line at the lowest part of setback zone. A beautiful violet color zone (−0.7) observed between *Y* ranges from 0.1 to 0.2. Simultaneously, model S2 has a light green color (−0.45) on that particular Y range. For along wind

Table 4.2 Wind pressure coefficient around models S2 and S3 at *YZ* and *XZ* plane for 0°, 90° and 180° wind angle

Wind angle	Pressure plane	S2	S3
0°	YZ		
	XZ		
90°	YZ		
	XZ		
180°	YZ		
	XZ		
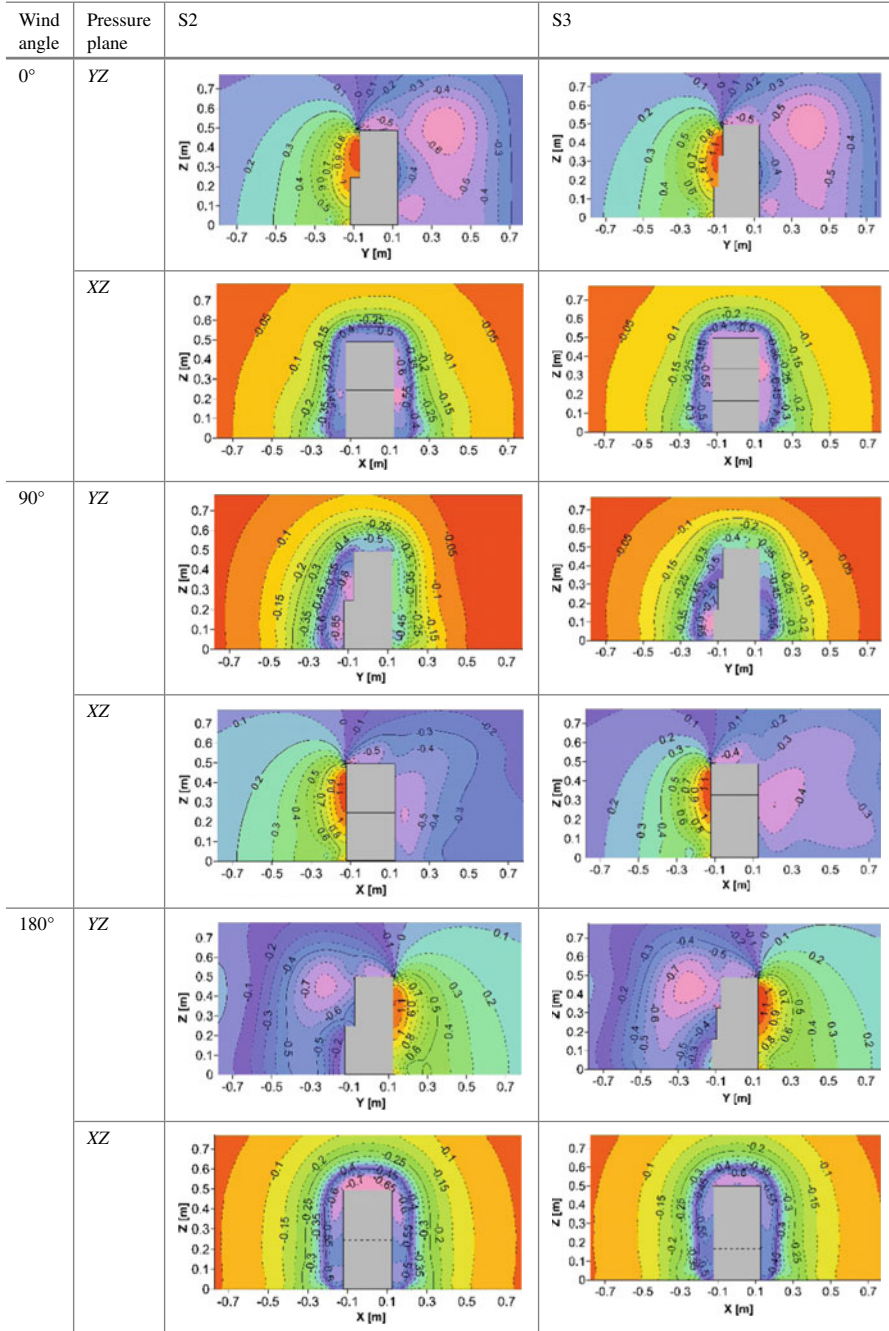
condition on the *XZ* plane has a pressure contour line −0.3, which covered in most of the area for the S3 model. However, S2 model has a line range from −0.2 to −0.6. Therefore, it is clear that the large amount of suction developed in the leeward region due to decrease of number of setback roof for 90° wind angle. For 180° wind angle, the windward face has line 1.2 and −0.1 at the leeward face of S2 model. On the other hand, the S3 model has a large area of line −0.6 on the leeward side, but no lines of 1.2 are visible at windward face. The *XZ* plane for 180° wind angle has large amount of suction on the top roof at line −0.7 for S2 model and line −0.6 at the rooftop of S3 model. It is clear that the pressure on top of the setback roof has maximum suction (−0.7) for S2 model compared to S1 model (−0.35).

4.6 Conclusion

The present paper focused on the wind pressure variation around the square and different setback models for along the wind and across the wind conditions. The following conclusions are made after a lot of analytical simulations.

- The leeward pressure is maximum on S1 model for 0° wind of line −0.5. A bulb region created on the leeward side of S2 and S3 models of line −0.4.
- The excessive amount of suction matured at leeward side due to decrease of number of setback roof for 90° wind angle.
- The pressure coefficient is quite large for along wind condition on S2 model for 180° wind angle.
- The pressure on the rooftop of S1 model has maximum compared to other two models.

References

1. Mendis, P., Ngo, T., Haritos, N., Hira, A., Samali, B., Cheung, J.: Wind loading on tall buildings. Electron. J. Struct. Eng. Special Issue: Loading on Structures. 41–54 (2007)
2. Irwin, P., Kilpatrick, J., Robinson, J., Frisque, A.: Wind and tall buildings: negatives and positives. Struct. Des. Tall Spec. Build. **17**, 915–928 (2008)
3. Kim, Y.M., You, K.P., Ko, N.H.: Across-wind responses of an aeroelastic tapered tall building. J. Wind Eng. Ind. Aerodyn. **96**, 1307–1319 (2008)
4. Kim, Y.C., Kanda, J.: Wind pressures on tapered and set-back tall buildings. J. Fluids Struct. **39**, 306–321 (2013)
5. Tanaka, H., Tamura, Y., Ohtake, K., Nakai, M., Kim, Y.C., Bandi, E.K.: Aerodynamic and flow characteristics of tall buildings with various unconventional configurations. Int. J. High-Rise Build. **2**, 213–228 (2013)
6. Bairagi, A.K., Dalui, S.K.: Evaluation of interference effects on parallel high-rise buildings for different orientation using CFD. In: 3rd World Conference on Applied Sciences, Engineering & Technology, pp. 764–774. Kathmandu, Nepal (2014)
7. Bairagi, A.K., Dalui, S.K.: Optimization of interference effects on high-rise building for different wind angle using CFD simulation. Electron. J. Struct. Eng. **14**, 39–49 (2014)

8. Mukherjee, A., Bairagi, A.K.: Wind pressure and velocity pattern around 'N' plan shape tall building—A case study. Asian J. Civil Eng. (BHRC) **18**(8), 1241–1258 (2017)
9. Mendis, P., Mohotti, D., Ngo, T.: Wind design of tall buildings, problems, mistakes and solutions. In: 1st International Conference on Infrastructure Failures and Consequences, Melbourne, Australia (2014)
10. Baby, S., Jithin,, P.N., Thomas, A.M.: A study of wind pressure on tall buildings and its aerodynamic modifications against wind excitation, Int. J. Eng. Dev. Res. **3** (2015)
11. Xu, Z., Xie, J.: Assessment of across-wind responses for aerodynamic optimization of tall buildings. Wind Struct. **21**, 505–521 (2015)
12. Roy, K., Bairagi, A.K.: Wind pressure and velocity around stepped unsymmetrical plan shape tall building using CFD simulation—A case study. Asian J. Civil Eng. (BHRC) **17**, 1055–1075 (2016)
13. Tamura, Y., Xua, X., Tanakac, H., Kima, Y.C., Yoshidaa, A., Yangd, Q.: Aerodynamic and pedestrian-level wind characteristics of super-tall buildings with various configurations. In: 10th International Conference on Structural Dynamics, EURODYN, vol. 199, pp. 28–37. Procedia Engineering (2017)
14. Mittal, H., Sharma, A., Gairola, A.: Pedestrian level wind characteristics around tall buildings: effect of building shape and wind direction. In: 9th Asia-Pacific Conference on Wind Engineering, Auckland, New Zealand (2017)
15. Bairagi, A.K., Dalui, S.K.: Comparison of aerodynamic coefficients of setback tall buildings due to wind load. Asian J. Civil Eng. Build. Housing **19**, 205–221 (2018)
16. Namchu, A.D., Bairagi, A.K, Chakroborty, S.: Aerodynamic coefficients of steel stacks under different terrain category. In: Proceeding of International Conference on Frontier in Engineering, Applied Science and Technology, (FEAST'18), pp. 133–138. NIT Tiruchirappalli (2018)
17. Bairagi, A.K., Dalui, S.K.: Aerodynamic effects on setback tall building using CFD simulation. In: 2nd International Conference on Advances in Dynamics, Vibration and Control, pp. 381–388. NIT Durgapur (2018)
18. Bairagi, A.K., Dalui, S. K.: Comparison of pressure coefficient between square and setback tall building due to wind load. In: SEC18: Proceedings of the 11th Structural Engineering Convention—2018. Jadavpur University, Kolkata, India (2018)
19. Franke, J., Hirsch, C., Jensen, A., Krüs, H., Schatzmann, M., Westbury, P., Miles, S., Wisse, J., Wright, N.G.: Recommendations on the use of CFD in wind engineering. In: COST Action C14. Impact of Wind and Storm on City Life and Built Environment. Von Karman Institute for Fluid Dynamics (2004)
20. Revuz, J., Hargreaves, D.M., Owen, J.S.: On the domain size for the steady-state CFD modelling of a tall building. Wind Struct. **15** (2012)
21. Kim, Y.C., Kanda, J.: Characteristics of aerodynamic forces and pressures on square plan buildings with height variations. J. Wind Eng. Ind. Aerodyn. **98**, 449–465 (2010)
22. Mou, B., Heb, B.J., Zhaoc, D.X., Chaud, K.: Numerical simulation of the effects of building dimensional variation on wind pressure distribution. Eng. Appl. Comput. Fluid Mech. **11**(1), 293–309 (2017)

Chapter 5
Material Characterization of Pin-Core Latex Polymer Foam Under Static and Dynamic Loads

K. Venkataramana [ID]**, R. K. Singh, Anindya Deb, Vivek Bhasin, K. K. Vaze and H. S. Kushwaha**

Abstract Cellular polymer foams find extensive applications as energy absorbers under static, impact and blast loads due to their capacity to absorb energy under constant stress up to full densification strain (Ashby et al. Metal foams: a design guide. Butterworth-Heinemann, Oxford, 2000 [1]; Gibson and Ashby, Cellular solids: structure and properties. Cambridge University Press, Cambridge, 1999 [2]). In the present paper, the material characterization of natural latex cellular polymer foam used in the field air blast experiments (Venkataramana et al. Proc Eng 173:547–554, 2017 [3]; Venkataramana et al. Numerical simulation of blast wave mitigation using foam impregnated with water. DAE BRNS Symposium on Multiscale Modeling of Materials and Devices (MMMD-2014), 2014 [4]) performed to assess the blast mitigation effect of fluid-filled open-cell pin-core polymer foam is presented. Static compression tests were performed to study the quasi-static behavior of the pin-core latex polymer foam. The Ogden hyper-elastic material parameters are determined from the analysis of static compression test data using ADINA (automatic dynamic incremental nonlinear analysis) v 9.2, ADINA R&D, Inc., Watertown [5]). Further, results of the static compression tests on dry foam and water-saturated foam are compared and discussed. In addition, the dynamic behavior of the pin-core latex cellular foam is investigated by conducting drop tower impact experiment and numerical simulation of the drop tower experiment using LS-DYNA (LS-DYNA v971, Livermore Software Technology Corporation, Livermore [6]). The stress–time history from the drop tower experiment is compared with that of simulation, and good correlation is found between the two sets of results.

K. Venkataramana (✉) · V. Bhasin
Reactor Safety Division, BARC, Mumbai 400085, India
e-mail: kvr_suru@yahoo.com

R. K. Singh · K. K. Vaze · H. S. Kushwaha
Raja Ramanna Research Fellow, DAE, BARC, Mumbai 400085, India

A. Deb
CPDM, Indian Institute of Science (IISc), Bengaluru 560012, India

5.1 Introduction

Cellular polymer foams consist of a three-dimensional array of interconnected cells with solid cell walls and cell faces. When the cell faces are open, they are called open-celled foams, and when the cell faces are closed, they are called closed-cell foams. The cellular polymer foams are characterized by their relative density defined as (ρ^*/ρ_s), where ρ^* is the overall density of the foam, and ρ_s is that of the solid of which the foam is made. The relative density of foams varies from less than 0.3 to as low as 0.003. The porosity of the foam is defined as $1 - (\rho^*/\rho_s)$. Low-density open-cell polymer foams have porosity up to 0.97. The densification strain for open-cell elastomeric polymer foams is given by [2] $\varepsilon_D = 1 - 1.4(\rho^*/\rho_s)$. Flexible polymer foams such as open-cell latex polymer foam absorb energy by elastic bending and buckling of cell walls and release the energy after the load is removed. Though their use as energy absorbers under static and low-velocity impact loads in automobile and packaging industry is well known, low-density open-cell polymer foams have also drawn the attention of researchers for military applications as energy absorbers under blast and impact loads [7–10]. Dawson [7] analyzed the fluid-filled open-cell polymer foam for blast mitigation, and Venkataramana et al. [3, 4, 11] have experimentally and numerically investigated the application of open-cell natural latex polymer foam filled with fluid for mitigating the close-range air blast effects on structures. However, the material properties of the pin-core latex polymer foam used in the blast experiments are not available in open literature.

Typical compositions and manufacturing methods of the pin-core natural latex polymer foam are discussed by Rani (Chap. 9) in Ref. [12]. The natural latex pin-core open-cell polymer foam used in the current experiments is manufactured by MM foam Ltd. [13]. The foam is categorized as low-density elastomeric cellular polymer foam with an overall density of 20 kg/m^3, relative density (ρ^*/ρ_s) of 0.022 and 97.8% porosity. This paper presents results of static compression tests and drop tower impact experiments performed to characterize the open-cell pin-core latex polymer foam under static and dynamic loading conditions. In addition, numerical simulations of the static compression tests and drop tower impact experiments are performed, and the simulation results are compared with the experimental data.

5.2 Drop Tower Experiment on Foam

The drop tower experiments were performed on a miniature drop tower, which is a small-scale drop tower designed to perform experiments on soft materials like polymer foams. The drop tower experimental setup is shown in Fig. 5.1. Drop tower tests were conducted on 100 mm thick foam block of base size 150 mm × 150 mm. The drop weight is allowed to fall freely under gravity on the foam block from a predetermined height. The impact of the drop weight imparts an initial velocity $V_0 = \sqrt{2gh}$ to the top surface of the foam block. The force–time history acting

Fig. 5.1 Experimental setup for drop tower experiment on foam block of 150 mm × 150 mm × 100 mm

on the foam block is acquired by the data acquisition system attached to the drop tower. The force–time history (Fig. 5.2) is converted into acceleration–time history and then is integrated twice to get the displacement–time history of the foam block. The displacement–time history is used to calculate the strain–time history developed in the foam and finally the dynamic stress–strain curve is derived. The experimental dynamic stress–strain response of the foam is shown in Fig. 5.3 which shows a 0.26 MPa stress at 19% strain.
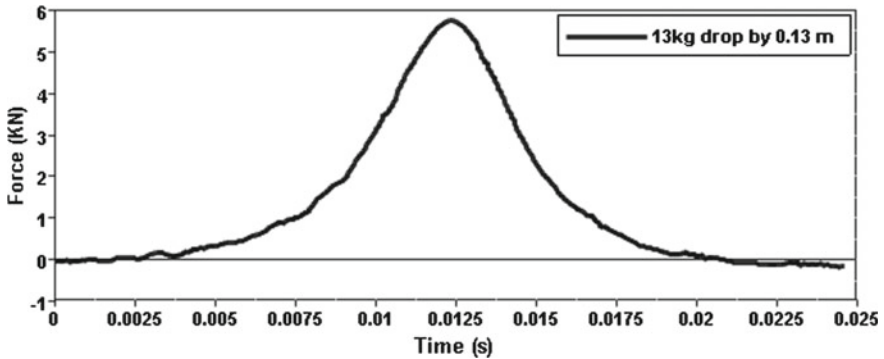
Fig. 5.2 Force–time history, with time from the point of contact between the drop weight and the foam
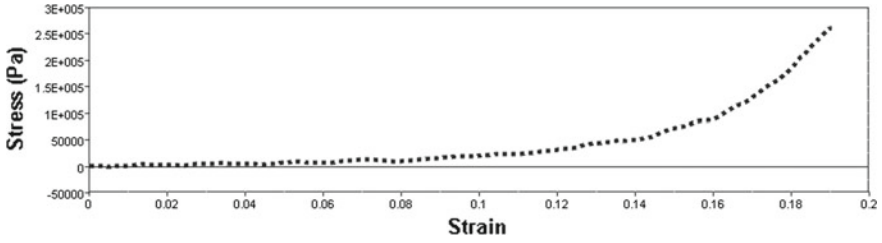
Fig. 5.3 Experimental dynamic stress–strain curve of foam block for up to 19% strain

5.2.1 Simulation of Drop Tower Experiment

Simulations of the drop tower experiments are performed with LS-DYNA [6] code. The simulation setup is shown in Fig. 5.4. The foam block and the drop weight are meshed with brick elements. The bottom of the foam block is fixed in all degrees of freedom. The drop weight is modeled as an elastic steel plate. In order to simulate the experimental conditions, the plate is given an initial velocity corresponds to the velocity acquired by the free-falling mass, $V = \sqrt{2gh}$. The interaction of the plate with the foam block is enforced by surface-to-surface contact algorithm in LS-DYNA. The dynamic behavior of the foam is modeled by MAT_FU_CHANG_FOAM material model (Mat_083) available in LS-DYNA. This material model is suitable to model dynamic compressive behavior of low-density foams, and it allows the stress–strain curves from drop tower experiments to be directly used as input to LS-DYNA material model. The stress–strain values of the foam derived from the drop tower experiment are given as input for the FU_CHANG_FOAM material model [14]. The LS-DYNA program internally calculates the other material parameters using the input test data. The force–time history from the drop tower experiment is converted into stress–time history and compared with that of simulation shown in Fig. 5.5. It is seen that there is a good agreement between the experimental and simulated stress–time history.

Fig. 5.4 Simulation of drop tower test using LS-DYNA
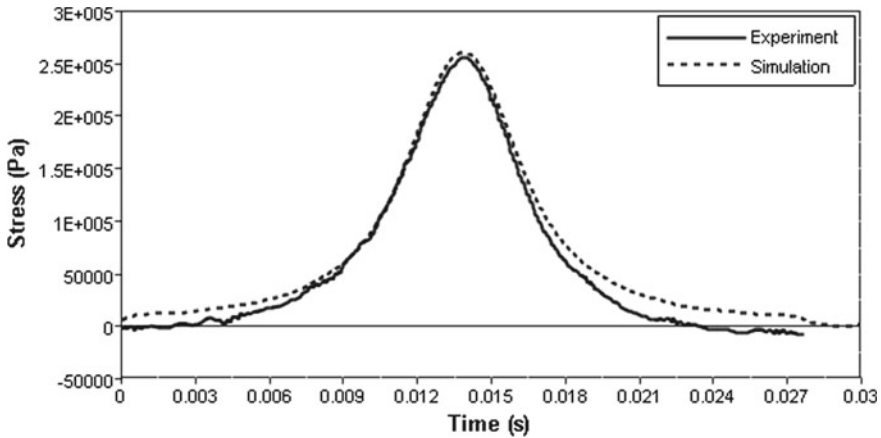
Fig. 5.5 Normal stress–time response of the foam block for 0.13 m height fall of drop weight of 13 kg

5.3 Static Compression Tests on Foam

The foam block used in the actual blast experiments is 100 mm in thickness. The foam is made from natural latex using pin-core method of manufacturing. The pin-core method introduces uniformly distributed cylindrical holes of approximately 5 mm diameter in the foam block. Foam specimens of full thickness (100 mm thick) of foam block used in the field air blast experiments are used in the static compression tests in order to determine the properties of the material in conditions as close as possible to the actual field conditions in which the foam is used. The test specimen is of square base size 150 mm × 150 mm and 100 mm thickness. The specimen size is greater than the minimum size (50 mm × 50 mm base and 25 mm thickness) recommended by the ASTM standard D3574-11 [15] for compression testing of flexible polymer foams. Figure 5.6 shows the natural latex polymer pin-core foam used in the field

Fig. 5.6 Natural latex pin-core polymer foam used in the field air blast experiments [3, 11]
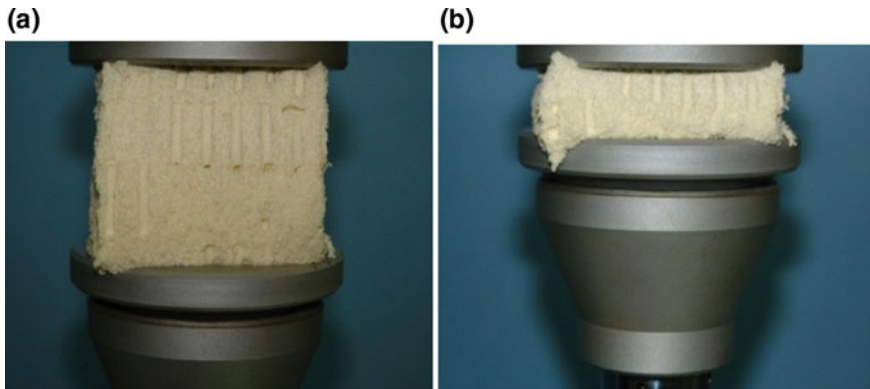
Fig. 5.7 Dry foam testing **a** foam at initial condition and **b** foam at 95% compression

Table 5.1 Summary of compression tests performed on dry foam

Test no.	Compression stroke length (mm)	Crosshead speed (mm/s)	Peak force (N)	Original thickness of foam specimen (mm)
1	95	10	2173	100
2	95	20	1980	100
3	94.2	40	1688	100

air blast experiments. The foam specimen during the compression test is shown in Fig. 5.7.

The uniaxial compression tests were performed at various crosshead speeds. Table 5.1 summarizes the compression tests performed on the dry foam. Figure 5.8 shows the compressive stress–strain response of the dry foam. There was no permanent set observed in the compression test. The foam block completely recovered its initial shape on removal of the load. The foam thus remained elastic during one static uniaxial compression loading and unloading cycle.

As it can be seen from Table 5.1, as the crosshead speed is increased from 10 mm/s to 40 mm/s, the peak load is decreased from 2173 to 1688 N and a 22% reduction in peak-load-carrying capacity at 95% compression. This reduction of peak load may be attributed to early crushing of cell walls at high crosshead speeds (high strain rates). When the foam is loaded slowly, the foam cells get enough time to come to equilibrium with the applied load till peak load is reached, whereas at higher crosshead speeds, early crushing of the foam cell walls results in reduction in the peak-load-carrying capacity of the foam.

Compression tests were also performed on foam fully saturated with water, and the corresponding stress–strain response is compared with that of dry foam in Fig. 5.9. It has been observed that water in the pores of the foam contributed to the load-carrying capacity of the foam. Peak stress in the dry foam is observed to be 96,489,
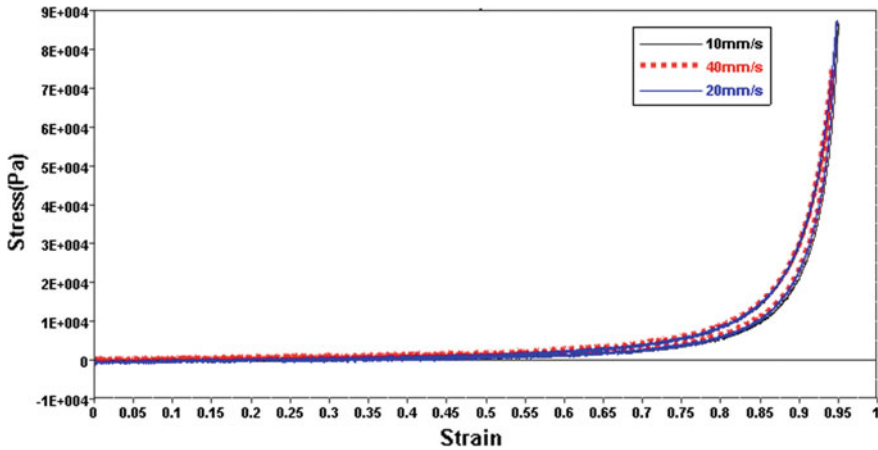
Fig. 5.8 Experimental stress–strain curves of foam at crosshead speeds of 10, 20 and 40 mm/s (corresponding strain rates are 0.1 s^{-1}, 0.2 s^{-1}, and 0.4 s^{-1}, respectively). The peak stress at 40 mm/s crosshead speed is less than the peak stress at 10 and 20 mm/s speed
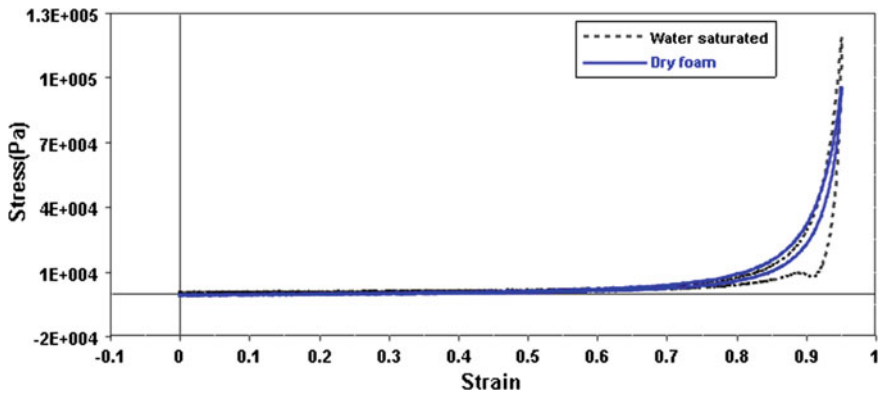
Fig. 5.9 Comparison of experimental stress–strain curves of foam at crosshead speeds of 10 mm/s (strain rates are 0.1 s^{-1}), for dry foam and water-saturated foam

and 118,489 Pa in water-saturated foam, an increase of 22.8% with the presence of water in the pores. This increase in strength is due to the additional work required to expel the fluid (water) from the foam during its compression [4]. It is further observed from Fig. 5.9 that the unloading curve is steeper for the water-saturated foam, with the stress decreasing rapidly at almost constant strain.

This is due to the loss of elasticity of the foam in the presence of water during the unloading cycle as the foam remained at maximum strain like a perfectly plastic material until the load is almost completely removed. The sudden change in the slope in the unloading curve shown in Fig. 5.9 is due to the sudden elastic recovery of the foam at the end of unloading cycle, when the load is almost removed. The

compression tests with water-saturated foam were repeated, and they gave the same stress–strain curve as shown in Fig. 5.9.

5.4 Simulation of Static Compression Tests

The static uniaxial compression tests on the dry foam are simulated using ADINA [5] finite element software. The 150 mm × 150 mm × 100 mm^3 test specimen is represented by a plane strain model. The bottom support and the top plate are treated as rigid surfaces. Frictionless contact between the foam and the supports is assumed. The top rigid plate is given downward displacement corresponding to the compression stroke during the uniaxial compression experiment. The problem is solved in small time steps considering the material and geometric nonlinearities.

5.4.1 Material Model

The dry foam is modeled with Ogden hyper-elastic material model [5] with its parameters determined from the uniaxial compression experimental data. Ogden material model is based on the following expression for strain energy density (i.e., strain energy per unit volume) [16]:

$$W_{\mathrm{D}} = \sum_{n=1}^{9} \left(\frac{\mu_n}{\alpha_n} \left[\lambda_1^{\alpha_n} + \lambda_2^{\alpha_n} + \lambda_3^{\alpha_n} - 3 \right] \right) \mathrm{N/m}^2 \qquad (5.1)$$

where μ_n and α_n are the Ogden material constants and λ_i's are the square roots of the principal stretches of the Cauchy–Green deformation tensor. Choosing only μ_n, $\alpha_n \neq 0$, n = 1, 2, 3, the standard three-term Ogden material description is recovered from the general model given by Eq. (5.1). The Ogden material model coefficients are determined by least-squares fit between the test data and the strain energy density function. The coefficients determined using ADINA for the latex polymer foam are given in Table 5.2, and the curve fit to compression experimental data is shown in Fig. 5.10.

Table 5.2 Ogden material model parameters for the natural latex pin-core cellular polymer foam

μ parameter	Value (N/m^2)	α parameter	Value
μ_1	681.5047	α_1	1.3
μ_2	11.45471	α_2	6.3
μ_3	43.09203	α_3	−2.5
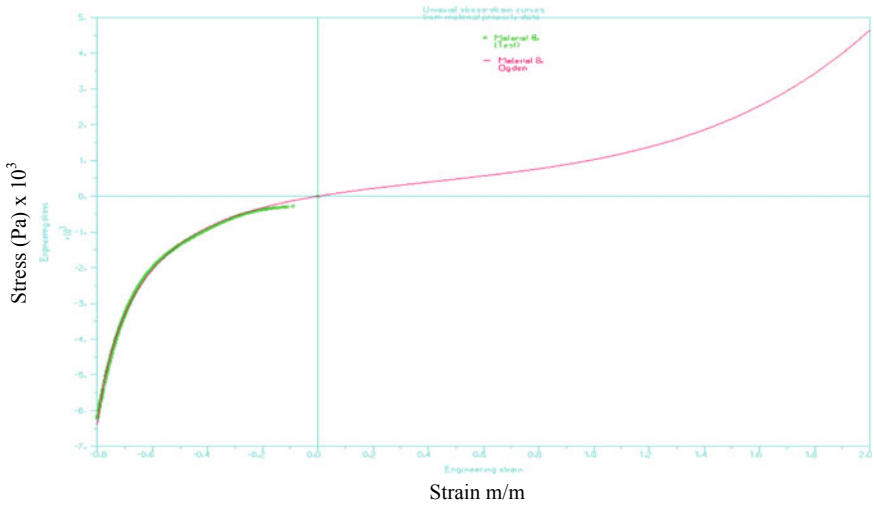
Fig. 5.10   Curve fit to the latex polymer foam compression test data in ADINA

Using the Ogden material parameters from Table 5.2, the stress–strain curves of the foam material from the UTM compression test and the simulation are shown in Fig. 5.11 which shows good agreement between the two.
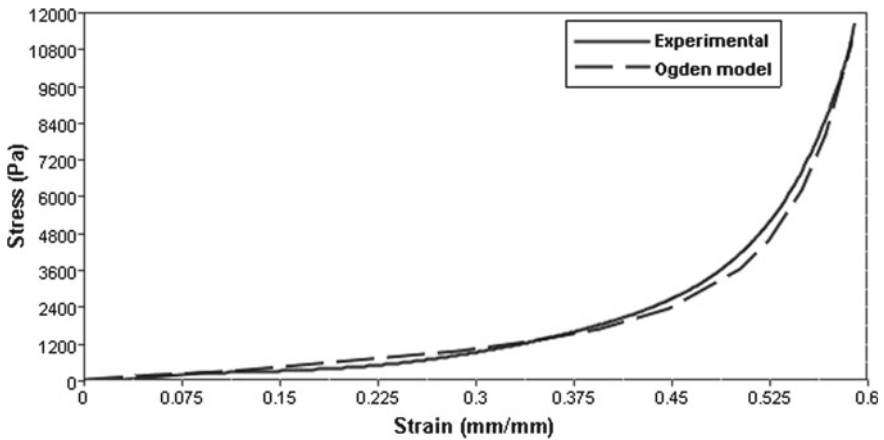
Fig. 5.11   Comparison of experimental and simulation stress–strain curves for compression test on latex foam

5.5   Conclusions

The dynamic response of pin-core natural latex open-cell polymer foam is determined by conducting drop tower impact experiments on the foam. Simulations of the drop tower experiments are performed with LS-DYNA, and good agreement is obtained for the force–time history derived from the experiments and simulation. Further, static uniaxial compression tests were carried out on the foam using universal testing machine (UTM). The compression test data were analyzed to determine the Ogden hyper-elastic material model parameters for the foam. In addition, numerical simulations of the uniaxial static compression tests on the foam were done using ADINA code, and good agreement was found between the test data and simulation results for the uniaxial compression stress–strain response. Furthermore, the effect of the water on the uniaxial compressive behavior of water-saturated open-cell latex polymer foam is demonstrated experimentally.

References

1. Ashby, M.F., Evans, A.G., Fleck, N.A., Gibson, L.J., Hutchinson, J.W., Wadley, H.N.G.: Metal Foams: A Design Guide. Butterworth-Heinemann, Oxford (2000)
2. Gibson, L.J., Ashby, M.F.: Cellular Solids: Structure and Properties, 2nd edn. Cambridge University Press, Cambridge (1999)
3. Venkataramana, K., Singh, R.K., Deb, A., Bhasin, V., Vaze, K.K., Kushwaha, H.S.: Blast protection of infrastructure with fluid-filled cellular polymer foam. In: 11th International Symposium on Plasticity and Impact Mechanics (IMPLAST-2016), IIT New Delhi, 11–14 Dec 2016. Proc. Eng. **173**, 547–554 (2017)
4. Venkataramana, K., Singh, R.K., Deb, A., Bhasin, V., Vaze, K.K., Kushwaha, H.S.: Numerical simulation of blast wave mitigation using foam impregnated with water. In: DAE BRNS Symposium on Multiscale Modeling of Materials and Devices (MMMD-2014), BARC, Mumbai, 30 Oct–02 Nov 2014
5. ADINA (Automatic Dynamic Incremental Nonlinear Analysis) v 9.2, ADINA R&D, Inc., Watertown, MA 02472, USA
6. LS-DYNA v971, Livermore Software Technology Corporation, Livermore, CA, USA
7. Dawson, M.A.: Composite plates with a layer of fluid-filled, reticulated foam for blast protection of infrastructure. Int. J. Impact Eng. **36**(10–11), 1288–1295 (2009)
8. Yost, A.L.: Fluid-filled helmet liner concept for protection against blast-induced traumatic brain injury. , Masters Thesis, Mechanical Engineering, Massachusetts Institute of Technology, Cambridge, MA (2012)
9. Goel, R.: Study of an advanced helmet liner concept to reduce TBI: experiments and simulation using sandwich structures. Masters thesis, Aeronautics and Astronautics, Massachusetts Institute of Technology. Cambridge, MA (2011)
10. Christou, G.A.: Development of a helmet liner for protection against blast induced trauma. Masters thesis, Aeronautics and Astronautics, Massachusetts Institute of Technology, Cambridge, MA (2010)
11. Venkataramana, K.: Blast effects on mild steel plates and blast protection using fluid-filled polymer foam. Ph.D. thesis, Indian Institute of Science (IISc), Bengaluru, May 2017
12. Rani, J.: Latex foam. In: Eves, D. (ed.) Handbook of Polymer Foams. Rapra Technology Limited, Shawbury, Shrewsbury, Shropshire, UK (2004). http://www.rapra.net, ISBN: 1-85957-388-6

13. MM foam Ltd., Chennai, Tamil Nadu, India. www.mmfoam.com
14. LS-DYNA Keyword Reference Manual, Vol-2, Material Models, Livermore Software Technology Corporation (LSTC), Livermore, CA (2013)
15. ASTM-D3574-11: Standard test methods for flexible cellular materials—slab, bonded, and molded urethane foams. Test C—compression force deflection test. ASTM International (2003)
16. ADINA Theory and Modeling Guide. vol. 1, ADINA Solids and Structures. ADINA R&D Inc., MA, USA

Chapter 6
Effect of Delamination on Static Behaviour of Point Supported Composite Conoidal Shells

Kamalika Das and **Suman Pandey**

Abstract Large column-free areas are a need of today's industrial units. This need can be fulfilled by thin laminated shell structures made of composite material. Conoidal shell, being a doubly curved shell structure with a ruled surface, is comparatively easy to construct and is ideal for roofing purposes of such large areas. High specific strength of composite materials and curved form of shells provide greater stability to these shell roofs. The behaviour of these shell structures under loading largely depends on support conditions. Now, separation of layers, known as delamination, is considered to be a major critical defect of composite laminates, which occurs due to repeated cyclic stresses, impact and manufacturing defects. Delamination causes remarkable loss in mechanical toughness and ultimate failure. The most notable thing regarding delamination is that, in most cases, it is not visible from outside. Hence, this type of damage needs a wider attention from researchers. In this paper, the composite conoidal shells with delamination under static loading have been studied. A finite element formulation has been developed with Fortran code to observe the change in deflection in a conoidal shell with varying number of support conditions. An in-depth analysis is done based on number of supports, laminations, stacking sequences and percentage of damage; thereafter, some helpful observations have been highlighted so as to narrate the characteristics of this shell structure as a roofing unit.

Keywords Composites · Conoidal shell · Deflection · Delamination · Finite element method · Thin shell

K. Das (✉) · S. Pandey
Civil Engineering Department, Techno India University, Kolkata, India
e-mail: kamalikad08@gmail.com

S. Pandey
e-mail: upadhyay.suman@gmail.com

Notations

μ_{12}	Poisson's ratio
E_{11}, E_{22}	Elastic moduli
G_{12}, G_{13}, G_{23}	Shear moduli of a lamina with respect to 1, 2 and 3 axes of fibre
hh, hl	Higher and lower heights of conoid, respectively

6.1 Introduction

Recent developments in manufacturing methods of composite materials have resulted in easy fabrication of composite shell structures of complex shell shapes: synclastic, anticlastic or a combination of both. Due to their high specific strength, composite materials result in low cost of supporting members and foundation.

With the increase in use of composite materials in all advanced engineering structures, the investigation on characteristics of damaged laminated composite shell structures is important so that one may judge the performance and stability of the structure. Delamination is a major type of damage in laminated shells, which, if unchecked, can result in reduction of strength, leading to sudden buckling and possible failure of the structure. Singly ruled surfaces, such as conoidal shells, are a popular choice for roofing purposes in civil engineering structures, due to their simplicity and elegance. Hence, problems associated with laminated conoidal shells require more attention from researchers and scientists, and separation of layers is one among the major problems.

Dey et al. [1] investigated the behaviour of composite shells during bending using finite element formulation. The shape of the shells used for the study is paraboloid of revolution. Gim [2] studied the transverse shear deformation on delaminated double cantilevered plates by developing a plate finite element formulation based on a lamination theory. Bolotin [3] discussed the research on delamination and related crack-like defects of laminated and fibre composites. Parhi et al. [4] analysed laminated composite plates for the first ply failure. The plates used for the study have random delamination located at multiple places. Kumari et al. [5] studied the static behaviour of damaged conoidal shells of graphite epoxy composite material by considering twelve different laminations, which include angle-ply and cross-ply shells with uniformly distributed loading. Nardi et al. [6] worked on sparse sensing detection of delaminated carbon-fibre-reinforced-plastic (CFRP) plates. Nikolayevich et al. [7] studied the recent increase in interest in thin shell structures for civil constructions. They explicitly stated the opportunities of the application of composite materials in construction of thin shell structures for civil engineering applications and industrial purposes and exemplified the same in their paper. Ismail et al. [8] worked on the buckling behaviour of damaged composite plate with woven reinforcement and evaluated the critical buckling load.

The above literature review suggests that the use of composite shell structures has been steadily rising since the last two decades, and even if the technology to detect delamination inside the laminations of a shell structure exists, a lot more remains to be known about the behaviour of conoidal shells with delamination damage. Hence, the purpose of this paper is to seek more information and insight on how damaged composite conoidal shells deflect with changes in number of supports, lamination layers, orientation of fibres and delamination area.

6.2 Mathematical Equations

An eight-noded curved quadratic isoparametric finite element with five degrees of freedom, u, v, w, α, β at each node is employed for solution [5]. Here, the displacement field can be written as:

$$u(x, y, z) = u^0(x, y) - z\alpha(x, y)$$
$$v(x, y, z) = v^0(x, y) - z\beta(x, y)$$
$$w(x, y, z) = w^0(x, y)$$

where u^0, v^0, w^0 are the displacement components along the x-, y-, z-coordinate directions, respectively, and α, β are rotational displacements about y- and x-axes, respectively, of a point on the mid-plane, i.e. $z = 0$ [9].

Hence, the static equilibrium problem can be written as:

$$[K]\{\delta\} = \{P\} \tag{6.1}$$

In the above equation,

[K] global stiffness matrix
{P} global load vector
{δ} global displacement vectors.

6.2.1 Constitutive Relations for Undelaminated Shells

Since the shell consists of a number of laminae, the total stress resultants of an n-layer laminate can be represented by Kumari et al. [5]:

$$\{F\} = [D]\{\varepsilon\} \tag{6.2}$$

In the above equation,

[D] laminate stiffness matrix

{F}   generalised force vectors

{ε}   represents the in-plane strain vectors.

6.2.2   Constitutive Relations for Delaminated Shells

Figure 6.1 represents cross-sectional geometry of a laminated shell having 'n' number
of layers and 'p' number of delamination.

Figure 6.2 represents cross-sectional details of the junction, marked as 'o', of
undelaminated part (segment 1) and delaminated part (segment 2 and 3) of a laminated
shell. In-plane strain and curvature can be related by the following equation for
undamaged segments of a thin delaminated conoidal shell:

$$\{\varepsilon\}_L = \{\varepsilon^0\}_1 + z_L^0 \{k\}_1 \tag{6.3}$$
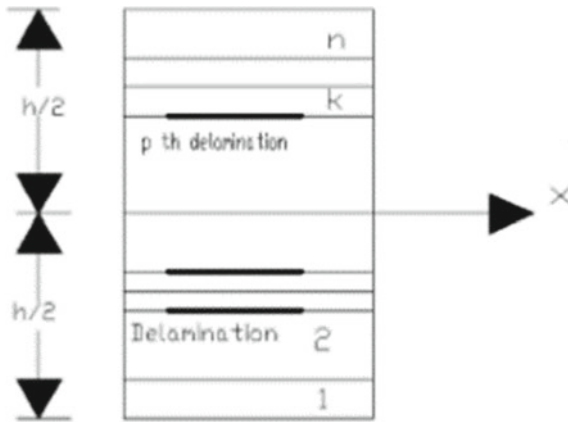
Fig. 6.1 Cross-sectional geometry of laminated shell showing multiple delaminations [5]
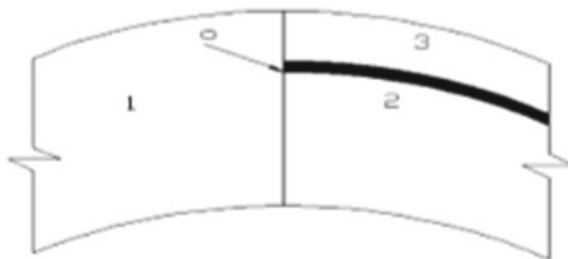
Fig. 6.2 Cross-sectional details of undelaminated and delaminated junction [5]

Table 6.1 Values of maximum non-dimensional downward deflection ($\times 10^{-4}$) for different laminations and SSSS boundary condition

Lamination	Das and Chakraborty [10]	Present approach
0°/90°	−5.63	−5.629
0°/90°/0°	−4.70	−4.701
45°/−45°	−3.12	−3.121
45°/−45°/45°	−2.41	−2.413

Note $E_{11} = 25\,E_{22}, G_{12} = G_{13} = 0.5\,E_{22}, G_{23} = 0.2\,E_{22}, \mu_{12} = 0.25, hl = hh = 0.25, a = b, c = d, h = 0.01$

where suffix 'L' is for delaminated portion, suffix '1' is for undelaminated portion, and $\{\varepsilon^0\}$ represents the vectors of in-plane strain present at the mid-surface, $\{k\}$ are curvature vectors and z_L^0 is the distance along transverse direction between the mid-surface of delaminated and undelaminated portions, respectively.

Consequently, Eq. 6.2 becomes

$$\{F\}_L = [D]_L \{\varepsilon^*\}_1 \tag{6.4}$$

where $\{\varepsilon^*\}$ are the generalised strain vectors.

6.3 Benchmark Problems

For validating the accuracy of present computer code and formulation, two benchmark problems have been solved.

The results obtained from the first benchmark problem, Das and Chakraborty [10], and present formulation are, to a great extent, similar. This shows the correctness of the conoidal shell formulation.

Again, output of present computer code and that of the second benchmark problem, Acharyya et al. [11], are in close agreement. For this, R_{xy} (twist radius of curvature) has been assigned a very large value and R_y (radius of shell surface along y-direction) is kept constant by authors. Hence, exactness of delaminated composite shell is also confirmed (Tables 6.1 and 6.2).

6.4 Results and Discussions

The delaminated area ($c \times d$) is centrally located in the square-shaped ($a/b = 1$) composite conoidal shell. The ratio c/d is unity, and the extent of delamination has been expressed with the ratio c/a (e.g. see Fig. 6.4). Here, 'a' and 'b' are length

Table 6.2 Maximum transverse non-dimensional deflections $(\times 10^{-4})$ of corner-supported delaminated cylindrical shells with different laminations

Lamination	c/a	Acharyya et al. [11]	Present approach
0°/90°/0°/90°	0.25	59.379	59.3789
	0.5	71.736	71.7361
45°/−45°/45°/−45°	0.25	26.011	26.0106
	0.5	30.371	30.3709

Note $E_{11} = 25\,E_{22}, G_{12} = G_{13} = 0.5\,E_{22}, G_{23} = 0.2\,E_{22}, \mu_{12} = 0.25, hl = hh = 0.25, a = b, c = d, h = 0.01$

and width of shell in plan, respectively, and 'c' and 'd' are length and width of delaminated area in plan, respectively (Fig. 6.3).

The purpose of this study is to analyse the deflection of damaged laminated conoidal shells of composite material subjected to uniformly distributed load, for which the following parametric variations have been considered:

1. The extent of delamination, i.e. c/a is variegated from 0 to 56.25% with respect to the total plan area.
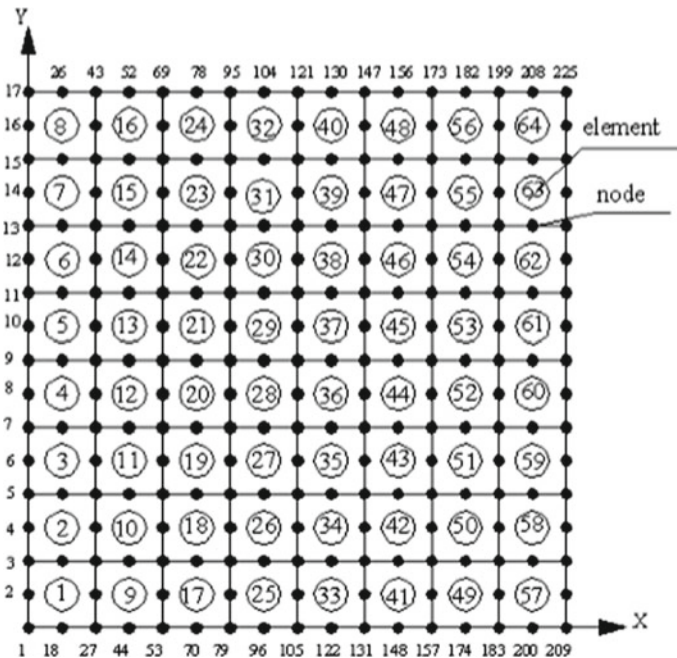
Fig. 6.3 A typical discretization of 8 × 8 mesh on plan area with element and node numbers ($c/a = 0$) [12]
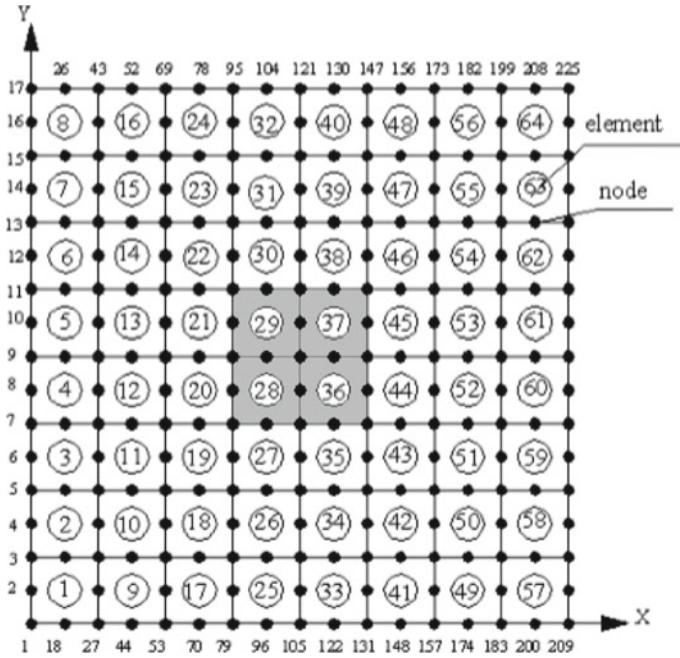
Fig. 6.4 An example of $c/a = 0.25$, i.e. 6.25% delamination (delamination area is shown by the shaded portion)

2. Twelve separate laminations are studied which includes angle-ply and cross-ply of both symmetric and anti-symmetric sequences.
3. Three separate point-support conditions are taken (shown by black dots), where Case 1 (see Fig. 6.5) has four, Case 2 (see Fig. 6.6) has eight and Case 3 (see Fig. 6.7) has sixteen supports, respectively.

Fig. 6.5 Case 1
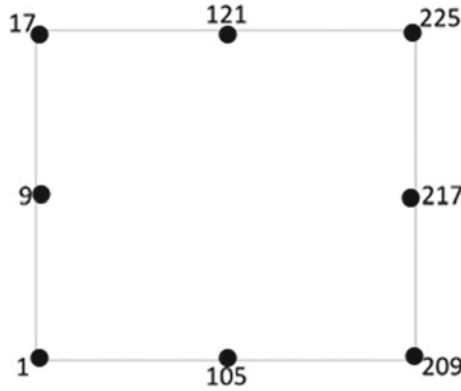
Fig. 6.6 Case 2
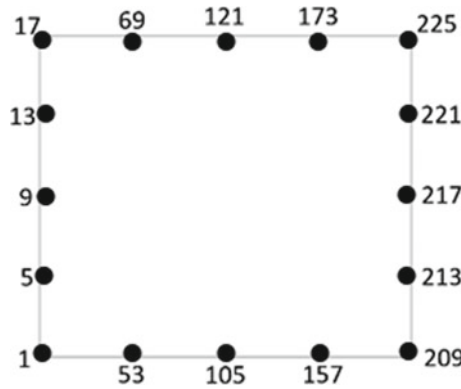
Fig. 6.7 Case 3

Case 1: The results of Table 6.3 indicate that:

- In most of the cases, there is an increase in maximum transverse deflection with increase in delamination area.
- The maximum deflection decreases with increase in number of lamination layers for each case of damage and in most of the cases for both symmetric and anti-symmetric laminations. For example, $45°/-45°$ and $45°/-45°/45°/-45°$ for c/a = 0.25, the maximum deflections are 30.4×10^{-4} and 15.5×10^{-4}, respectively.
- For the same number of laminae, the maximum deflections for each case of delamination are lower in symmetric laminations than that for anti-symmetric laminations for cross-ply shells, whereas this is reverse for angle-plies.

Case 2: The results of Table 6.4 indicate that the:

- Maximum transverse deflection is observed to increase with increase in the delamination area in most cases.

Table 6.3 Maximum non-dimensional deflections ($\times 10^{-4}$) and the corresponding nodes for each lamination (in parentheses below corresponding deflections) of Case 1

Stacking sequence	c/a	Maximum deflection			
		Case 1			
		0	0.25	0.5	0.75
0°/90°		40.61 [70]	40.69 [70]	40.77 [70]	40.57 [78]
45°/−45°		30.07 [78]	30.4 [78]	31.9 [78]	32.4 [78]
0°/90°/0°		25.1 [53]	26.1 [53]	29.5 [69]	36.2 [69]
45°/−45°/45°		31.4 [78]	32.6 [78]	36.7 [95]	25.2 [83]
0°/90°/0°/90°		24.8 [78]	26.5 [78]	30.6 [78]	37.2 [78]
45°/−45°/45°/−45°		14.9 [78]	15.5 [78]	17.4 [78]	22.9 [78]
0°/90°/90°/0°		22.8 [69]	23.8 [69]	26.9 [78]	32.1 [69]
45°/−45°/−45°/45°		20.3 [78]	21.2 [78]	25.3 [95]	32.2 [104]
0°/90°/0°/90°/0°/90°		23 [70]	24.1 [70]	26.52 [70]	29.8 [70]
45°/−45°/45°/−45°/45°/−45°		13.4 [78]	13.8 [78]	15.1 [78]	17.9 [78]
0°/90°/0°/0°/90°/0°		22.3 [78]	23.5 [78]	26.51 [78]	31.2 [78]
45°/−45°/45°/45°/−45°/45°		15.5 [78]	16 [78]	17.8 [78]	22.1 [95]

Note $E_{11} = 25\,E_{22}$, $G_{12} = G_{13} = 0.5\,E_{22}$, $G_{23} = 0.2\,E_{22}$, $\mu_{12} = 0.25$, $hl = hh = 0.25$, $a = b$, $c = d$, $h = 0.01$

- Maximum transverse deflection decreases as compared to Case 1 for almost all the cases.
- For cross-ply laminations, the maximum deflections increase from the 0°/90° to the 0°/90°/0° laminations, then decrease with further increase in number of laminations. For angle-ply laminations, the maximum deflections increase from the 45°/−45° to the 45°/−45°/45° laminations, then decrease with further increase in number of laminations.
- In general, the maximum deflections for each case of delamination are lower in anti-symmetric laminations.
- The overall performance of angle-ply shells is better than that of the cross-ply ones for the same number of laminae.

Case 3: The results of Table 6.5 indicate that:

Table 6.4 Maximum non-dimensional deflections ($\times 10^{-4}$) and the corresponding nodes for each lamination (in parentheses below corresponding deflections) of Case 2

Stacking sequence	c/a	Maximum deflection			
		Case 2			
		0	0.25	0.5	0.75
0°/90°		3.31 [52]	3.47 [74]	3.56 [74]	3.53 [74]
45°/−45°		3.99 [14]	4.03 [14]	4.13 [14]	4.5 [14]
0°/90°/0°		5.13 [43]	5.15 [43]	5.27 [43]	5.82 [43]
45°/−45°/45°		4.23 [52]	4.27 [52]	4.37 [52]	13.4 [57]
0°/90°/0°/90°		2.47 [41]	2.49 [40]	3.06 [74]	3.88 [87]
45°/−45°/45°/−45°		2.45 [14]	2.46 [14]	2.51 [14]	3.26 [40]
0°/90°/90°/0°		3.87 [44]	3.88 [44]	4.04 [44]	4.22 [27]
45°/−45°/−45°/45°		2.9 [4]	2.94 [4]	3.16 [4]	16.8 [84]
0°/90°/0°/90°/0°/90°		2.41 [41]	2.42 [40]	2.63 [74]	2.96 [74]
45°/−45°/45°/−45°/45°/−45°		2.3 [14]	2.31 [14]	2.36 [14]	2.7 [40]
0°/90°/0°/0°/90°/0°		3.18 [44]	3.16 [44]	3.14 [44]	3.25 [44]
45°/−45°/45°/45°/−45°/45°		2.65 [4]	2.66 [4]	2.72 [4]	3.23 [31]

Note $E_{11} = 25\,E_{22}$, $G_{12} = G_{13} = 0.5\,E_{22}$, $G_{23} = 0.2\,E_{22}$, $\mu_{12} = 0.25$, $hl = hh = 0.25$, $a = b$, $c = d$, $h = 0.01$

- In most of the cases, there is an increase in maximum transverse deflection with increase in delamination area.
- Maximum transverse deflection decreases further, from Case 1 and Case 2, as number of supports increases.
- Maximum deflection decreases with increase in lamination layers for most cases. For example, with $c/a = 0.5$, as the number of laminae increases from 0°/90°/0°/90° to 0°/90°/0°/90°/0°/90°, maximum deflection reduces from 0.953×10^{-4} to 0.902×10^{-4}.
- Maximum deflections are lower in anti-symmetric laminations for most cases.
- There is no noticeable trend in two- and three-layered laminations, but with increase in lamination layers, the maximum deflections are lower in cross-ply

Table 6.5 Maximum non-dimensional deflections ($\times 10^{-4}$) and the corresponding nodes for each lamination (in parentheses below corresponding deflections) of Case 3

Stacking sequence	c/a	Maximum deflection			
		Case 3			
		0	0.25	0.5	0.75
0°/90°		1.17 [48]	1.29 [87]	1.3 [61]	1.1 [48]
45°/−45°		1.26 [48]	1.268 [62]	1.29 [62]	1.35 [48]
0°/90°/0°		1.13 [27]	1.14 [27]	1.12 [27]	3.59 [83]
45°/−45°/45°		1.04 [60]	1.06 [60]	1.21 [60]	1.44 [60]
0°/90°/0°/90°		0.879 [61]	0.902 [74]	0.953 [74]	0.113 [48]
45°/−45°/45°/−45°		0.914 [61]	0.935 [61]	1.05 [74]	1.29 [48]
0°/90°/90°/0°		0.908 [48]	1.01 [87]	11.6 [139]	2.07 [35]
45°/−45°/−45°/45°		0.922 [60]	0.945 [60]	1.18 [60]	1.6 [59]
0°/90°/0°/90°/0°/90°		0.846 [61]	0.88 [74]	0.902 [74]	0.914 [48]
45°/−45°/45°/−45°/45°/−45°		0.881 [61]	0.895 [61]	0.957 [61]	1.11 [48]
0°/90°/0°/0°/90°/0°		0.779 [48]	0.781 [48]	0.785 [48]	0.976 [48]
45°/−45°/45°/45°/−45°/45°		0.937 [60]	0.953 [60]	1.04 [60]	1.23 [60]

Note $E_{11} = 25\,E_{22}$, $G_{12} = G_{13} = 0.5\,E_{22}$, $G_{23} = 0.2\,E_{22}$, $\mu_{12} = 0.25$, $hl = hh = 0.25$, $a = b$, $c = d$, $h = 0.01$

lamination for most cases. For example, in six-layered anti-symmetric lamina-tions, the maximum deflections for $c/a = 0.5$ are 0.902×10^{-4} for cross-ply and 0.957×10^{-4} for angle-ply laminations.

6.5 Conclusion

In the present work, an eight-noded isoparametric finite element is used to generate a software system. This system is used to investigate the static behaviour of composite conoidal shells with delamination. Following conclusions can be drawn based on the present study:

1. Results obtained using present system are nearly matching with the two benchmark problems. This confirms the usefulness of the software system used here.
2. The above research on deflection of composite conoidal shells concludes that maximum deflection decreases as the number of supports and number of laminates increases.
3. It is noted that maximum deflection increases as the extent of delamination increases from 0 to 56.25%. However, as the number of supports increases, maximum deflection in each case of delamination decreases (except for 0°/90°/90°/0° lamination of Case 3 with delamination area $c/a = 0.5$).
4. It is also observed that in cases with four supports, the maximum deflection is lower in symmetric laminations for cross-ply laminates, whereas it is lower in anti-symmetric laminations for angle-ply laminates. With the increase in number of supports, the conoidal shell shows lower maximum deflection in the anti-symmetric sequences for angle-ply and cross-ply shells as well, with the exception of the six-layered cross-ply laminates for Case 3.
5. The best performing laminate for both Case 1 and Case 2 has been observed to be 45°/−45°/45°/−45°/45°/−45°, and for Case 3, it is 0°/90°/0°/0°/90°/0°.

References

1. Dey, A., Bandyopadhyay, J.N., Sinha, P.K.: Finite element analysis of laminated composite conoidal shell structures. Comput. Struct. **43**(3), 469–476 (1992)
2. Gim, C.K.: Plate finite element modeling of laminated plates. Comput. Struct. **52**(1), 157–168 (1994)
3. Bolotin, V.V.: Delaminations in composite structures: its origin, buckling, growth and stability. Compos. B Eng. **27**(2), 129–145 (1996)
4. Parhi, P.K., Bhattacharyya, S.K., Sinha, P.K.: Failure analysis of multiple delaminated composite plates due to bending and impact. Bull. Mater. Sci. **24**(2), 143–149 (2001)
5. Kumari, S., Chakravorty, D.: Bending of delaminated composite conoidal shells under uniformly distributed load. J. Eng. Mech. **137**(10), 660–668 (2011)
6. Gaudenzi, P., Nardi, D., Chiappetta, I., Atek, S., Lampani, L., Pasquali, M., Sarasini, F., Tirilló, J., Valente, T.: Sparse sensing detection of impact-induced delaminations in composite laminates. Compos. Struct. **133**, 1209–1219 (2015)
7. Nikolayevich, K.S., Lvovna, S.S., Bock, H.C.A.: Thin-walled composite and plastic shells for civil and industrial buildings and erections. Mater. Sci. Forum **895**, 45–51 (2017)
8. Ismail, M.R., Ali, Z.A.A.A., Al-Waily, M.: Delamination damage effect on buckling behavior of woven reinforcement composite materials plate. Int. J. Mechanical & Mech. Eng. **18**(5), 83–93 (2018)
9. Reddy, J.N.: Mechanics of Laminated Composite Plates—Theory and Analysis, 2nd edn. CRC Press, Boca Raton (2004)
10. Das, H.S., Chakraborty, D.: Design aids and selection guidelines for composite conoidal shell roofs—a finite element application. J. Reinf. Plast. Compos. **26**(17), 1793–1819 (2007)

11. Acharyya, A.K., Chakravorty, D., Karmakar, A.: Bending characteristics of delaminated composite cylindrical shells—a finite element approach. J. Reinf. Plast. Compos. **28**(8), 965–978 (2009)
12. Kumari, S.: Finite Element Bending and Vibration Characteristics of Delaminated Composite Conoidal Shell Roofs. PhD Thesis, Jadavpur University, West Bengal (2014)

Chapter 7
Wind Excitation Study of a Corner-Modified Square Tall Structure

Arghyadip Das and **Sujit Kumar Dalui**

Abstract The modern buildings are becoming taller due to lack of land space and this makes the tall buildings more sensitive to lateral loads such as wind. The outer shape of the building is one of the main parameters which affects the design wind loads. Various types of minor corner modifications on tall buildings result a huge change in force and pressure. The present study is carried out to find the effect of corner modification on square plan-shaped tall building. The corners are modified as corner recessed, corner chamfered, and corner rounded, and a series of simulation is done in ANSYS CFX ($k - \varepsilon$ model) to find out the effects on force coefficients, pressure coefficients, wind flow pattern around the buildings, etc. The numerical analyses are done considering the model scale as 1:300 and for 0° angle of wind attack.

Keywords Tall buildings · Pressure coefficients · Force coefficients · Domain · Boundary layer · Meshing · Wind attack

7.1 Introduction

The population of the world is increasing drastically, and to accommodate this population, the modern-day technology prefers to build the high-rise buildings due to lack of land space. So, these tall buildings are very much sensitive in lateral forces such as wind. The outer shape is one of the main parameters which affects the wind loads and responses. Various International Standards like IS:875 (part-3):2015 [7], ASCE-16 [2], and AS-NZS: 1180-2011 [1] are providing guidelines to calculate the wind-induced loads and responses for regular plan-shaped buildings but there are no such guidelines for the irregular and unconventional plan-shaped buildings.

A. Das (✉) · S. K. Dalui
Department of Civil Engineering, Indian Institute of Engineering Science and Technology, Shibpur, Howrah, India
e-mail: arghyadip16@gmail.com

S. K. Dalui
e-mail: sujit_dalui@rediffmail.com

Many research works are done on various irregular plan-shaped buildings to find the wind-induced loads and responses. Tanaka et al. [16] provide some guidelines on aerodynamic forces and wind pressure on various unconventional configurations like corner cut, corner chamfered, tilted, tapered, helical, and cross-opening with basic square-shaped model by a series of wind tunnel investigation. Charkraborty et al. [3] investigated the '+'-shaped tall building for 0°–45° wind incidence angle. Gomes et al. [6] investigated on experimental outcomes of 'L'- and 'U'-shaped models with 1:100 length scale. Tse et al. [17] carried out his research to find out the wind loadings and wind-induced responses of square tall buildings with different sizes of chamfered and recessed corners. Li et al. [11] suggested that among the horizontal modifications, 10% corner cut model is most greatly reduced along wind load for specific wind direction. Verma et al. [18] investigated the variation of the pressure distribution of tall square plan-shaped building for various wind incidence angle. Kumar and Dalui [9] compare the pressure coefficients and force coefficients for regular and angular cross-plan-shaped buildings. Pal and Dalui [12] studied the pressure and force coefficients for 'Z' plan-shaped tall buildings. Sanyal and Dalui [14] studied the variation of pressure on courtyard and opening of a rectangular plan-shaped building. Elshaer et al. [4] studied the building corner modification effects on square-shaped tall building and concluded that the corner round model has less drag coefficients among all models. Kwok et al. [10] studied on finned and slotted finned corner buildings and concluded that the fins and slotted fins increase the along wind responses and reduce the across wind responses. Kawai [8] investigated on square sections with rounded, chamfered, and recessed corners and concluded that the small chamfers and recessions are effective in preventing aeroelastic instability but rounded corners increase the aerodynamic damping. Tamura et al. [15] carried out his research on square sections with rounded and chamfered corners using smooth uniform flows and concluded about the reliability of CFD in predicting the wind loads.

7.2 Scope of the Work

In this study, the square model is considered as the basic model with cross section 250 mm × 250 mm and 750 mm height with length scale 1:300 shown in Fig. 7.1a. The corner recessing is done in the next model with 25 mm recess that is 10% corner recess and shown in Fig. 7.1b, and the corner rounding and corner chamfering are also done successively with 25 mm rounding radius and 25 mm chamfering distance and shown in Fig. 7.1c, d. The isometric view of square model is shown in Fig. 7.1e. All the models are prepared using ANSYS CFX software package. The wind incidence angle is considered as 0° for each case. Pressure distribution is evaluated for each model, and pressure coefficients are represented in tabulated form as well as graphical form.
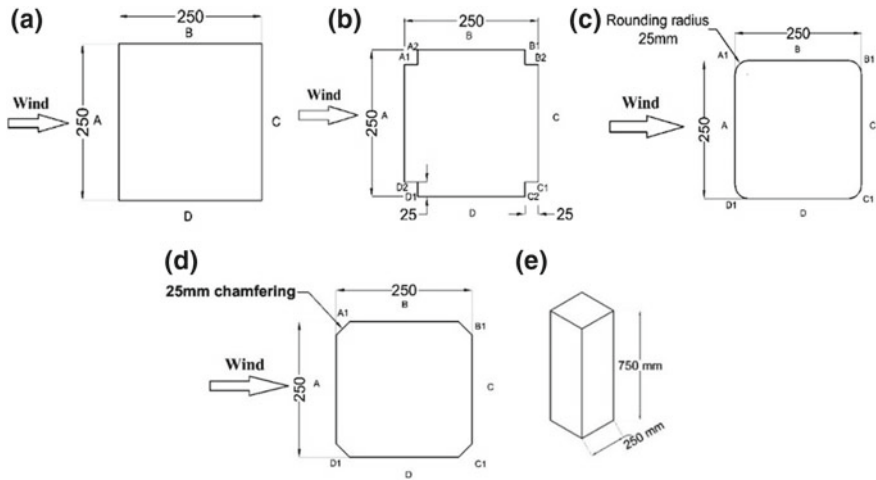
Fig. 7.1 Model details of various corner modifications. **a** Square model, **b** corner recessed model, **c** corner rounded model, **d** Corner chamfered model, and **e** isometric view of square model

7.3 Computational Domain, Boundary Condition and Meshing

The computational domain has some specific sizes as per the guidelines of Frank et al. [5] and Revuz et al. [13]. As per the guidelines, the upstream, downstream, sidewall, and top wall clearance is taken as 5*H*, 15*H*, 5*H,* and 6*H* successively, where *H* is the height of the mode. The details of domain size are shown in Fig. 7.2a, b.

The velocity of the wind is considered as 10 m/s, and the turbulence intensity is taken as 1% (low intensity). The relative pressure at outlet is taken as zero. Sidewalls of the domain boundary are considered as the free slip walls, and the model walls are considered as the no slip walls. The ground roughness (α) is taken as 0.133. Overall temperature of the domain is considered as 25 °C. The numerical analysis
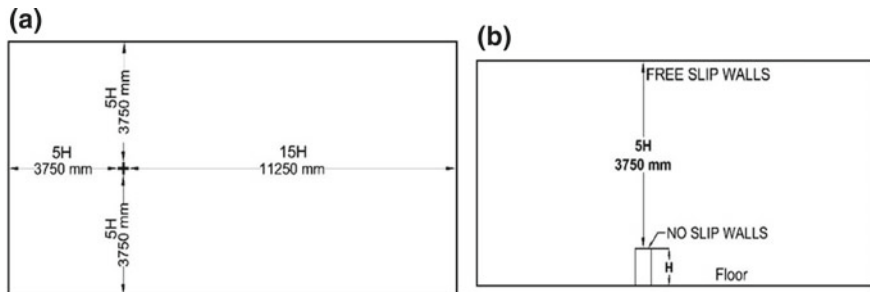
Fig. 7.2 a Plan and **b** elevation view of computational domain used in CFD
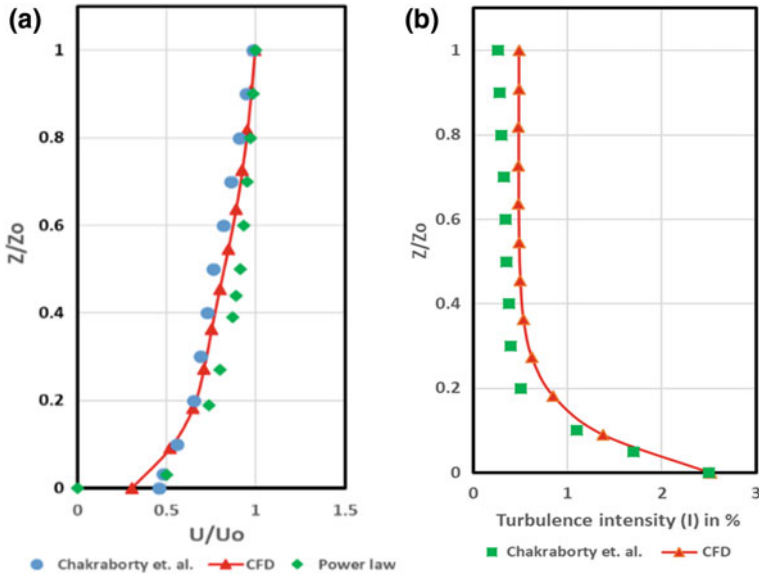
Fig. 7.3 Comparison of **a** velocity profile and **b** turbulent profile

data are compared with previously published data of same type of geometric model, and power law is also used to generate such profile with exponent coefficient as 0.133.

$$\frac{U}{U_0} = \left(\frac{Z}{Z_0}\right)^{\alpha} \tag{7.1}$$

where U_0 is the basic wind speed taken as 10 m/s and Z_0 is boundary layer height of 1 m. A similar type of velocity profile was used by Chakraborty et al [3]. A comparison of the velocity profile and turbulent profile is shown in Fig. 7.3a, b. Tetrahedron meshing is used throughout the whole domain, and finer meshing is provided near the building to measure the accurate responses on the surface of the building. Comparatively coarser meshing is provided in the outer edges of the domain. The overall y+ values for all models are kept within the range of 30–300. A typical meshing of the corner chamfered model is shown in Fig. 7.4.

7.4 Results and Discussion

The average pressure coefficients and force coefficients of corner-modified models for various faces are calculated for 0° angle of wind attack and shown in Table 7.1. The average Reynolds number is calculated as 3.72×106. The basic square model has maximum positive pressure in windward face (face A) but side faces (face B
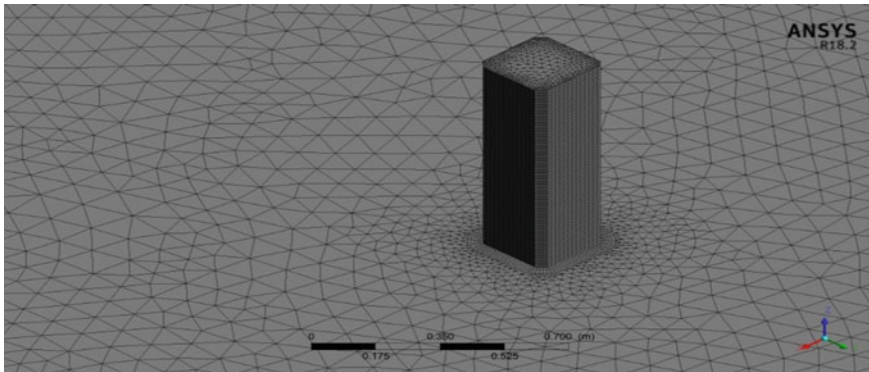
Fig. 7.4 Mesh pattern of corner chamfered model

Table 7.1 Average pressure and force coefficients for all types of model

Sl. No.	Corner modification	Mean pressure coefficient				Force coefficient
		A	B	C	D	
1	Basic square model	0.83	−0.58	−0.43	−0.58	1.20
2	Corner recessed model	0.82	−0.55	−0.40	−0.55	0.98
3	Corner rounded model	0.82	−0.62	−0.38	−0.62	0.70
4	Corner chamfered model	0.80	−0.64	−0.37	−0.64	0.71

and face D) and leeward face (face C) are experiencing negative pressure at the same time, whereas the corner recessed model is experiencing a bit lower positive pressure compared to the square model. Corner rounded and corner chamfered models are subjected to lesser pressure in face A, but corner chamfered model is experiencing the maximum negative pressure in face D (leeward face). Among all four models, the square model has maximum force coefficient as 1.20 and corner chamfered model has minimum force coefficient as 0.70 along 'X'-direction.

7.4.1 Variation of Pressure Coefficients Along the Vertical Centerline, Flow Pattern and Pressure Contour of Various Faces of the Building

The pressure coefficients (C_p) along vertical centerline of all faces of the building models are evaluated and plotted in graph shown in Fig. 7.5. In face A, it is found that the maximum pressure coefficient is at 600 mm height. The square model is showing less C_p value at 600 mm height compared to corner recessed and corner chamfered models for face A. In the comparison of face B, the corner recessed model
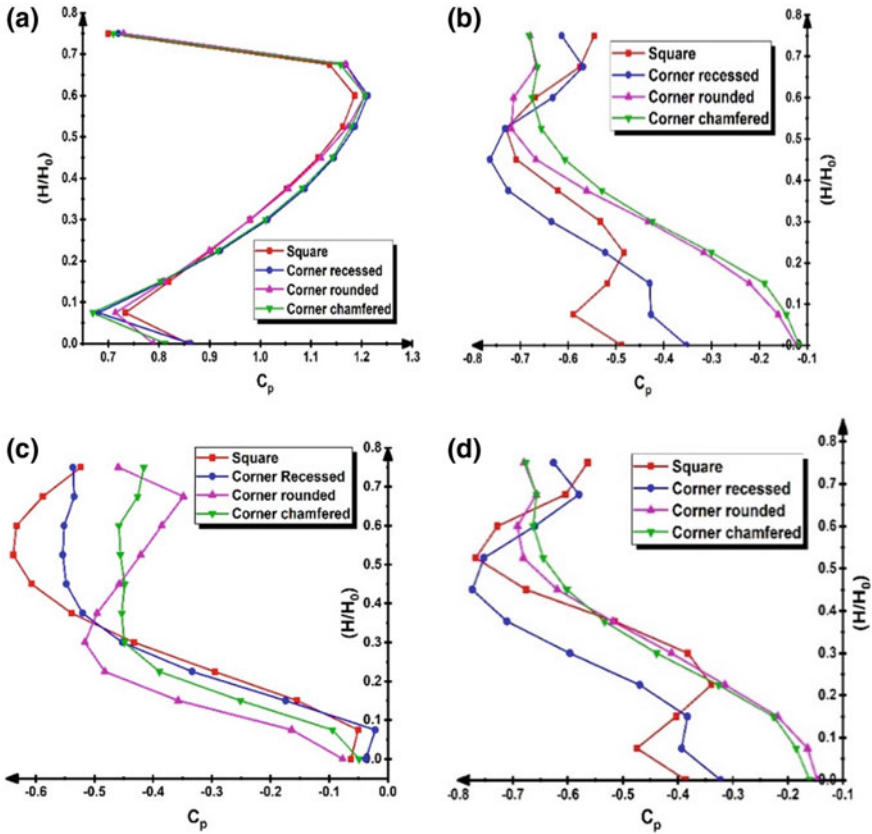
Fig. 7.5 Comparison of avg. C_p values along vertical centerline for various faces of all type of buildings

is showing maximum suction at 450 mm height, whereas the corner recessed and corner chamfered models have maximum suction at 600 mm height. Face B and face D are showing maximum negative pressure along the vertical centerline. The ratio of height of any point from the base (H) with respect to the overall height of the building (H_o) is depicted in the Y-axis as the ratio of (H/H_o). Due to symmetry of the building models and 0° angle of wind attack, the pressure coefficients (C_p) along vertical centerline are similar for sidewalls. The wind flow pattern around the building models is shown in Fig. 7.6. The vortex generated in the leeward side of the building models indicates the generation of negative pressure. Due to symmetry of the building models with respect to both axes and 0° wind angle, the vortex formation is also symmetric in the wake region of the buildings. Large separation of flow is observed for corner rounded and corner chamfered building models. The side view of vortex generation around the corner rounded building is also shown in Fig. 7.6. The comparison of pressure contour is shown in Fig. 7.7.

(a) Square model

(b) Corner recessed model

(c) Corner rounded model

(d) Corner chamfered model

(e) Side view of vortex generation around corner rounded model
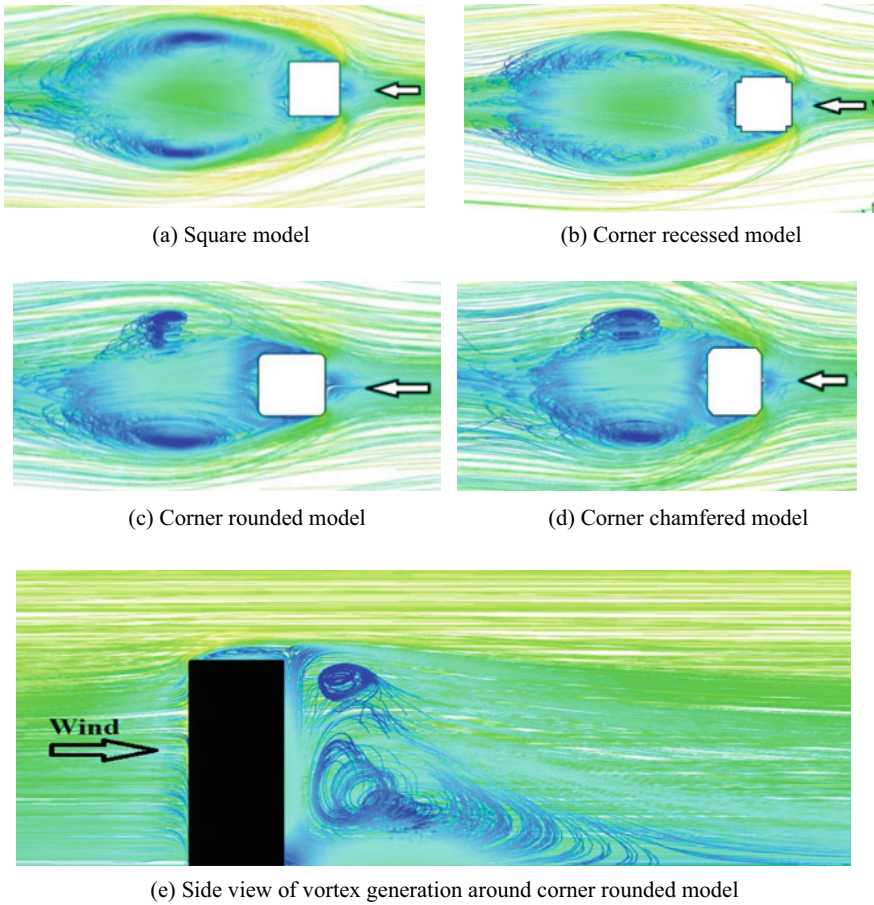
Fig. 7.6 Flow pattern around all type of building model at 0° angle of wind attack

7.5 Conclusion

The corner modification has a huge impact in reducing the force and pressure coefficients on the building boundaries. Force and pressure coefficients are the most important parameters of building design, and reduction of those parameters is very much appreciated in the design point of view. The force coefficients are reduced around 18% in the case of corner recessed model as compared to the square basic model. But the best suited model is corner rounded model as it gives around 41% reduction in force coefficients along 'X'-direction for 0° angle of wind attack. Corner chamfered model also gives satisfactory results (reduction of mean drag coefficient around 40%). Due to some complicacy in construction works for corner rounded
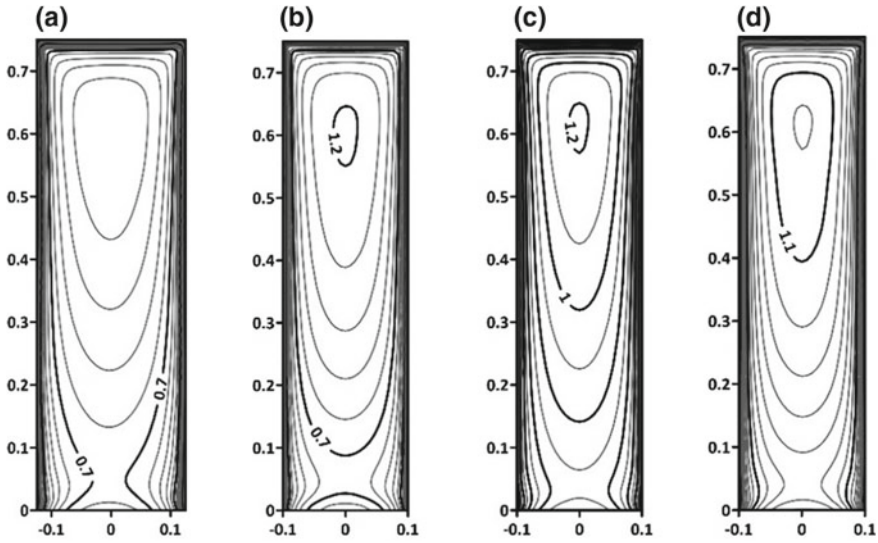
Fig. 7.7 Comparison of pressure contour for face A for **a** square model, **b** corner recessed model, **c** corner rounded model, and **d** corner chamfered model

model, the corner chamfered model is the preferred model for reduction of wind-induced loads and responses. As compared to other minor modifications in building corners, chamfered model gives maximum utilization of plan area.

References

1. AS/NZS: 1170.2:2011, Structure design actions, Part-2: wind actions. Australian/ New Zealand Standard; Sydney and Wellington
2. ASCE: 7-16, Minimum design loads for buildings and other structures. Structural Engineering Institute of the American Society of Civil Engineering, Reston (2016)
3. Chakraborty, S., Dalui, S.K., Ahuja, A.K.: Wind load on irregular plan shaped tall building—A case study. Wind Struct. **19**(1), 59–73 (2014)
4. Elshaer, A., Bitsuamlak, G.T., El Damatty, A.: Wind load reductions due to building corner modifications. In: 22nd Annual Conference of the CFD Society of Canada Toronto, Canada (2014)
5. Franke, J., Hirsch, C., Jensen, A.G., Krűs, H.W., Schatzmann, M., Westbury, P.S., Miles, S.D.,Wisse,J.A., Wright, N.G.: Recommendations on the use of CFD in wind engineering. In: International Conference on Urban Wind Engineering and Building Aerodynamics:COST C14: Impact of Wind and Storm on City life and Built Environment (2004)
6. Gomes, M., Rodrigues, A., Mendes, P.: Experimental and numerical study of wind pressures on irregular-plan shapes. J. Wind Eng. Ind. Aerodyn. **93**(10), 741–756 (2005)
7. IS: 875(Part-III):2015, Indian standard code of practice for design loads (other than earthquake) for buildings and structures, Part 3 (wind loads). Bureau of Indian Standards, New Delhi, India (2015)
8. Kawai, H.: Effects of corner modifications on aeroelastic instabilities of tall buildings. J. Wind Eng. Ind. Aerodyn. 74–76, 719–729 (1998)

9. Kumar, D., Dalui, S.K.: Effect of internal angles between limbs of cross plan shaped tall building under wind load. Wind Struct. **24**(2), 95–118 (2017)
10. Kwok, K.C.S., Wilhelm, P.A., Wilkie, B.G.: Effect of edge configuration on wind induced response of tall buildings. Eng. Struct. **10**, 135–140 (2018)
11. Li, Y., Tian, X., Tee, K.F., Li, Q.S., Li, Y.G.: Aerodynamic treatments for reduction of wind loads on High-rise Building. J. Wind Eng. Ind. Aerodyn. **172**, 107–115 (2018)
12. Pal, R., Dalui, S.K.: Wind effects on 'Z' plan shaped tall building: a case study. Int. J. Adv. Struct. Eng. **8**(3), 319–335 (2016)
13. Revuz, J., Hargreaves, D.M., and Owen J. S.: On the domain size of steady state CFD modelling of tall building. Wind Struct. **15**(4), 313–329 (2012)
14. Sanyal, P., Dalui, S.K.: Effect of courtyard and opening on a rectangular plan shaped tall building under wind load. Int. J. Adv. Struct. Eng. **10**(2), 169–188 (2018)
15. Tamura, T., Miyagi, T., Kitagishi, T.: Numerical prediction of unsteady pressures on a square cylinder with various corner shapes. J. Wind Eng. Ind. Aerodyn. **74–76**(1), 531–542 (1998)
16. Tanaka, H., Tamura, Y., Ohtake, K., Nakai, M., Kim, Y.C.: Experimental investigation of aerodynamic forces and wind pressures acting on tall buildings with various unconventional configurations. J. Wind Eng. Ind. Aerodyn. 107–108, 179–191 (2012) (Elsevier)
17. Tse, K.T., Hitchcock, P.A., Kwok, K.C.S., Thepmongkorn, S., Chan, C.M.: Economic perspectives of aerodynamic treatments of square tall buildings. J. Wind Eng. Ind. Aerodyn. **97**(9), 455–467 (2009)
18. Verma, S.K., Ahuja, A.K., Pandey, A.D.: Effects of wind incidence angle on wind pressure distribution on square pan tall buildings. J. Acad. Ind. Res. **1**(12), 747–752 (2013)

Chapter 8
Experimental Investigations on SCC with Indigenously Developed Geopolymer Aggregates

Check for updates

M. P. Naveena, G. Narayana, Vijayalakshmi Akella and C. M. Thejas

Abstract The excessive use of natural aggregates is having an adverse effect on the environment and raises major environmental issues; hence, an attempt has been made to develop artificial aggregates. These artificial aggregates are made from using GGBS, sodium hydroxide and sodium silicate. This paper focuses on the fresh, hardened and durability properties of self-compacting concrete with artificial geopolymer aggregates (GPAs) as partial to full replacement of natural aggregates. Mix design was carried out with varying content of GPA (0–100%) and cements contents (300, 350 and 400 kg/m^3). Flow, passing ability and segregation resistance were found to increase when 400 kg of cement and 100% replacement of 10 mm GPA is used as compared to crushed gravel. However, the compressive strength was found to be marginally less with the increase in aggregate size. After examining, the properties of SCC with geopolymer aggregate of size varying from 10 to 20 mm are used in casting of the sleepers. The sleepers were precast in Malu sleeper yard, Birur, Karnataka, and subjected to bending, electrical resistivity and durability tests. The results from static bending test showed that the resistance load of a sleeper with 50% of 6 M aggregate is 238 and 230 kN for conventional concrete. Electrical resistivity and durability of a sleeper with 6 M was found better than conventional concrete sleeper. The prediction of self-compacting concrete properties with artificial geopolymer aggregate and natural aggregate was investigated by using MATLAB.

M. P. Naveena (✉) · G. Narayana
Department of Civil Engineering, S.J.C Institute of Technology, Chikkaballapur, Karnataka 562101, India
e-mail: mpsnaveena@gmail.com

G. Narayana
e-mail: narayangbgs@gmail.com

M. P. Naveena · V. Akella · C. M. Thejas
Department of Civil Engineering, K.S.School of Engineering and Management, Bangalore, Karnataka 560109, India
e-mail: Vijaya.akella@gmail.com

C. M. Thejas
e-mail: thejaschittapuram@gmail.com

8.1   Introduction

Natural river sand and coarse aggregate have caused rapid depletion of this nat-
ural source due to widely used in the production of cement mortar and concrete
[1]. According to Freedonia, World Construction Aggregates Report, the global
demand for construction aggregates exceeded 48.3 billion tons in the year 2015
and is expected to grow 5.2% annually. In India, the consumption of aggregate was
about 2.2 billion metric tons in 2010, and further, the demand is going to be more
than 5 billion metric tons by 2020 [2].

Since aggregate is the main occupants of concrete (about 65–75% of total concrete
volume), type of aggregates have a significant influence on the fresh and hardened
property of high-strength concrete [3]. The replacement of cement by GGBS not only
increases the compressive strength but also reduces the cement content which even-
tually leads to the decreases in emission of CO_2. Current standards allow only 50%
of total binder content GGBS to be used in the production of concrete. The remain-
ing GGBS goes unused and disposed as landfills [4]. Geopolymer is ceramic-type
inorganic polymers produced at low temperature, generally below 100 °C. The raw
material is mainly minerals of geological origin, and hence, the name is geopolymer.
Creating geopolymer cement requires an alumina silicate material, a user-friendly
alkaline reagent, sodium- or potassium-soluble silicates [5]. Geopolymer possesses
excellent mechanical property, fire resistance and acid resistance [6]. The geopoly-
mer product with fly ash and GGBS shows considerable resistance to chemical attack
compared to the Portland cement product [7]. The property of geopolymer concrete
with a fly ash aggregate mainly depends on the type of method of curing of aggregate
[8]. Aluminosilicate network having Si–O–Al–O bonds in polymeric form, which are
formed by dispersion of a precursor material such as fly ash or metakaolin (which has
silica and alumina) in an alkaline solution which contains reagents such as sodium
hydroxide (NaOH) and sodium silicate (Na_2SiO_3) or potassium hydroxide (KOH)
and potassium silicate (K_2SiO_3) [9].

8.2   Mix Design

Designing an appropriate mix proportion of SCC using geopolymer aggregate was
challenging task. EFNARC method of mix design was adopted using different sizes
of graded aggregates making suitable adjustments (Table 8.1).

Table 8.1 Mix design of self-compacted concrete

Sl. No.	Volume (m³)	Proportion	Cement (kg)	Fly ash (kg)	Fine aggregate (kg)	Coarse aggregate (kg)	Water (l)	Superplasticizer (kg)
1	1	1:1.47:1.42	300	240	796.5	767	175	5.4
2	1	1:1.42:1.7	350	210	796.5	767	175	5.6
3	1	1:1.37:132	400	178	796.5	767	175	5.78

8.3 Experimental Investigations

Table 8.2 shows various properties of natural and GPA aggregate. From the table, it is observed that elongation index, flakiness index and angularity index are absent as coarse aggregate developed is round in nature.

Concrete cubes were cast with aggregate sizes varying from 10 to 20 mm. Fresh and hardened properties were found for the design mix. Natural aggregates were replaced in the range of 0–100% by geopolymer aggregates as shown in Table 8.3. Same investigations have been carried out for both 350 and 400 kg of cement. Figures 8.1 and 8.2 reflect the data

Table 8.2 Physical characterization of geopolymer aggregate

Sl. no.	Tests	Geopolymer aggregate	Conventional aggregate
1.	Fineness modulus	6.28	7
2.	Flakiness index (%)	0	19.2
3.	Elongation index (%)	0	15
4.	Angularity index	1.17	11
5.	Specific gravity	2.67	2.72
6.	Water absorption (%)	0.66	0.3
7.	Bulk density (kg/m³)	1463	1542
8.	Aggregate crushing value (%)	26	24
10.	Aggregate impact value (%)	21	20
11.	Aggregate abrasion value (%)	20	18

Table 8.3 Fresh and hardened properties of SCC

Sl. no.	Cement content (kg/m^3)	Aggregate size (mm)	Percentage of replacement	Slump flow (mm)	V funnel (s)	J ring (mm)	L box ratio	U box (mm)	Compressive strength (N/mm^2)
1	300	10	0	700	8.5	2	1	12	42.04
			25	712	8	2	1	11	43.06
			50	730	7.9	1	1	10	47
			75	742	7.1	0	1	8	46.5
			100	760	7.1	0	1	6	43
2	300	12.5	0	678	9.9	4	0.89	16	49.46
			25	682	9.2	4	0.9	16	56.6
			50	700	8.8	3	0.95	15	58.2
			75	710	8.9	2	0.98	14	51.25
			100	724	8.1	2	1	12	48.9
3	300	20	0	666	11.5	8	0.8	22	37.5
			25	682	11.1	8	0.84	21	41.2
			50	695	10.5	7	0.87	18	46.1
			75	702	10.2	6	0.88	18	44.2
			100	714	10.2	6	0.91	16	39.3
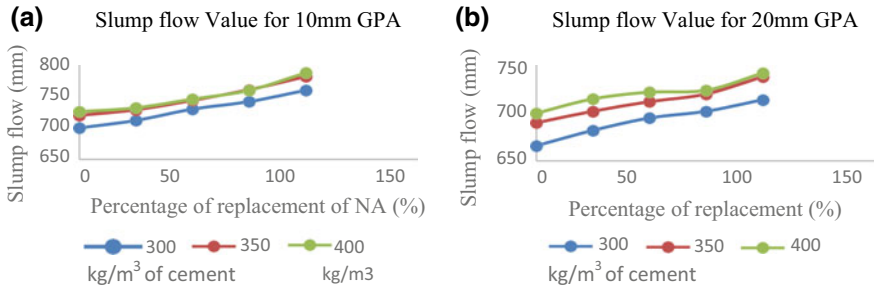
Fig. 8.1 Slump flow value of GPA
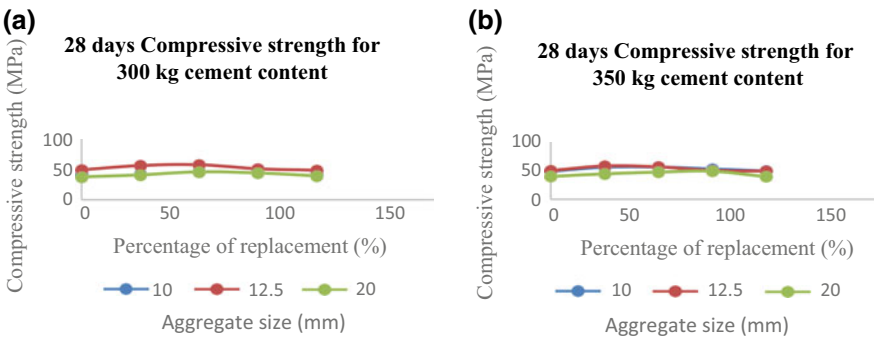
Fig. 8.2 Compressive strength value of GPA

8.4 Results and Discussion

8.4.1 Flow Characteristics

Figure 8.1a, b shows the slump of SCC for 10 mm and 20 mm aggregate, respectively. It is observed from Fig. 8.1 that higher the cement content higher is the slump. It is also seen that with increase in aggregate size slump also decreases.

From Table 8.3, it is also observed that V funnel, L box and J ring test show increase in flowability of SCC. However, the U box values have decreased with increase in aggregate size. This could be due to the filling ability of geopolymer aggregate.

8.4.2 Compressive Strength

The compressive strength was observed to be high for SCC mix with 350 kg cement content and 10 mm aggregate with a value of 56.9 N/mm^2. From Fig. 8.2a, b, it

Table 8.4 Rapid chloride penetration and bond stress of SCC

Sl. No.	Cement content (kg/m^3)	Percentage of replacement	RCPT (C)			Bond stress (MPa)		
			Aggregate size (mm)					
			10	12.5	20	10	12.5	20
1	300	0	3500	3500	3560	12.15	12.37	11.71
		25	3650	3700	3750	12.37	12.81	12.37
		50	3800	3820	3900	12.81	13.04	12.59
		75	4000	4020	4010	13.04	13.48	13.14
		100	4250	4300	4215	12.59	12.81	12.90

is observed that as the aggregate size increases compressive strength is reducing. Further studies need to be carried out to study the size effect of the aggregate.

8.4.3 Rapid Chloride Penetration Test (RCPT)

From Table 8.4, it is observed that penetration of chlorine increases with increase in aggregate size as well as cement content. The aggregates being round in nature increase the voids.

8.4.4 Bond Strength

Concrete cubes were cast with rods inserted with 200 mm projections. These were tested in UTM to find the bond strength. It is observed from Table 8.3 that bond stress is in the range of 12–14 N/mm^2 which is satisfactory.

8.4.5 Microstructure Analysis

Figure 8.3a, b is SEM images of natural aggregate and GPA. It is observed the natural particle size varies from 1.2 to 9.28 µm and geopolymer particle size from 2.98 to 4.70 µm. Geopolymer particles are more densely packed as compared to natural aggregate.
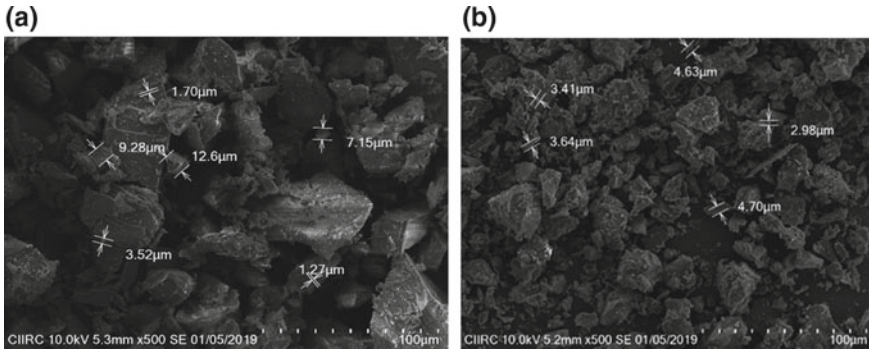
Fig. 8.3   SEM images of natural and geopolymer aggregate
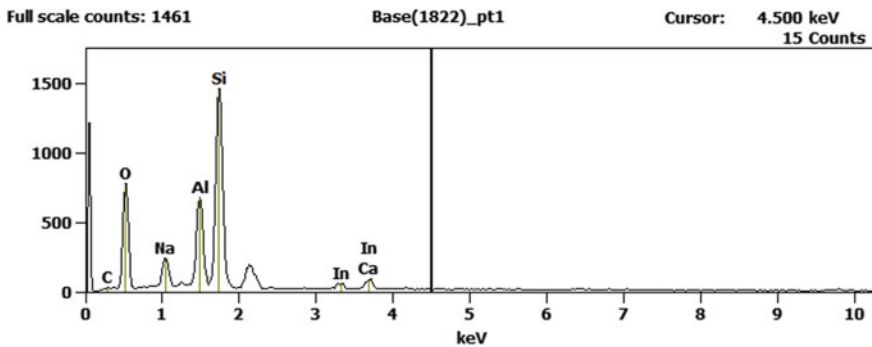
Fig. 8.4   EDS image of natural aggregate

8.4.6   Energy Dispersive Spectroscopy (EDS)

EDS is an analytical technique used for the elemental analysis or chemical characterization of a sample. It is found that silica content is higher in natural aggregate as compared to geopolymer aggregate. Calcium content is high in geopolymer aggregate as shown in Figs. 8.4 and 8.5.

8.5   Regression Analysis

It is of interest to predict strength of compressive strength of concrete for different percentage replacements of natural aggregates with GPA for varying cement content. Regression Analysis is carried out in MATLAB. Figure 8.6 shows graphical representation of predicted values for various percentage replacements of natural aggregates with geopolymer aggregate. Figure 8.7 represents surface plot of the
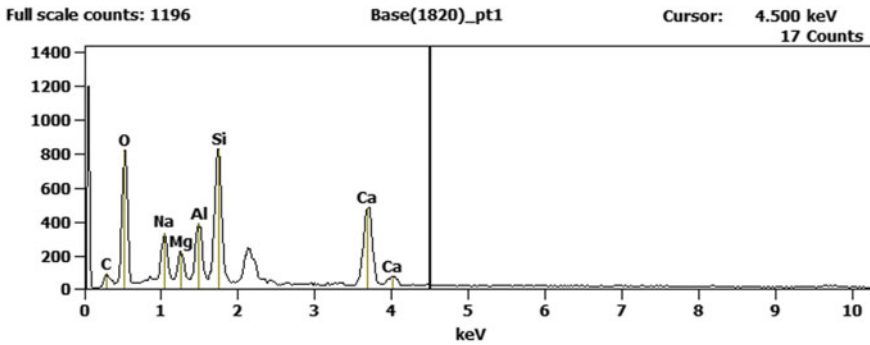
Fig. 8.5 EDS image of geopolymer aggregate
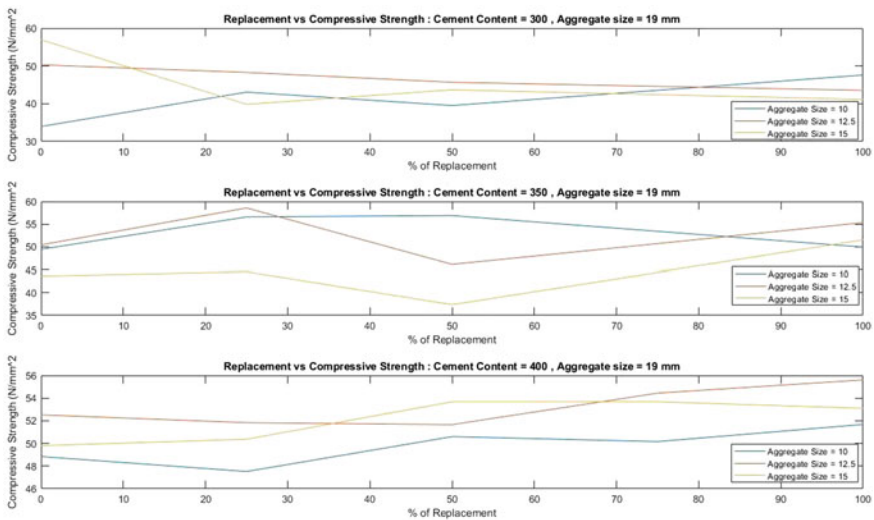
Fig. 8.6 Compressive strength for different sizes of aggregates

predicted values.

8.6   Application of Geopolymer Aggregate

Further investigations were carried out to check the suitability of geopolymer aggregate in sleepers. The sleepers were cast in Malu sleepers Pvt. Ltd., who are one of the suppliers for Indian Railways. The bending and electric resistivity tests of sleepers were carried out in yard. It was found that the bending strength of sleepers cast by
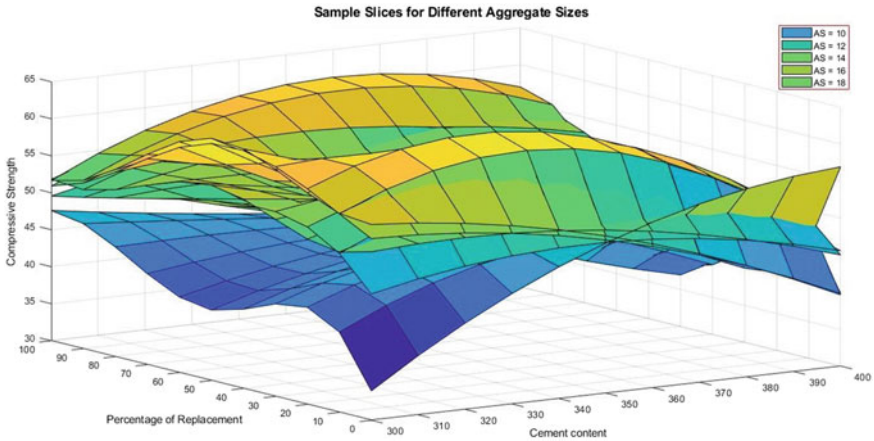
Fig. 8.7   Surface plot

Table 8.5   Static bending and electrical resistivity test results

Sleeper	Center top in (kN)	Center bottom in (kN)	Rail seat				Electrical resistivity (V)
			Resistance load (kN)		Failure load (kN)		
			R.H.S	L.H.S	R.H.S	L.H.S	
Sleeper (GPA)	70	65	238	236	380	378	160
Standard value as per RDSO	60	52.50	230	230	370	370	Max. 240

6 M GPA with 50% replacement met with standards prescribed by Indian railways. It was also found that electrical resistivity was also within the limits from Table 8.5.

8.7   Conclusions

Geopolymer aggregate is indigenously developed in KSSEM Laboratories. It was observed from the studies that with increase in aggregate size slump decreases. It was found that *V* funnel, *L* box and *J* ring test show increase in flowability of SCC. However, the *U* box values have decreased with increase in aggregate size. This could be due to the filling ability of geopolymer aggregate. The compressive strength was observed to be high for SCC mix with 350 kg cement content and 10 mm aggregate with a value of 56.9 N/mm^2. The penetration of chlorine increases with increase in aggregate size as well as cement content. The aggregates being round in nature increase the voids. The bond stress is in the range of 12–14 N/mm^2

which is satisfactory. SEM and EDS show the morphological properties as well as chemical properties of the aggregate. It is of interest to predict the compressive strength for intermediate values. Regression analysis has been carried out using MATLAB. However, the values should be validated by testing these mixes.

References

1. Sethu Parvathy, S., Sharma, A.K., Anand, K.B.: Comparative study on synthesis and properties of geopolymer fine aggregate from fly ashes. Constr. Build. Mater. **163**, 428–437 (2018)
2. Saint-Gobain and Bosch.: Fredonia, World Construction Aggregates—Industry Study with Forecasts for 2015 and 2020. The Freedonia Group, USA (2012)
3. Vishalakshi, K.P., Revathi, V., Sivamurthy Reddy, S.: Effect of type of coarse aggregate on the strength properties and fracture energy of normal and high strength concrete. Eng. Fract. Mech. (2018)
4. Oner, A., Akyuz, S.: An experimental study on optimum usage of GGBS for the compressive strength of concrete. Cement Concr. Compos. **29**, 505–514 (2007)
5. Davidovits, J.: Geopolymers: ceramic-like inorganic polymers. J. Ceram. Sci. Technol. **8**(3) (2017)
6. Davidovits, J., Davidovits, M.: Geopolymer room temperature ceramic matrix for composites. Ceram. Eng. Sci. Proc. **9**(842), e853 (1988)
7. Sakkas, K., Nomikos, P., Sofianos, A., Panias, D.: Fire resistant geopolymer for passive fire protection. Fire Mater. (Special issue) D (2014)
8. Venkata Suresh, G., Pavan Kumar Reddy, P., Karthikeyan, J.: Effect of GGBS and fly ash aggregates on properties of geopolymer concrete. J. Struct. Eng. **43**(5), 436–444 (2017)
9. Menon, S.U., Anand, K.B., Sharma, A.K.: Performance evaluation of alkali-activated coal ash aggregate in concrete. Waste Resour. Manage. **171**(1), 4–13 (2018)

Chapter 9
Experimental Studies and Numerical Validation on Bearing Capacity of Skirted Footings on c-Φ Soils

Arekal Vijay, Vijayalakshmi Akella and B. K. Raghu Prasad

Abstract This work discusses the suitability of inclined internal skirts along with outer vertical plates or skirts on bearing capacity of skirted footings on c-Φ soils. The parameters considered are thickness and depth of vertical plates and the spacing of inclined internal skirts. The scaled model footings were made up of mild steel which was considered for this research work. Square and rectangle are the two shapes adopted. The size was designed in such a way that the lateral confinement effect does not affect the test results. The foundation soil was in dry condition. The various parameters considered are thickness, depth and spacing of internal skirts. In square footing, for a 5-mm-thick skirt, 40-mm-skirt depth and 10-mm-internal skirt spacing, increase in bearing capacity observed was 2.4 times. If the depth of skirt is increased to 120 mm keeping all other parameters unchanged, the bearing capacity was increased to 13 times. For square footing, the highest improvement in bearing capacity was 14 times for skirt depth of 120 mm with skirt thickness of 5 mm and internal skirts spacing of 10 mm. Increase in spacing of internal skirts from 10 to 30 mm for square footing with 5-mm-thick skirt with 40-mm-skirt depth showed a reduction in bearing capacity from 238 to 150%. Numerical validation of experimental test results was carried out by using Plaxis software.

Keywords Skirted footings · Bearing capacity · Settlement

9.1 Introduction

The present study aims at improving the bearing capacity of foundations soil by confinement. The confinement of soil is achieved by providing vertical insertions along with the periphery of footings. These vertical insertions resist the lateral movement of foundation soil. These vertical insertions are termed as skirts, and foundations with these skirts are termed as skirted footings or bucket foundations. These foundations are employed in offshore structures to replace deep foundations. However, skirted

A. Vijay (✉) · V. Akella · B. K. Raghu Prasad
KS School of Engineering and Management, Bengaluru, Karnataka 560109, India
e-mail: arekalvijay@gmail.com

foundations are yet to be adopted for onshore structures. Presently, researchers are focusing on this aspect. Most of the previous research focused on footings with vertical insertions. In this work, apart from outer vertical insertions, footings are provided with additional inner inclined insertions for improved load-carrying capacity.

9.2 Literature Survey

Eid [1] conducted numerical studies on axially loaded skirted shallow foundations. The results showed that bearing capacity and settlement values of skirted foundations were close to pier foundations of the same width and depth. Bearing capacity of shallow foundation increased with increase in skirt depth and decrease in relative density of sand. Settlement reduction exceeds 70% for a ratio of skirt depth/foundation width equal to 2.

Finite element limit analysis conducted by Mana et al. [2] identifies the critical internal skirt spacing. With the increasing skirt depth, fewer internal skirts are required. But increasing soil strength heterogeneity requires more internal skirts. The results also indicate that the reduction in number of skirts reduced bearing capacity.

Laboratory tests were conducted by El Sawwaf and Nazer [3] to study the influence of soil confinement on the behaviour of a footing resting on granular soil. The parameters considered are the diameter and depth of cell and the embedded depth of footing. The results showed soil confinement increase bearing capacity of circular footing. The cells with small cell diameters exhibit deep foundation behaviour, while this pattern was not found with large cell diameters.

9.3 Methodology

9.3.1 Model Footings Without Skirt

In the present work, square-shaped footing with and without skirts are used for the testing. The footing sizes were smaller than (1/5) B (where B = width of container) to avoid lateral confinement effect. The plan area of footings is 80 mm × 80 mm. The thickness of footings is 10 mm made of mild steel. Vertical plates of thickness 1, 3 and 5 mm are used as skirts. The skirt depths of $0.5B$, $1.0B$ and $1.5B$ were used to understand the effect of bearing capacity due to variation in skirt depth where B is the least lateral dimension of the model footing.

Fig. 9.1 Square footing with vertical and inclined skirts
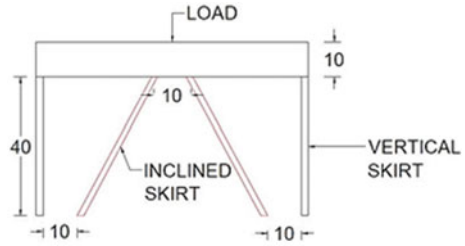
Fig. 9.2 Square footing with vertical and inclined skirts
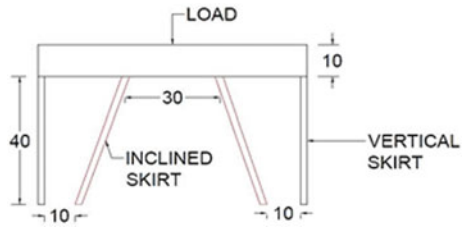
9.3.2 Model Footings with Skirts

Model footings and skirts are connected by welded joints so as to form a monolithic footing. The line diagrams of square footing are shown in Figs. 9.1 and 9.2. Totally, 18 model square footings of varying skirt depths (40–120 mm) and skirt thicknesses (1–5 mm) were used for the study.

9.3.3 c-Φ Soil

An oven-dried soil was used in the experiment program. The soil was sieved as per Indian Standard specifications. The geotechnical properties of the soil are given in Table 9.1.

Table 9.1 Geotechnical properties of soil

Property	Value
Specific gravity (G)	2.67
Effective particle size (D_{10}), mm	0.022
Particle size (D_{30}), mm	0.068
Particle size (D_{60}), mm	0.36
Unit weight (γ), kN/m^3	13.73
Angle of internal friction	30°
Cohesion (c), kN/m^2	11

Fig. 9.3 Test tank and loading frame

9.3.4 Test Tank and Loading Frame

The steel tank of size of 0.75 m (length), 0.45 m (width) and 0.75 m (depth) as shown in Fig. 9.3 was used to hold foundation soil. To avoid buckling of sidewalls of the tank during loading, stiffeners were provided. Static vertical loads were applied, and load-settlement readings were taken.

9.3.5 Test Procedure

Raining technique was adopted to prepare the bed of soil. This was done in lift of 50 mm thick up to full tank height. The soil was poured from a predetermined height and with controlled intensity of pouring, required relative density of soil was obtained. To keep the model footing in full contact with the soil, the top of soil layer was levelled. This will also facilitate the load applied to the footing was vertical (normal). The unit weight of the soil was maintained at 13.73 kN/m^3 in dry state. After each test cycle, the soil beneath the footing was excavated to a depth of 1.5B. The footing was placed on the predetermined prepared surface of the soil in the tank. The vertical load at a constant rate was gradually applied to the footing until the settlement is seized. Two dial gauges were used to record the settlements of the footing. For each cycle, the load-settlement readings were recorded.

9.3.6 Numerical Modelling

An extensive 2D finite element modelling and analysis was carried out to evaluate the behaviour of the footing with and without structural skirts. The axisymmetry model is used for square footing with 15-node triangular element, and the dimensions were set for modelling. The dimensions of c-ϕ soil 450 mm × 750 mm and thickness of 750 mm are modelled in the drawing area, and the standard boundary condition is assigned. The footing model with and without structural skirts with varying skirt thickness of 1 and 3 mm, skirt depths of $0.5B$ where 'B' is the least lateral dimension of the footing is modelled. The interface is given between footing and soil structure and between the structural skirt and soil structure. The point load is applied concentrically on the footing. The geometry of the finite element soil model adopted for the analysis is 450 mm × 750 mm × 750 mm shown. Soft soil model is adopted for soil modelling. The main feature of soft soil model is that the stiffness of soil is dependent on stress applied. The failure behaviour of soil is in accordance with the Mohr–Coulomb criterion. The material properties of c-ϕ soil are defined according to soft soil model.

The stresses initially are more at the bottom of the soil model and gradually decrease towards the surface of the soil model due to the fixity at the bottom and sides. The load is applied concentrically as in experimental study for 24 mm settlement. Stress point nodes are selected to get the load. The deformation of the footing and soil model is obtained as shown in Fig. 9.4. From the analysis, vertical displacement is obtained.
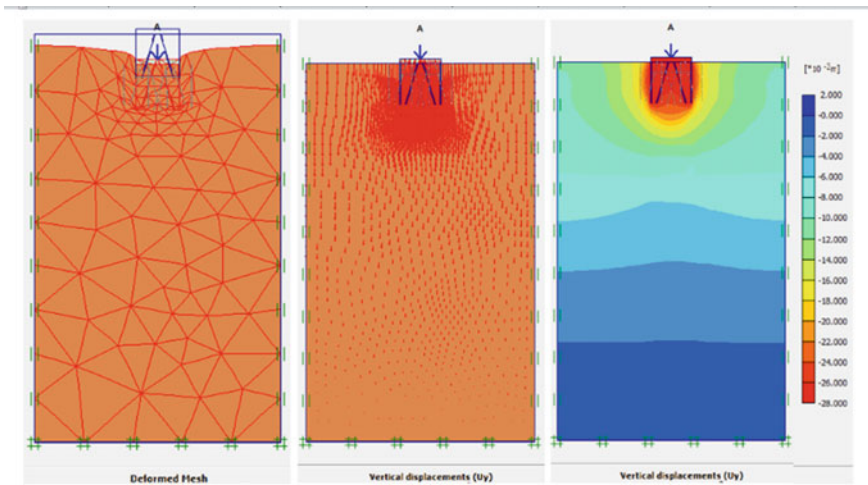
Fig. 9.4 Deformed mesh and vertical displacement

9.4 Results and Discussions

Extensive pressure-settlement experiments on square-shaped skirted footings on c-Φ soil were carried out. The pressure-settlement curves for a square footing of size 80 mm × 80 mm with thickness varying from 1 to 5 mm with constant depth of 40 mm are shown in Fig. 9.5. It is evident from the figure that the bearing capacity increases with an increase in the skirt thickness. The bearing capacity was improved by 55.50% (6.90–10.73 kN/m^2) for a skirt thickness of 1 mm, 125.60% (6.90–15.56 kN/m^2) for 3 mm skirt thickness and 238.90% (6.90–23.38 kN/m^2) for 5 mm skirt thickness for a constant skirt depth of 40 mm. It is due to increased thickness of skirts increase rigidity of skirt and hence higher resistance to lateral pressure.

The pressure-settlement curves for a model square footing of size 80 mm × 80 mm are shown in Fig. 9.6. For a concentric load, the variation in bearing capacity without skirts and with skirts of thickness 1, 3 and 5 mm with internal skirts having 30 mm spacing and constant skirt depth of 40 mm is plotted. The values of bearing capacity of footings with skirts are compared with the bearing capacity values of footings without skirts.

From Fig. 9.6, it is evident that the bearing capacity increases with increase in the skirt thickness. The bearing capacity was improved by 44.40% (6.90–9.96 kN/m^2) for a skirt thickness of 1 mm, 73.40% (6.90–11.96 kN/m^2) for 3 mm skirt thickness and 150% (6.90–17.24 kN/m^2) for 5 mm skirt thickness in c-ϕ soil for a constant skirt depth of 40 mm.
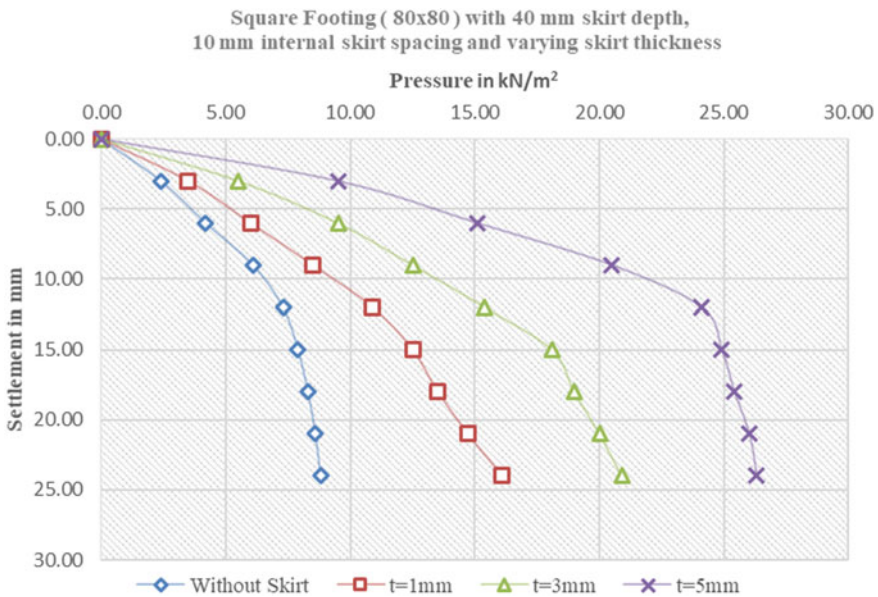
Fig. 9.5 Pressure-settlement curves for a square footing (skirt spacing = 10 mm)
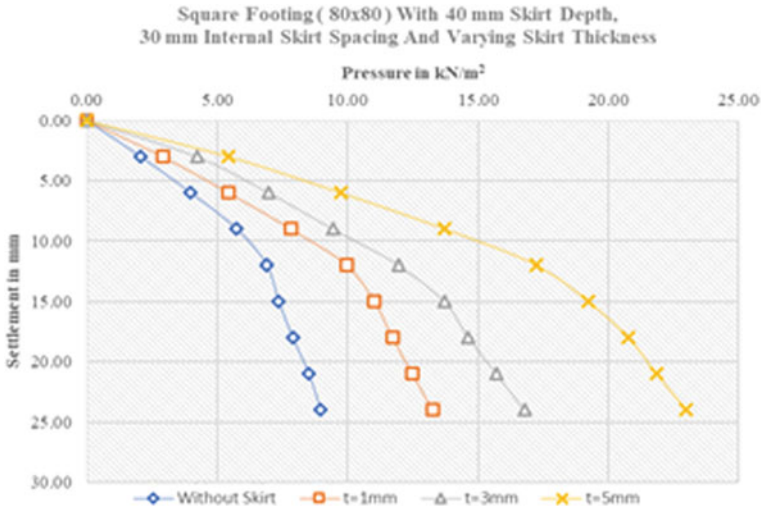
Fig. 9.6 Pressure-settlement curves for a square footing (skirt spacing = 30 mm)

Figures 9.5 and 9.6 indicate that the bearing capacity for the square footing with
10-mm-internal skirt spacing is greater when compared to the model square footing
with 30-mm-internal skirt spacing. The comparison of bearing capacity improve-
ments in model square footings with 10- and 30-mm-internal skirt spacing for a skirt
depth of 40 mm is discussed in Table 9.2.

The pressure-settlement curves for a model square footing of size 80 mm × 80 mm
are shown in Fig. 9.7. For a concentric load, the variation in bearing capacity without
skirts and with internal skirts of thickness 1, 3 and 5 mm having 10 mm spacing and
constant skirt depth of 80 mm is plotted. The values of bearing capacity of model
footings with skirts are compared with the bearing capacity values of model footings
without skirts.

Figure 9.8 shows that the bearing capacity increases with increase in the skirt
thickness. The bearing capacity was improved by 198.80% (6.90–20.62 kN/m^2) for
a skirt thickness of 1 mm, 269.90% (6.90–25.52 kN/m^2) for 3 mm skirt thickness

Table 9.2 Bearing capacity improvement in square footings with 10- and 30–mm-internal skirt
spacing for 40-mm-skirt depth

Skirt thickness	Bearing capacity improvement in square footing having 10–mm-internal spacing	Bearing capacity improvement in square footing having 30-mm-internal spacing
$t = 1$ mm	1.6 times	1.4 times
$t = 3$ mm	2.3 times	1.7 times
$t = 5$ mm	3.4 times	2.5 times
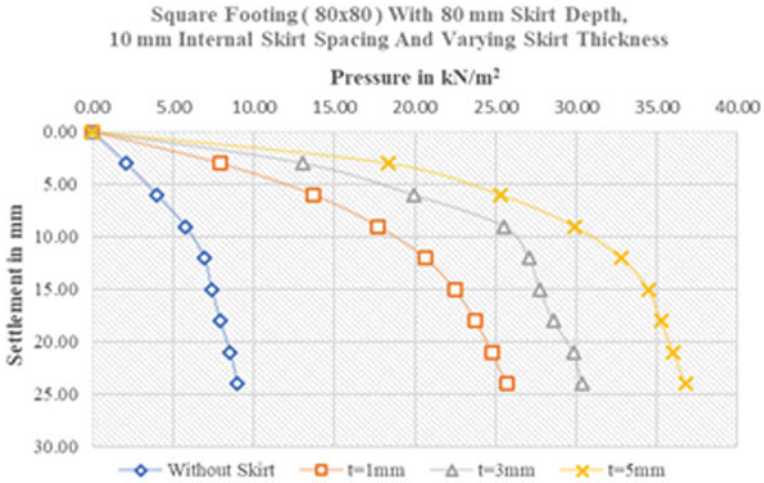
Square Footing (80x80) With 80 mm Skirt Depth,
10 mm Internal Skirt Spacing And Varying Skirt Thickness

Fig. 9.7 Pressure-settlement curves for a square footing (skirt spacing = 10 mm)

Square Footing (80x80) With 80 mm Skirt Depth,
30 mm Internal Skirt Spacing And Varying Skirt Thickness
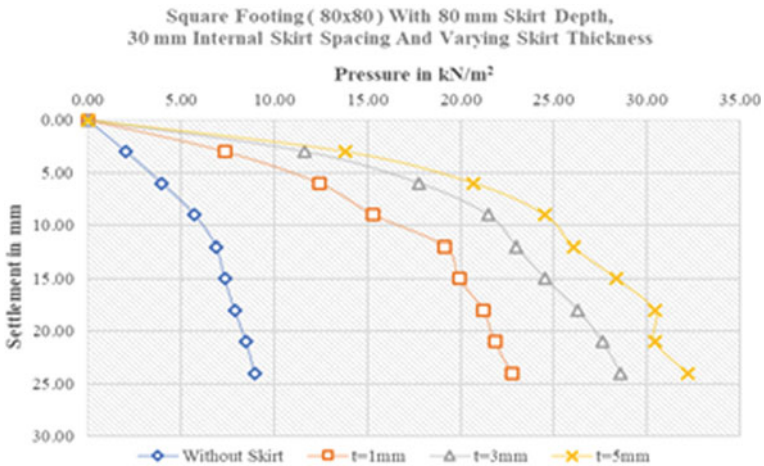
Fig. 9.8 Pressure-settlement curves for a square footing (skirt spacing = 30 mm)

and 375.40% (6.90–32.80 kN/m^2) for 5 mm skirt thickness in c-ϕ soil for a constant skirt depth of 80 mm.

In Fig. 9.8, pressure-settlement curve for different thickness of internal skirt with constant depth and spacing of 80 mm and 30 mm, respectively, is shown. It is evident that the bearing capacity increases with increase in the skirt thickness. The bearing capacity was improved by 177.70% (6.90–19.16 kN/m^2) for a skirt thickness of 1 mm, 211% (6.90–21.46 kN/m^2) for 3 mm skirt thickness and 255.50% (6.90–24.53 kN/m^2) for 5 mm skirt thickness for a constant skirt depth of 80 mm. From

Figs. 9.7 and 9.8, it is clear that the bearing capacity for the same square footing with 10-mm-internal skirt spacing is greater when compared to the square footing with 30-mm-internal skirt spacing. The comparison of bearing capacity improvements with increasing skirt thickness in model square footings with 10 and 30 mm spacing for a skirt depth of 80 mm is shown in Table 9.3. Table 9.4 shows similar trend for 120-mm-skirt depth.

- Figures 9.9, 9.10 and 9.11 show numerical analysis results of square footings with skirts ($d = 40$ mm, $s = 10$ mm and $t = 1$, 3 and 5 mm). From the figures, the effect of thickness of skirts on the deformation in the foundation soil and stress concentration in the footing and the skirts can be compared.

Table 9.3 Bearing capacity improvement in square footings with 80-mm-skirt depth and varying skirt thickness and internal skirt spacing

Skirt thickness	Bearing capacity improvement for square footing having 10-mm-internal spacing	Bearing capacity improvement for square footing having 30-mm-internal spacing
$t = 1$ mm	3 times	2.8 times
$t = 3$ mm	3.7 times	3.1 times
$t = 5$ mm	4.8 times	3.6 times

Table 9.4 Bearing capacity improvement in square footings with 120-mm-skirt depth and varying skirt thickness and internal skirt spacing

Skirt thickness	Bearing capacity improvement in footing having 10-mm-internal spacing	Bearing capacity improvement in footing having 30-mm-internal spacing
$t = 1$ mm	6.6 times	4 times
$t = 3$ mm	12.9 times	8.9 times
$t = 5$ mm	14.6 times	10.7 times

Fig. 9.9 Square footing with skirt $t = 1$ mm
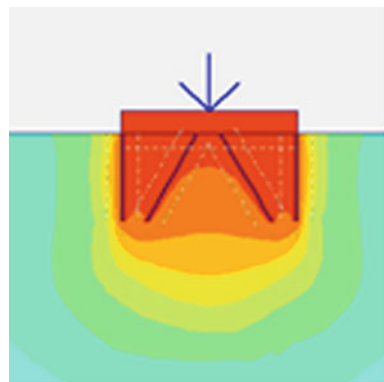
Fig. 9.10 Square footing
with skirt $t = 3$ mm
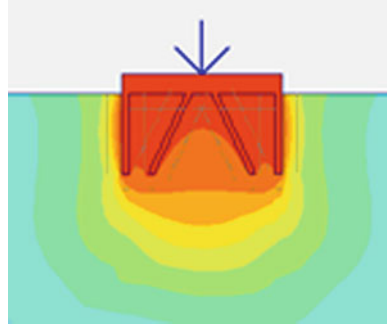
Fig. 9.11 Square footing
with skirt $t = 5$ mm
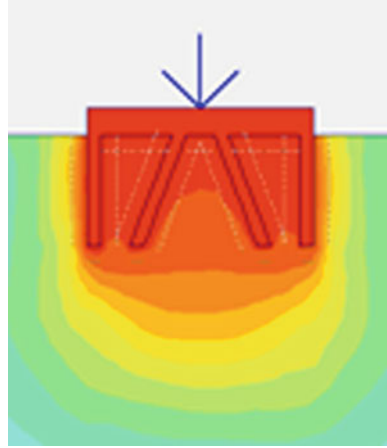
- The higher intensity of stress is found in the internal inclined skirts as compared to peripheral vertical skirts as shown in Figs. 9.12, 9.13 and 9.14. The maximum

Fig. 9.12 Max principal
stress (5000 kN/m^2)
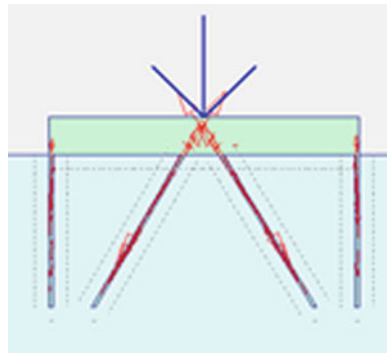
Fig. 9.13 Max principal stress (766 kN/m^2)
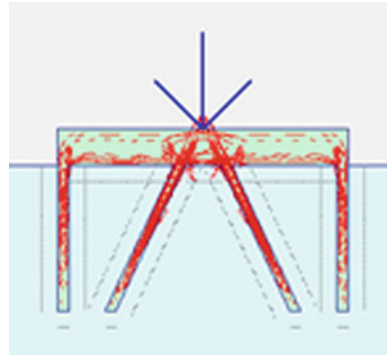
Fig. 9.14 Max principal stress (237 kN/m^2)
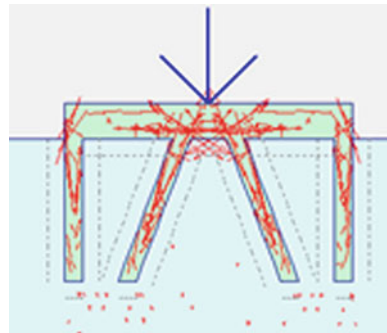
deformation is found between the skirts and deformation reduces significantly below the skirt tip.

- Further, the deformation between the inclined skirts is significantly lesser as compared to outside the inclined skirts indicating that inclined skirts resist vertical loads better than the vertical loads as shown in Figs. 9.15, 9.16 and 9.17.

9.5 Summary

- Results showed that spacing of internal inclined skirts has a significant effect on the bearing capacity of square footings on c-Φ soil. Increase in spacing of internal skirts from 10 to 30 mm for square footing with 5-mm-thick skirt with 40-mm-skirt depth showed reduction in bearing capacity from 238 to 150%. This trend confirms that smaller cells are more effective in confining foundation soil.
- Pressure-settlement curves showed improvement in bearing capacity with the increase in skirt depth for both square footings. The maximum effect on bearing capacity value was found to be for a skirt depth of 1.5B. For example, in square footing, for a 5-mm-thick skirt, 40-mm-skirt depth and 10-mm-internal

Fig. 9.15 Deformed mesh
for skirt thickness 1 mm
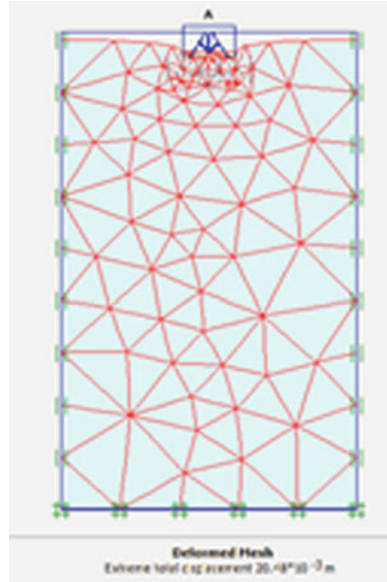
Fig. 9.16 Deformed mesh
for skirt thickness 3 mm
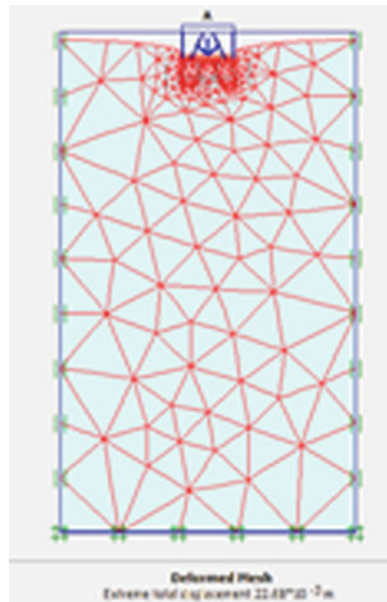
Fig. 9.17 Deformed mesh
for skirt thickness 5 mm
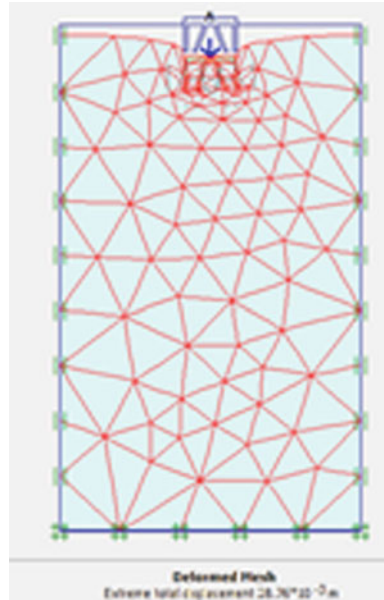
Deformed Mesh
Extreme total displacement 28.76*10⁻⁷ m

skirt spacing, increase in bearing capacity observed was 2.4 times. If the depth of skirt is increased to 120 mm keeping all other parameters constant, the bearing capacity was increased by 13 times.

- Increase in skirt thickness for square footing increased the bearing capacity. For a skirt thickness of 5 mm, the bearing capacity was found to be higher when compared to 1- and 3-mm-thick skirts. For square footing, the highest improvement in bearing capacity was 14 times for skirt depth of 120 mm with skirt thickness of 5 mm and internal skirts spacing of 10 mm. This trend is attributed to the increased thickness of skirts increase rigidity of skirt and hence higher resistance to lateral pressure.

- The percentage of difference in settlement for square footing (for 40 mm skirt depth) ranges between 5.5 and 19.83%. Similar trend is observed for 80 mm skirt depth. The percentage of difference ranges between 6.58 and 29.25%.

- The higher intensity of stress is found in the internal inclined skirts as compared to peripheral vertical skirts. The maximum deformation is found between the skirts and deformation reduces significantly below the skirt tip. Further, the deformation between the inclined skirts is significantly lesser as compared to outside the inclined skirts indicating that inclined skirts resist vertical loads better than the vertical loads. It may be concluded that the analytical result closely matches with experimental results in terms of percentage difference in settlement.

References

1. Eid, H.: Bearing capacity and settlement of skirted shallow foundations on sand. Int. J. Geomech., 645–652 (2013). https://doi.org/10.1061/(asce)gm.1943-5622.0000237
2. Mana, D.S.K., Gourvenec, S., Martin, C.M.: Critical skirt spacing for shallow foundations under general loading. J. Geotech. Geoenviron. Eng. **139**(9), 1554–1566 (2013)
3. El Sawwaf, M., Nazer, A.: Behavior of circular footings resting on confined granular soil. J. Geotech. Geoenviron. Eng. **131**(3), 359–366 (2005)

Chapter 10
Effect of Aerodynamic Modifications on a Tall Building with Horizontal Irregularity

Shanku Mandal 📷**, Sujit Kumar Dalui** 📷 **and Soumya Bhattacharjya**

Abstract Impact of wind force is more critical on tall buildings with an increase in height. Horizontal irregularity on plan shape and randomness of wind makes the structure more vulnerable. A detail analytical study has been done considering various wind incidence angle ranging from 0° to 90° at an interval of 30° using computational fluid dynamics (CFD) on U-plan shaped tall building with corner modifications. The present study has shown that the introduction of minor aerodynamic modifications has major a role in minimizing the wind-induced responses. Drag coefficient and the lift coefficient are reduced due to the application of corner chamfered and corner roundness on the basic model. Most of the cases both maximum pressure and suction occur on the different faces of corner chamfered models. It is also noted that the modified corner exerts more pressure than the basic model.

Keywords Horizontal irregularity · Wind incidence angle · Computational fluid dynamics · Aerodynamic modification

10.1 Introduction

Corner modifications do not only enhance the aesthetic beauty of the structure but also play a major role for drastic chance in wind pressure on structural elements of tall building faces. The unconventional shape of the buildings makes them more sensitive to wind than those with a regular shape. Kim and You [1] performed several wind tunnel tests and concluded that the tapering effect has a more significant effect in across-wind direction than that in along-wind direction. Gomes et al. [2] used a

S. Mandal (✉) · S. K. Dalui · S. Bhattacharjya
Department of Civil Engineering, Indian Institute of Engineering Science and Technology, Shibpur, Howrah, India
e-mail: shankumandalce@gmail.com

S. K. Dalui
e-mail: sujit_dalui@rediffmail.com

S. Bhattacharjya
e-mail: soumya@civil.iiests.ac.in

closed circuit wind tunnel for testing 1:100 scale irregular-plan shaped models with different wind incidence angles and find out the noticeable difference in pressure distributions on inner faces due to the influence of the additional wing which transforms the L into U-shaped model. Ilgin and Gunel [3] suggested different design methods and major aerodynamics modification like tapering, setbacks, sculptured building tops, varying the shape and openings, etc., should be adopted to ensure the functional performance of flexible structure and control the wind-induced motion of tall buildings. Tse et al. [4] investigated the impact of the amount and type of corner modifications. Recessed corners modifications are shown to be an effective minimizer of the wind-induced loads than chamfered corners. The overall construction costs can be reduced with the application of corner modifications. Sevalia et al. [5] numerically studied the force coefficient of different geometric plan configurations like square, circular, hexagon and octagon tall building having the same plan area. They conclude that the circular plan shape of building is much better when compare to the other plan shape of building in terms of both wind pressure coefficient as well as total drag force on building. Tanaka et al. [6] found out that helical has better aerodynamics behavior over other configurations like corner cut, setback due to shed irregularity throughout the height. Xie [7] considered aerodynamic optimization is the most efficient way to ensure the structure safety in strong winds and control the wind-induced motion of super-tall buildings. Kim and Kand [8] discussed the effectiveness of aerodynamic modification in reducing wind loads due to the fact that change in building shape with height promotes frequent, random and incoherent vortex formation at different levels. Bandi et al. [9] tested different cross-sectional tall buildings with configurations of straight triangle, corner cut, 60° helical, 180° helical and 360° helical, and clover to investigate the variations in along-wind and crosswind overturning moment coefficients. Sharma et al. [10] experimentally investigate the advantages of tapered and setback model over regular conventional shapes. Setback building model is the effective minimizer of the wind loads compare to taper modified building. Present study mainly focuses on the effect of rounded corner and chamfered corner on U-plan shaped tall building at different wind incidence angles. Comparison of force coefficient and mean pressure coefficient of various models are shown.

10.2 Scope of Study

The effect of wind force on regular-plan shaped building is available in various codal provisions but very limited data are available for irregular-plan shaped building. Detail study should be done to evaluate the wind responses due to the abundant presence of U-plan shaped buildings. Numerical simulation using computational fluid dynamics (CFD) is the best-suited alternative where wind tunnel facility is not available.

Different models as shown in Fig. 10.1 have been analyzed by ANSYS CFX considering 0° to 90° wind incidence angle at an interval of 30°. The U1 model has a
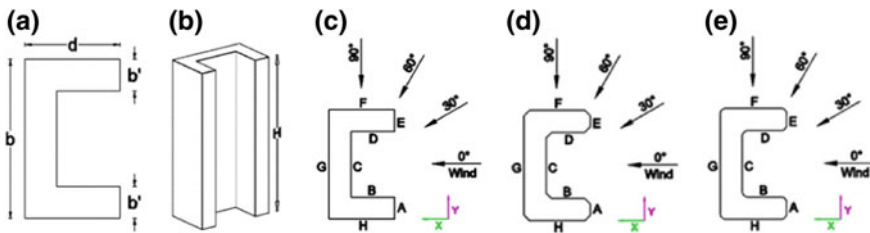
Fig. 10.1 Analytical models **a** plan view of basic model, **b** elevation view of basic model, **c** basic model with face name and wind incident angle (U1), **d** corner chamfered model with face name and wind incident angle (U2) and **e** corner rounded model with face name and wind incident angle (U3)

uniform cross section throughout the height. U2 model has been modified with corner chamfer of $0.25b'$ and the same amount of corner roundness has been provided in case of U3 model. Here, b, b', d and H are considered as 250 mm, 50 mm, 150 mm and 500 mm, respectively.

10.3 Computational Setup and Meshing

The wind-induced responses of the analytical models have been studied on the domain recommended by Frank et al. [11] and Revuz et al. [12]. The building model has been placed at $5H$ from inlet, sidewalls and roof of the domain, and $15H$ from the outlet as shown in Fig. 10.2. The height of the analytical model has been taken as H. The flow of the wind is not restricted and all the characteristic behaviors of wind can be observed in this domain. No blockage correction is needed for this domain.

The k-ε turbulence model is considered in our present study. The boundary condition for sidewalls and roof of the domain has been taken as free slip walls, and the walls of the building and the floor of the domain are taken as no-slip walls. The terrain category II is adopted as per Indian standard IS: 875-2015 (part 3) [13]. The analytical model has been modeled at a geometric scale of 1:300. The free stream velocity of wind at inlet is taken 10 m/s.

The equation of atmospheric boundary layer (ABL) wind profile is taken as
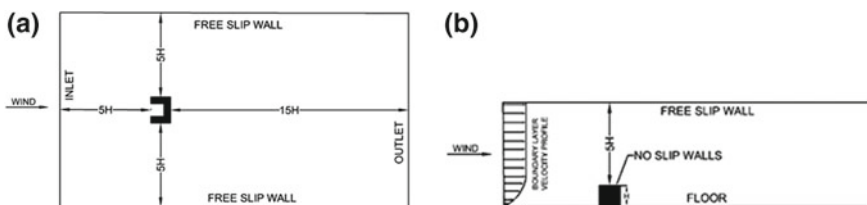
Fig. 10.2 **a** Plan view and **b** elevation view of computational domain used for CFD simulation
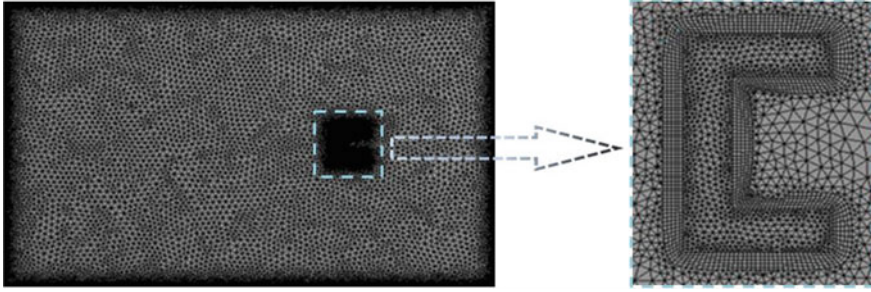
Fig. 10.3 Domain meshing of U-plan shaped building model

$$\frac{U_x}{U_\infty} = \left(\frac{x}{x_0}\right)^\alpha \tag{10.1}$$

U_x is the velocity at any height 'x' from ground.
U_∞ is the free steam velocity.
x is the height at any point above ground surface.
x_0 is the atmospheric boundary layer height.
α is a power-law exponent which depends on the roughness of the terrain.

The value of the exponent α is taken as 0.133 conforming to terrain category II as per IS: 875-2015 (part 3) [13]. The boundary layer height (x_0) is taken as 1 m.

The domain and the building meshing are done using tetrahedral elements as recommended by Lo et al. [14]. Finer meshing is employed around building models to capture the more efficient flow for accurately analyze the higher gradient of the wind flow as shown in Fig. 10.3.

10.4   Comparison with the Previous Study

Figure 10.4a, b shows the comparison of wind velocity profile and turbulence intensity profile between the data obtained from the present study, wind tunnel study by Dalui [15] and CFD by Kar et al. [16]. The comparison shows more or less similar characteristics with the previous study due to generation of similar type of wind environment on every case. Figure 10.4c displays pressure coefficients along vertical centerline at face C of U-plan shaped model for 0° wind incidence angle. To validate the current analytical study, a comparison of pressure coefficient between the current study and the previous study of Gomes et al. [2] has been done.
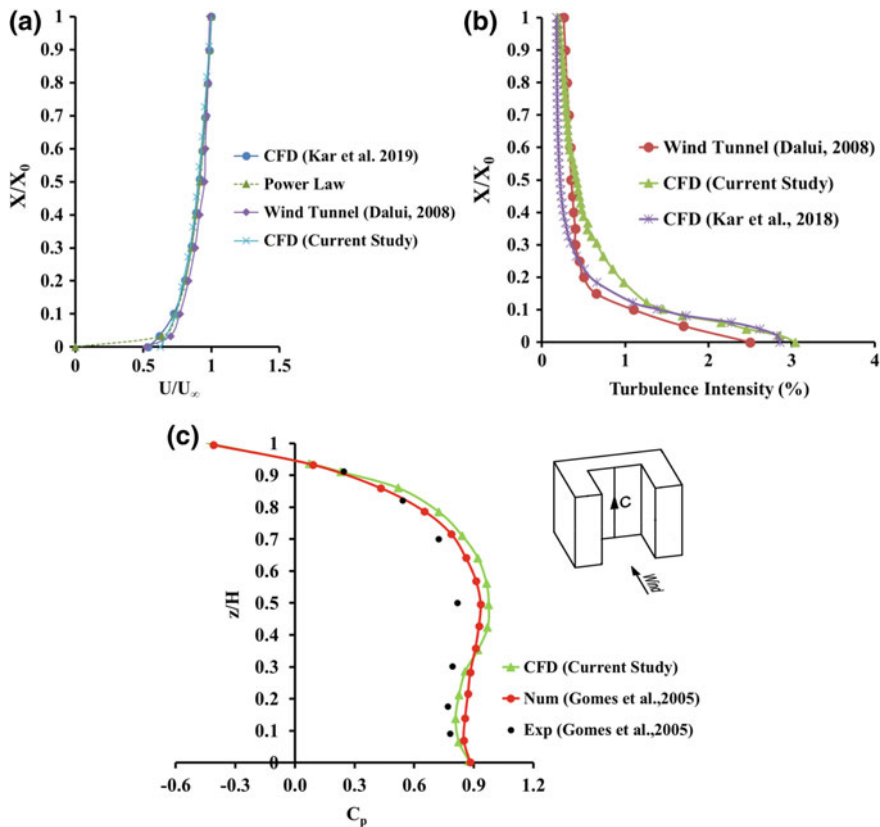
Fig. 10.4 Comparison with the previous study **a** velocity profile, **b** turbulence intensity and **c** pressure coefficients along vertical centerline at face C of U-shaped model for 0° wind incidence angle

10.5 Results and Discussion

The wind-induced effect on different faces of basic and corner modified U-plan shaped tall buildings are shown considering 0° as well as 30°, 60° and 90° wind incidence angle. The typical wind flow patterns around basic and corner modified building models are shown in Fig. 10.5. Symmetrical vortices are formed on the leeward side of basic model due to normal wind incidence angle, but asymmetric vortices are formed on the corner modified building models. The formation of vortices varies significantly with the change in wind angle. The horizontal irregularity of the U-plan shaped building promotes the production of unsymmetrical and irregular vortices in the wake region. Corner modification as well as self-interfering limbs of the building also form irregular vortices with the change in angle of wind attack.
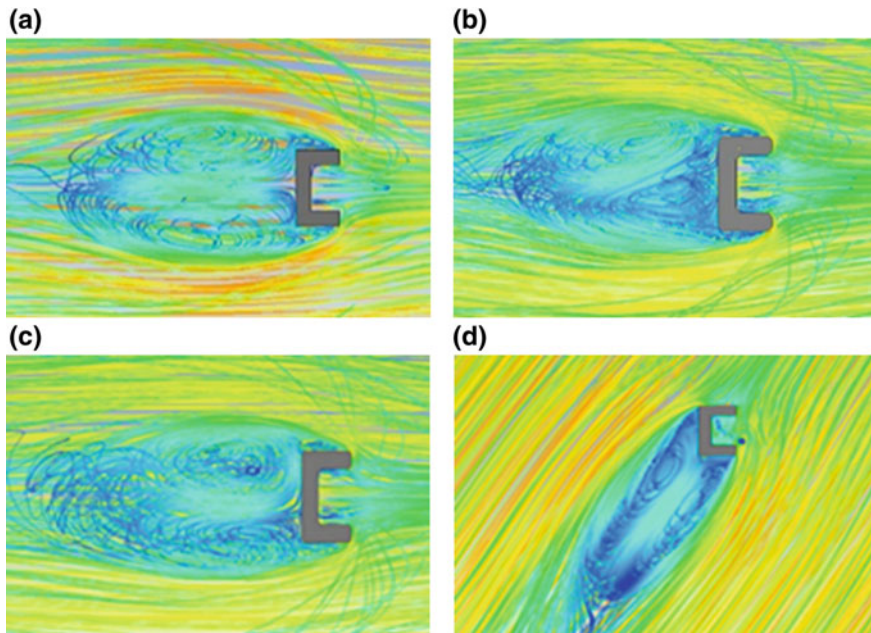
Fig. 10.5 Wind flow pattern around various model **a** basic, **b** corner chamfered, **c** corner rounded and **d** 60° wind incidence angle

Comparison of drag coefficient and lift coefficient of basic U-shaped and corner modified U-shaped models are shown in Fig. 10.6. It is clearly visible that sharp corner model or basic U-shaped model attracts more wind force in comparison with corner modified models. Corner modifications are efficient to reduce drag coefficient as well as lift coefficient. Corner roundness is more effective to reduce wind-induced responses in along-wind direction. In some cases, corner chamfered shows less attraction to wind force on across-wind direction with change in attack of wind angle. At 60° wind incidence angle, the effect of wind-induced responses is critical in across-wind direction.
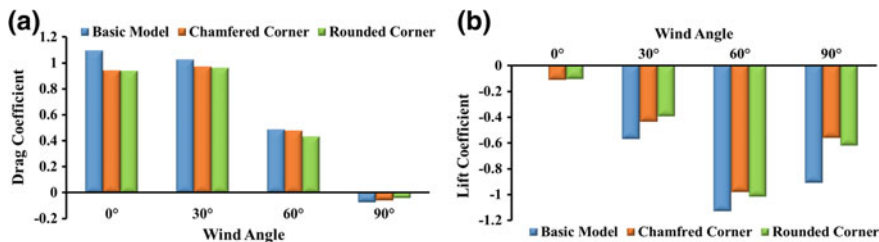
Fig. 10.6 Comparison of force coefficient of various models with different wind incidence angle **a** drag coefficient and **b** lift coefficient
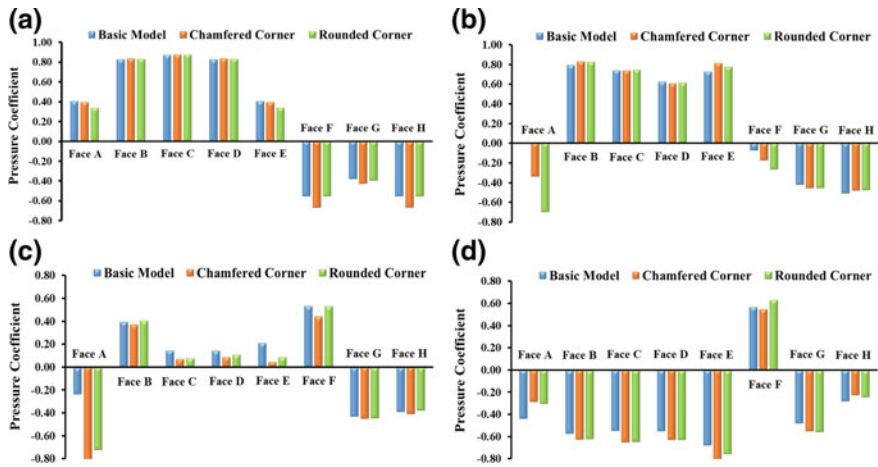
Fig. 10.7 Comparison of mean pressure coefficient on all faces of various model at **a** 0°, **b** 30°, **c** 60° and **d** 90° wind incidence angle

The mean pressure coefficients on different faces are shown in Fig. 10.7. Mean pressure coefficient on corner rounded models are less compare to other models in case of normal wind incidence angle. Corner chamfered models exert more pressure on side faces in most of the cases. Maximum positive pressure occurred on windward direction. Side faces and leeward faces exert suction due to side wash and formation of vortex, respectively. The change in mean pressure coefficient on various faces changes due to change in wind incidence angle. At 30° wind incidence angle on face A of basic model, mean wind pressure is negligible due to presence in both positive and negative pressure, but in case of corner modified models negative pressure is predominant on this face. At 60° wind angle maximum suction is occur on face A of corner chamfered model, but at 90° wind angle maximum suction is occur on face E. It is a clear indication that with the change in wind incidence angle, the variation in wind-induced responses shows mainly due to the presence of limbs on U-shaped buildings.

The comparison of pressure coefficient (C_p) along perimeter of building models is shown in Fig. 10.8 at 250 mm height from the base on horizontal direction. The important observation is to be noted that on the modified corner the pressure is more as compare to basic model in most of the cases.

10.6   Conclusion

The role of corner modification on irregular-plan shaped tall building at different wind incidence angles is presented in the current study. The effects of modification can be summarized as follows.
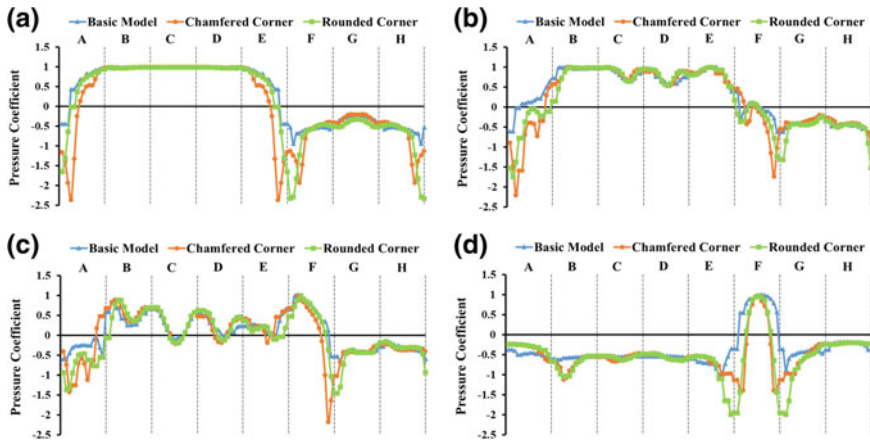
Fig. 10.8 Comparison of pressure coefficient along the horizontal center line of different models at **a** 0°, **b** 30°, **c** 60° and **d** 90° wind incidence angle

- The drag coefficient is maximum in case of normal wind incidence angle and minimum in case of 90° wind incidence angle.
- It is noticeable that the drag coefficient is reduced with the introduction of corner modifications. Though rounded and chamfered modification show almost similar reduction in drag coefficient, corner roundness is more efficient in reducing the drag coefficient.
- At 60° wind incidence angle, the lift coefficient is maximum in every case.
- It is observed that on corner rounded model lift coefficient is less than corner chamfered model at 0° and 30° wind incidence angle, but at 60° and 90° wind incidence angle the lift coefficient is more on corner rounded models than that of corner chamfered models.
- For each case, maximum positive pressure is generated on face C at 0° wind incidence angle, and face A of corner Chamfered model is experienced the maximum negative pressure at 60° wind incidence angle.
- At 90° angle, all the faces except face F exert suction.
- Most of the cases the corner modification exert more positive as well as negative pressure than that of basic model.

On the basis of obtained results, it is clear that corner modifications play an important role in reducing force coefficient on tall building. Providing corner roundness on basic model is more effective than chamfered corner. Current investigation gives a serious indication that the designer may provide modifications to minimize the wind force on structure but should take special care in case of designing the clad structural elements. The above study shows the necessity of detailed study considering the various angle of wind attack to find out the worst cases before designing any structure.

References

1. Kim, Y.M., You, K.P.: Dynamic responses of a tapered tall building to wind loads. J. Wind Eng. Ind. Aerodyn. **90**, 1771–1782 (2002)
2. Gomes, M.G., Moret Rodrigues, A., Mendes, P.: Experimental and numerical study of wind pressures on irregular-plan shapes. J. Wind Eng. Ind. Aerodyn. (93), 741–756 (2005)
3. Ilgin, H.E., Gunel, M.H.: The role of aerodynamic modifications in the form of tall buildings against wind excitation. Metu Jfa (2), 2 (2007)
4. Tse, K.T., Hitchcock, P.A., Kwok, K.C.S., Thepmongkorn, S., Chan, C.M.: Economic perspectives of aerodynamic treatments of square tall buildings. J. Wind Eng. Ind. Aerodyn. **97**, 455–467 (2009)
5. Sevalia, J.K., Desai, A.K., Vasanwala, S.A.: Effect of geometric plan configuration of tall building on wind force coefficient using CFD. Int. J. Adv. Eng. Res. Stud. (I), 4 (2012)
6. Tanaka, H., Tamura, Y., Ohtake, K., Nakai, M., Chul Kim, Y.: Experimental investigation of aerodynamic forces and wind pressures acting on tall buildings with various unconventional configurations. J. Wind Eng. Ind. Aerodyn. (107–108), 179–191 (2012)
7. Xie, J.: Aerodynamic optimization in super-tall building designs. In: Seventh International Colloquium on Bluff Body Aerodynamics and Its Applications, pp. 104–111 (2012)
8. Kim, Y.C., Kand, J.: Wind pressures on tapered and set-back tall buildings. J. Fluids Struct. **39**, 306–321 (2013)
9. Bandi, E.K., Tamura, Y., Yoshida, A., Chul Kim, Y., Yang, Q.: Experimental investigation on aerodynamic characteristics of various triangular-section high-rise buildings. J. Wind Eng. Ind. Aerodyn. (122), 60–68 (2013)
10. Sharma, A., Mittal, H., Gairola, A.: Wind-induced forces and flow field of aerodynamically modified buildings. Environ. Fluid Mech. 1–25 (2019). https://doi.org/10.1007/s10652-019-09687-9
11. Franke, J., Hirsch, C., Jensen, A.G. Krus, H.W., Schatzmann, M., Miles, S.D., Westbury, P.S., Wisse, J.A., Wright, N.G.: Recommendations on the use of CFD in wind engineering. Cost Action C 1–11 (2004)
12. Revuz, J., Hargreaves, D.M., Owen, J.S.: On the domain size for the steady-state CFD modelling of a tall building. Wind Struct. Int. J. **15**, 313–329 (2012)
13. IS: 875 (Part-3): Code of Practice for Design Loads (other than Earthquake Loads), for Building and Structures—Wind Loads (2015)
14. Lo, Y.L., Kim, Y.C., Li, Y.C.: Downstream interference effect of high-rise buildings under turbulent boundary layer flow. J. Wind Eng. Ind. Aerodyn. **159**, 19–35 (2016)
15. Dalui, S.K.: Wind Effects on Tall Buildings with Peculiar Shapes. Ph.D. thesis, Indian Institute of Technology Roorkee (2008)
16. Kar, R., Dalui, S.K., Bhattacharjya, S.: An efficient optimization approach for wind interference effect on octagonal tall building. Wind Struct. Int. J. **28**, 111–128 (2019)

Chapter 11
Flexural Behaviour of 2D Cellular Lattice Structures Manufactured by Fused Deposition Modelling

Harshini Gullapalli, Syed H. Masood, Syed Riza and Panneer Ponnusamy

Abstract Cellular lattice structures have applications in crash resistant and protective equipment. This study involves designing rectangular beams of lattice structures with different unit cell configurations, fabricating them on fused deposition modelling (FDM) 3D printing machine and subsequently finding out the structural design for the best flexural performance in engineering applications. All the test specimens were fabricated on Stratasys Dimension 1200 ES FDM machine in acrylonitrile butadiene styrene (ABS) material. Five types of 2D unit cells for building lattice structures were investigated which included honeycomb, diamond, square, circle, and triangle shapes. Three-point bending tests were carried out to study flexural properties like flexural strength and modulus of these cellular lattice structures. After mechanical testing, the obtained data for the five different lattice structures were mutually compared for their flexural behaviour and also with the beams built in solid and sparse shapes. Results of flexural tests indicate that the cellular lattice structures based on triangular and honeycomb shapes exhibit maximum flexural strength. The triangular structure also proved to be the highest in the value of flexural modulus among all the five cellular lattice structures. This study also includes investigating the effects of varying porosity of a particular cellular structure (honeycomb) on its flexural behaviour. Results show that for honeycomb structures, the higher porosity led to higher flexural strength and flexural modulus and shorter build time up to a porosity of 61%.

Keywords Cellular structures · Flexural behaviour · Fused deposition modelling · 3D printing

H. Gullapalli · S. H. Masood (✉) · S. Riza · P. Ponnusamy
Department of Mechanical and Product Design Engineering, Swinburne University of Technology, Melbourne, Australia
e-mail: smasood@swin.edu.au

11.1 Introduction

The fused deposition modelling (FDM) by Stratasys Inc. is one of the most widely used additive fabrication technologies that manufacture various complex geometry parts using layered manufacturing concept [1]. Materials usually used by FDM process include acrylonitrile butadiene styrene (ABS) plastic, PLA and polycarbonate materials. In this paper, the build material used is ABS plastic because it is considered as one of the best materials of the styrene family due to its characteristics like toughness, hardness, rigidity, good chemical resistance and dimensional stability. In the FDM process, the ABS raw material filament is heated and melted inside the nozzle and extruded in the form of thin layers along the two-dimensional (X-Y) layer pattern path to produce the parts as per the designed CAD model. FDM process is one of the additive manufacturing processes that is cost-effective and provides the user with greater flexibility in manufacturing intricate complex parts such as cellular structures.

Cellular lattice structures of both stochastic and non-stochastic types are gaining increasing attention by researchers due to the advent of additive manufacturing (AM) technologies, which now offer much more convenient methods of manufacturing such complex structures compared to conventional manufacturing processes. Several researchers have investigated various AM technologies, in both metals and polymers, to design and manufacture such lattice structures and to examine their mechanical properties. There is a wealth of research that has investigated the additive manufacturing of metallic cellular structures and their mechanical properties like the extensive work done by Williams et al. [2]. Iyibilgin et al. [3] conducted a thorough experimental investigation using fused deposition modelling (FDM) process for evaluating the time taken to build up a given lattice structure and subsequently tested these structures for their compressive properties. Cansizoglu et al. [4] carried out experiments to evaluate the non-stochastic lattice structures fabricated by electron beam melting process to conduct an observational study on the metal foam structures. Yang et al. [5] investigated cellular core sandwich panels for comparing their bending properties. Electron beam melting (EBM) and selective laser melting (SLM) are the two most important technologies for developing cellular metallic structures. Number of researches can be found that have employed these systems like Yan et al. [6] studying the behaviour of lattice structures using SLM; Horn et al. [7] carrying out investigations on Ti6Al4V cellular structures built on EBM and Li et al. [8] experimenting on the influence of cellular form upon the mechanical properties of meshes of Ti6Al4V fabricated by EBM. Gunay et al. [9] had performed studies to calculate the measurement uncertainty for plastic (ABS) material in flexural testing. A thorough literature survey also indicates that though many types of research can be found regarding the study of the compressive and material properties of cellular and lattice structures, very few studies have been carried out for determining the flexural behaviour of polymeric parts fabricated using the fused deposition modelling AM process.

In this paper, five different types of cellular lattice structures were manufactured in ABS material on an FDM machine. The care is taken that all these structures have more or less the same porosity (~52%). Subsequent testing was done for evaluating their flexural behaviour and build times. The values obtained were used for mutual comparison and also for comparison with two other beam structures called sparse and solid parts based on build styles available on the FDM machine software. Five different types of 2D geometric unit cells (honeycomb, square, diamond, circle and triangle) were used to design the cellular beams using Creo computer-aided design (CAD) software. Honeycomb structures were also studied for mechanical behaviour under variable porosities. The comparisons eventually lead to determining which structural design can provide the best flexural properties and performance for engineering applications.

11.2 Flexural Testing of FDM Cellular Beams

The required lattice beam structures were fabricated using ABS plastic material on the Stratasys 1200 ES FDM Machine. The dimensions of parts that can be fabricated on this setup are limited to 254 × 254 × 305 mm. The fabricated beams were of rectangular structures with 235 mm in length, 35 mm in width and 15 mm in thickness. Figure 11.1a shows the CAD models of the five beam structures, namely square, circular, triangular, diamond-shaped and honeycomb forms. Figure 11.1b shows the fabricated beam structures. Since the flexural strength of triangular and honeycomb structures was found to be higher than their counterparts, it was considered appropriate to produce extra samples of the honeycomb type and investigate these for the effect of varying porosity on their flexural behaviour. Two other beams (solid and sparse) of the same size were also fabricated using FDM while employing the solid and sparse build style options of the FDM processing software.
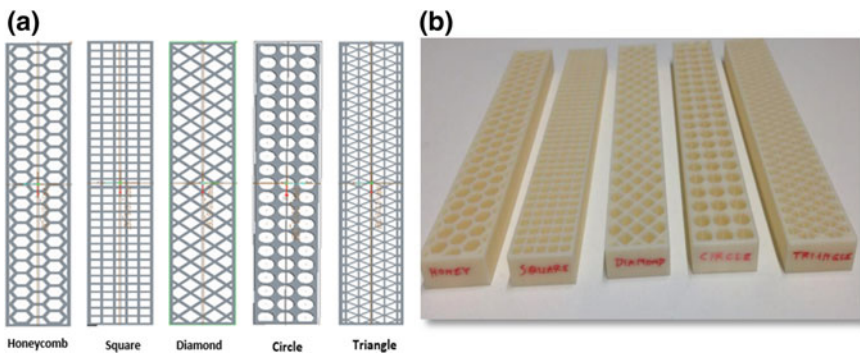
Fig. 11.1 a CAD models of five cellular beam structures, **b** beams made using FDM in ABS
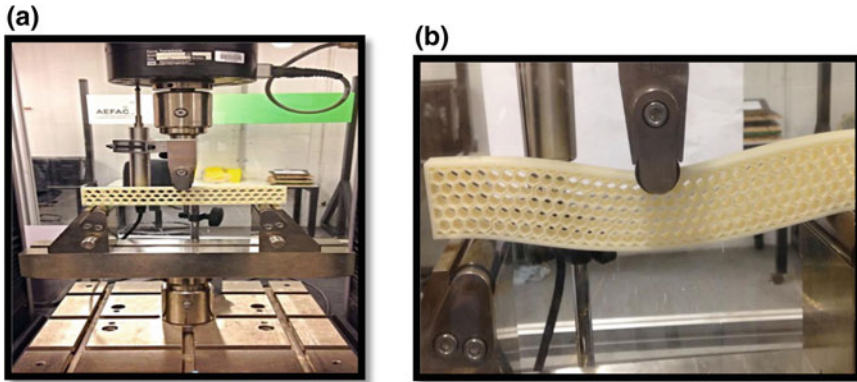
Fig. 11.2 **a** Three-point bending set up, **b** example of honeycomb cellular beam in bending

Three-point flexural tests were performed using on the MTS Criterion Model 43 machine, which combines high performance with a maximum capacity of 50 kN. The machine is controlled by MTS TestSuite Software. Using the software and data acquisition unit of the machine, the test parameters can be adjusted in a wide range. The test specimen was deformed at a speed of 0.5 mm/min, and the resulting recorded data helps in evaluating the flexural strength and flexural modulus for the fabricated specimens. Figure 11.2a shows the three-point bending set-up, and Fig. 11.2b shows the honeycomb cellular beam in bending.

11.3 Results and Discussion

11.3.1 Effects of Cellular Lattice Structures

The flexural behaviour of five different types of cellular lattice structure, as well as sparse and solid beam structures, is investigated. All five cellular specimens possess approximately the same porosity (i.e. 52%). The sparse build style of FDM software allows interior toolpaths with air gaps to create a non-solid internal structure saving material and build time. Figure 11.3 shows the flexural stress–strain curves obtained from three-point bending tests conducted on the above-mentioned structures and beams. From the obtained plots, it is clear that all the stress–strain curves of cellular structures exhibit similar trends in the elastic region. However, the stress–strain curves for the sparse and solid build styles indicate slightly different behaviour. The cellular structures experienced failure within the strain range of 13 and 40%, but for solid build structures, the strain at failure was 55% and the value was 32% for the sparse build beams. The parts manufactured with the solid build style seem to be more elastic in nature. It is observed that the triangular structure has a more brittle
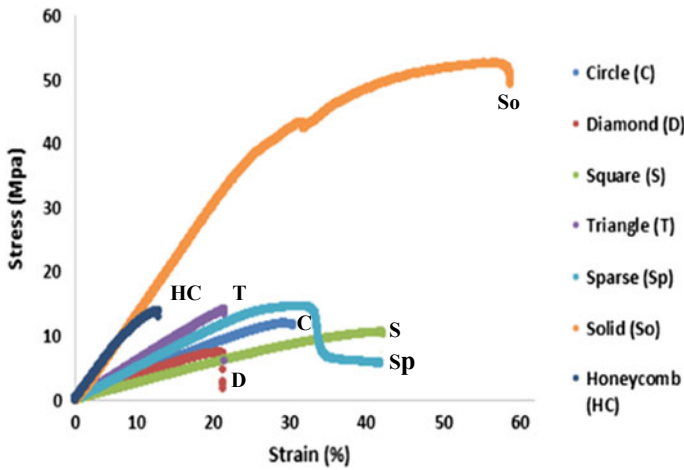
Fig. 11.3 Flexural stress–strain curves for five cellular structures

nature and higher stiffness among all the cellular lattice part structures. Square and honeycomb structures have high ductile nature and higher elongation. Triangular and diamond cellular structures are said to be more brittle in nature than other cellular parts. Triangular and honeycomb structures have high flexural strength, high strain energy, high toughness and stronger than all other cellular lattice part structures.

The build times for all the tested lattice and solid and sparse structures are plotted in Fig. 11.4. Minimum build time of 352 min was recorded for the circular structures while the triangular structures took the maximum time of 550 min. Solid and sparse beam structures took appreciably fewer times of 195 and 117 min, respectively. The vast difference between the build times is due to the fact that the investigated cellular lattice structures needed complex FDM toolpaths for fabrication. The triangular
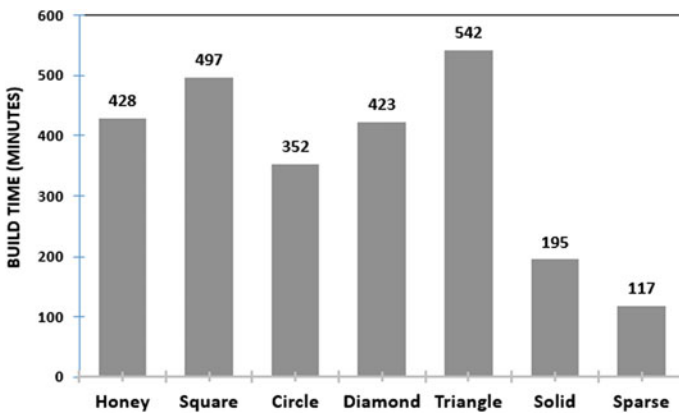
Fig. 11.4 Build times for various flexural beams in FDM structures of the same porosity

structure took the highest build time of all the five lattice structures because of its intricate shape and complex toolpaths.

Figures 11.5 and 11.6 each show the comparison of flexural strength and flexural modulus, respectively, for the five cellular structures with the sparse and solid built structures. According to the data, triangular and honeycomb lattice structures exhibit the highest comparative flexural strength, while the triangular structure shows the maximum flexural modulus among all the five cellular lattice structures. It is clear the flexural strength of honeycomb and triangular lattice structures is lower than the solid and sparse structures, but the flexural modulus of honeycomb and triangular
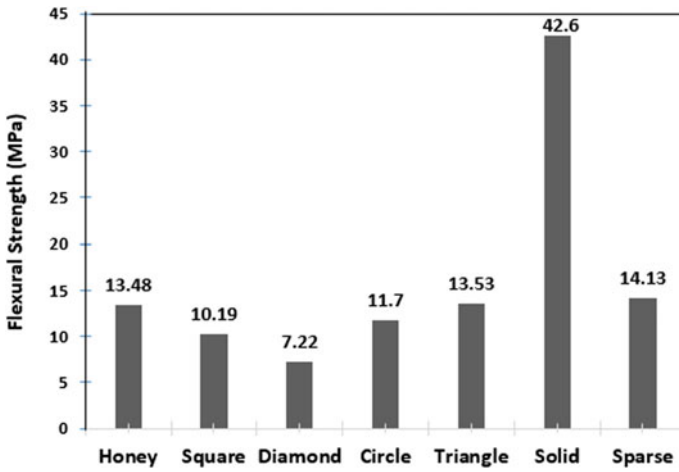
Fig. 11.5 Flexural strength for different cellular structures
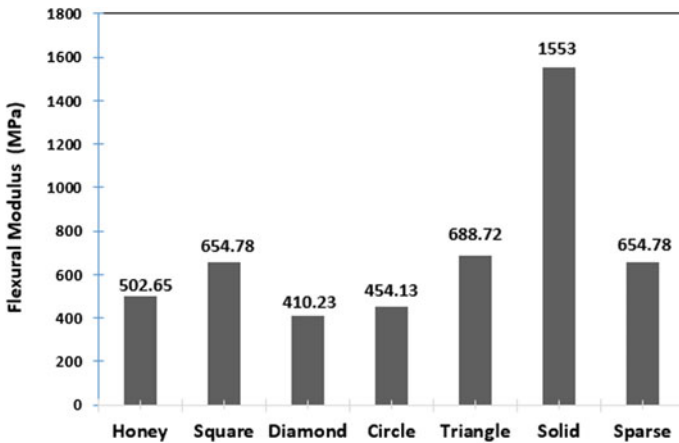
Fig. 11.6 Flexural modulus for different cellular structures

structure is comparable to the sparse structure. From the flexural tests, it is clear that the solid part structure possesses much higher flexural strength and flexural modulus than all other lattice part structures, but it will use several times more material than cellular structures.

11.3.2   Effects of Varying Porosity

For honeycomb structures, further investigations were carried out to find the effects of porosity on flexural properties. Porosity may be defined as the measure of the void or empty spaces within the mass of material, and it can be calculated as the ratio of the volume of pores to the total volume of a sample. Figure 11.7 shows the flexural stress–strain curves obtained for honeycomb lattice structures with three porosities (50, 56 and 61%). During the initial stages of loading, almost every curve exhibits a linear elastic behaviour. The range of 'strain at failure' is found to be between 25 and 30% for all specimens with different porosities. From the graphs, it is noted that all the honeycomb structures with varying porosity undergo brittle failure and the structure with 61% porosity is stronger and possesses higher stiffness than structures with 50 and 56% porosity.

Figure 11.8 highlights the comparison of the flexural strength and flexural modulus for the tested honeycomb cellular structures. An increase in the flexural properties is noticed with rise in porosity. Such behaviour is an expected because an increase in the porosity within a prescribed limit will not only decrease the amount of material in the part but also allow more room for flexibility. A sharp increase is noticeable in flexural strength and modulus for the structures having 61% porosity in comparison with the other two honeycomb structures with porosities of 50 and 56%. This observation demands that the porosity effect demands more in-depth investigation over a wider range of porosity ratios.

While comparing the build times for the varying porosity honeycomb structures, it can be observed that build time reduces with an increase in porosity. This behaviour

Fig. 11.7 Flexural stress–strain curves of varying porosity of the honeycomb structure
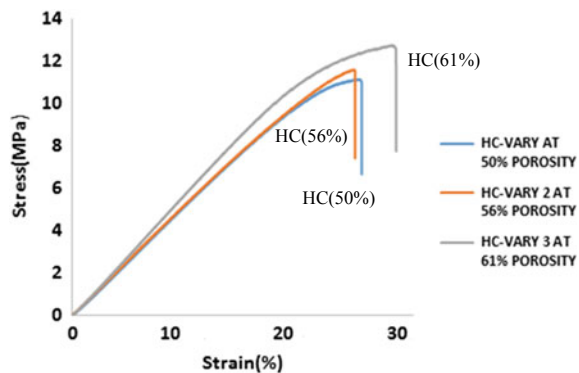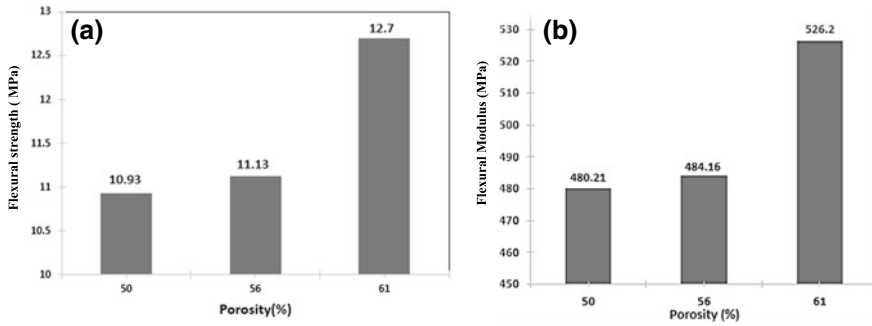
Fig. 11.8 **a** Flexural strength versus porosity and **b** flexural modulus versus porosity for honeycomb beams

may be due to the reason that the amount of material used in part building decreases with an increase in part porosity. For a 61% porous honeycomb structure, the build time was reduced to less than half in comparison with the build time for the structure with 50% porosity.

11.4 Conclusions

Fused deposition modelling process was used to prepare lattice and solid sparse structures. Flexural properties and build times were evaluated and compared by conducting experimental studies. Results show that triangular and honeycomb cellular lattice structures possess the highest flexural strength, and the triangular structure possesses the highest flexural modulus of all the five cellular lattice structures; it is clear the flexural strength of honeycomb and triangular lattice structures is lower than the solid and sparse structures; and flexural modulus of the triangular structure is lower than the solid structure. From the flexural tests, it is clear that a solid part structure possesses much higher flexural strength and flexural modulus than all other lattice part structures. A significant difference was observed in build times of the five fabricated FDM structures, which were almost double of the build times of the solid and sparse structures. Therefore, a contrasting set of properties can be observed between the cellular structures and the solid and sparse beams in terms of flexural properties and build time. Several stress–strain curves produced for the five cellular structures conclusively illustrate that the triangular structure has more brittle nature but higher stiffness among all the cellular lattice part structures, while square and honeycomb structures have higher ductility and experience failure at higher values of elongation. Triangular and honeycomb structures were found to provide best flexural performance due to their possession of high flexural strength, high strain energy, high toughness than all other cellular lattice structures created on FDM.

References

1. Ziemian, C., Sharma, M., Ziemian, S.: Anisotropic mechanical properties of ABS parts fabricated by fused deposition modeling. In: Mechanical Engineering, InTechOpen (2012)
2. Williams, C.B., Cochran, J.K., Rosen, D.W.: Additive manufacturing of metallic cellular materials via three-dimensional printing. Int. J. Adv. Manuf. Technol. **53**(1–4), 231–239 (2011)
3. Iyibilgin, O., Yigit, C., Leu, M.C.: Experimental investigation of different cellular lattice structures manufactured by fused deposition modeling. In: Proceedings of the Solid Freeform Fabrication Symposium, Austin, TX, USA, pp. 895–907 (2013)
4. Cansizoglu, O., Harrysson, O., Cormier, D., West, H., Mahale, T.: Properties of Ti–6Al–4V non-stochastic lattice structures fabricated via electron beam melting. Mater. Sci. Eng., A **492**(1–2), 468–474 (2008)
5. Yang, L., Harrysson, O., West, H., Cormier, D.: A comparison of bending properties for cellular core sandwich panels. Mater. Sci. Appl. **4**(08), 471 (2013)
6. Yan, C., Hao, L., Hussein, A., Raymont, D.: Evaluations of cellular lattice structures manufactured using selective laser melting. Int. J. Mach. Tools Manuf. **62**, 32–38 (2012)
7. Horn, T.J., Harrysson, O.L., Marcellin-Little, D.J., West, H.A., Lascelles, B.D.X., Aman, R.: Flexural properties of Ti6Al4V rhombic dodecahedron open cellular structures fabricated with electron beam melting. Addit. Manuf. **1**, 2–11 (2014)
8. Li, S., Xu, Q., Wang, Z., Hou, W., Hao, Y., Yang, R., Murr, L.: Influence of cell shape on mechanical properties of Ti–6Al–4V meshes fabricated by electron beam melting method. Acta Biomater. **10**(10), 4537–4547 (2014)
9. Gunay, A., Fank, S., Gulmez, T., Durakbasa, N.: Calculation of measurement uncertainty for plastic (ABS) material in flexural testing. Int. J. Metrol. Qual. Eng. **4**(1), 29–33 (2013)

Chapter 12
Power Spectral Density on Principal Building Due to Setback Interfering Building

Soumya Mukherjee and **Amlan Kumar Bairagi**

Abstract The problem of getting living and working spaces is increasing with the rise in human population. To minimize the effects of this problem, modern technology introduces tall buildings. Wind-based structural analysis of tall buildings helps us to build tall structures keeping them safe. Interference effect is one such important wind phenomenon, which affects the structure greatly. That is why the need of the study on interference effect is so significant these days. In this study, two virtual building models are used. The principal one is a square-plan tall building, and the interfering one is a setback tall building, which is placed in front of the principal building obstructing a time bound wind flow of a gust lasting for 3 s. This particular study offers power spectral density (PSD) variation with respect to Strouhal number for top near corner target points at a level of $0.975h$ on each surface of the principal model as well as the streamline variation in the altitude level of $0.475h$. All the variations are obtained due to the positional changes of the interfering building, as it is rotated about its own axis with an interval of $15°$ from $0°$ to $90°$. The maximum PSD value is obtained for $15°$ orientation of the interfering building from the windward face of the principal building. For the $90°$ orientation of the interfering building, the PSD values obtained from leeward and side faces of the principal building are nearly same.

Keywords Power spectral density · Strouhal number · Interfering model

S. Mukherjee (✉)
Techno India University, Salt Lake, Kolkata, India
e-mail: mysoumya89@gmail.com

A. K. Bairagi
Department of Civil Engineering, Indian Institute of Engineering Science and Technology, Shibpur, Howrah, India
e-mail: bairagiak@gmail.com

12.1 Introduction

The advancement of human civilization initiates the need of tall structures because the shrinkage of building spaces is increasing with the growing number of human population on the earth. Many remarkable tall structures were destroyed by natural catastrophe; one of these impactful natural forces is wind. That is why wind-loading analysis of tall structures is very much necessary. One of the important wind-based phenomenons is interference, which caused by an obstruction by any interfering object to the flow of wind toward the principal object. Through the years in the modern era, many research works have been done to study the wind loading and its nature on tall building structures, some of which played integral parts during this study. Xie and Gu [1] studied the shielding effect of interference factor using two and three high-rise buildings having the same height. Lam et al. [2] focused on the interference effects between two closely spaced high-rise buildings. Blocken et al. [3–5] analyzed the venturi effects of wind at the pedestrian level between two tall buildings using CFD method and wind tunnel experimentation. Kim et al. [6] studied the comparison of wind pressure coefficients between isolated and principal buildings along with the effects of interference on wind pressure coefficients. Bairagi and Dalui [7, 8] studied the optimum distance for nullifying the wind interference effects on a principal building due to the presence of an interfering building for 0° and 90° wind angles. Kheary and Dalui [9] discussed the wind interference effect between two buildings for different elevations and distances. Roy and Bairagi [10] analyzed the wind force and pressure parameters for unconventional tall buildings having different geometry. Bairagi and Dalui [11–13] analyzed the aerodynamic behavior of different types of setback tall buildings using power spectral density (PSD) function. Yu et al. [14] analyzed the envelope interference factors (EIFs) of wind on principal building for different aspect ratios of interfering building. The current research deals with application of computational fluid dynamics (CFD) for studying the wind interference effects on a tall square-plan-shaped principal building model (PM) due to the obstructive presence of an interfering tall building model (IM), which is rotating on its own axis. This study focused on the nature of streamlining of a wind flow generated by a time bound gust, the vibration generated by the same time bound gust in the principal building model (PM) is analyzed, and the frequencies and PSDs are accumulated for certain critical faces of the principal building model (PM) for certain critical positional orientations of the interfering building model (IM).

12.2 Domain, Meshing, and Model Detail

The most important guidelines for domain creation are made based on the concept by Franke et al. [15], which are the inlet, top, and side walls of the simulative wind tunnel domain at a distance of 5th multiplier of the overall height [5*h*] of the model. The outlet of the domain is at a distance of 15th multiplier of the overall
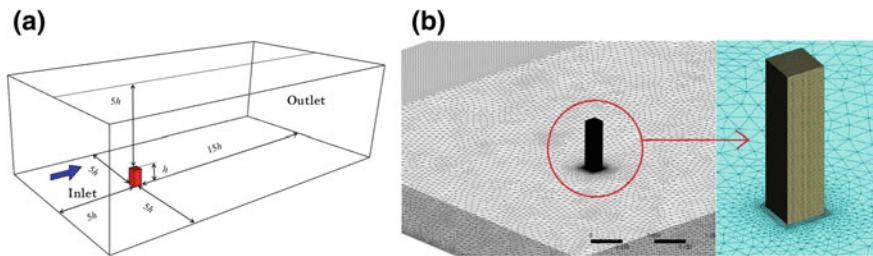
Fig. 12.1 a Domain and **b** meshing of square bluff body

height [15h] of the model (for the domain details, see Fig. 12.1a). In this study, to calculate the solution while the simulation is running on, both the domain and the model meshes are improved at locations depending upon specified adoption criteria. At these locations, the solution variables are hanging most rapidly while solving the flow features at these particular locations. The tetrahedron meshing method has been utilized during this study, and by the usage of this mesh, the regions near the boundaries can be made so inflated that the flows with unusual characteristics can be avoided (for the meshing details, see Fig. 12.1b).

In this case, the study of CFD method has been used to analyze the wind loading. Two numbers of square-plan tall building models are used here, of which the shapes and the surface areas of the bottom faces are same. One of the model is the principal model (PM) of which the measurement of wind pressure variation with respect to time has been taken during a gust, which lasted for 3 s. The other model is the interfering model (IM), which is obstructing the gust in the way toward the PM. The measurements have been taken for seven different positional orientations based upon the rotation of the model IM from 0° to 90° at an interval of 15° about its own axis along the *XY* plane with respect to the angle of the flow of the gust. The dimensional parameters of the PM and the IM are described at length (l) = 100 mm, width (b) = 100 mm, and overall height (h) = 400 mm. Setbacks of (0.2l) = 20 mm are provided at half the overall height (0.5h) = 200 mm on the IM from two opposite sides. The spacing between both of the models is (2b) = 200 mm for all seven orientations of the IM. The four faces of the IM excluding the top are labeled as windward face (A), leeward face (B), and side faces (C and D) (for the modeling details, see Fig. 12.2a).

12.3   Boundary Condition

The present study has been done using CFD methodology depending upon software-based simulation. This study is run and analyzed by creating virtual domain and observing the effects on PM after placing of IM in the path of a gust. The simulated flow conditions have been generated as per the criteria of terrain category 2 taken from IS 875: (part 3) [16]. The magnitude of inlet velocity was considered normal to the
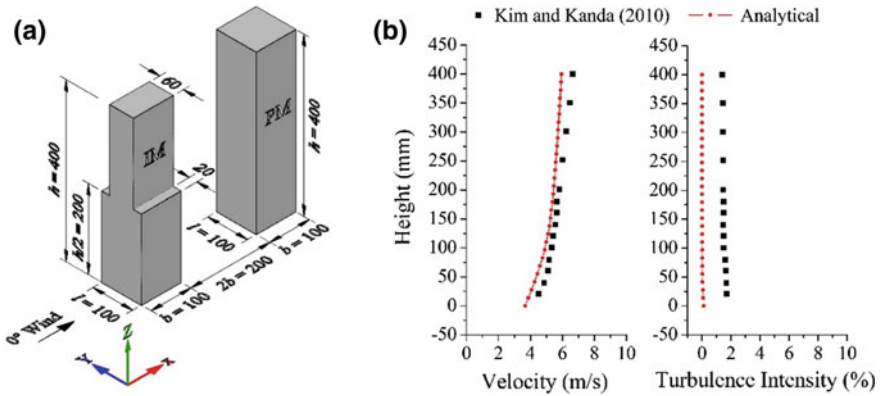
Fig. 12.2 a Schematic diagram of interfering and principal models, **b** validation with Kim Kanda (2010) and analytical model

boundary. Following the requirements of directional constraints, the flow direction was considered parallel to the normal of the surface of the boundary. The inlet and outlet are specified in the virtual domain. The sidewalls of this virtual domain are specified to be as free slip wall in this study. The walls of both of the virtual models are specified to be as no slip wall with no surface roughness. In this study, power law has been used which is shown in Eq. (12.1). The velocity profile of atmospheric boundary layer is considered as per SP 64 (S&T) [17]. On the other hand, the formulation to calculate the turbulence intensity is shown in Eq. (12.2).

$$(u/u_h) = (z/z_h)^{\alpha} \qquad (12.1)$$

$$I = u'/u_{\mathrm{mean}} \qquad (12.2)$$

where u represents the speed of wind in horizontal direction at a certain elevation z. u_h represents the speed of the wind at a reference elevation z_h. The value of u_h is taken as 10 m/s. The value of z_h is taken as 1.0 m. α represents the coefficient of surface roughness 0.133 for terrain category 2. I represents the turbulence intensity, and u' represents the root mean square of turbulence velocity. u_{mean} represents the average velocity of wind.

12.4 Validation of Present Study

This study is based on CFX application, which creates the simulation of a virtual wind tunnel testing. That is why it is necessary to validate the simulative results with past wind tunnel test of a same model with the same aspect ratio. The present study has been validated with Kim and Kanda [18]. The length scale of the model used

in this analytical study is about 1:4, which is same as the experimental research by Kim and Kanda. The boundary conditions of this study have been created as per the experimental conditions for open flat area flow of wind. The power law exponent has been taken as 0.13, and the turbulence intensity has been taken as 15%, which is same as the experimental work. The virtual domain is created in such a manner that the blockage ratio of the present analytical study is same as the experimental study, which is 1.2% as a square-plan model is used to analyze the behavior of wind excitation for both the studies (for the parametric graphical representation of wind velocity and turbulence intensity versus the height of the model, see Fig. 12.2b).

12.5   Results and Findings

The study analyzed the effects of wind interference on a PM caused by a gust lasts for 3 s, which is nothing but a strong and intensified flow of wind. This gust is interfered by another setback tall building IM in its way toward the PM. The measurements have been done by obtaining the pressure variation with respect to time and plotting the PSD versus Strouhal number (S_t) graph, which are taken from top corner points of all the faces of the PM.

12.5.1   Power Spectral Density (PSD) of Principal Model

The concept of using power spectrum to describe the distribution of power into frequency components initiated by a certain vibration of a particular time series is done as per Fourier analysis. This vibration is generated due to the force of gust on the PM, which is interfered by setback IM. When the energy created by the vibration is concentrated around a certain time interval, the PSD can be calculated. The expression for PSD is expressed in Eq. (12.3).

$$\text{PSD} = S_\text{p}(f)/\sigma^2 \tag{12.3}$$

where PSD represents the power spectral density, S_p represents the peak wind spectra function, f represents the frequency, and σ represents the standard deviation.

12.5.2   Strouhal Number (S_t) of Principal Model

The Strouhal number (S_t) is a dimensionless parameter used in dimensional analysis, where the object is under dynamic loading condition. Strouhal number (S_t) is generally utilized to describe the oscillating flow mechanisms, and Strouhal number (S_t) is expressed in Eq. (12.4).

$$S_t = fB/U \tag{12.4}$$

where S_t represents the Strouhal number, B represents the width of the model, and U represents the gradient wind speed.

The marking and directional orientation of all the four faces A, B, C and D on the model PM as well as the considered impact points on each faces are shown in Fig. 12.3. The results have been taken by creating certain impact points on the PM. The impact points have been taken at $0.975h$, i.e., near the top corners of each face of the model PM, which results in two impact points for each faces. The maximum value of spectral density 0.277 is obtained for Strouhal number 0.031 due to 15° orientation at face A (see Fig. 12.3a). Again, 90° orientation has maximum spectral densities 0.07, 0.068, and 0.08 for Strouhal numbers 0.048, 0.032, and 0.048, respectively, for the faces B, C, and D (see Fig. 12.3b–d). An interesting point has been observed for 0° orientation that the minimum spectral densities are 1.90×10^{-4} and 9.3×10^{-5} for same Strouhal number 0.048 at faces C and D. The streamline diagram of the wind flow of the gust inside the virtual domain has been shown here for 15° and 90° orientations of the interfering building at the level of 190 mm ($0.475h$), respectively (see Fig. 12.4).
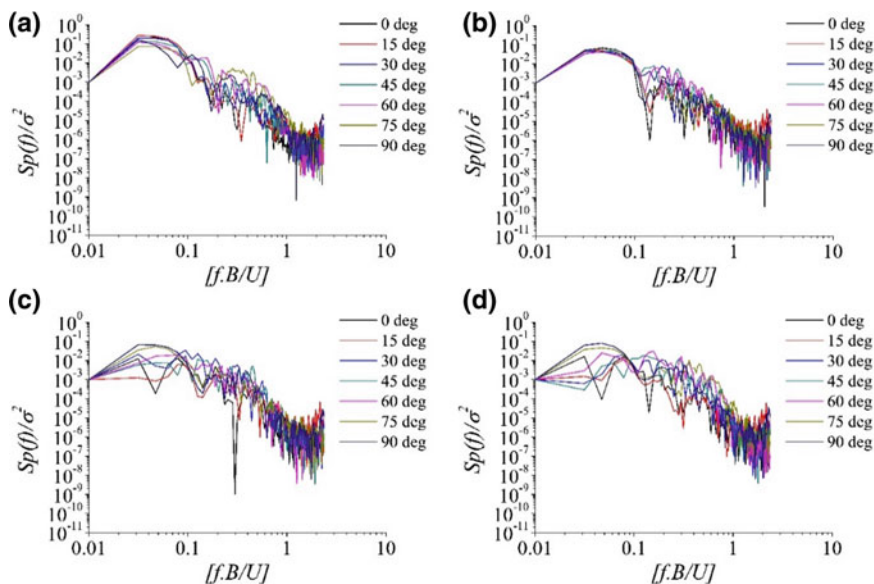
Fig. 12.3 Variation of PSD of principal model at topmost edge point ($0.975h$) for different orientations of interfering model **a** face A, **b** face B, **c** face C, and **d** face D
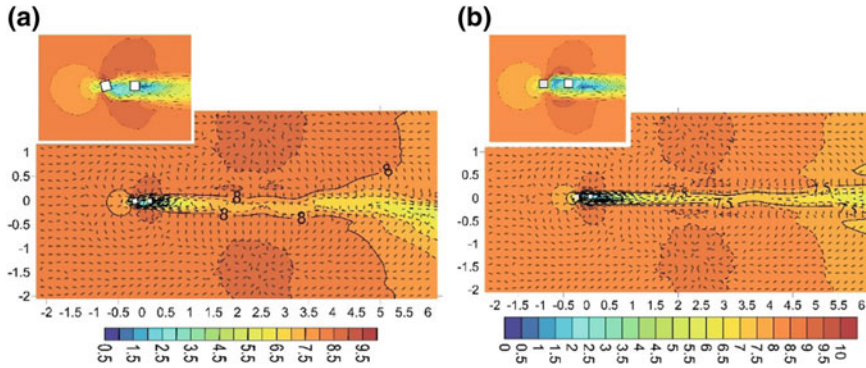
Fig. 12.4 Streamline for velocity at 0.475h for different orientations of interfering model **a** for 15° orientation and **b** for 90° orientation

12.6   Conclusions

The present analytical study is done by a series of simulative iterations, which is a time-consuming and rigorous method. After the complete simulative analysis, the following conclusions are made based on the obtained results.

- According to the spectral density calculation, face A of the principal model has maximum frequency 0.277 for 15° orientation of interfering model, which means the face A suffering large amount of positive pressure at the topmost corner, and this pressure is developed due to the side wash of the interfering model.
- Faces B, C, and D have high frequency for 90° orientation, but face D has maximum spectral density 0.08 at the topmost edge.
- Faces C and D experienced with low frequency 1.90×10^{-4} and 9.3×10^{-5} for the same Strouhal number 0.048 for 0° orientation.
- The streamlines varies for different orientation of the interfering building model for the time bound wind flow of the gust.

References

1. Xie, Z.N., Gu, M.: Mean interference effects among tall buildings. Eng. Struct. **26**, 1173–1183 (2004)
2. Lam, K.M., Leung, M.Y.H., Zhao, J.G.: Interference effects of wind loading of a row of closely spaced tall buildings. J. Wind Eng. Ind. Aerodyn. **96**, 562–583 (2008)
3. Blocken, B., Stathopoulos, T., Carmeliet, J.: Wind environmental conditions in passages between two long narrow perpendicular buildings. J. Aerosp. Eng. ASCE **21**(4), 280–287 (2008)
4. Blocken, B., Moonen, P., Stathopoulos, T., Carmeliet, J.: A numerical study on the existence of venturi-effect in passages between perpendicular buildings. J. Eng. Mech. ASCE **314**(12) (2008)

5. Blocken, B., Carmeliet, J.: Pedestrian wind conditions at outdoor platforms in a high-rise apartment building: generic sub-configuration validation, wind comfort assessment and uncertainty issues. Wind Struct. **11**(1), 51–70 (2008)
6. Kim, W., Tamura, Y., Yoshida, A.: Interference effects of two buildings on peak wind pressure. In: The Seventh Asia-Pacific Conference on Wind Engineering, Taipei, Taiwan (2009)
7. Bairagi, A.K., Dalui, S.K.: Evaluation of interference effects on parallel high-rise buildings for different orientation using CFD. In: 3rd World Conference of Applied Sciences, Engineering & Technology, Kathmandu, Nepal, pp. 764–774 (2014)
8. Bairagi, A.K., Dalui, S.K.: Optimization of interference effects on high-rise buildings for different wind angle using CFD simulation. Electron. J. Struct. Eng. **14**, 39–49 (2014)
9. Kheyari, P., Dalui, S.K.: Estimation of wind load on tall building under interference effects. Jordan J. Civil Eng. **9**(1), 84–108 (2015)
10. Roy, K., Bairagi, A.K.: Wind pressure and velocity around stepped unsymmetrical plan shape tall building using CFD simulation—a case study. Asian J. Civil Eng. (BHRC) **17**(8), 1055–1075 (2016)
11. Bairagi, A.K., Dalui, S.K.: Aerodynamic effects on setback tall building using CFD simulation. Int. J. Mech. Prod. Eng. Res. Dev., 413–420 (2018)
12. Bairagi, A.K., Dalui, S.K.: Comparison of aerodynamic coefficients of setback tall buildings due to wind load. Asian J Civil Eng Build Hous. **19**(2), 205–221 (2018). (Springer International Publishing)
13. Bairagi, A.K., Dalui, S.K.: Aerodynamic effects on setback tall building using CFD simulation. In: 2nd International Conference on Advances in Dynamics, Vibration and Control, NIT Durgapur, pp. 381–388 (2018)
14. Yu, X., Xie, Z.N., Gu, M.: Interference effects between two tall buildings with different section sizes on wind induced acceleration. J. Wind Eng. Ind. Aerodyn. **182**, 16–26 (2018)
15. Franke, J., Hirsch, C., Jensen, A., Krüs, H., Schatzmann, M., Westbury, P., Miles, S., Wisse, J., Wright, N.G.: Recommendation on the use of CFD in wind engineering. COST Action C14. Impact of Wind and Storm on City Life and Built Environment. Von Karman Institute for Fluid Dynamics (2004)
16. IS:875 (Part-3): 2015. Indian Standard Code of Practice for the Design Loads (other than Earthquake) for Buildings and Structures (part-3. Wind Loads). Bureau of Indian Standards, New Delhi, India (2015)
17. SP 64 (S&T): 2001. Explanatory Hand Book on Indian Standard Code of Practice for the Design Loads (other than Earthquake) for Buildings and Structures (part-3. Wind Loads) [IS:875 (Part-3):1987]. Bureau of Indian Standards, New Delhi, India (2001)
18. Kim, Y.C., Kanda, J.: Wind pressure on tapered and setback tall buildings. J. Fluids Struct. **39**, 306–321 (2013)

Chapter 13
Effect of Solar Optical Properties of Building Envelope on Time Lag, Decrement Factor and Energy Saving of Buildings

Debasish Mahapatra and T. P. Ashok Babu

Abstract World has been suffering from energy crisis since 1970. This is because of the increased population and industrialization. Buildings have a significant contribution to total energy consumption across the globe. The increased urbanization leads to boom in construction of buildings. The materials used for the construction of buildings affect the climate of the city up to a great extent and affect the energy consumption as well. So, construction materials should be chosen wisely. The surface temperature of the building envelope is affected by the coatings used. Cool coatings help in reducing the surface temperature of the building envelope. Time lag and decrement factor are the indicators of energy saving in building. In this paper, the effect of cool coating on time lag and decrement factor was studied. Values of time lag and decrement factor were evaluated in different climatic zones of India. It has been found that as the absorptivity of the building envelope increases, the decrement factor increases. By changing the absorptivity from 0.2 to 0.73, a minimum change of 16% (New Delhi) in decrement factor and 11.75% (Jodhpur) in surface temperature was observed. The maximum change in decrement factor was 56.44% (Jodhpur). The maximum change in surface temperature was 39.02% (Bangalore). So, it should always be practised to keep the absorptivity of the building envelope as low as possible.

D. Mahapatra (✉) · T. P. Ashok Babu
Department of Mechanical Engineering, National Institute of Technology, Surathkal, Karnataka, India
e-mail: dmahapatra94@gmail.com

T. P. Ashok Babu
e-mail: tpab57@gmail.com

13.1 Introduction

Reasons such as social, political and economic compel individuals to migrate towards urban areas. They get an easy platform to live because of the comfort lifestyle of the city. But the drawback of urbanization is that, the heat released from various human activities such as vehicular emissions, heat released from air conditioners, industrial heat gets accumulated and creates an island of heat called **urban heat island (UHI)**. It had been reported by Valson and Bharat that, because of UHI, the city centre temperature is around 5.6 °C higher than the suburban areas [1]. Increase in the city centre temperature enforces increased use of air conditioner. Use of air conditioner should be minimized considering the fact that heating and ventilation consumes around 31% of total energy in commercial buildings and 7% in residential buildings as per Centre for Science and Environment (CSE).

In India, creation of UHI is not so far as urbanization is taking place at a great pace. In 1901, only 11.4% of the people were residing in urban areas. In 2001, the count was 28.53%, and in 2011, the census rose to 31.1% [2]. Mumbai, Delhi and Kolkata have witnessed the most of the urban migration in 2011 from rural areas. The rise in migration is reported to be 4.1%, 3.1% and 2% in Mumbai, Delhi and Kolkata, respectively, in 2011 as compared to 2001. So, utmost care should be taken while selecting construction materials in order to avoid the problem of UHI in India as the effects are adverse in nature. The heat stress caused by UHI increases the risk of mortality. Heat stress damages thermoregulatory system in the form of heat syncope, thermal exhaustion and cardio respiratory diseases [3]. The relation between "heat island" and "Death island" was found from the study of Buechley et al. [4]. The mortality rate increases exponentially with the maximum temperature. A study in Italy during 2003 by Conti et al. found that the residents of urban areas are having a higher risk of death compared to the residents of suburban areas because of UHI [5].

Use of cool coatings is an emerging technique used to mitigate UHI. Cool coatings are the coatings which are characterized by their high reflectivity. Cool coatings not only help in mitigating UHI but also help in saving energy. Because of the high reflectivity of the coating, the surface temperature does not rise much. Because of the less surface temperature, heat transfer into the building reduces which in turn helps in energy saving. Synnefa et al. [6] studied the effect of cool coating on energy saving in various cities worldwide. From their study, it was found that an increase of solar reflectance from 0.2 to 0.6 reduced up to 75% cooling load. Similarly, increase of reflectance from 0.2 to 0.85 reduced cooling load up to 93%.

Hernandez-Perez et al. [7] measured the inside and outside surface temperature for coatings of reflectivity 0.80, 0.84 and 0.33. The outside surface temperature was measured to be 30.5 °C, 23.7 °C and 38.3 °C to 40 °C for coatings having solar reflectance of 0.80, 0.84 and 0.33, respectively. Similarly, the inside air temperatures were 25 °C, 24 °C and 31 °C to 33 °C for coatings having solar reflectance of 0.80, 0.84 and 0.33, respectively. The heat flux was 19 W/m^2, 8 W/m^2 and 45.6 W/m^2 for coatings having solar reflectance of 0.80, 0.84 and 0.33, respectively.

An experimental study was carried out by Shen et al. [8], and the effect of reflective coatings on surface temperature of buildings and energy consumption was found for both conditioned and non-conditioned buildings. For non-conditioned building, in summer, the maximum decrease in exterior building surface temperature was 19.9 °C. Similarly, in winter, it was 15.6 °C. The maximum surface temperature reduction was observed in the west direction for both summer and winter seasons.

13.1.1 Time Lag and Decrement Factor

Because of the variation of solar radiation throughout the day, the ambient temperature also varies. Maximum ambient temperature and maximum temperature inside the building do not happen at the same time because of the thermal mass of the wall [9]. The maximum ambient temperature and maximum inside temperature are not the same as well. So, the time difference between the maximum ambient temperature and maximum temperature inside the building is called time lag. The ratio of difference of maximum and minimum temperature inside to outside is called decrement factor (Fig. 13.1).

Mathematically,

$$\varphi = t_{T_0^{max}} - t_{T_e^{max}} \tag{13.1}$$

And

$$f = \frac{A_0}{A_e} = \frac{T_0^{max} - T_0^{min}}{T_e^{max} - T_e^{min}} \tag{13.2}$$
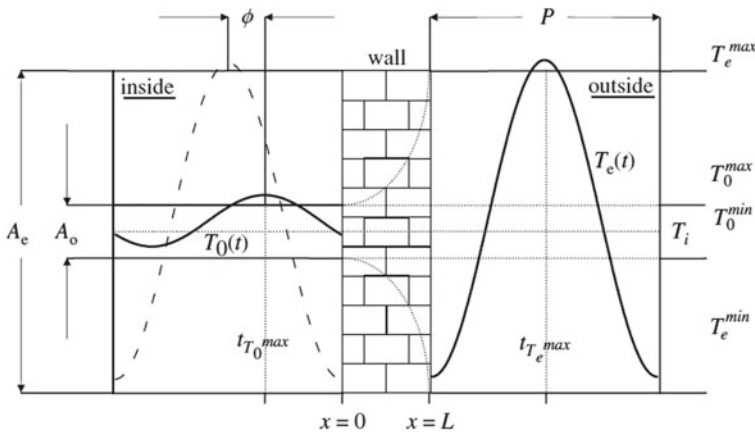
Fig. 13.1 Schematic presentation of time lag and decrement factor. *Source* Asan [10]

Time lag and decrement factor are significant in places where the variation of outside temperature is large. For example, places where the outside temperature in day time reaches 40 °C and the following night it falls to 10–15 °C. If a material of time lag 10–12 h is used, then the low night temperature will reach inside during day and vice versa. By doing so, the building can be cooled or heated passively and the use of air conditioner can be minimized thereby saving energy.

13.2 Methodology

13.2.1 Sole Air Temperature

Equation of heat transfer from the environment to the outside surface of the wall is given by

$$q_0 = f_0(t_0 - t_{so}) + aI \tag{13.3}$$

It has been found convenient to combine the effect of outside temperature and the solar radiation so an equivalent temperature is introduced called as sol-air temperature (Fig. 13.2).

$$q_0 = f_0(t_e - t_{so}) \tag{13.4}$$

where

$$t_e = t_0 + \frac{aI}{f_0} \tag{13.5}$$

Fig. 13.2 Heat transfer to outside surface of a building wall
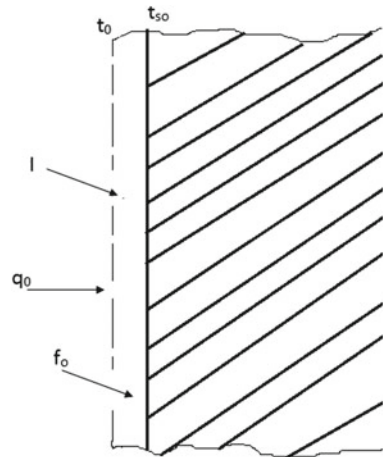
From the above equation, it can be noticed that the heat transfer from the environment to the outside surface of the wall is dependent on the absorptivity of the surface. The heat transfer can be reduced by reducing the absorptivity of the surface. As cool coatings have low absorptivity, they can be used to reduce the absorptivity of the surface thereby reducing the heat transfer from the environment to the wall surface, which in turn reduce the heat transfer inside the building and will save cooling load.

13.2.2 Finite Difference Method for Solving One-Dimensional Heat Transfer Equation

13.2.2.1 Node in the Conduction Region

See Fig. 13.3.

$$\left(\frac{\partial t}{\partial x}\right)_B = \frac{t_{m+1} - t_m}{\Delta x}$$

$$\left(\frac{\partial t}{\partial x}\right)_A = \frac{t_m - t_{m-1}}{\Delta x}$$

The temperature gradient can be expressed as

$$\left(\frac{\partial^2 t}{\partial x^2}\right)_m = \frac{\left(\frac{\partial t}{\partial x}\right)_B - \left(\frac{\partial t}{\partial x}\right)_A}{\Delta x}$$
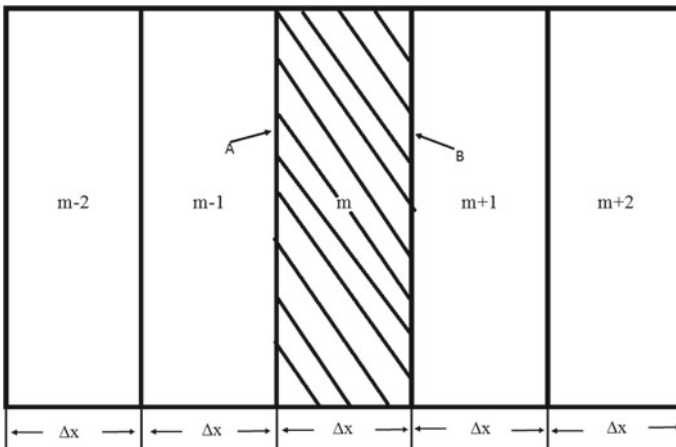
Fig. 13.3 Wall representing nodes in the conduction region

$$= \frac{t_{m+1} - 2t_m + t_{m-1}}{\Delta x^2} \tag{13.6}$$

The time derivative can be written as

$$\frac{\partial t}{\partial \tau} = \frac{t'_m - t_m}{\Delta \tau}$$

where t'_m is the temperature at m after 1 $\Delta \tau$ time when the temperature at m was t_m. Substitution of the above values in Eq. 13.1 gives

$$\frac{t'_m - t_m}{\Delta \tau} = \frac{\alpha}{\Delta x^2}(t_{m+1} - 2t_m + t_{m-1})$$

$$= t'_m = \frac{\alpha \Delta \tau}{\Delta x^2}(t_{m+1} + t_{m-1}) + \left[1 - \frac{2\alpha \Delta \tau}{\Delta x^2}\right]t_m \tag{13.7}$$

Suppose

$$M = \frac{\Delta x^2}{\alpha \Delta \tau}$$

Then,

$$= t'_m = \frac{1}{M}(t_{m+1} + t_{m-1}) + \left[1 - \frac{2}{M}\right]t_m \tag{13.8}$$

From Eq. 13.6, it can be seen that if,

$$\frac{2}{M} > 1$$

For higher value of t_m the value of t'_m will be less.
So,

$$\frac{2}{M} < 1$$
$$M > 2$$
$$M = \frac{\Delta x^2}{\alpha \Delta \tau} > 2$$

13.2.2.2 Nodes at the Surface and Nodes Next to Surface

See Fig. 13.4.

Energy balance for the node S can be written as
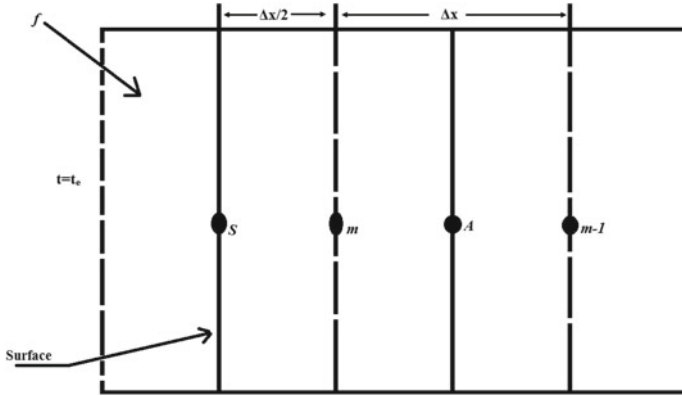
Fig. 13.4 Wall representing nodes on the surface

$$f(t_e - t_s) + \frac{2k}{\Delta x}(t_m - t_s) = 0 \tag{13.9}$$

where
"f" is the convective heat transfer coefficient, and "k" is the thermal conductivity of the wall.

Equation 13.9 can be simplified to

$$\left(f + \frac{2k}{\Delta x}\right)t_s = f t_e + \left(\frac{2k}{\Delta x}\right)t_m$$

$$t_s = \left[\frac{f}{\left(f + \frac{2k}{\Delta x}\right)}\right]t_e + \left[\frac{2k/\Delta x}{\left(f + \frac{2k}{\Delta x}\right)}\right]t_m$$

$$= \left(\frac{Bi}{Bi + 2}\right)t_e + \left(\frac{2}{Bi + 2}\right)t_m \tag{13.10}$$

where
$Bi = \frac{f \Delta x}{k}$ is a dimensionless number called "Biot number" and is used to represent convection boundary. For node point "m", the finite difference is

$$\left(\frac{\partial t}{\partial x}\right)_A = \frac{t_{m-1} - t_m}{\Delta x}$$

$$\left(\frac{\partial t}{\partial x}\right)_S = \frac{t_m - t_s}{\Delta x/2}$$

$$\left(\frac{\partial^2 t}{\partial x^2}\right)_m = \frac{\left(\frac{\partial t}{\partial x}\right)_A - \left(\frac{\partial t}{\partial x}\right)_S}{\Delta x}$$

$$= \frac{1}{(\Delta x)^2}(2t_s + t_{m-1} + 3t_m) \tag{13.11}$$

The finite difference approximation of temperature at node m after time $\tau + \Delta\tau$ is

$$= t'_m = \frac{1}{M}(2t_s + t_{m-1}) + \left[\frac{M-3}{M}\right]t_m$$

For stability, $M \geq 3$.
So at $M = 3$

$$= t'_m = \frac{1}{3}(2t_s + t_{m-1})$$

13.2.3 Climatic Zones of India

Indian climatic zone is basically divided into six categories such as hot and dry, warm and humid, composite, moderate, cold and sunny and cold and cloudy. Time lag and decrement factor were calculated for Bangalore (moderate), Kolkata (warm and humid), Jodhpur (hot and dry), New Delhi (composite) and Bhubaneswar (warm and humid) on peak summer day.

13.2.4 Time Lag and Decrement Factor Calculation

The one-dimensional heat conduction equation was solved by using finite difference method by considering nodes at the surfaces. The different parameters required for solving are hourly outside temperature, inside temperature, i.e. room temperature, incident solar radiation, absorptivity of the surface, outside heat transfer coefficient, inside heat transfer coefficient, thickness of the wall and thermal conductivity of the wall.

The outside air temperature was taken from the book ISHRAE Indian weather data 2017 [11].

Inside room temperature was taken at 25 °C to maintain comfort condition.

The incident solar radiation which is the sum of direct and diffuse radiation was calculated by using the necessary formula. For calculation of incident solar radiation, a MATLAB program was developed. The results obtained were validated with the result of Indian standard value of Delhi [12]. The deviation was within 10%. Hence, the program was considered as reliable and used for calculating the solar radiation of other cities. Table 13.1 shows the comparison between the literature value and values obtained from MATLAB.

Different colours such as red, yellow, green, brown and black were considered for this study. The reflectance value for these colours was taken from literature. The

Table 13.1 Validation of calculated solar radiation with literature (Indian standard) value

Time	E cal	E lit	Error	W cal	W lit	Error	N cal	N lit	Error	S cal	S lit	Error
6	455.45	458	0.56	65.12	65	−0.19	213.21	216	1.29	65.12	65	−0.19
7	662.13	665	0.43	75.31	76	0.91	229.56	234	1.90	75.31	76	0.91
8	682.88	685	0.31	81.93	81	−1.15	176.99	177	0.01	81.93	81	−1.15
9	606.53	653	7.12	85.90	83	−3.49	112.83	113	0.15	85.90	83	−3.49
10	467.94	463	−1.07	88.76	88	−0.86	88.76	88	−0.86	119.45	121	1.28
11	288.89	295	2.07	90.05	90	−0.05	90.05	90	−0.05	158.35	160	1.03
12	90.50	91	0.55	90.50	91	0.55	90.50	91	0.55	172.02	178	3.36
13	90.05	90	−0.05	288.89	295	2.07	90.05	90	−0.05	158.35	160	1.03
14	88.76	88	−0.86	467.94	463	−1.07	88.76	88	−0.86	119.45	121	1.28
15	85.90	83	−3.49	606.53	654	7.26	112.83	113	0.15	85.90	83	−3.49
16	81.93	81	−1.15	682.88	685	0.31	176.99	177	0.01	81.93	81	−1.15
17	75.31	76	0.91	662.13	665	0.43	229.56	234	1.90	75.31	76	0.91
18	65.12	65	−0.19	455.45	458	0.56	213.21	216	1.29	65.12	65	−0.19

Table 13.2 Absorptivity of different colour coating taken from literature

Colours	Solar reflectivity	Absorptivity	Source
Yellow	0.59–0.75	0.41–0.25	Sameera et al. [13]
Black	0.27	0.73	Synnefa et al. [14]
Green	0.27	0.73	Synnefa et al. [14]
Brown	0.35	0.65	Thongkanluang et al. [15]
White	0.8	0.2	Hernandez-Perez et al. [7]

absorptivity was calculated by considering the transmittance as zero. The reflectance value and absorbance value for different colour are given in Table 13.2.

So, based on the literature, the absorptivity values considered were 0.2, 0.25, 0.65 and 0.73. The variation of time lag and decrement factor with absorptivity was studied.

The thickness of the wall considered was 25 cm.

Thermal conductivity and diffusivity considered were 1.5 W/m °C and 8×10^{-7} m^2/s, respectively [16].

Inside heat transfer coefficient was taken as 7 W/m^2 K and outside heat transfer coefficient was taken as 23 W/m^2 K as per CIBSE 2006 [17].

13.3 Results and Discussion

13.3.1 Time Lag and Decrement Factor Calculation for Composite (New Delhi) Climatic Zone

The time lag and decrement factor for composite climatic zone (New Delhi) were calculated on peak summer day, i.e. on June 21st. Variation of time lag and decrement factor with absorptivity of the wall was analysed. Variation of time lag with absorptivity was random. The decrement factor increased with increase in absorptivity. The decrement factor was highest in west direction and lowest in north direction, for all absorptivity value of the wall. Inside surface temperature of the wall, which majorly affects the cooling load, was also found. It was noticed that, inside surface temperature varied same as decrement factor. For all the cases, the inside surface temperature was the highest for the wall facing west and the lowest for the wall facing south (Fig. 13.5).

Fig. 13.5 a Decrement factor. **b** Excess inside surface temperature. **c** Time lag for different absorptivity in composite (New Delhi) climatic zone

13.3.2 Time Lag and Decrement Factor Calculation for Warm and Humid (Kolkata) Climatic Zone

Time lag and decrement factor for the warm and humid climatic zone (Kolkata) were calculated on peak summer day, i.e. on May 15th. Variation of time lag and decrement factor with absorptivity of the wall was analysed and it was found that time lag varied randomly. The decrement factor increased with increase in absorptivity. The decrement factor was highest in west direction and lowest in south direction, for all absorptivity value of the wall. Inside surface temperature of the wall, which majorly affects the cooling load, was also found. It was noticed that inside surface temperature varied same as decrement factor. For all the cases, the inside surface temperature was the highest for the wall facing west and the lowest for the wall facing south (Fig. 13.6).

Fig. 13.6 **a** Decrement factor. **b** Excess inside surface temperature. **c** Time lag for different absorptivity in warm and humid (Kolkata) climatic zone

13.3.3 Time Lag and Decrement Factor Calculation for Moderate (Bangalore) Climatic Zone

The time lag and decrement factor for moderate climatic zone (Bangalore) were calculated on peak summer day, i.e. on April 21st. Variation of time lag and decrement factor with absorptivity of the wall was analysed, and it was found that time lag varied randomly. The decrement factor increased with increase in absorptivity. The decrement factor was highest in west direction and lowest in south direction, for all absorptivity value of the wall. Calculation of inside surface temperature showed that inside surface temperature varied same as decrement factor. For all the cases, the inside surface temperature was the highest for the wall facing west and the lowest for the wall facing south (Fig. 13.7).
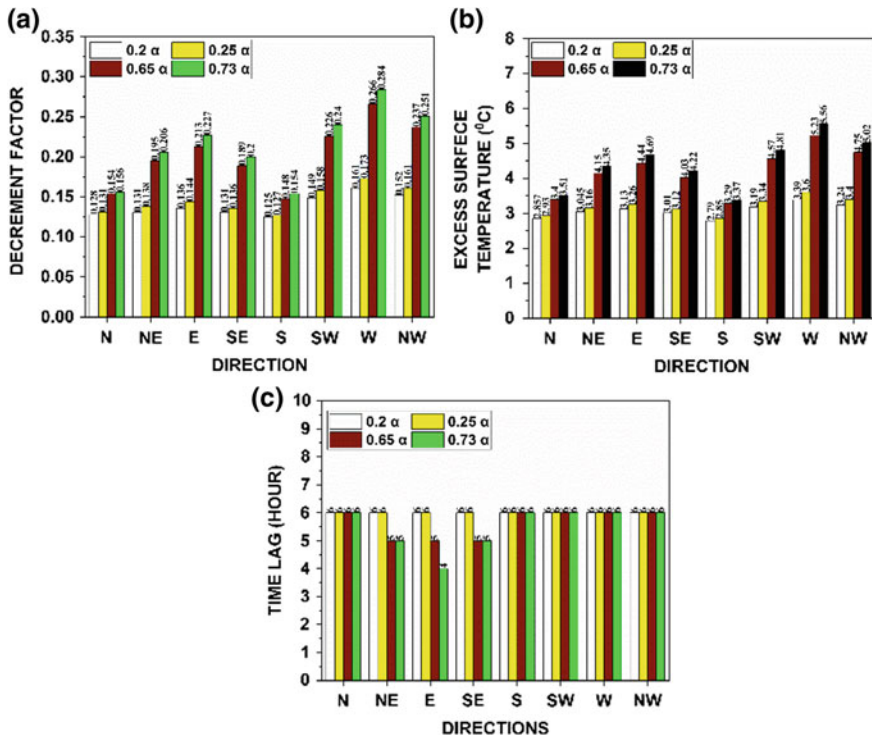
Fig. 13.7 a Decrement factor. **b** Excess inside surface temperature. **c** Time lag for different absorptivity in moderate (Bangalore) climatic zone

13.3.4   Time Lag and Decrement Factor Calculation for Hot and Dry (Jodhpur) Climatic Zone

The time lag and decrement factor for hot and dry climatic zone (Jodhpur) were calculated on peak summer day, i.e. on June 21st. Variation of time lag and decrement factor with absorptivity of the wall was analysed and it was found that time lag varied randomly. The decrement factor increased with increase in absorptivity. The decrement factor was highest in west direction and lowest in south direction, for all absorptivity value of the wall. Calculation of inside surface temperature showed that inside surface temperature varied same as decrement factor. For all the cases, the inside surface temperature was the highest for the wall facing west and the lowest for the wall facing south (Fig. 13.8).
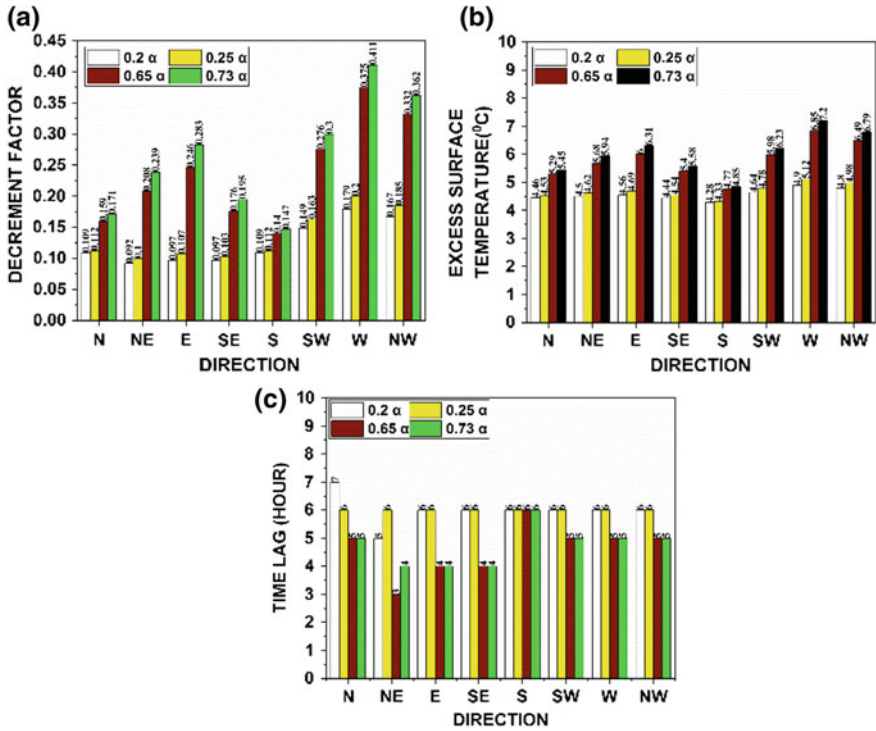
Fig. 13.8 **a** Decrement factor. **b** Excess inside surface temperature. **c** Time lag for different absorptivity in hot and dry (Jodhpur) climatic zone

13.3.5 Time Lag and Decrement Factor Calculation for Warm and Humid (Bhubaneswar) Climatic Zone

The time lag and decrement factor for warm and humid climatic (Bhubaneswar) were calculated on peak summer day, i.e. on May 15th. Variation of time lag and decrement factor with absorptivity of the wall was analysed and it was found that time lag varied randomly. The decrement factor increased with increase in absorptivity. The decrement factor was highest in west direction and lowest in south direction, for all absorptivity value of the wall. Calculation of inside surface temperature showed that inside surface temperature varied same as decrement factor. For all the cases, the inside surface temperature was the highest for the wall facing west and the lowest for the wall facing south (Fig. 13.9).
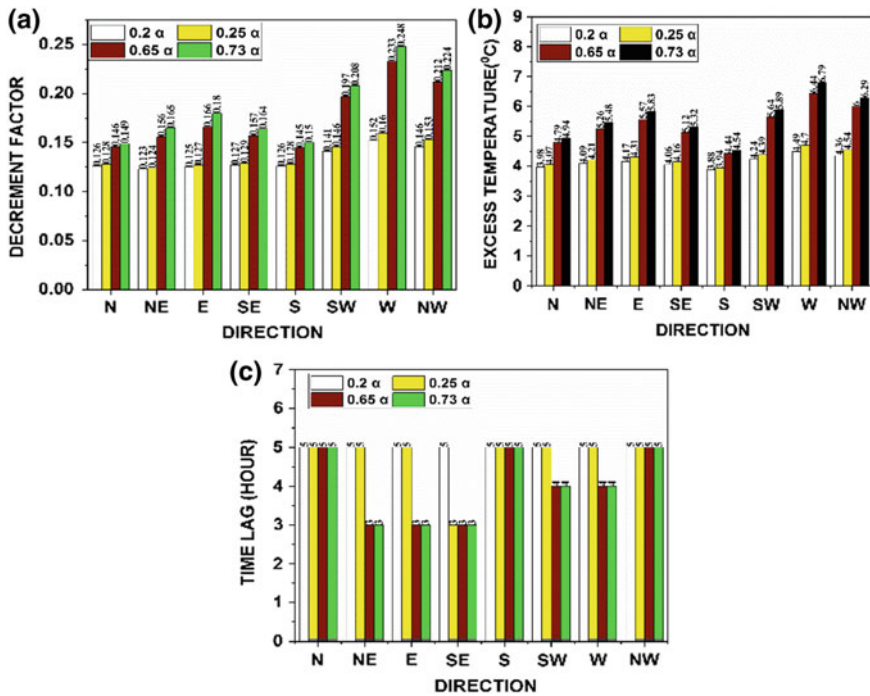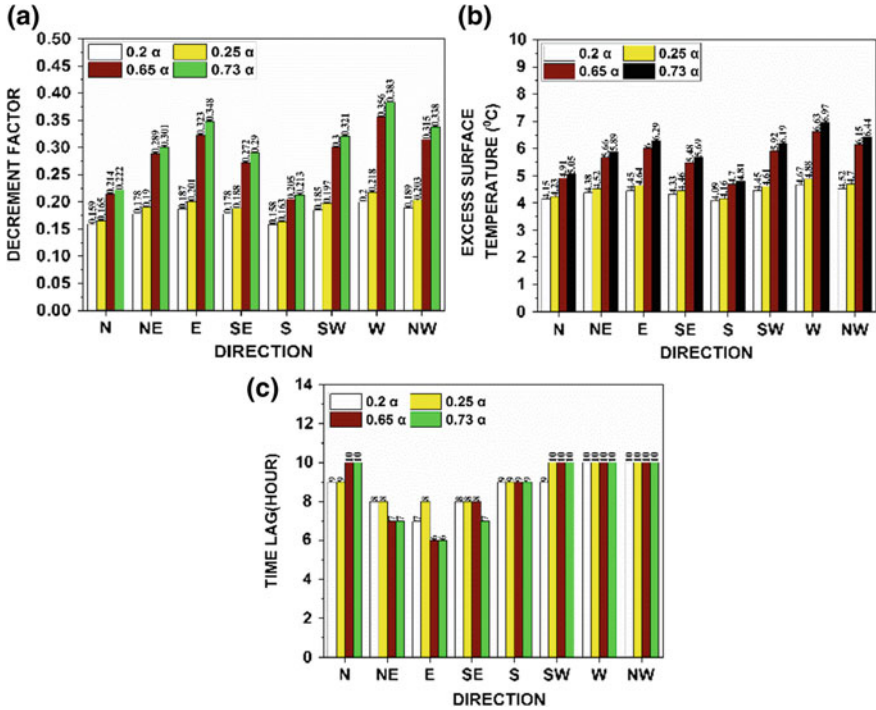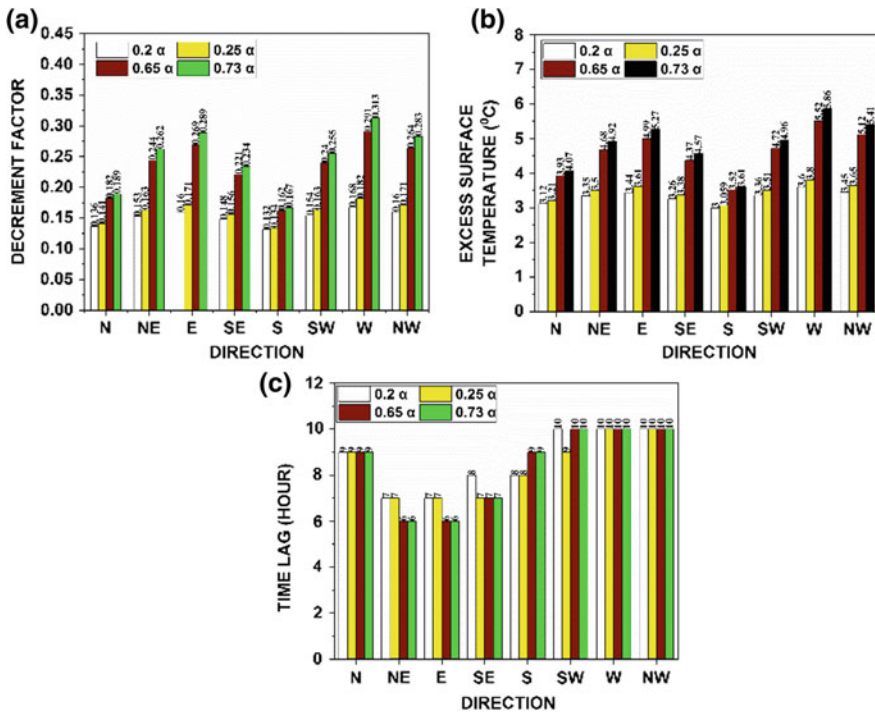
Fig. 13.9 a Decrement factor. **b** Excess inside surface temperature. **c** Time lag for different absorptivity in warm and humid (Bhubaneswar) climatic zone

13.4 Conclusions

Analysis of variation of time lag, decrement factor and inside temperature of the wall surface with absorptivity of the wall surface draws the following conclusions

- The time lag shows random variation with absorptivity. So, it can be concluded that time lag is completely dependent on the thermal mass of the wall.
- Decrement factor increases with an increase in the value of absorptivity of the wall surface. For all the climatic zones studied, the decrement factor was the highest in west direction in all cases of absorptivity. The value was the least in south direction in all cities except New Delhi. For New Delhi, it was lowest in north direction.
- The inside surface temperature showed the same variation pattern as decrement factor with absorptivity of the wall in all climatic zones. The inside surface temperature increases with an increase in the value of absorptivity. For all climatic zones, the inside surface temperature was the least for the wall facing south and the highest for the wall facing west.
- Decrement factor and inside surface temperature of the wall play an important role in determining the cooling load of a building. So, it should always be practised to keep the absorptivity of the wall as low as possible to reduce the cooling load

thereby saving energy. Special care must be taken in case of the wall facing west as the decrement factor and inside surface temperature are highest for it.

References

1. Valsson, S., Bharat, A.: Urban heat Island: cause for micro climate variation. Arch.-Time Space & People 20–25 (2009)
2. Urbanization in India. https://en.wikipedia.org/wiki/Urbanisation_in_India. Last accessed 23 Feb 2019
3. Kleerekoper, L., Van Esch, M., Salcedo, T.B.: How to make a city climate-proof, addressing the urban heat island effect. Resour. Conserv. Recycl. **64**, 30–38 (2012)
4. Buechley, R.W., Van Bruggen, J., Truppi, L.E.: Heat island = death island? Environ. Res. **5**(1), 85–92 (1972)
5. Conti, S., Meli, P., Minelli, G., Solimini, R., Toccaceli, V., Vichi, M., Beltrano, C., Perini, L.: Epidemiologic study of mortality during the Summer 2003 heat wave in Italy. Environ. Res. **98**(3), 390–399 (2005)
6. Synnefa, A., Santamouris, M., Akbari, H.: Estimating the effect of using cool coatings on energy loads and thermal comfort in residential buildings in various climatic conditions. Energy Build. **39**(11), 1167–1174 (2007)
7. Hernández-Pérez, I., Xamán, J., Macías-Melo, E.V., Aguilar-Castro, K.M., Zavala-Guillén, I., Hernández-López, I., Simá, E.: Experimental thermal evaluation of building roofs with conventional and reflective coatings. Energy Build. **158**, 569–579 (2018)
8. Shen, H., Tan, H., Tzempelikos, A.: The effect of reflective coatings on building surface temperatures, indoor environment and energy consumption—an experimental study. Energy Build. **43**(2–3), 573–580 (2011)
9. Arora, C.P.: Refrigeration and Air Conditioning, 3rd edn. Tata McGraw-Hill, New Delhi (2009)
10. Asan, H.: Investigation of wall's optimum insulation position from maximum time lag and minimum decrement factor point of view. Energy Build. **32**(2), 197–203 (2000)
11. ISHRAE: Indian society of Heating, Refrigerating and Air conditioning Engineers. India (2017)
12. IS 11907-1986: Recommendation for calculation of solar radiation in buildings
13. Sameera, S., Rao, P.P., Divya, S., Raj, A.K., Thara, T.A.: High IR reflecting BiVO4-CaMoO4 based yellow pigments for cool roof applications. Energy Build. **154**, 491–498 (2017)
14. Synnefa, A., Santamouris, M., Apostolakis, K.: On the development, optical properties and thermal performance of cool colored coatings for the urban environment. Sol. Energy **81**(4), 488–497 (2007)
15. Thongkanluang, T., Chirakanphaisarn, N., Limsuwan, P.: Preparation of NIR reflective brown pigment. Procedia Eng. **32**, 895–901 (2012)
16. IS: 3792: Indian standard guide for heat insulation of non-industrial buildings. India: Indian standards institution (1978)
17. CIBSE: CIBSE Environmental Design Guide-A. 7th ed, Chartered Institution of Building services engineers, London (2006)

Chapter 14
Study and Estimation of Static Stiffness of Machine Tool Spindle

Vibish S. Bhardwaj, Ramesh H. Aralaguppi, Ashok N. Badhe, Bhargav and Arun R. Rao

Abstract Spindle stiffness is the ability of spindle to resist deformations under the influence of cutting forces. The magnitude of deflections at the spindle nose, where cutting forces from the tool are transmitted, decides the machining accuracy of the machine tool. In this paper, a method to evaluate the static stiffness of the spindle with a bearing system subjected to cutting force is presented. The static stiffness of the spindle is calculated analytically by evaluating the radial stiffness of the bearings and the deflection at the front end of the spindle. Finite Element Analysis is carried out on the spindle bearing system, and results are compared with analytical results. Further, experiments are carried out to validate the analytical and numerical results.

Keywords Bearing force components · Static stiffness of spindle bearing system · Finite element analysis · Experimental setup

14.1 Introduction

Machine tools are used to produce high precision components in a short time with greater accuracy. The global market demands for very low machining tolerances. The stiffness of the machine tool spindle plays a very important role in achieving higher machining accuracy. Accuracy of machining operations depends on the cutting forces and the deflections caused on the spindle. For a spindle to take both radial and axial forces, it is important to select appropriate bearings and their arrangements. The optimum bearing arrangement contributes to the stability, working accuracy, revolving speed and stiffness of the spindle bearing system. Bearing arrangement of the spindle system affects the surface profile, quality and dimensional accuracy of the manufactured parts. Static stiffness decides the deflection the spindle undergoes when

V. S. Bhardwaj · Bhargav (✉) · A. R. Rao
Department of Mechanical and Manufacturing Engineering, M. S. Ramaiah University of Applied Science, Bengaluru, India
e-mail: 93.bhargav@gmail.com

R. H. Aralaguppi · A. N. Badhe
Dr. Abdul Kalam Center for Innovation, Bharat Fritz Werner Ltd., Bengaluru, India

a static force is acting on the spindle nose. When the operating frequency of these high-speed spindles falls under the resonant zone, the amplitude of vibration in the spindle will reduce the stiffness of the spindle bearing system considerably. Hence, stiffness estimation of spindle with the bearing system in the static and dynamic conditions is very important.

Shuzi [1] discussed the significance of the radial stiffness during static stiffness analysis of a spindle bearing system. Influences of various spindle parameters like bearing span length, overhang and bearing stiffness are studied. The bearing reaction forces are derived from direct and indirect influence methods, and relations for spindle stiffness with two and more bearing supports are arrived. To enhance the static stiffness of the spindle, the stiffness of the front bearing, area moment inertia of the spindle and reduction in the spindle overhang length are important. However, there are no experimental validations made for the suggested methods. Sarenac [2] studied the methods of creating a rigid spindle by optimizing the spindle parameters. Paper suggests the ratio of bearing span length to the spindle overhang which can help to decide the spindle stiffness. It also suggests that the higher spindle stiffness can be achieved by improving the stiffness of the bearing and spindle cross section. Kutlu [3] worked on the performance requirements of a machine tool spindle by considering high loads concentrated on the spindle nose and analyzing the static and dynamic stiffness of the spindle. The static stiffness is arrived by the superposition method for the spindle bearing system, and the analytical values are verified with FEA results. Soos [4] estimated the deflection on the spindle nose by considering the spindle bearing system divided into nodes and solving analytically as the static parameters. The bending moments on the overhang and the deflection due to bearing compliances are used to estimate the deflections at the spindle nose. Prakosa and Wibowo [5] built a mathematical model of the spindle bearing system and studied the stiffness results by changing the bearing preload, span length, number of bearing and spindle length. Later, they optimized these parameters to improve the stiffness. Using Dunkley's method, the resonating frequencies are obtained and compared with experimental results.

In this paper, a methodology to estimate the static stiffness of the machine tool spindle is developed. Radial deflection of the spindle is determined by considering the bearing compliance when it is subjected to cutting forces analytically. The correctness of the analytical deflections is verified numerically by using FEA software. Finally, the deflection results obtained are validated with experimental results.

14.2   Static Stiffness Analysis Using Analytical Approach

In the spindle bearing system, shown in Fig. 14.1, a hollow spindle is supported by angular contact ball bearings which take both axial and radial forces at high speeds. Bearings are arranged in a quad back-to-back arrangement to accommodate axial forces in both directions. The static stiffness of the spindle bearing system under the
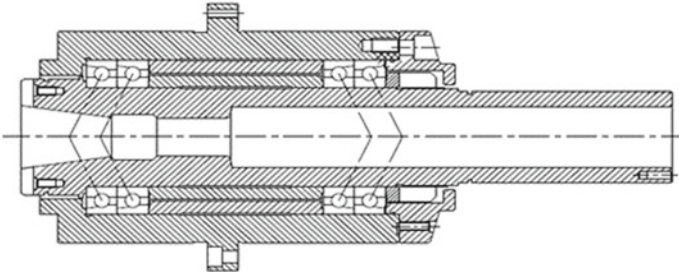
Fig. 14.1 Schematic of spindle bearing system

influence of cutting forces transmitted to the spindle nose during milling operations is evaluated.

14.2.1 An Evaluation of Axial and Radial Forces on Bearing Compliance

The axial force is acting parallel to the spindle axis due to the preload applied on the bearings using a locknut. Tightening torque is applied on the locknut to provide necessary preload on the bearings. The axial force is derived from the tangential force generated by the locknut [6]. The relation between the axial force and the tightening torque is shown in Eq. (14.1).

$$F_A = \frac{T}{(0.16662d)} \tag{14.1}$$

where T is the tightening torque, d is the effective diameter of the locknut, 0.16662 is the locknut pitch angle factor, and F_A is the axial force acting on the bearing. Radial forces are acting perpendicular to the axis of the shaft. When the cutting forces are transmitted to the spindle nose during milling operation, it creates reaction force at the bearings as shown in Fig. 14.2. Reaction forces acting in the radial direction are arrived using moment and equilibrium equations. Reaction forces at the front bearing FR1 and the rear bearing FR2 are evaluated. From Fig. 14.2, it can be observed that due to the cutting forces acting on the spindle nose, a reaction force FR1 acts in the upward direction on the front bearing and reaction force FR2 acts in the downward direction on the rear bearing.
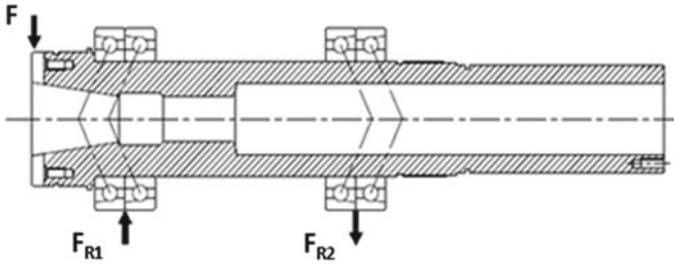
Fig. 14.2 Bearing reaction forces

14.2.2 Bearing Radial Stiffness

Bearing arrangement and the contact angle of the bearing play a major role in deciding its radial stiffness. The radial stiffness of the bearings is evaluated by multiplying the contact angle factor and axial stiffness of the bearing. The axial stiffness value (K_A) and the contact angle (θ_{Factor}) of the bearing are selected from the bearing catalog [7]. The front and rear bearings are of the same dimensions. The relation for the radial stiffness of the bearing is given in Eq. (14.2). Using this equation, the radial stiffness of the bearing is calculated.

$$K_R = K_A * \theta_{Factor} \tag{14.2}$$

14.2.3 Static Stiffness of Spindle Bearing System

Various methodologies for evaluating deflections at spindle nose when subjected to cutting forces are discussed [3]. Deflections are evaluated using the superposition technique. In the first case, the spindle bearing system is considered to have a rigid shaft with elastic bearings, and in the second case, the system has an elastic shaft with rigid bearings. Both the cases are combined to obtain deflection at spindle nose where the shafts and bearings deform elastically. In another technique [4], the bending moments acting on the spindle bearing system are combined with the deflections caused by the bearing arrangements to evaluate the deflection at the spindle nose.

The spindle system shown in Fig. 14.3 is supported by front and rear bearings, and cutting force P is acting on the spindle overhang section. Deflection at the spindle nose is evaluated using Eq. (14.3) by considering the spindle and its support as elastic bodies to arrive at the real-time deflections [1].
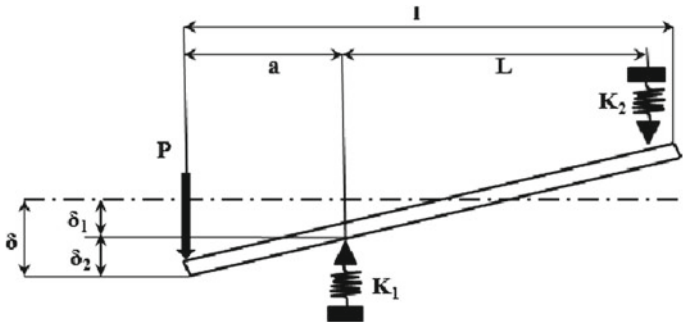
Fig. 14.3 Nature of deflection at the spindle nose

$$\delta = P\left[\frac{a^3}{3EJ_a} + \frac{La^2}{3EJ_L} + \frac{1}{K_1}\left(1 + \frac{a}{L}\right)^2 + \frac{1}{K_2}\left(\frac{a}{L}\right)^2\right] \tag{14.3}$$

where

A	Spindle overhang
E	Modulus of elasticity
δ	Deflection at spindle nose
J_a and J_L	Area moment of inertia at overhang and bearing span
L	Bearing span length
P	Cutting force
K_1 and $K_2=$	Front and rear bearing stiffness.

Assumptions made to evaluate the deflection at the spindle nose are as follows:

(a)   The spindle is a flexible overhang beam body
(b)   The beam is simply supported
(c)   Flexible supports with stiffness values and
(d)   Point load acting at the end of the overhang section.

In Eq. (14.3), the first term signifies the deflections at the overhang section, the second term signifies the deflection at the span length where the spindle acts as a simply support beam, and the remaining terms signify the deflection at the spindle nose due to the deflection of the front and rear bearings. All these deflections act in the radial direction. The sum of these deflections results in the static deflection at the spindle nose as shown in Eq. (14.3). The static stiffness of the spindle bearing system is arrived by using Eq. (14.4).

$$K = P/\delta \tag{14.4}$$

14.3 Finite Element Analysis

A hollow spindle model is developed, and angular contact ball bearings are mounted in a quad back-to-back arrangement with respect to the schematic of the spindle bearing system. COMBIN 14 element type is used to provide radial stiffness to the bearing. Convergence study for results up to 0.1% difference in results is carried out, and discretization of 5 mm based on convergence study is performed. The material properties of steel are specified. Appropriate boundary conditions where the bearings are constrained in all degrees of freedom with respect to the spindle housing are specified, and load is applied in *X*-axis at the spindle nose as cutting forces. Static structural analysis is carried out using ANSYS Workbench.

14.4 Experimental Setup

Machine tool spindle of a vertical machining center is considered. An experimental setup is made to measure the deflection on the spindle nose due to static load. Static load is applied on the tool holder using a beam load cell as shown in Fig. 14.4 to create a cutting force on the spindle nose. The maximum cutting forces experienced on the machine tool spindle during machining operations is 2000 N. The load cell used here has a capacity of load from 0 to 1000 kg.

A Linear Variable Displacement Transducer (LVDT) with up to 0.1 μ resolution having a magnetic base is used to measure the deflections at the spindle nose and the tool holder. The magnetic base is placed on the stationary part of the spindle unit close to the bearing housing. A gradual incremental load is applied, and the corresponding deflections are measured. One of the LVDT styluses is placed on the spindle nose and the other on the tool holder as shown in Fig. 14.4; the respective deflections are identified. Experimental study is carried out to evaluate the spindle bearing stiffness which is discussed in the next section.
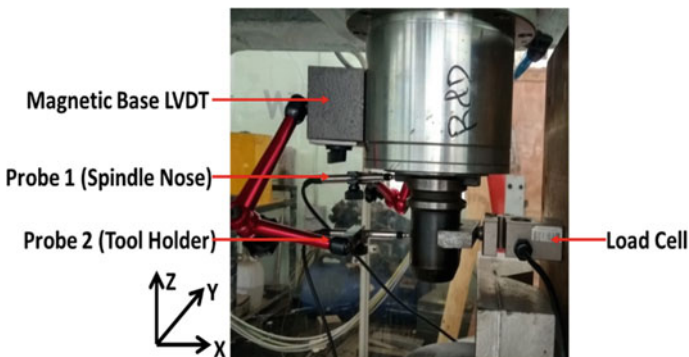
Fig. 14.4 Experimental setup for spindle deflection test

14.5   Results and Discussion

14.5.1   Deflection Result

The deflections on the spindle nose for various external force values applied using a load cell are evaluated analytically using Eq. (14.3). These results are compared with experimental results and FEA results, and differences in terms of percentage are tabulated in Table 14.1.

Table 14.1 shows the percentage difference between the deflections at the spindle nose arrived from analytical and experimental approach. It can be observed that the difference tends to reduce as the externally applied force increases. This is due to the stiffness of the spindle bearing system which resists deflecting the spindle nose more at lesser applied force. The spindle behavior is similar to that of its operating conditions, when it performs machining operations along a particular axis. It can be observed from Sl. No. 5 and onwards in Table 14.1, where the differences are below 10%. The spindle nose deflections are more realistic after this point. A plot of external force versus displacement is plotted as shown in Fig. 14.5a, representing the comparison of displacement values between the analytical and experimental results.

FEA results of the spindle bearing system are used for total deformations. Table 14.1 shows the results for deflection at the spindle nose using a numerical approach. These results are compared with experimental values which are tabulated in Table 14.1. A plot of external force versus displacement is plotted as shown in Fig. 14.5b, representing the comparison of displacement values between FEA and experimental results. Study is performed to estimate the deflection of the spindle

Table 14.1 Comparison between analytical, experimental and FEA results

Sl. No	External force F (N)	Deflection, δ, at spindle nose (μm)			Percentage difference	
		Analytical result	Experimental result	FEA result	Analytical and experiment	FEA and experiment
1	200	1.23	0.50	1.24	59.34	59.82
2	392	2.42	1.20	2.43	50.41	50.80
3	595	3.68	2.37	3.70	35.59	35.96
4	788	4.87	3.87	4.90	20.53	21.08
5	984	6.08	5.47	6.10	10.03	10.33
6	1194	7.38	7.03	7.41	4.74	5.14
7	1386	8.57	8.63	8.62	0.70	0.05
8	1543	9.54	10.17	9.60	6.60	5.91
9	1778	11.0	11.67	11.06	6.09	5.46
10	1968	12.2	13.37	12.24	9.59	9.16
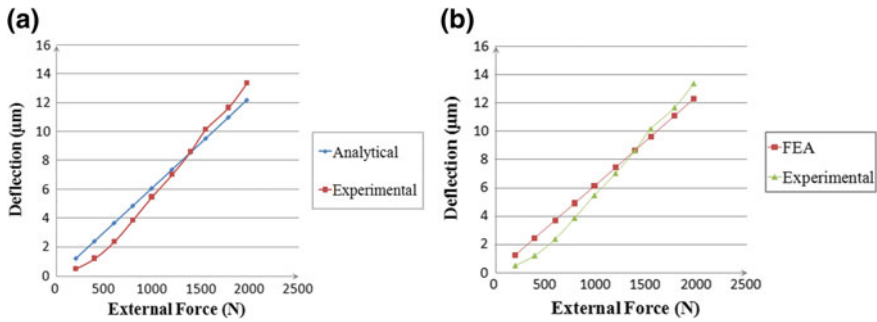
Fig. 14.5 **a** Comparison of analytical versus experimental results. **b** Comparison of FEA versus experimental results

Table 14.2 Deflection results for spindle nose and tool holder

Sl. No.	External force F (N)	Deflection δ (μm)	
		At spindle nose	At tool holder
1	200	0.50	2.03
2	392	1.20	4.63
3	595	2.37	7.87
4	788	3.87	11.07
5	984	5.47	14.40
6	1194	7.03	17.80
7	1386	8.63	21.13
8	1543	10.17	24.23
9	1778	11.67	27.50
10	1968	13.37	30.77

bearing system when a tool holder is attached to the system. Comparisons between experimental deflection at spindle nose and tool holder are tabulated in Table 14.2.

It is noticed that there is a considerable difference in deflection results between both the conditions. Hence, it is also important to evaluate the stiffness of the spindle bearing system with an attached tool holder.

14.5.2 Stiffness Results

The real-time deflections are considered from the point where the difference in results is within 10% (Sl. No. 5 in Table 14.1), and the mean static stiffness of the spindle bearing system for the set of force and deflection values is evaluated using the relation in Eq. (14.4) and tabulated in Table 14.3. Since the current work concentrates on the deflections in the spindle nose, the deflection at tool holder is not considered for

Table 14.3 Static stiffness of spindle bearing system

Methodology	Static stiffness of spindle bearing system (N/µm)
Analytical	162.92
Finite Element Analysis	160.80
Experimental (At spindle nose)	166.53

further calculations. The experimental static stiffness of the spindle bearing system considering attached tool holder is compared with the static stiffness of the spindle bearing system without tool holder.

From Table 14.3, it is observed that the difference between the static stiffness results at the spindle nose is 2.83% between analytical and experimental results and 3.44% between FEA and experimental results. This indicates that various approaches used, as shown in Table 14.3, for the stiffness analysis yield similar results. Thus, the analytical and FEA results are validated with the experimental values. The static stiffness of the spindle nose reduces due to joint stiffness between the spindle nose and the tool holder when it is attached with tool holder.

14.6   Conclusions

The machining accuracy and working performance of a machine tool directly depend upon tool deformation under operating condition. This deformation depends upon the stiffness of the spindle, and the evaluation of this stiffness is very important. In this paper, a methodology to arrive at the spindle bearing stiffness by identifying the force components acting on the system is proposed. The deflection of the spindle nose is evaluated analytically, numerically and validated with experimental data. The differences in total deformations between the three methods are within 10%. The stiffness of the spindle bearing system is evaluated using the three approaches. The difference in results between analytical and experimental approaches is 2.83% and between numerical and experimental results is 3.44%. Deflections from the tool holder are also measured experimentally. The stiffness of the spindle unit at tool holder point reduces to 72 N/µm due to joint stiffness between the tool holder and spindle. Future studies to identify the joint stiffness between the spindle nose and the tool holder need to be carried out.

References

1. Shuzi, Y.: A study of static stiffness of machine tool spindles. Int. J. Mach. Tool Des. **21**(1), 23–40 (1980)
2. Sarenac, M.: Stiffness of machine tool spindle as a main factor for treatment accuracy. Sci. J. Facta Univ. **1**(6), 665–674 (1999)
3. Asimkutlu.: Design and development of a lathe spindle. Master of science thesis, Stockholm (2016)
4. Lubomír, S.: Radial ball bearings with angular contact in machine tools. IntechOpen Ltd., London (2012)
5. Prakosa, T., Wibowo, A., Llhamsyah, R.: Optimizing static and dynamic stiffness of machine tools spindle shaft for improving machining product quality. J. Kones Powertrain Transp. **20**(4), 363–370 (2013)
6. IBC High precision locknuts. http://www.ibc-waelzlager.com. Last accessed 24 May 2018
7. NSK.: Machine tool spindle bearing selection and mounting guide, England (2009)

Chapter 15
Effect of Surface Corrosion of Steel Reinforcement on Bond Strength Characteristics of Concrete

Vineet Kothari and **Hemanth Kamplimath**

Abstract Corrosion is the degradation of a metal by an electrochemical reaction with its surrounding environment. The corrosion of embedded steel reinforcement in concrete causes durability issue in reinforced concrete structures and cement concrete pavements. The impact of corrosion of embedded steel rebars on the performance of reinforced concrete structures and pavements is a subject of concern for the engineers and scientists working in the construction industry. One of the effective ways of studying such influence is to understand the effect of corrosion on the mechanical and durability properties of concrete. The bond strength between steel rebar and concrete is also an important parameter of study. This study focuses on probing the effect of corrosion on bond strength and other mechanical properties of reinforced concrete. A pull-out test was conducted on 18 concrete cube specimens having steel bars of 12 and 16 mm diameter Fe500 grade. These bars were corroded with the help of commercial grade hydrochloric acid solution 10% v/v. Each group of bar specimens included three levels of corrosion: 0, 3 and 5%. Tension test on steel bars and compression test for concrete cubes were conducted.

Keywords Reinforced concrete · Rebar corrosion · Bond strength · Pull-out test

15.1 Introduction

Corrosion is the degradation of a metal by an electrochemical reaction with its surrounding environment. This is an undesirable process which causes premature failure of structures. The steel bars may get corroded during its stages of service life such as production, storage, construction and also during the service life of the structure [1]. Carbonation and increase in the chloride ionic concentration in concrete are the two main factors which severely corrode the embedded steel in concrete

V. Kothari · H. Kamplimath (✉)
Nirma University, Ahmedabad, India
e-mail: hemanth.kamplimath@nirmauni.ac.in

V. Kothari
e-mail: vineet.kothari@nirmauni.ac.in

beyond acceptable limits [2]. Durability properties of concrete such as porosity, pore size distribution and permeability affect the rate of corrosion of steel.

Corrosion of steel in concrete is a complex phenomenon and has a higher impact on the mechanical properties of concrete especially its strength. The bond strength depends upon bar geometry, surface condition of the bar, presence of confinement and the properties of concrete [3]. The corrosion of reinforcement causes an increase in its volume due to the increase in the diameter of the steel bar initially. This in turn leads to splitting and weakened bond between steel and concrete. This affects the serviceability as the durability of the structure is decreased [4]. Corrosion of steel reinforcement causes a reduction in yield strength and bond strength due to the delamination of rust elements formed on the surface of steel. Corrosion may lead to reduction in the ductility of rebar. The ratio of yield strength to the ultimate strength of the rebar at maximum load is reduced. This reduction leads to early failure of the rebar [5]. Bond strength between rebar and concrete does not have any standard quantitative definition. Pull-out test is adopted to compare the bond strength of various types of rebar with concrete [6].

15.2 Research Methodology

This study focuses on some of the factors affecting the serviceability of RC structures such as

1. Calculating the mechanical properties of corroded rebar.
2. Correlation between rebar corrosion levels and bond strength of reinforced concrete.

This study focuses on the acceptability of the results of bond strength for various levels of rebar corrosion, and thus, helping site engineers in deciding the use of surface corroded steel rebar on the construction site.

15.2.1 Level of Corrosion

The main significance of this study is to assess the effect of rebar corrosion on the bond characteristics between rebar and concrete. The effect of corrosion on the mechanical properties of rebar is also assessed. Table 15.1 represents various material

Table 15.1 Material properties

Material properties	Characteristics
Strength of concrete	M25
Bar size	12 and 16 mm
Level of corrosion	0, 3 and 5%

Table 15.2 Level of corrosion for trial test

Material properties	Characteristics
Length of reinforcing bar	400 mm
Initial weight of reinforcing bar	0.179 kg
Weight of reinforcement bar after 6 days	0.148 kg
Reduction in weight	0.031 kg
Percentage reduction in weight	17%

parameters of steel and concrete considered for the pull-out test. Table 15.2 represents the levels of the corrosion considered for a trial test. In the present study, the pull-out test was conducted for two levels of rebar corrosion and compared with a corrosion less specimen.

For the trial test, 400 mm long rebar specimen was completely submerged in 10% v/v solution of commercial grade hydrochloric acid. It was possible to achieve 17% corrosion in just 6 days. Details of the test conducted are given in Table 15.2.

Corroded rebars were prepared in a laboratory by submerging 170 and 400 mm long rebar in 10% v/v solution of commercial grade hydrochloric acid. It was possible to achieve 17% corrosion in just 6 days. Details of the test conducted are given below.

The above mentioned method is suitable for corroding rebar up to the desired limit. To study the effect of corroded rebar on the mechanical properties of concrete and its bond strength, two sizes of rebars (12 and 16 mm diameter) having a standard length of 0.8 m have been tested. Figure 15.1 shows 12 mm rebar for the three levels of corrosion. The 12 and 16 mm diameter bars were corroded up to a length of 170 mm by submerging it in 10% v/v HCl solution. This is due to the fact that the corroded specimen is inserted into specially made cube molds of size 150 mm × 150 mm × 150 mm as shown is Fig. 15.2. Table 15.3 provides the details of the corroded specimens. The rebars are numbered in such a way that B1 represents the first bar out of twelve bars used, D12 represents the diameter of the bar, i.e., 12 mm, and L5 indicated the level of corrosion, i.e., 5%. The level of corrosion is calculated from the equation given below. The length of rebar for all the specimens is 0.8 m,
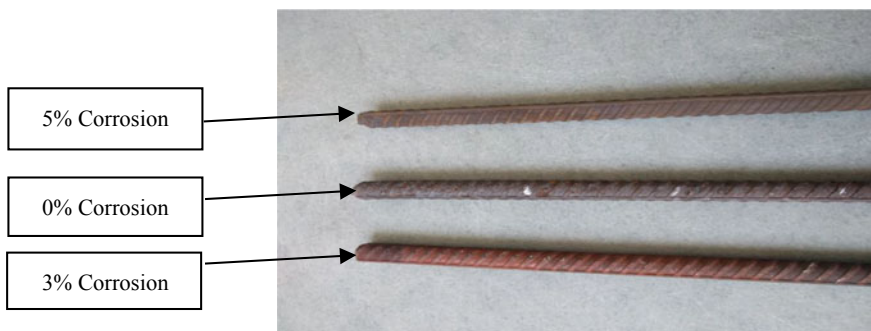
Fig. 15.1 Twelve mm bars with different corrosion levels

Fig. 15.2 Concrete
specimen prepared for
pull-out test
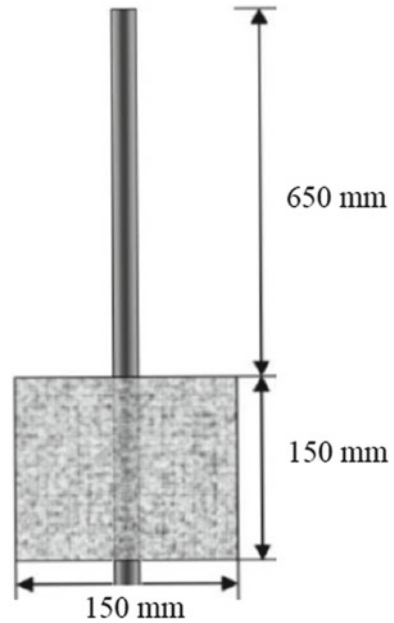
Table 15.3 Details of corroded rebar specimens

Rebar no.	Wt. (gm/m)	Initial weight (gm)	Embedded length (mm)	Corrosion level (%)	Final weight (gm)	Result (%)
$B_1D_{12}L_5$	891	713	170	5	705.50	4.95
$B_2D_{12}L_3$	888	712	170	3	707.50	2.98
$B_3D_{12}L_5$	887	710	170	5	701.67	5.52
$B_4D_{12}L_5$	891.5	715	170	5	707.65	4.85
$B_5D_{16}L_5$	1559	1247.6	170	5	1235.10	4.72
$B_6D_{16}L_5$	1558	1246.7	170	5	1234.24	4.70
$B_7D_{16}L_3$	1553	1242.3	170	3	1234.80	2.84
$B_8D_{16}L_5$	1571	1257	170	5	1244.00	4.87
$B_9D_{16}L_3$	1572	1258	170	3	1249.00	3.37
$B_{10}D_{16}L_3$	1568	1267	170	3	1258.00	3.38
$B_{11}D_{12}L_3$	883	704.67	170	3	0699.85	3.21
$B_{12}D_{12}L_3$	888	711	170	3	0706.4	3.05

and the embedded corroded length is 170 mm.

$$\% \text{ Corrosion} = \frac{(\text{Initial Weight of Bar} - \text{Final Weight of Bar}) \times \text{Length of Rebar}}{\text{Embedded Length of Rebar} \times \text{Inital Weight of Rebar}} \times 100$$

Table 15.4 Mix proportioning of concrete

Description of material	Quantity per m^3 of concrete
Grade of concrete	M25
Cement	382 kg
Fine aggregates	712 kg
Coarse aggregates	1140 kg
Water	153 kg
W/C ratio	0.4
Super plasticizer (PCE-based)	0.9% by weight of cement

15.2.2   Mix Proportioning of Concrete

Twelve mm and 16 mm steel rebars were used for the study. M25 grade of concrete was used. Table 15.4 provides the mix design quantities used for the study.

15.2.3   Fabrication of Specimens for Pull-Out Test

The concrete cubes of size 150 mm × 150 mm × 150 mm and M25 grade of concrete were prepared and used for the pull-out test as shown in Fig. 15.2. Twelve specimens were prepared for the pull-out test at different corrosion levels, i.e., 0, 3 and 5%.

15.3   Experimental Program

15.3.1   Compression Strength of Cubes

IS 2770:1967 (PART 1) [7] requires that the average compressive strength of three cubes representing the concrete used for test specimen made and tested in accordance with relevant requirements of IS: 516-1959 shall be 200–300 kg/cm^2 at the time of making pull-out tests. The compression testing machine of capacity two thousand kilo newton was used to evaluate the compressive strength of concrete cube specimens. Three concrete cubes of size 150 mm were tested in compression as per IS 516 [8]. The equation for calculating the compressive strength of the cube specimen is given below.

$$\text{Compressive Strength } \left(\text{N/mm}^2\right) = P \times 10^3/A$$
$$P = \text{Failure load of cube (KN)}$$
$$A = \text{Area of cube } (150 \times 150) \left(\text{mm}^2\right)$$

Fig. 15.3 Test setup for
pull-out test of specimen

15.4 Bond Strength of Concrete

Pull-out test is an effective and standard method for comparison of bond
characteristics of corroded rebar with concrete [9]. Concrete cubes of 150 mm ×
150 mm × 150 mm size along with 12 and 16 mm corroded rebar were used to
gauge the bond strength characteristics as per IS: 2770: 1967 (Part 1) [7]. The details
of corroded specimens are provided in Table 15.3. In this test, the load value is noted
at a relative slip of 0.02 mm at the free end of the specimen. The ratio of load value
recorded at failure load versus the surface area of the bar provides the bond strength.
Dial gauges with a least count of 0.01 mm were used for measuring the slip. Dial
gauges are arranged in such a way that it is possible to record the movement of
rebar at both the unloaded and loaded ends. The concrete specimen prepared for the
pull-out test is shown in Fig. 15.2, and the pull-out test setup is shown in Fig. 15.3.

15.5 Tensile Test on Rebar

To study the impact of corrosion on mechanical properties of rebar, tension test has
been performed. The test consists of straining the test specimen by applying tensile
force until fracture. All steel rebar samples were tested to determine the yield and

Fig. 15.4 Test setup for tension test on reinforcing bar

ultimate strength, in accordance with IS: 1608-1995 [10], using a universal testing machine of 500 KN capacity. The ultimate load and the breaking load are noted. Stress–strain characteristics are determined to evaluate yield strength of material. Figure 15.4 presents the test setup for the tension test.

15.6 Results and Discussions

15.6.1 Compressive Strength of Concrete

The 28-day compressive strength of three sets of concrete cubes (a total of nine cubes) representing the concrete used for pull-out test was evaluated. The average of the three sets of results is represented in Table 15.5. It has been noted that the average cube compressive strength is 27 MPa which satisfies the requirements of minimum compressive strength of pull-out test specimen at the time of test.

Table 15.5 Cube compressive strength of concrete

Cube no.	Compressive strength in MPa	Avg. compressive strength in MPa
1	25.3	27
2	27.7	
3	28.0	

Table 15.6 Tensile strength of rebar at various corrosion levels

Corrosion level (%)	Yield strength (MPa)		Ultimate strength (MPa)	
	12 mm dia.	16 mm dia.	12 mm dia.	16 mm dia.
0	494.41	571.96	585.49	691.33
3	477.80	539.60	570.60	634.87
5	463.79	524.00	552.70	623.97

15.6.2 Effect of Corrosion on Tensile Strength of Concrete

Tension test has been performed to evaluate the effect of various levels of corrosion on mechanical properties of steel rebar. The average results of the yield strength and ultimate strength have been presented in Table 15.6. It was observed that the increase in corrosion levels decreases the yield and ultimate strength of rebar.

15.6.3 Effect of Corrosion on Bond Strength of Concrete

The bond strength at an age of 28 days has been evaluated for cube specimen prepared for all three corrosion levels, i.e., 0, 3 and 5%. Average results of three specimens tested are calculated, and the results are tabulated in Table 15.7.

A graph of average values of bond strength versus the three corrosion levels (0, 3 and 5%) is plotted as shown in Fig. 15.5. The results indicated that the bond strength of both 12 and 16 mm diameter bars decreased with an increase in corrosion levels. The average bond strength of 12 mm diameter bar with 3% corrosion level is 10.68 MPa (2.5% decrement), whereas for 5% corrosion level, it is 8.5 MPa (22% decrement). For 16 mm diameter bars, average bond strength value for 3% corrosion level is 11.47 MPa (3% decrement) and 9.76 MPa (19% decrement) for 5% corrosion level. Up to 3% corrosion level, the decrease in bond strength is minor. However, for 5% corrosion level, there was a drastic decrease in bond strength up to 15–20% for both rebars of size 12 and 16 mm. Figure 15.5 shows the effect of corrosion on bond strength for both types of reinforcing bars.

The bond strength of the deformed bars may have decreased due to reduction in mechanical resistance to slip because of decay in twirls provided on TMT bars up to 5% corrosion level. Due adequate bond capacity, bond failure due to pulling of

Table 15.7 Effect of corrosion on bond strength of concrete

Corrosion level (%)	Average bond strength (MPa)	
	12 mm dia.	16 mm dia.
0	10.96	11.84
3	10.68	11.47
5	8.50	9.76
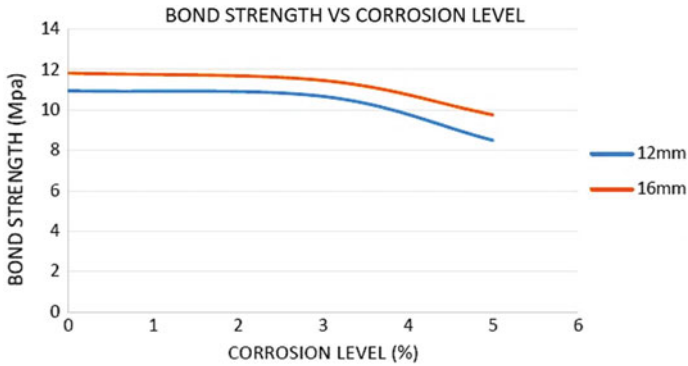
Fig. 15.5 Bond strength versus corrosion level of rebar

Fig. 15.6 Failure pattern of pull-out test specimen for TMT bars

the bar did not occur. The surrounding concrete which was subjected to excessive circumferential tensile stress failed by splitting for all the pull-out test specimens. The interacting force between the deformed bar and the surrounding concrete may have led to the splitting of the concrete into two segments as shown in Fig. 15.6.

15.7 Conclusion

Method of corroding reinforcing bars in laboratory by submerging bars into 10% v/v solution of commercial grade hydrochloric acid is suitable to stimulate actual field scenario as well as long-term serviceability scenario quickly. The tensile strength of the steel bar decreases with the increase of corrosion level. Variation of modulus of elasticity of the rebar does not change significantly as there is no much effect of the

corrosion level on the initial linearity of the stress–strain curve. With the increase in the corrosion level of the rebar, the yield strength and ultimate strength of the steel decrease by approximately 5–10% as compared with the standard rebar. The bond strength of the corroded rebar decreases slightly for 3% corrosion level of rebar and marginally for 5% corrosion level of rebar.

References

1. Huang, C.-H.: Effect of rust and scale of reinforcing bars on the bond performance of reinforcement concrete, ASCE J. Mater. Civ. Eng. **26**(4), 576–581 (2014)
2. Ahmad S: Reinforcement corrosion in concrete structures, its monitoring and service life prediction—a review. Cem Concr Compos **25**(4–5), 459–471 (2003)
3. ACI 222-R19: Guide to protection of reinforcing steel in concrete against corrosion. American Concrete Institute, Farmington Hills, MI, USA (2019)
4. Cabrera JG: Deterioration of concrete due to reinforcement steel corrosion. Cement and Concrete Composites **18**(1), 47–59 (1996)
5. Mansoor, Y.A, Zhang, Z.Q.: The reinforcement bond strength behavior under different corrosion condition. Res. J. Appl. Sci., Eng. Technol. **5**, 2346–2353 (2013)
6. IS 2770 (part-1:1967): Method of testing bond in reinforced concrete part-1 pull out test
7. Shetty, A., Venkataramana, K., Gogoi, I., Praveen, B.B.: Performance enhancement of TMT rebar in accelerated corrosion. J. Civ. Eng. Res. **2**, 12–14 (2012)
8. IS-10262 (2009): Concrete mix proportion guidelines, Bureau of Indian Standards, New Delhi (2009)
9. Tondolo, F.: Bond behaviour with reinforcement corrosion. J. Constr. Build. Mater. **93**, 926–932 (2015)
10. IS: 1608-1995: Mechanical testing of metals, Bureau of Indian Standards, New Delhi (1995)
11. IS: 516-1959: Methods of tests for strength of concrete, Bureau of Indian Standards, New Delhi (1959)

Chapter 16
Stress Distribution in an Infinite Plate with Circular Hole by Modified Body Force Method

Shrikrishna Badiger and **D. S. Ramakrishna**

Abstract Stress distribution in an infinite plate with circular hole subjected to uniform tension is determined by employing a modified body force method. In this method, the problem of a plate with a hole under uniform tension is considered as a plate with an imaginary hole. The boundary of the imaginary hole is divided into a number of divisions. At the mid-point of each division, concentrated forces known as body forces are applied. The magnitudes of these body forces are computed from complex potential functions, and stress at an arbitrary point is obtained by the summation of stresses due to these body forces applied at the mid-point of each division and stresses due to applied load. Results obtained from the modified body force method show trends in line with theoretical results. However, more accurate results can be obtained by using better estimate of body forces which satisfy boundary conditions at the circular hole. Setting Poisson's ratio $\nu = 0$ has little effect on the computed stress distribution.

Keywords Body force method · Boundary force method · Stress concentration

16.1 Introduction

The solution to the problem of stress distribution in an infinite plate with circular hole subjected to uniaxial loading was first obtained by Kirsch [1]. The details of the analytical solution are found in Timoshenko [2] and Wang [3]. Complex variables approach was first introduced into plane elastic problems in 1909 by Kolosov [4, 5], which was further utilised in solving various problems in elastostatics by Muskhelishvili [6] and others. With improvements in computer performance, numerical techniques like finite element method (FEM) and boundary element method (BEM)

S. Badiger (✉)
Ramaiah University of Applied Sciences, Bengaluru, India
e-mail: krishnabadiger@yahoo.com

D. S. Ramakrishna
Jawaharlal Nehru National College of Engineering, Shivamogga, India
e-mail: ramak_ds@yahoo.com

became popular methods of solving various engineering problems. However, FEM and BEM have the limitation of increased computing cost and accuracy when discontinuities like holes and cracks are present in the material. Body force method (BFM) originally proposed by Nisitani [7, 8] is a boundary type technique for stress analysis. The software program named BFM2D, developed by Nisitani [8] and based on BFM is reported to provide accurate results even with coarse mesh. More recently, Manjunath and Ramakrishna have applied BFM and solved various problems including Flamant and Melan problem [9–11].

16.2 Body Force Method

Body force method is a boundary type technique based on the principle of superposition. For a plate with circular hole subjected to uniform tension as shown in Fig. 16.1a, the circular hole is considered as imaginary hole, which is divided into a number of divisions (imaginary hole is divided into four divisions in Fig. 16.1b), at the mid-point of each division, body forces ρ_{xi}, ρ_{yi} are applied in x- and y-directions, the magnitudes of which are unknown to begin with. Applying equilibrium condition to each division in x- and y-directions due to the body forces and external applied load, we obtain a set of linear equations which can be expressed in the form, $Ax = b$ where A is influence coefficient matrix obtained from Kelvin's problem (point load in an infinite plane) where unit loads are applied in x- and y-directions, x is the unknown body force vector and b is a vector consisting of forces on each division in x- and y-directions due to external applied load. The stress at an arbitrary point $P(x, y)$ (Fig. 16.1a) is obtained by the summation of stresses at point $P(x, y)$ due to body forces ρ_{xi}, ρ_{yi} and stresses due to the applied uniform load as shown in Fig. 16.1b.
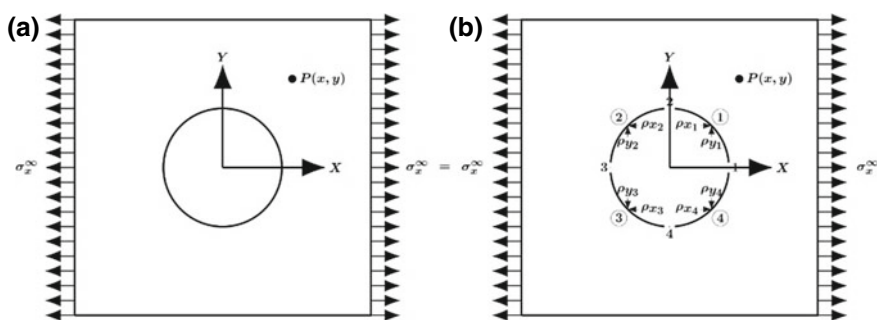
Fig. 16.1 Plate with a circular hole subjected to uniform tension and its equivalence in BFM

16.3 Modified Body Force Method

Body forces ρ_{xi}, ρ_{yi} can also be computed from complex potential functions which describe the given loading and boundary conditions. The complex potential functions for an infinite plate subjected to uniform tensile stress in x-direction are well known [10]. In this study, body forces are obtained from complex potential function given by Honein [10]. These body forces are applied at the mid-point of each division. The stress at an arbitrary point $\mathbf{P}(x, y)$ is obtained by the summation of stresses due to the computed body forces and stresses due to the applied load.

Stresses are related to complex potential functions $\varphi(z)$ and $\psi(z)$ [2, 3, 5, 6] by the following relations:

$$\sigma_x + \sigma_y = 2\big(\varphi'(z) + \overline{\varphi'(z)}\big) = 4\Re\big\{\varphi'(z)\big\} \tag{16.1}$$

$$\sigma_y - \sigma_x + 2i\,\tau_{xy} = 2\big(\bar{z}\varphi''(z) + \psi'(z)\big) \tag{16.2}$$

Forces acting on an arc from A to B are related to complex potential functions by the following relations [12]:

$$P_x + P_y = -i\big[\varphi(z) + z \cdot \overline{\varphi'(z)} + \overline{\psi(z)}\big]_A^B \tag{16.3}$$

Complex potential functions for an infinite plate subjected to uniform tensile stress in x-direction are as follows [10]:

$$\varphi(z) = \frac{z}{4} \cdot \sigma_x^\infty \tag{16.4}$$

$$\psi(z) = -\frac{z}{2} \cdot \sigma_x^\infty \tag{16.5}$$

Complex potential functions $\varphi(z)$ and $\psi(z)$ from Eqs. (16.4) and (16.5) when substituted in Eqs. (16.1) and (16.2), the following stresses are obtained:

$$\sigma_x = \sigma_x^\infty \tag{16.6}$$

$$\sigma_y = 0 \tag{16.7}$$

$$\tau_{xy} = 0 \tag{16.8}$$

Equations (16.6), (16.7) and (16.8) accurately describe the state of stress at arbitrary point $\mathbf{P}(x, y)$ in an infinite plate without any discontinuity.

Complex potential functions from Eqs. (16.4) and (16.5) when substituted in Eq. (16.3), the following forces are obtained:

Table 16.1 Body force values for four divisions of the imaginary circle

Body forces	P_{x1}	P_{y1}	P_{x2}	P_{y2}	P_{x3}	P_{y3}	P_{x4}	P_{y4}
Numerical values	500	0	−500	0	−500	0	500	0

$$P_x = \sigma_x^\infty \cdot [y_B - y_A] \tag{16.9}$$

$$P_y = 0 \tag{16.10}$$

Body forces are computed for an infinite plate with unit thickness having a circular hole of 5 mm radius subjected to uniform tensile stress of 100 MPa. Table 16.1 shows numeric values of the body forces obtained from Eqs. (16.9) and (16.10), for four divisions of the imaginary circle.

16.4 Theoretical Results

In an infinite plane with thickness h, the stress in polar coordinates at an arbitrary point $z = x + i \cdot y$ due to concentrated load $P_x + i \cdot P_y$ acting at location $z = x_0 + i \cdot y_0$ is reproduced from Wang [13].

$$\sigma_r = -\frac{(3+v)}{4\pi h} \left(\frac{P_x \cos\theta + P_y \sin\theta}{r} \right) \tag{16.11}$$

$$\sigma_\theta = \frac{(1-v)}{4\pi h} \left(\frac{P_x \cos\theta + P_y \sin\theta}{r} \right) \tag{16.12}$$

$$\tau_{r\theta} = \frac{(1-v)}{4\pi h} \left(\frac{P_x \sin\theta - P_y \cos\theta}{r} \right) \tag{16.13}$$

Stress at arbitrary point $\mathbf{P}(x, y)$ is obtained by summing stresses (Eqs. 16.11–16.13) due to body forces obtained for Eqs. (16.9) and (16.10) and stresses due to applied load.

The expression for stresses in polar coordinates for an infinite plate with circular hole (Fig. 16.1a) is available in Timoshenko [12]. These equations are reproduced here from [12].

$$\sigma_r = \frac{\sigma_x^\infty}{2} \left(1 - \frac{a^2}{r^2} \right) + \frac{\sigma_x^\infty}{2} \left(1 + \frac{3a^4}{r^4} - \frac{4a^2}{r^2} \right) \cos 2\theta \tag{16.14}$$

$$\sigma_\theta = \frac{\sigma_x^\infty}{2} \left(1 + \frac{a^2}{r^2} \right) - \frac{\sigma_x^\infty}{2} \left(1 + \frac{3a^4}{r^4} \right) \cos 2\theta \tag{16.15}$$

$$\tau_{r\theta} = -\frac{\sigma_x^\infty}{2}\left(1 - \frac{3a^4}{r^4} + \frac{2a^2}{r^2}\right)\sin 2\theta \qquad (16.16)$$

16.5   Numerical Results

A plate with unit thickness having a circular hole of 5 mm radius is considered with an applied uniform tensile stress of 100 MPa. The radial, hoop and shear stresses along radial direction at angles 0°, 45° and 90° are computed using body force Eqs. (16.9) and (16.10) (legend BFM) and are compared with analytical results (Eqs. 16.14–16.16).

Figures 16.2, 16.3 and 16.4 show stresses along 0° radial line. Radial and hoop stresses show trends in line with the theoretical results.

Figures 16.5, 16.6 and 16.7 show stresses along 45° radial line. Radial, hoop and shear stresses show trends in line with the theoretical results. However, it is observed that the magnitudes of these stresses in the proximity of the circular hole deviate from theoretical values.

Figures 16.8, 16.9 and 16.10 show stresses along 90° radial line. Radial and hoop stresses show trends in line with the theoretical results.
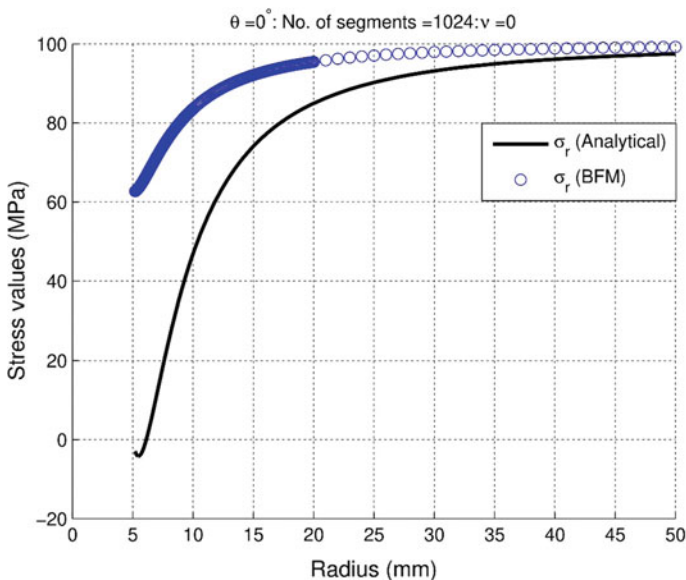
Fig. 16.2 Radial stress (σ_r) along radial line making 0° with x-axis, and circle is divided into 1024 divisions
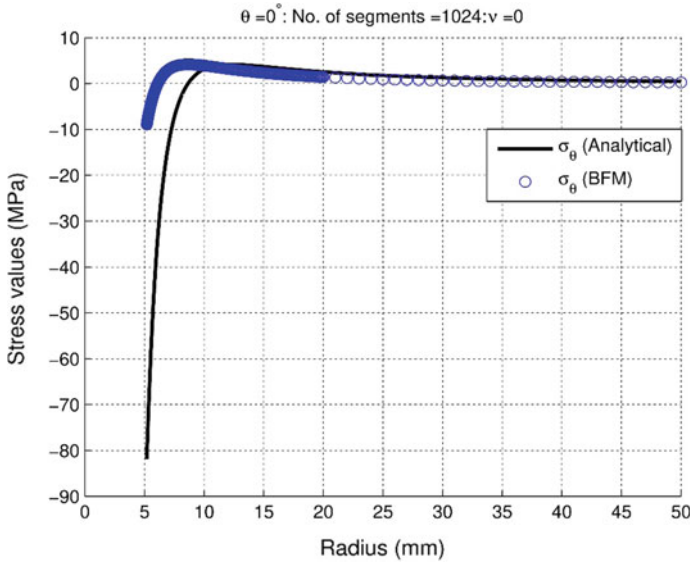
Fig. 16.3 Hoop stress (σ_θ) along radial line making $0°$ with x-axis, and circle is divided into 1024 divisions
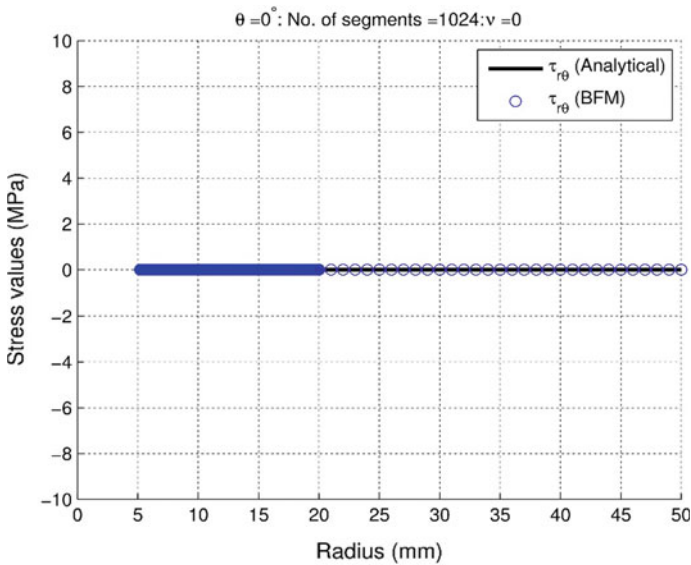
Fig. 16.4 Shear stress ($\tau_{r\theta}$) along radial line making $0°$ with x-axis, and circle is divided into 1024 divisions
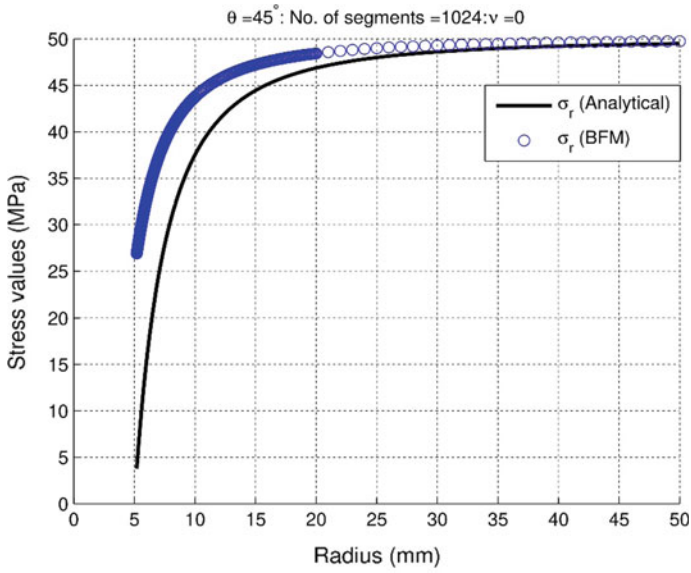
Fig. 16.5 Radial stress (σ_r) along radial line making 45° with x-axis, and circle is divided into 1024 divisions
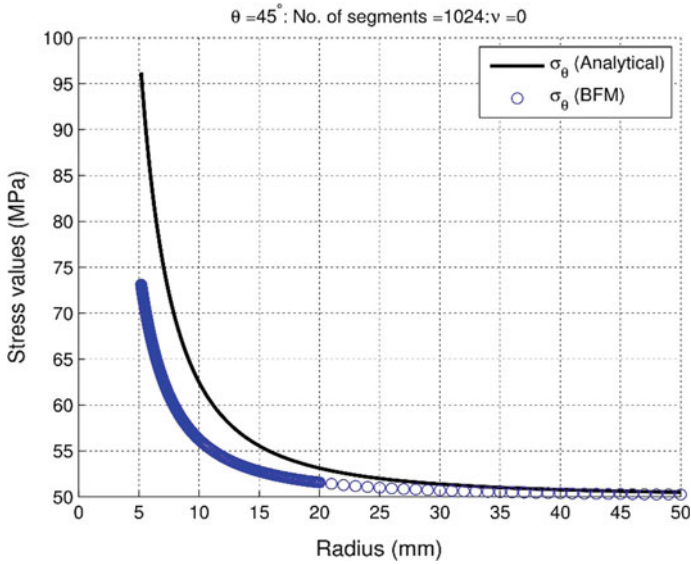
Fig. 16.6 Hoop stress (σ_θ) along radial line making 45° with x-axis, and circle is divided into 1024 divisions
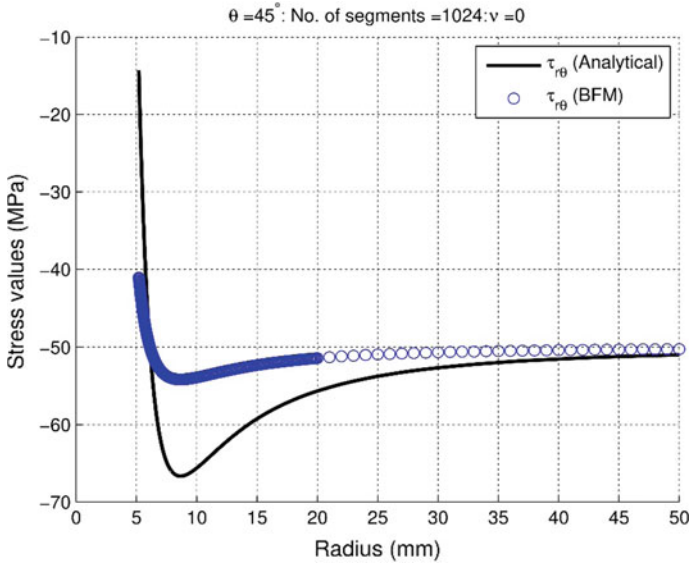
Fig. 16.7 Shear stress ($\tau_{r\theta}$) along radial line making 45° with *x*-axis, and circle is divided into 1024 divisions
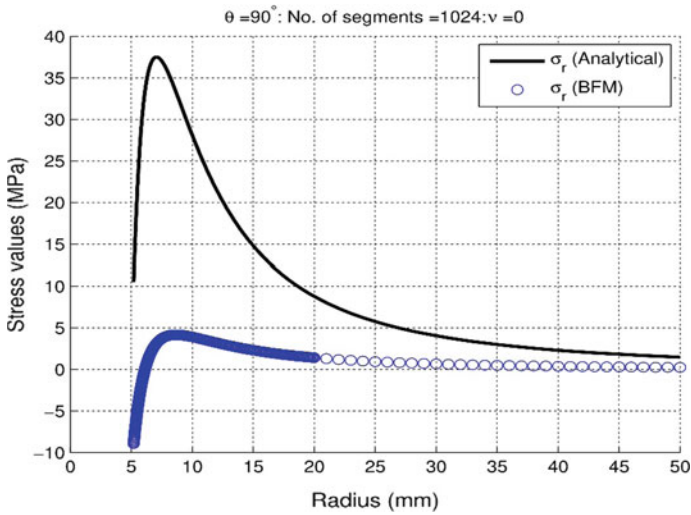
Fig. 16.8 Radial stress (σ_r) along radial line making 90° with *x*-axis, and circle is divided into 1024 divisions
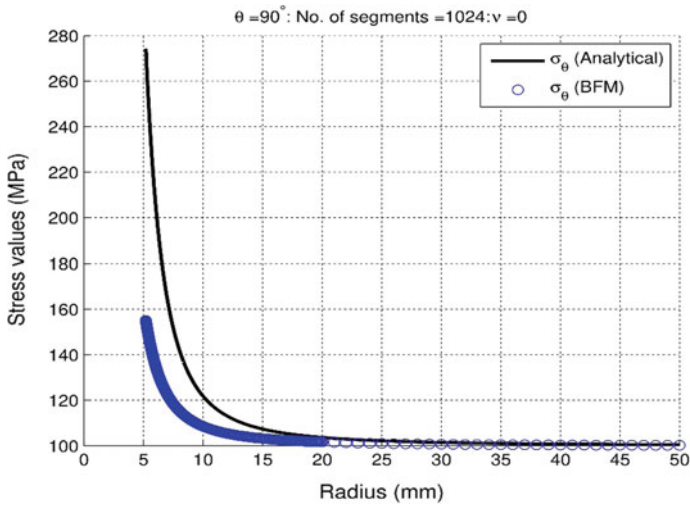
Fig. 16.9 Hoop stress (σ_θ) along radial line making 90° with x-axis, and circle is divided into 1024 divisions
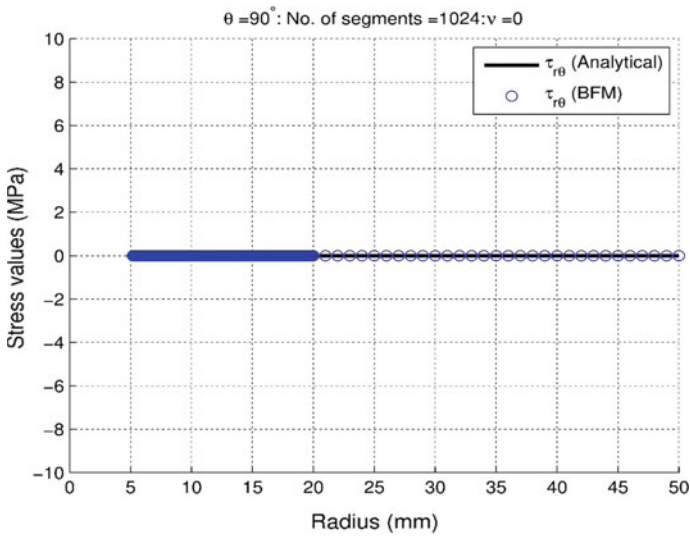
Fig. 16.10 Shear stress ($\tau_{r\theta}$) along radial line making 90° with x-axis, and circle is divided into 1024 divisions

Figures 16.11, 16.12 and 16.13 show radial, hoop and shear stresses along 0° radial line. Here, circle is divided into 1024 divisions, with Poisson's ratio (a) $\nu = 0$, (b) $\nu = 0.32$. It is observed that taking Poisson's ratio as zero has little effect on
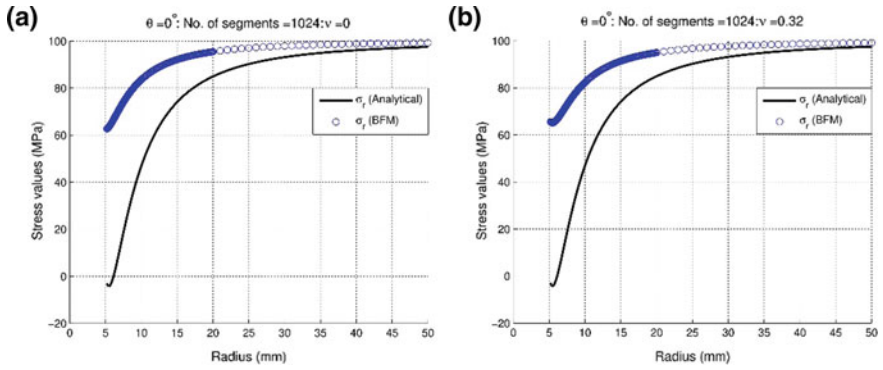
Fig. 16.11 Radial stress along radial line making 0° with *x*-axis, circle is divided into 1024 divisions, **a** $\nu = 0$, **b** $\nu = 0.32$
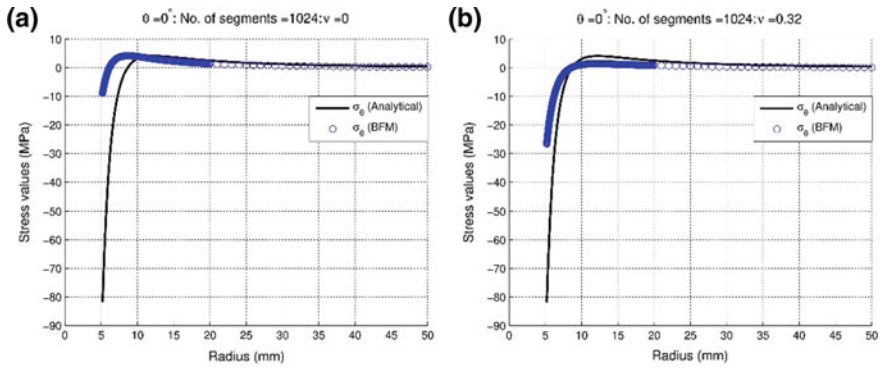
Fig. 16.12 Hoop stress along radial line making 0° with x-axis, circle is divided into 1024 divisions, **a** $\nu = 0$, **b** $\nu = 0.32$
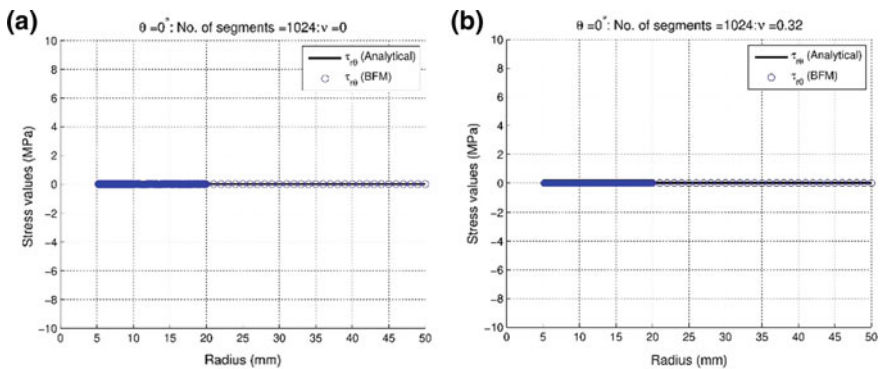
Fig. 16.13 Shear stress along radial line making 0° with *x*-axis, circle is divided into 1024 divisions, **a** $\nu = 0$, **b** $\nu = 0.32$

the radial and shear stresses. With nonzero Poisson's ratio, hoop stress shows little improvement in its trend towards theoretical results.

16.6   Conclusion

In this study, stress distribution is obtained by summation of stresses due to body forces derived from complex potential functions for a plate with uniform load in x-direction and stresses due to applied load (modified body force method). Results obtained from this method show trends in line with theoretical solution. However, numerical values obtained deviate from the theoretical solution. One of the possible reasons for this deviation in numerical values is that the boundary of the imaginary circle being stress-free may not be completely satisfied. Better results can be obtained when accurate estimates of the body forces on the boundary of the imaginary circle are made. Alternately, body forces obtained from a set of linear equations $Ax = b$ (body force method) can be used to obtain the stress distribution.

Modified body force method may be useful in the instances where theoretical results are unavailable and this method can give values of stresses approaching actual stresses.

As suggested by Nisitani [14], it is acceptable to take Poisson's ratio $\nu = 0$ since the marginal improvement in computed stresses is observed when nonzero Poisson's ratio is used.

References

1. Kirsch, E.G.: Die Theorie der Elastizität und die Bedürfnisse der Festigkeitslehre. Zeitschrift des Vereines deutscher Ingenieure **42**, 797–807 (1898)
2. Timoshenko, S.P., Goodier, J.N.: Theory of Elasticity, 3rd edn. McGraw-Hill, New York (1970)
3. Wang, C.-T.: Applied Elasticity, pp. 171–208. McGraw-Hill, New York (1953)
4. Kolosov, G.V.: On an application of complex function theory to a plane problem of the mathematical theory of elasticity. Doctoral thesis, Yuriev (1909)
5. England, A.H.: Complex Variable Methods in Elasticity, Dover edn. Dover Publications, Mineola, N.Y. (2003)
6. Muskhelishvili, N.I.: Some Basic Problems of the Mathematical Theory of Elasticity, 2nd edn. Noordhoff International Publishing, Leyden (1977). https://doi.org/10.1007/978-94-017-3034-1
7. Nisitani, H., Saimoto, A.: Short history of body force method and its application to various problems of stress analysis. Mater. Sci. Forum **440–441**, 161–168 (2003). https://doi.org/10.4028/www.scientific.net/MSF.440-441.161
8. Nisitani, H., Saimoto, A.: Effectiveness of two-dimensional versatile program based on body force method and its application to crack problems. Key Eng. Mater. **251–252**, 97–102 (2003). https://doi.org/10.4028/www.scientific.net/KEM.251-252.97

9. Manjunath, B.S., Ramakrishna, D.S.: Body force method for flamant problem using complex potentials. In: ASME Engineering Systems Design and Analysis, Volume 4: Fatigue and Fracture, Heat Transfer, Internal Combustion Engines, Manufacturing, and Technology and Society, pp. 99–103 (2006). https://doi.org/10.1115/esda2006-95303
10. Manjunath, B.S., Ramakrishna, D.S.: Body force method for melan problem with hole using complex potentials. In: ASME International Mechanical Engineering Congress and Exposition, Volume 10: Mechanics of Solids and Structures, Parts A and B: pp. 861–865 (2007). https://doi.org/10.1115/imece2007-42885
11. Manjunath, B.S.: Body force method in the field of stress analysis. Ph.D. thesis, Visvesvaraya Technological University, Belgaum (2009)
12. Nisitani, H., Chen, D.: Body force method and its applications to numerical and theoretical problems in fracture and damage. Comput. Mech. **19**(6), 470–480 (1997). https://doi.org/10.1007/s004660050195
13. Honein, T, Herrmann, G.: The Involution correspondence in plane elastostatics for regions bounded by a circle. J. Appl. Mech. **55**(3), 566–573 (1988). https://doi.org/10.1115/1.3125831
14. Nisitani, H.: Stress analysis of notch problem by body force method. In: Sih G.C. (ed.) Mechanics of Fracture 5, Sijthoff & Noordhoff, Chapter 1, pp. 1–68 (1978)
15. Chen, D., Nisitani, H.: Int. J. Fract. **86**(1–2), 161–189 (1997). https://doi.org/10.1023/A:1007337210078

Chapter 17
Wind Load Analysis of a Tall Structure with Sharp and Corner Cut Edges

Abhipsita Rej and **Amlan Kumar Bairagi**

Abstract The massive wind load is always harmful to tall building structure, especially the structure which has sharp edges. The separation of wind near the sharp edge creates local effects around the neighbor faces of the building and also creates enormous damage on that region. The present study illuminated the pressure variation around the sharp edge setback and corner cut setback tall building models. The models are inducted inside the computational domain and simulated with different wind angles. One model has a sharp edge corners and other models has a corner cut at the bottom part of setback zone and rounder corner at top part of setback zone. The considerable amount of pressure, drag and lift variation has been detected for across- and along-wind consideration. The tremendous amount of pressure fluctuation observed at corner cut region. The local pressure recognized on the wall due to sharp edges for the sharp edge model. However, the local pressure is minimized by the use of rounded edges at the top portion of the setback. The drag and lift coefficient decrease with the decrease of sharpness of edges. The study tries to catch the minimum local pressure due to corner cut edges of the tall building model.

Keywords Sharp and corner cut edge · Set back tall building · Pressure variation

17.1 Introduction

Wind effects are the challenges that designers have to deal with in super-tall building design. In association with high slenderness, low natural frequencies, low inherent damping level and high wind speed at upper lever, super-tall buildings are more susceptible to wind. Wind pressures on building surfaces result in both steady and

A. Rej (✉)
Department of Civil Engineering, Techno India University, Salt Lake, Kolkata, India
e-mail: abhipsit07@gmail.com

A. K. Bairagi
Department of Civil Engineering, Indian Institute of Engineering Science and Technology, Shibpur, Howrah, India
e-mail: bairagiak@gmail.com

unsteady loading, while air motion over and around buildings transports heat, mass and momentum. In this study, the method of corners cutting and setback condition is effective for the reduction of wind-induced vibrations in an across-wind, direction for high-rise buildings with a regular square plane. Wind forces acting on high-rise buildings with corner cuts in along-wind direction were measured by wind tunnel tests. During this study, Kawai [1] gave the concept of the corner modifications promote the instability at low speed. Tanaka et al. [2] determined the aerodynamic forces and wind pressures acting on the square-plan tall building models with various configurations like corner cut, setbacks and helical. Elshaer et al. [3] examined the aerodynamic shape optimization (ASO) example is to reduce the drag force acting on a tall building by changing the shape of its corners. Roy and Bairagi [4] illustrated the pressure variation and velocity around the multiple shape setback tall building. Mooneghi and Kargarmoakhar [5] reviewed the past/recent work on various aerodynamic mitigation techniques developed for reducing wind loads on buildings by modifying their shapes and/or adding simple architectural elements. Bairagi and Dalui [6, 7] conferred the pressure fluctuation at top roof of setback model and also highlighted the power spectral density (PSD) at neighbor faces of the setback and top roof. Alminhana et al. [8] modified corner cuts, reduce significantly the aerodynamic forces on the building structures and improve flow conditions near the building locations. The current research is based on the analytical method by computational fluid dynamics (CFD) where an isolate setback tall building is set inside the domain to estimate the dynamic behavior of setback corner cut tall building due to wind excitation. Horizontal pressure coefficient, drag and lift coefficients are observed for along different wind directions.

17.2   Description of Meshing and Model

In this study, the domain has been created using the concept of Frank et al. [9] according to which the inlet and the lateral and top boundary of the domain should be apart for 5 times of the overall height (5H) from the furthest point of the model on that side. The outlet of the domain should be at a distance of 15 times the overall height (15H) from the furthest point of the model on that side. The domain details are shown (see Fig. 17.1a). The meshing has been done to calculate the solution while the run is ongoing, in such a manner that the mesh can automatically be refined in locations that depends on specified adoption criteria, where solution variables are hanging most rapidly so that it can resolve the flow features in these regions. To avoid unusual flows inside the domain, tetrahedron meshing has been used and it is inflated near the boundary. By the use of this mesh, the regions near the boundaries can be made so inflated that the flows with unusual characteristics can be avoided. The meshing details are shown (see Fig. 17.1b).

The analytical model has been simulated by computational fluid dynamics (CFD) method. Two setbacks tall building model has same length: breadth ratio (1:1) and length: height ratio (1:4) has been adopted in this study. The models are square-plan
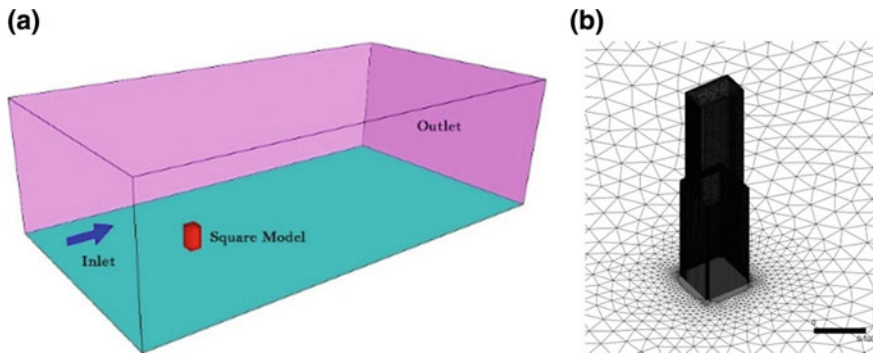
Fig. 17.1 **a** Model inside the domain and **b** meshing of corner cut model

shape and setback at half of the model height. The sharp edge model, namely M1 has setback level H/2 and setback distance 0.2L from both the opposite edges. Similar pattern model M2 has been considered but has a corner cut at the bottom part and the curve cut at the top part. The corner cut size has been demarcated by D1 and curved portion is R1. The attacking wind angle is 0° for along-wind direction and 90° for across-wind condition and an intermediate wind angle 45° also considered to observe the deviation of flow pattern around the model. The detail description of model M1 and M2 are shown (see Fig. 17.2a–b).
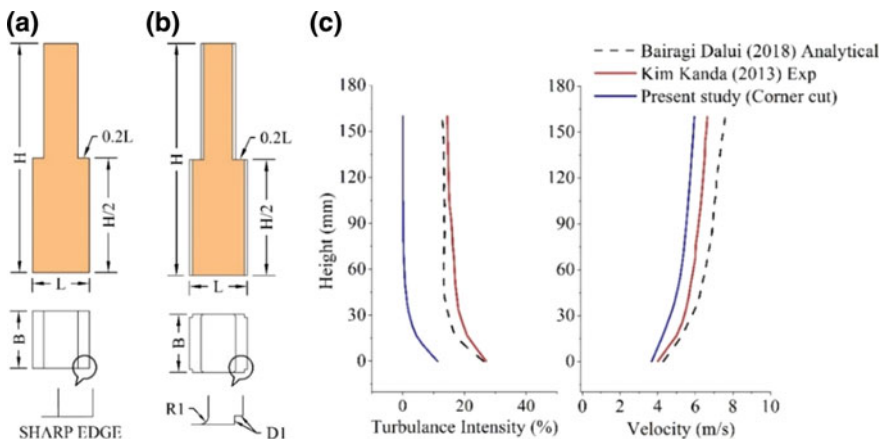
Fig. 17.2 Dimension of **a** model M1, **b** model M2 and **c** profile of velocity and turbulence inside the domain

17.3   Boundary Condition of the Domain

This study is conceived and analyzed by creating virtual domain and simulate the wind flow pattern around the model. The simulated flow conditions have been generated as per the criteria of terrain category two taken from IS 875 (part 3) [10]. The magnitude of inlet velocity has been considered normal to the boundary. Following the requirements of directional constraints, the flow direction was considered parallel to the normal of the surface of the boundary. The inlet and outlet are specified in the virtual domain. The sidewalls of this virtual domain are specified to be as free-slip wall in this study. The walls of both of the models are assumed no-slip walls with no surface roughness. In this study, power law has been used which is shown in Eq. (17.1), to calculate the velocity profile of the atmospheric boundary level in this CFD-based study.

$$V/V_z = (Z/Z_h)^\alpha \tag{17.1}$$

where V represents the speed of wind in horizontal direction at a certain elevation. V_Z represents the speed of the wind at a reference elevation Z_h. The value of V_z is taken as 10 m/s. The value of Z_h is taken as 1.0 m. α represents the coefficient of surface roughness 0.133 for terrain category 2.

17.4   Acceptance of Present Study

The numerical simulation used in the computational domain also validated with different researchers used by experimentally and analytically. The experimental study on sharp edge setback tall building was presented by Kim and Kanda [11] and conducted by Eiffel-type wind tunnel (1.8 m × 1.8 m × 12.5 m) at the University of Tokyo. The adopted factors are 1:400 scale, height of model 160 m, breadth of model 40 m and the power law exponent was 0.13, and the turbulence intensity was 15%. Wind speed at the tunnel was 6.5 m/s with 1.2% blockage ratio. Same size and same factors are considered and presented by Bairagi and Dalui [12, 13]. The present study also considered the same conditions for corner cut model and presented the profile of velocity and turbulence (see Fig. 17.2c).

17.5   Results

Two unconventional square setback tall building model, namely M1 and M2 have been simulated in a computational domain for 0°, 45° and 90° attacking wind. The pressure variation, drag and lift coefficients are observed and presented in this section.

17.5.1 Pressure Variation Around the Models

The pressure contours at different faces of both the models are conducted by using the formulas as stated in Eq. 17.2 and presented in Table 17.1.

$$C_p = C_{p(\text{cal})} / \left(0.5\, \rho V_z^2\right) \tag{17.2}$$

where C_p is the pressure coefficient, $C_{p(\text{cal})}$ is the pressure coefficient from the analytical data, ρ is the density of fluid at 25 °C and V_z is the velocity of wind at the particulate height. For along-wind condition, the windward face has positive pressure for both the models and suction at the sidewalls and leeward face. An interesting point comes out from the local pressure zone. The local pressure zone observed in the wall and to roof of setback part of model M1, but model M2 has minimum amount of wall and negligible amount of top roof. Therefore, it may be said that the local pressure depends upon the sharpness of the edge. The top setback part of the M1 model has a sharp edge, but the model M2 has curved edges. According to this condition, the flow pattern around the sharp edge of the model M1 has high amount of turbulence and create tremendous suction. On the other hand, the model M2 has curved edges at the top setback part, so the wind passed smoothly on that particular edge.

To understand the proper pressure fluctuation, horizontal pressure variation carried out in this study. A pressure belt considered at height 0.475H from the base of both the model M1 and M2. The initial pressure tapping point considered at the corner of face *A* and assumed a pressure belt around the model. The pressure variation of different azimuth is presented in (see Fig. 17.3). For 0° wind angle, the initial point at the corner of face A has 3.82% difference of suction with respect to M1 model. The high amount of suction detected at the corner cut region of M2 model as shown in Fig. 17.3a. In this zone, the pressure difference is 163% less than the M1 model. According to this analysis, it is clear that the large amount of suction developed at the corner cut region. At the same time, for 45° wind has less pressure fluctuation at the corner cut zone compare with M1 and M2 model. The similar amount of pressure difference observed for 90° wind angle.

17.5.2 Drag and Lift Coefficient

The drag and lift coefficient for both the models are calculated by using the equation as stated in Eqs. 17.3–17.4

$$F_d = 0.5\, \rho v_z^2\, C_d A \tag{17.3}$$

$$F_l = 0.5\, \rho v_z^2\, C_l A \tag{17.4}$$

Table 17.1 Comparison of pressure coefficient between M1 and M2 model for 0°, 45° and 90° wind angles

Wind angle	Model	Legend	Face A	Face B	Face C	Face D	Roof
0°	M1						
	M2						
45°	M1						
	M2						
90°	M1						
	M2						
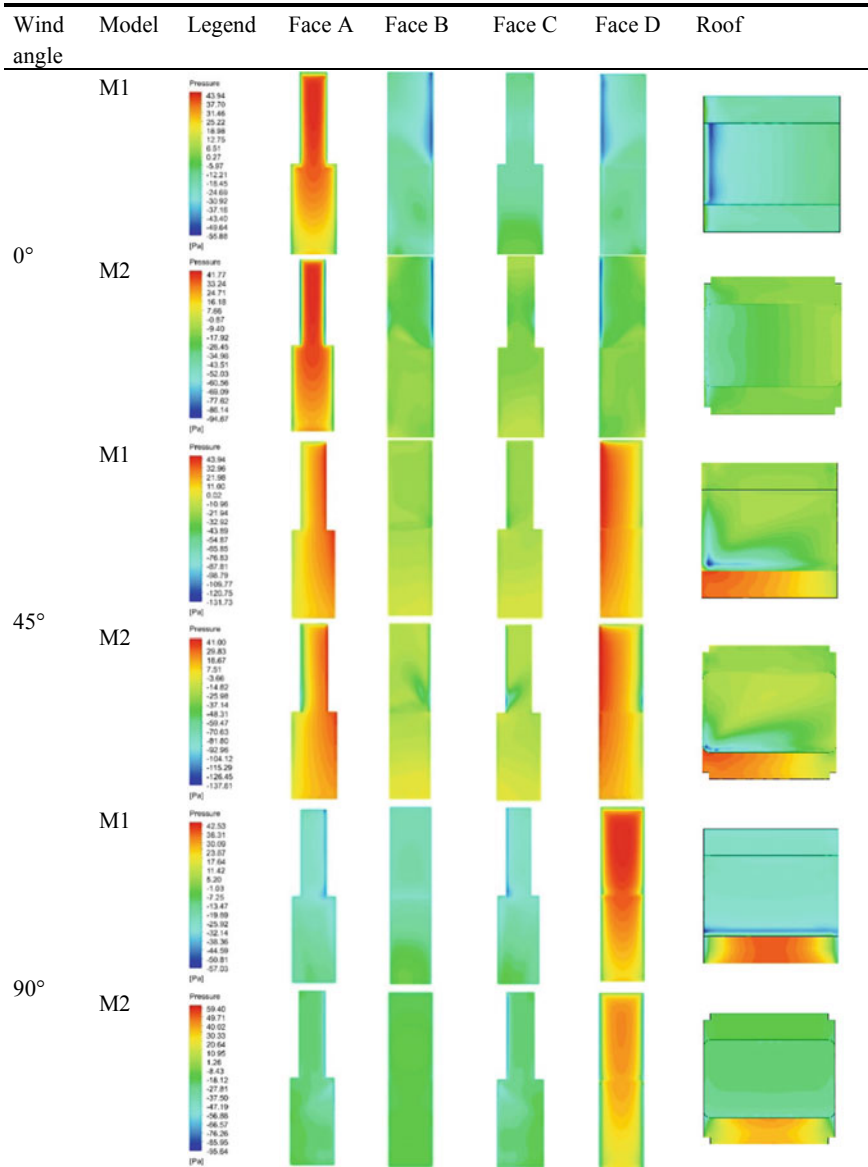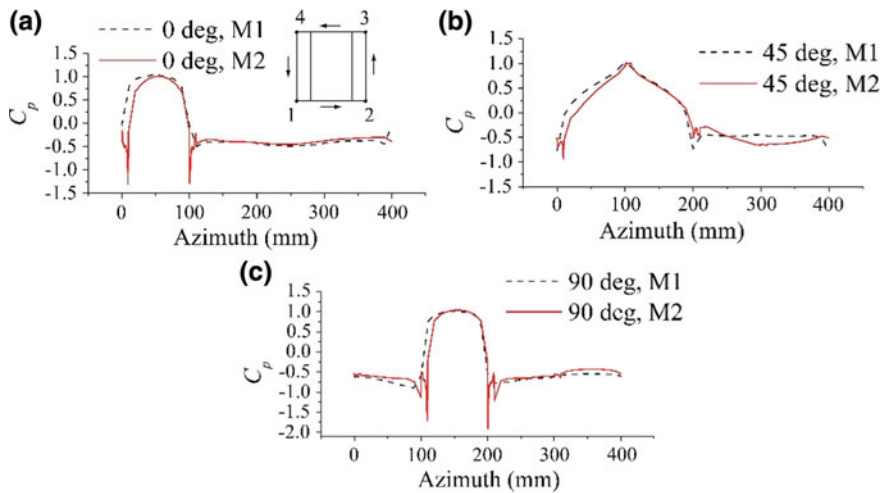
Fig. 17.3 Azimuth of pressure coefficient at 0.475H for **a** 0° wind, **b** 45° wind and **c** 90° wind angle

where F_d and F_l are drag and lift force, A is the attacking wind area of the model, C_d and C_l are the drag and lift coefficient. The comparative study of drag and lift force coefficient between M1 and M2 model showcased under (see Fig. 17.4). The maximum drag coefficient for model M1 is 1.06 for 0° wind and gradually decreasing with the increase of the wind angle. For 45° and 90° wind angle has 0.56 and −0.03, respectively, for M1 model as shown in (see Fig. 17.4). On the other hand, model M2 has 0.34, 0.23 and zero for the wind angle 0°, 45° and 90°. The lift coefficient values also vice versa, and the values also increasing with the increase of the wind angle. For 0°, the wind has minimum value and 90° has maximum value 1.17 for the M1 model as shown in (see Fig. 17.4). However, the M2 has a negative force coefficient for both the 0° and 45° wind angles. From the graphical representation of the drag
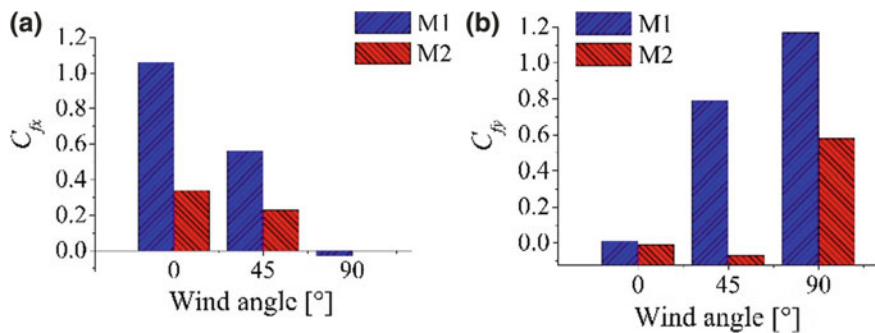
Fig. 17.4 **a** Drag and **b** lift coefficient on M1 and M2 model for 0°, 45° and 90° wind angles

and lift coefficient, it may be said that the corner cut model experienced less drag and lift forces compared with the sharp edge model.

17.6 Conclusion

The numerical simulation conducted in a computational domain to determine the pressure coefficient of different faces also drag and lift coefficients for different angles. After a number of iterations, the following conclusions are made.

As both the models are setback, so the top part of setback model has a different local pressure zone. The sharp edge model has high suction at this local pressure zone, but the corner cut model has curved zone at the top part of setback section, therefore, the wind passes smoothly at that corner. Due to this, the local pressure zone also decreases.

- High amount of pressure difference (163%) observed at the corner cut region at 0.475H distance from the base of the model. The pressure drop is due to the corner cut of the model.
- The drag coefficients are gradually changed from 1.06 to −0.03 and lift coefficient from 0.01 to 1.17 for sharp edge corner model. However, for corner cut model does not satisfy this rule.
- The drag and lift coefficients create a huge amount of variation on corner cut model compare to the sharp edge model.

References

1. Kawai, H.: Effect of corner modifications on aeroelastic instabilities of tall buildings. J. Wind Eng. Ind. Aerodyn. **74–76**, 719–729 (1998)
2. Tanaka, H., Tamura, Y., Ohtake, K., Nakai, M., Kim, Y.C.: Experimental investigation of aerodynamic forces and wind pressures acting on tall buildings with various unconventional configurations. J. Wind Eng. Ind. Aerodyn. **107–108**, 171–191 (2012)
3. Elshaer, A., Bitsuamlak, G., Damatty, A.E.: Aerodynamic shape optimization for corners of tall buildings using CFD. In: 14th International Conference on Wind Engineering, Porto Alegre, Brazil (2015)
4. Roy, K., Bairagi, A.K.: Wind pressure and velocity around stepped unsymmetrical plan shape tall building using CFD simulation—A case study. Asian J. Civ. Eng. (BHRC) **17**(8), 1055–1075 (2016)
5. Mooneghi, M.A., Kargarmoakhar, R.: Aerodynamic mitigation and shape optimization of buildings: Review. J. Building Eng. (2016)
6. Bairagi, A.K., Dalui, S.K.: Comparison of aerodynamic coefficients of setback tall buildings due to wind load. Asian J. Civ. Eng. Building Hous. **19**(2), 205–221 (2018)
7. Bairagi, A.K., Dalui, S.K.: Aerodynamic effects on setback tall building using CFD simulation. In: 2nd International Conference on Advances in Dynamics, Vibration and Control (ICADVC-2018). pp. 381–388. NIT Durgapur (2018)

8. Alminhana, G.W., Braun, A.L., Loredo-Souza, A.M.: A numerical study on the aerodynamic performance of building cross sections using corner modifications. Lat. Am. J. Solids Struct. **15**(7), e88 (2018)
9. Franke, J., Hirsch, C., Jensen, A., Krüs, H., Schatzmann, M., Westbury, P., Miles, S., Wisse, J., Wright, N. G.: Recommendation on the use of CFD in wind engineering. COST Action C14. Impact of Wind and Storm on City Life and Built Environment. Von Karman Institute for Fluid Dynamics (2004)
10. IS: 875 (Part-3), Indian standard code of practice for the design loads (other than earthquake) for buildings and structures (part-3. wind loads). Bureau of Indian Standards, New Delhi, India (2015)
11. Kim, Y.C., Kanda, J.: Wind pressures on tapered and set-back tall buildings. J. Fluids Struct. **39**, 306–321 (2013)
12. Bairagi, A.K., Dalui, S.K.: Aerodynamic effects on setback tall building using CFD simulation. Int. J. Mech. Prod. Eng. Res. Dev. 413–420 (2018)
13. Bairagi, A.K., Dalui, S.K.: Comparison of pressure coefficient between square and setback tall building due to wind load. In: SEC18: Proceedings of the 11th Structural Engineering Convention—2018, Jadavpur University, Kolkata, India (2018)

Chapter 18
Comprehensive Characterization of Carbon Fiber-Reinforced Epoxy Composite for Aerospace Application

D. Bino Prince Raja, B. Niharika, R. S. Manoj Kumar and C. G. Tejaswini

Abstract Carbon fiber-reinforced polymer (CFRP) is used in the aeronautical industry in the manufacture of different aircraft components. This paper is about studying the mechanical (tensile, flexural, interlaminar shear strength), thermal and moisture characterizations of the laminate. A carbon-reinforced polymer laminate of G939 material and 913 resin systems are selected to study the effect of moisture and thermal on the properties of the laminate. The composite lamina is made of different layer orientations like 0°/90°, 0°/45°, 0°/45°/90°, 0°/0° and 90°/90°. The laminate is fabricated by vacuum bagging and cured using autoclave. Interlaminar shear strength (ILSS) was carried out for the specimens. Thermal degradation of CFRP is molecular deterioration as a result of overheating, and as the temperature increases the bonding between the molecules gets weaker and starts reacting with each other which results in the change of properties of composites. Laminates of 0–90 orientation are fabricated, and interlaminar shear strength (ILSS) at 50, 100 and 150 °C was carried out according to Dutch Institute for Norms (DIN) for the specimens. Micro cracks in the matrix are observed due to moisture diffusion. Five different test liquids are chosen: water, diesel, petrol, lubricating oil and acid in which specimens are immersed for 2 days, 5 days and 7 days. This work will help composite materials' designers and manufacturers in designing high strength composite parts for aerospace.

Keywords Carbon fiber · Epoxy matrix · Mechanical · Thermal characterization · Aerospace applications

18.1 Introduction

Composite materials are made up of two or more constituent materials to obtain a new material with the desired properties. Composite materials are being developed and made with two kinds of objectives: One is to enhance the material properties and performance efficiency and another to design materials with combinations of

D. Bino Prince Raja (✉) · B. Niharika · R. S. Manoj Kumar · C. G. Tejaswini
Department of Aeronautical Engineering, S.J.C. Institute of Technology, Bangalore, India
e-mail: binoaero87@gmail.com

desired properties [1]. Carbon fiber is used in industries where high strength and rigidity are required in relation to weight. We know that material density has a direct impact on its weight, and carbon fiber composite has a density two times less than aluminum and more than five times less than steel [2]. We have used carbon prepreg in which the resin system already includes the proper curing agent. Advantage of prepreg is it is less mess and less waste. In this paper, we have studied material, thermal and moisture characterization of CFRP laminate. Material characterization includes tensile, flexural and interlaminar shear strength. Interlaminar shear strength is the stress existing between layers of a laminated material [3]. Flexural test is done to know the bending strength of the laminate; it is the maximum stress acting on the outermost fiber of the laminate. Tensile test is done to determine the maximum load that a material can withstand. When moisture diffuses into the material, the strength of the material is decreased and fiber/matrix is degraded which results in the decrease of glass transition temperature [4].

A large share of growing market value is accounted for composites which are being used in both military and commercial applications of aeronautics. Nowadays, in the aeronautical industry, carbon fiber-reinforced polymer (CFRP) offers significant improvements over current conventional materials [5]. Different structural components are manufactured by composite materials due to their attractive specific mechanical properties [6]. When compared with metallic materials, polymeric composites have high strength to weight ratio, hence CFRP is processed using thermoset polymers, especially epoxy resins [7]. The bonding material that allows the fabric to form a composite material is the resin. Resin is a type of matrix which acts as a medium to transfer load. We have used carbon prepreg in which resin is pre-impregnated, and it is ready to use in the component. The resin system used is typically epoxy. Interlaminar shear strength is the stress acting between layers of a laminated material; usually, it is performed to characterize both fiber and matrix interfacial bonding [8]. Flexural test is done to know the bonding strength of the laminate, and it is the maximum stress acting on the outermost fiber of the laminate. And it is an important tool for optimization of process and evaluation of matrices and fiber resin interface. In order to verify specifications, quality assurance of project and also analysis of failure mode, tensile tests are carried out [9]. Moisture content is absorbed by epoxy resins from their surroundings which results in the decrease of glass transition temperature, Tg: typically 1% absorbed water reduces the glass transition temperature by 20 °C [9]. The result at elevated temperature strength and stiffness of resin is being reduced [9]. Thermal degradation is the process which is caused due to heat and chemical properties of a substance and changes due to temperature, and as the temperature increases the bonding between the molecules gets weaker and starts reacting with each other which results in the change of properties of composites. The result of physical and chemical changes composite degrades with environment [10, 11].

18.2   Experimental Work

18.2.1   Preparation of Material

The prepreg used in this work is HEXPLY G939, bidirectional (BD) material with 913 epoxy matrix system which is widely used in the fabrication of high strength composite materials. 913 epoxy matrix systems can be processed using a wide range of techniques.

18.2.2   Fabrication of Laminate

To fabricate composite laminate, consider material of size 200 × 200 mm which is prepared with different layers of orientation. A flat plate was considered as a base, and followed by vacuum bagging procedure the laminate was cured at 135 °C using autoclave. After completing the curing cycle, laminate was demolded and trimmed for extra part to required size. Now, the laminate is used for further testing process (Fig. 18.1).
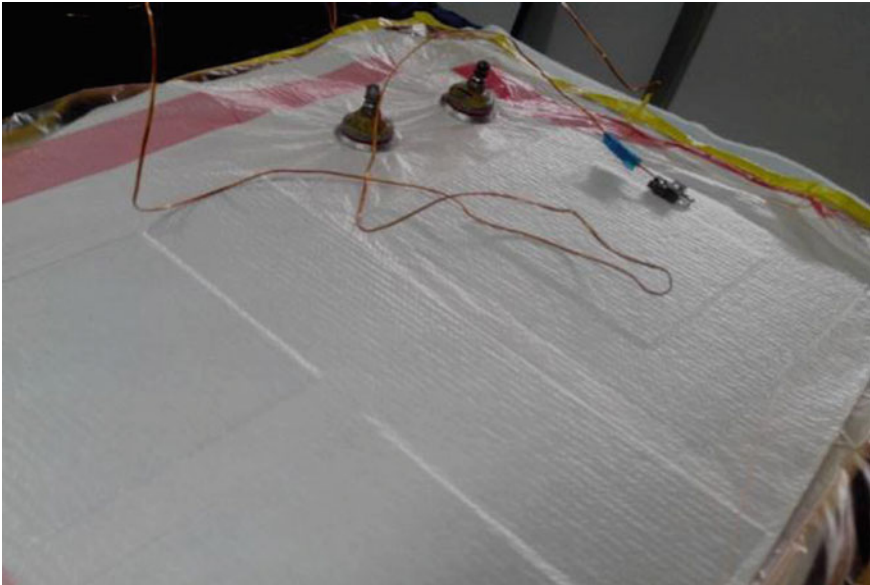
Fig. 18.1   Vacuum bag of laminates

18.3   Material Characterization of Composites

Five different orientations 0°/90°, 0°/45°, 0°/45°/90°, 0°/0° and 90°/90° were considered to study tensile, flexural and interlaminar shear strength (ILSS). The orientations and layers of the laminate are listed in Table 18.1.

18.3.1   Tensile Test

The tensile tests were performed according to ASTM D638 standard using a minimum of ten specimens (250 × 25 × 2 mm) for each laminate family. By bonding end tabs of carbon fiber/epoxy laminate, the specimens were prepared. The tests were carried out in an UTM (Fig. 18.2).

Table 18.1 Features of the layers and its orientations

Laminate No.	Orientation	0° layers used	90° layer used	45° layer used	Total no. of layers used
1	0/90	4	4	–	8
2	0/45	4	–	4	8
3	0/45/90	3	2	3	8
4	0/0	8	–	–	8
5	90/90	–	8	–	8

Fig. 18.2 Tensile test specimens

Fig. 18.3 Flexural test specimens

18.3.2   Flexural Test

This test was performed according to ASTM D790 standard. This is a bending test (three point loading) considering five samples ($100 \times 10 \times 2$ mm) for every laminate. The tests were carried out in an UTM at exact speed of 2 mm/min at room temperature (Fig. 18.3).

18.3.3   Interlaminar Shear Strength

The interlaminar shear tests (ILSS) were performed according to ASTM D2344 standard by considering five samples (short beam: $20 \times 10 \times 2$ mm) for every laminate. The tests were carried out in an UTM (Figs. 18.4 and 18.5).
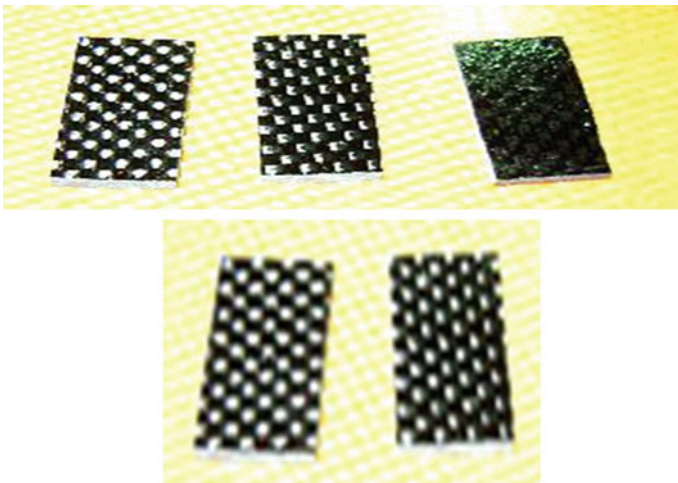
Fig. 18.4 ILSS test specimens

18.3.4 Thermal Degradation

Select the specimen of 0/90 orientation and cut the specimen (20 specimens) as per
ASTM D2344 standard for the ILSS test by increasing the atmospheric temperature.
Now take the five specimens, test in the room temperature using UTM (ILSS) setup
and note down the obtained values. Carry out the same procedure by taking 15 pieces
into three parts and increase the test chamber temperature to 50, 100 and 150 °C,
respectively. Now, calculate the percentage decrease in the strength of the material
as the temperature increases.

18.3.5 Moisture Test

Select the specimen of 90/90 orientation and test the cut down laminate into required
size as per ASTM D2344 standard. Then, weigh the specimen before dipping into
various atmospheric samples like water, petrol, diesel, acid and lubricating oil in the
room temperature and leave the specimen to absorb moisture for 2 days, 5 days and
7 days. Take out the specimens after the specified duration and weigh the specimens.
Now, compare the results of normal room temperature tested specimen with the
moisture absorbed specimens for 2 days, 5 days and 7 days (Fig. 18.6).

Fig. 18.6 Moisture test specimens

18.4   Results and Discussion

18.4.1   Material Characterization

18.4.1.1   Result of Tensile Test

Table 18.2 shows the mean outcome of tensile strength. The outcome obtained is according to ASTM D638 as represented. It is concluded that the 0°/90° orientation shows maximum strength, and comparison of different orientation with tensile strength is represented in Fig. 18.7.

Table 18.2 Tensile test values of the laminates studied

Sl. No.	Orientation	Tensile strength (Mpa)
1	0°/0°	887
2	90°/90°	945
3	0°/45°	857
4	0°/90°	1250
5	0°/45°/90°	998
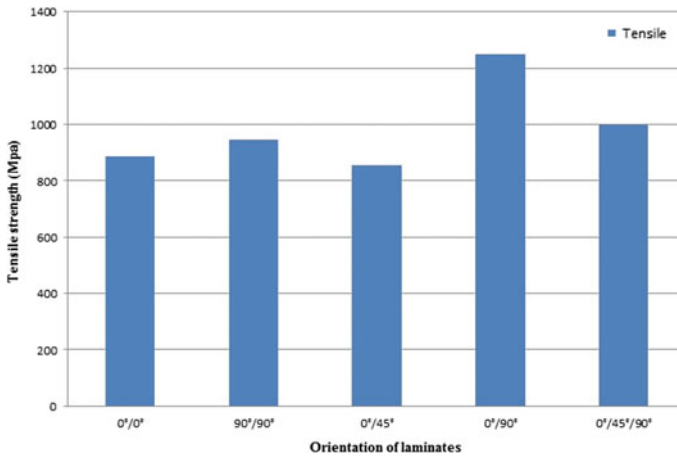
Fig. 18.7 Tensile values at different orientation

Table 18.3 Flexural values of the laminates studied

Sl. No.	Orientation	Peak load (N)	Flexural strength (Mpa)
1	0°/0°	374.36	844.313
2	90°/90°	341.04	835.101
3	0°/45°	390.00	671.26
4	0°/90°	284.20	859.33
5	0°/45°/90°	284.2	686.15

18.4.1.2 Result of Flexural Test

Table 18.3 shows the mean outcome of flexural strength. The outcome obtained is according to ASTM D790 standard. It is concluded that the 0°/90° orientation shows maximum strength, and comparison of different orientation with flexural strength is shown in Fig. 18.8.

18.4.1.3 Result of ILSS Test

Table 18.4 shows the mean results of ILSS. The outcome obtained is according to ASTM D2344 standard. It is found that the 0°/0° orientation shows maximum strength, and comparison of different orientations with ILSS is represented in Fig. 18.9.
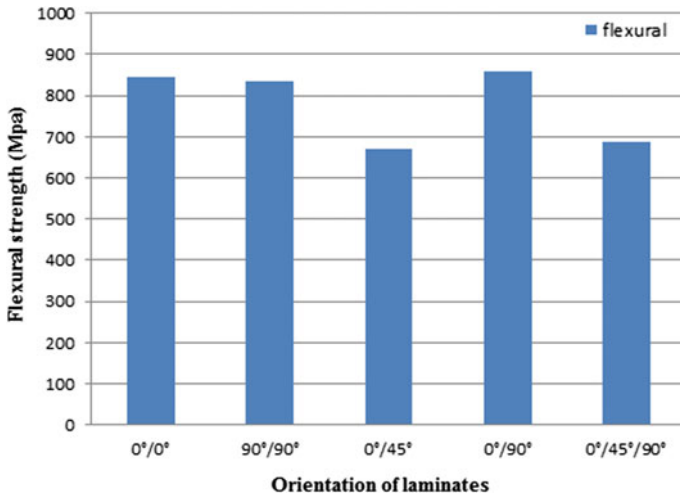
Fig. 18.8 Flexural values at different orientations

Table 18.4 Interlaminar shear values of the laminates studied

Sl. No.	Orientation	Load (kN)	Peak load (N)	ILSS (Mpa)
1	0°/0°	2.36	2365.62	81.20
2	90°/90°	2.31	2312.53	80.96
3	0°/45°	2.14	2144.73	74.00
4	0°/90°	2.52	2519.27	75.47
5	0°/45°/90°	2.21	2212.28	75.42
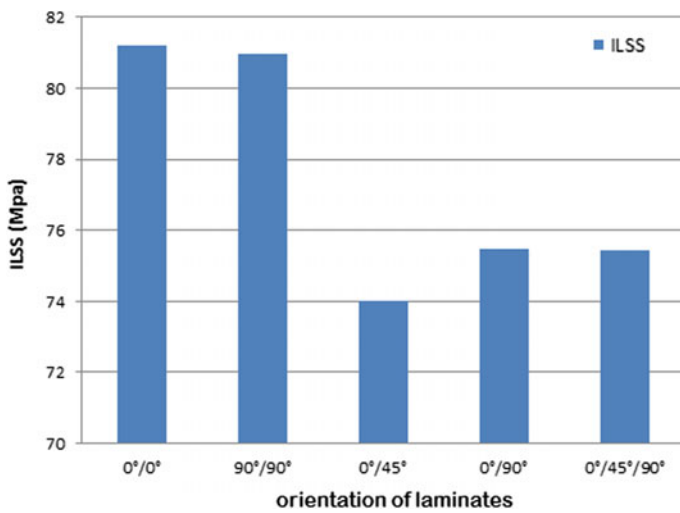
Fig. 18.9 ILSS values at different orientations
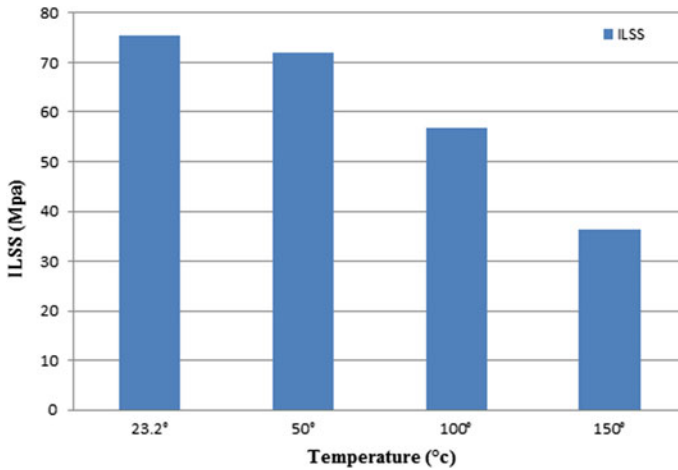
Fig. 18.10 ILSS values at different temperature conditions

Table 18.5 Interlaminar shear values of the laminates for thermal degradation

Sl. No.	Temperature in °C	Load (kN)	Peak load (N)	ILSS (Mpa)	Mode of failure
1	23.2 (room temperature)	2.52	2519.27	75.47	A
2	50	2.29	2288.63	71.85	A
3	100	1.84	1840.03	56.67	C
4	150	1.21	1207.77	36.17	C

A = Single shear; C = Plastic deformation

18.4.2 Thermal Degradation

The table below represents the mean outcome of interlaminar shear strength values for different laminates for thermal degradation. It is observed that as the temperature increases, the strength of the specimen decreases. Figure 18.10 represents variation of ILSS values at different temperatures (Table 18.5).

18.4.3 Moisture Test

The table below represents the average results of interlaminar shear strength values for studied laminates. Considering the ILSS results obtained in accordance with ASTM D2344 standard, it is observed that there is maximum decrease in strength

as the moisture content increases. And comparison of ILSS at different moisture conditions is represented in plot 4 (Fig. 18.11; Tables 18.6, 18.7 and 18.8).
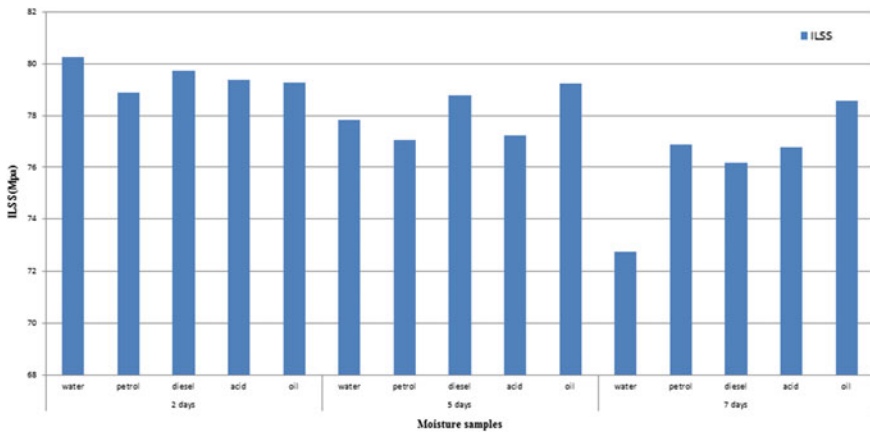
Fig. 18.11 ILSS values at different moisture conditions

Table 18.6 Moisture test values for 2 days

Sl. No.	Atmospheric environment	Load (kN)	Peak load (N)	ILSS (Mpa)
1	Water	2.32	2312.99	80.24
2	Petrol	2.30	2299.98	78.88
3	Diesel	2.26	2265.02	79.73
4	Acid	2.33	2327.84	79.37
5	Oil	2.29	2290.09	79.27

Table 18.7 Moisture test values for 5 days

Sl. No.	Atmospheric environment	Load (kN)	Peak load (N)	ILSS (Mpa)
1	Water	2.29	2292.62	77.81
2	Petrol	2.30	2298.64	77.07
3	Diesel	2.34	2338.65	78.79
4	Acid	2.32	2318.39	77.22
5	Oil	2.36	2358.81	79.25

Table 18.8 Moisture test values for 7 days

Sl. No.	Atmospheric environment	Load (mm)	Peak load (mm)	ILSS (Mpa)
1	Water	2.16	2158.67	72.76
2	Petrol	2.33	2328.16	76.89
3	Diesel	2.23	2211.99	76.18
4	Acid	2.31	2307.87	76.77
5	Oil	2.34	2344.70	78.57

18.5 Conclusion

- The composite laminate with 0°/90° orientation possesses maximum tensile strength of 1250 Mpa, which is higher than several other orientations of 0°/0°, 90°/90°, 0°/45° and 0°/45°/90°, respectively.
- The composite laminate with 0/90 orientation possesses maximum flexural strength of 859.33 Mpa, which is higher than several other orientations of 0°/0°, 90°/90°, 0°/45° and 0°/45°/90°, respectively.
- The composite laminate with 0/0 orientation possesses maximum ILSS of 81.20 Mpa, which is higher than several other orientations of 0°/0°, 90°/90°, 0°/45° and 0°/45°/90°, respectively.
- As the temperature increases, there is decrease in strength, and the laminate studied can withstand load up to 1207.77 N at 150 °C with ILSS of 36.17 Mpa.
- For the laminate studied, the ILSS decreased with an increase in the amount of absorbed moisture. The ILSS decreased by 80.24–72.76 Mpa for water, 78.88–78.81 Mpa for petrol, 79.73–76.18 Mpa for diesel, 77.22–76.77 Mpa for acid and 79.27–79.48 Mpa for oil.

References

1. Kennedy, G.J., Martins, J.R.R.A.: A comparison of metallic and composite aircraft wings using aero structural design optimization
2. Shivakumar, S., Guggari, G.S.: Literature review of fiber reinforced polymer composites. Int. J. Adv. Eng. Technol. (IJAET) **1**(5), 218–226
3. Bino Prince Raja, D., Stanly J.R., Antony Samuel Prabu, G., Alagu Sundaram, A.: Mechanical, morphological and thermal characterization of hybrid bamboo/glass fibre reinforced polyster composites. Rasayan J. Chem. **11**(3), 990–998 (2018)
4. Ryan, J.M., Adams, R., Brown, S.G.R.: Moisture Ingress Effect on Properties of CFRP. Material Research Centre
5. Bino Prince Raja, D., Stanly J.R., Shukla, M.: Analysis of mechanical properties of hybrid bamboo/jute fiber reinforced vinyl ester composite materials. Int. J. Mech. Eng. Technol. **8**(10), 318–324 (2017)
6. Trapani, J.R., Milan, M.T., Spinelli, D., Bose, W.W.: Mechanical performance of carbon-epoxy laminates. Mat. Res. **9**, 115–120 (2006)

7. Shabbier, K.P., Murtaza, M.A.: Optimization of aircraft wing with composite material. **2**, ISSN: 2319-8753
8. De Paiva, J.M.F., De Nadaidos Santos, A., Rezenda, M.C.: Mechanical and morphological characterization of carbon fiber fabric reinforced epoxy composites used in aeronautical field. Mat. Res. **12**, 367–374 (2009)
9. De Paiva, J.M.F., Mayer, S., Rezende, M.C.: Comparison of tensile strength of different carbon fabric reinforced epoxy composites. Mat. Res. **9**, 83–89 (2006)
10. Jhosi, O.M.: The effect of moisture on the shear properties of carbon fiber. Compos. Butterworth **14**(3), 196–200 (1983)
11. Go, S.H., Hong, S.W., Kim, H.G., Kwae, L.K.: A study on the degradation of mechanical properties for the carbon composites at a high temperature and high humidity of environment. ISOR J. Mech. Civ. Eng. (IOSR-JMCE) **13**(15), 17–24 (2016)

Chapter 19
Design and Simulation of Single-Axis MEMS Accelerometer for Low Acceleration Applications

K. J. Rudresh, Kin Gopalakrishna, K. Bharath Gowda, R. Harshith Gangatkar and Hemanth Kumar

Abstract This work involves the design of a MEMS single-axis capacitive-type accelerometer for low acceleration applications. In this paper, the displacement amplification complaint mechanism (DaCM) is used to increase sensitivity of the device by amplifying displacement. The DaCM model was designed using graphical method, and ANSYS tool is used to compare the displacement results. The DaCM model with maximum displacement is integrated with capacitive-type accelerometer. This integration was done using Coventerware turbo tool. The results obtained were compared with the accelerometer without DaCM. The displacement values that were obtained with and without DaCM are $3.1e{-}1$ and $4.2e{-}2$ μm, respectively. The results prove that DaCM gives an improved sensitivity.

Keywords MEMS · DaCM · Capacitance

19.1 Introduction

Microelectro mechanical systems (MEMS) had been a fast-growing technology. MEMS devices can act both as sensors and actuators. Some of the widely used MEMS devices are microphone, gyroscope, accelerometers, etc. MEMS accelerometers are sensing devices used for the detection of acceleration. Capacitive-type accelerometers are the most commonly used. It consists of proof mass and interdigitated fingers for capacitive sensing. When acceleration is applied to the proof mass, it displaces. There will be a change in distance (d) or area (A) between any sensing fingers. When one of the parameter changes, the capacitance also changes. Capacitive-type

K. J. Rudresh (✉)
Department
of Electronics and Communication Engineering, Nitte Meenakshi Institute of Technology, Bangalore, Karnataka, India
e-mail: kjrudresh@gmail.com

K. Gopalakrishna · K. Bharath Gowda · R. Harshith Gangatkar · H. Kumar
Department of Mechanical Engineering, Nitte Meenakshi Institute of Technology, Bangalore, Karnataka 560064, India

accelerometers have advantages [1], like high sensitivity, good noise performance, low-temperature sensitivity and low power dissipation. All the fingers in capacitive type are connected parallel, and if the number of capacitors is increased, then this increases the sensitivity [2]. Capacitive-type accelerometers can be used for low g sensing ranging from 2 µg to several g's. Some of the examples for low g sensor applications are structural health monitoring, border infiltration, earthquake detection, etc.

For low g applications since the acceleration that is applied is very low, displacement is also low. In order to improve the device sensitivity, amplification is required. There are two types of amplification: mechanical amplification and electronic amplification. Researchers had found how mechanical amplification is preferred over electronic amplification [3]. Mechanical noise is less compared to electronic noise [3]. There are many types of mechanical amplification like force amplification and displacement amplification. Force amplification has been explained in [4] and with an amplification of 11. Further researchers have taken the idea of displacement amplification to design a displacement amplifier. Displacement amplification was done with compliant mechanisms. Compliant mechanisms are those that transmit motion, force or energy by elastic deflection of flexural members. Displacement amplification compliant mechanisms (DaCMs) are single-input-single-output-type mechanism where an input displacement is applied at the input point which generates an amplified output at output point.

19.2 Design Methodology

This section explains about modelling of basic MEMS accelerometer and the design of DaCM using graphical method as well as modelling of integration of basic accelerometer with DaCM.

19.2.1 Modelling of Basic MEMS Accelerometer

When an accelerometer is subjected to acceleration, there is some force that is induced and this makes the accelerometer to vibrate in certain direction depending on the spring and damper. Due to this vibration, there is some displacement of proof mass. The mechanical sensitivity is defined as the displacement of the proof mass per unit gravitational acceleration, and sensitivity is given by capacitance per unit gravitational acceleration. The model of a spring-mass-damper system is shown in Fig. 19.1. The basic equation of the spring-mass-damper system is given by

$$m\ddot{x} + b\dot{x} + kx = F = ma \tag{19.1}$$
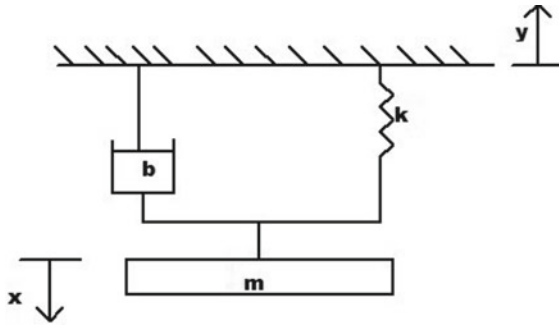
Fig. 19.1 Spring-mass-damper model of accelerometer

where m = proof mass, b = damping coefficient, k = spring stiffness, F = force, a = acceleration, x = displacement of proof mass.

19.3   Design of DaCM Using Graphical Method

Instantaneous centre method

Consider a rigid body in a plane having two points, and each point on the rigid body has different velocities. There will be point on the plane where there will be zero velocity, which makes the body to rotate about that point known as instantaneous centre of rotation. In order to compute this point, one has to draw a perpendicular line to the velocity and the point where both of them intersect; this is called instant centre point as shown in Fig. 19.2. The DaCM drawn using this method is shown in Fig. 19.3. By applying the instantaneous centre method, the DaCM was designed. The theoretical amplification of 16 was obtained. A solid model was drawn using solid edge and is shown in Fig. 19.4.

DaCM is a single member of flexure joints, whose required points are fixed. The designed model can be used for planar amplification that is for anyone of the single planar amplification. The input displacement and the output displacement are in the same direction. This DaCM design is integrated with a basic accelerometer for improving the sensitivity.

19.4   Modelling of Integrated Accelerometer with DaCM

The device is modelled using MEMS CAD tool called Coventerware turbo. The tool is used in 3D building of model and analysis of the accelerometer device. Here CoSolveEM which consists of mechanical domain and electrical domain analysis is used. All the electrodes and suspension ends are fixed, and acceleration of 1 g
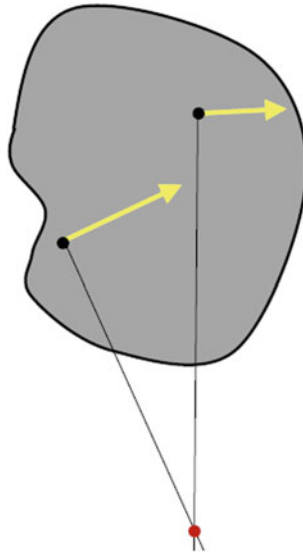
Fig. 19.2 Instantaneous centre method
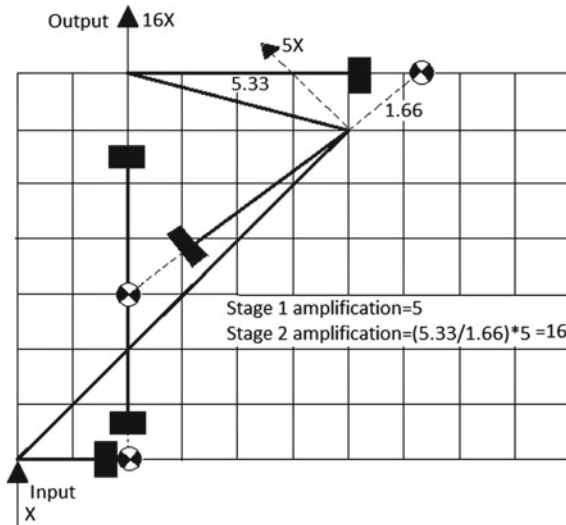
Fig. 19.3 Graphical design of DaCM

is applied in *y*-direction for the movable proof mass for mechanical domain. For electrical domain, 5 V is applied to the fixed electrodes and proof mass is connected to the ground.

Fig. 19.4 DaCM model using solid edge

The basic accelerometer model integration with DaCM is shown in Fig. 19.5. Here single crystalline silicon is used due to its properties like high melting point and low thermal expansion. The material has a density (*r*) of 2330 kg/m³, Young's modulus (*E*) of 137 GPa, relative permittivity (*v*) of 11.7 and Poisson's ratio (*m*) of 0.278. Dimensions of the model are shown in Table 19.1. The meshed model of
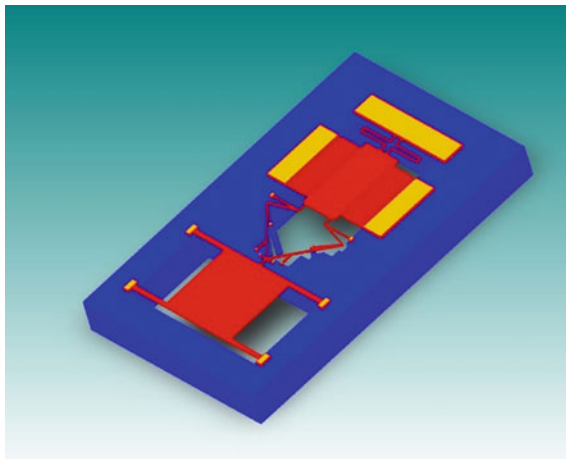
Fig. 19.5 Integrated accelerometer with DaCM

Table 19.1 Dimensions of integrated accelerometer model

Parameters	Length (μm)	Width (μm)	Thickness (μm)
Proof mass	1000	500	30
Fingers	10	300	30
DaCM spring suspension	50	500	30
DaCM proof mass	1000	1000	30
Folded beam suspension (one side)	1070	10	30
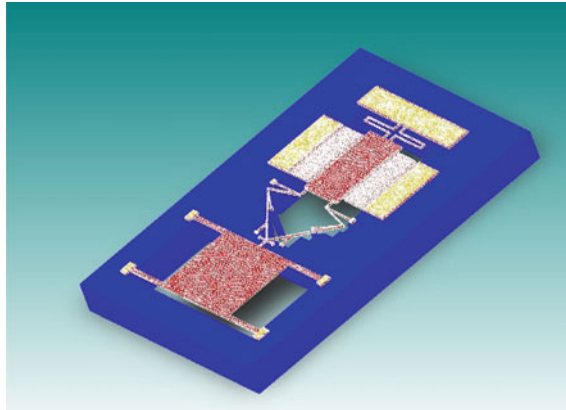
Fig. 19.6 Meshed integrated acceleration model

integrated accelerometer model is shown in Fig. 19.6.

19.5 Results and Discussion

ANSYS simulation of DaCM: The DaCM model that was designed graphically using instantaneous centre method was simulated using ANSYS tool by applying required boundary condition and suitable mesh size. The results obtained as shown in Fig. 19.7. There is a difference between theoretical graphical method and ANSYS as shown in Table 19.2. This difference is because of elastic losses in DaCM, mesh approximations done in ANSYS and some constraint that these tool uses to solve partial differential equations.

Displacement can be calculated using the basic formula

$$kx = ma ==\rightarrow x = ma/k \tag{19.2}$$

where x = displacement, m = mass, a = acceleration, k = stiffness.
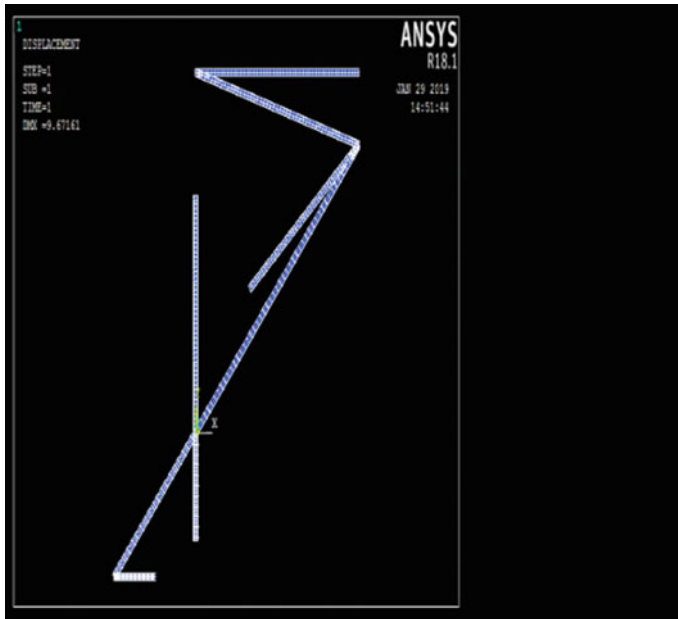
Fig. 19.7 ANSYS simulation

Table 19.2 Displacement amplifying factor comparison theoretical and ANSYS		Theoretical	ANSYS
	Displacement amplifying factor	16	9.5

Capacitance is given by

$$C = (\varepsilon A / d) N \quad \text{(general capacitance)} \tag{19.3}$$

where ε = permittivity, A = area, d = distance between the plates, N = number of fingers on both the sides.

Figure 19.8 shows the when 1 g of acceleration is applied on an accelerometer without DaCM, a maximum displacement of 4.8×10^{-2} mm is observed. The displacement in y-direction is 4.170842×10^{-2} mm. The variation of capacitance, displacement and sensitivity with respect to applied acceleration is shown in Table 19.3.

When the applied acceleration increases, the displacement increases and the capacitance decreases. But the differential capacitance increases. The capacitance observed for 1 g acceleration is 1.895073 pF. Table 19.4 shows the results for input values. The simulation result of MEMS-based capacitive accelerometer integrated with DaCM is shown in this section. The analysis of displacement and capacitance is obtained in Coventerware. When 1 g acceleration is applied, a displacement of
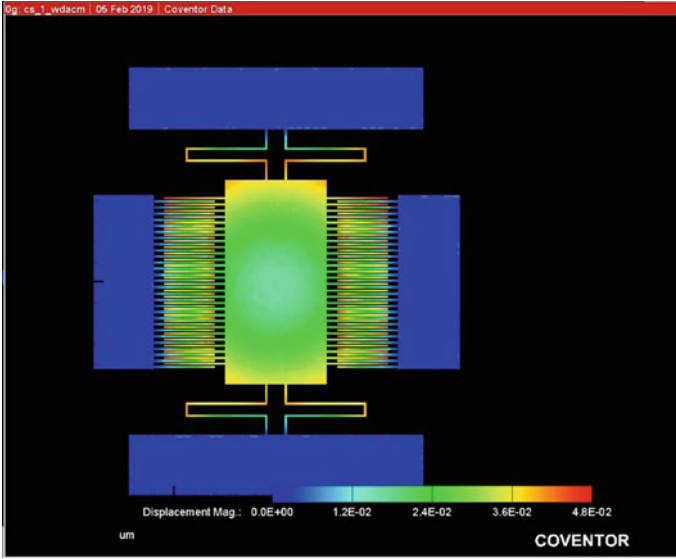
Fig. 19.8 Accelerometer without DaCM for 1 g

Table 19.3 Variation of displacement, capacitance and sensitivity with applied accelerations without DaCM

Acceleration (g)	Displacement (µm)	Capacitance (pF)	Sensitivity (pF/g)
0	0.03696418	1.884471	–
0.1	0.03743861	1.884468	18.84468
0.2	0.03791303	1.884465	9.422325
0.4	0.03886188	1.884460	4.711150
0.6	0.03981073	1.884455	3.140758
0.8	0.04075958	1.884449	2.355561
1	0.04170842	1.884444	1.884444

Table 19.4 Variation of displacement, capacitance and sensitivity with applied accelerations with DaCM

Acceleration (g)	Displacement (µm)	Capacitance (pF)	Sensitivity (pF/g)
0	0.08767009	1.895127	–
0.1	0.08767850	1.895121	18.95121
0.2	0.08768151	1.895116	9.47558
0.4	0.08769294	1.895105	4.7377625
0.6	0.08770437	1.895094	3.15849
0.8	0.08771580	1.859084	2.368855
1	0.08772723	1.895073	1.895073
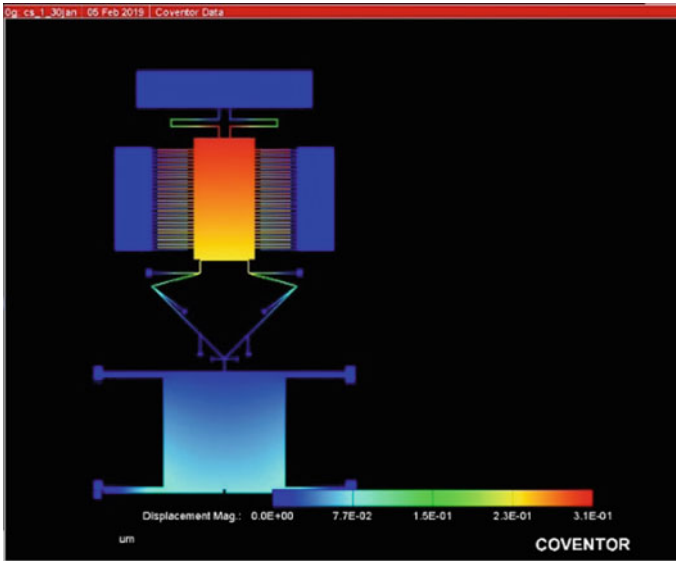
Fig. 19.9 Integrated accelerometer with DaCM for 1 g acceleration

8.772723×10^{-2} mm was observed in y-direction, and maximum displacement of 3.1×10^{-1} mm can be observed in Fig. 19.9.

On plotting for various accelerations, the values obtained for displacement vary linearly and this increases with g. The plot can be observed in Fig. 19.10. The plot is generated by acceleration versus capacitance.

One can observe from Fig. 19.11 that capacitance decreases with the increase in acceleration. On comparing the values from Tables 19.3 to 19.4, we can observe that displacement, capacitance and sensitivity are higher in case of accelerometer with DaCM (Table 19.5).

19.6 Conclusion

In this paper, single-axis MEMS accelerometer is designed, simulated and analysed for measuring low acceleration applications. The amplified displacement factor that is obtained theoretically and in ANSYS is 16 and 9.5, respectively. The results that were obtained from simulation of accelerometer with DaCM show that for 1 g acceleration; sensitivity of 1.895073 pF/g was achieved and without DaCM for 1 g acceleration; sensitivity of 1.88444 pF/g was achieved. The accelerometer model with DaCM gives higher displacement and sensitivity.
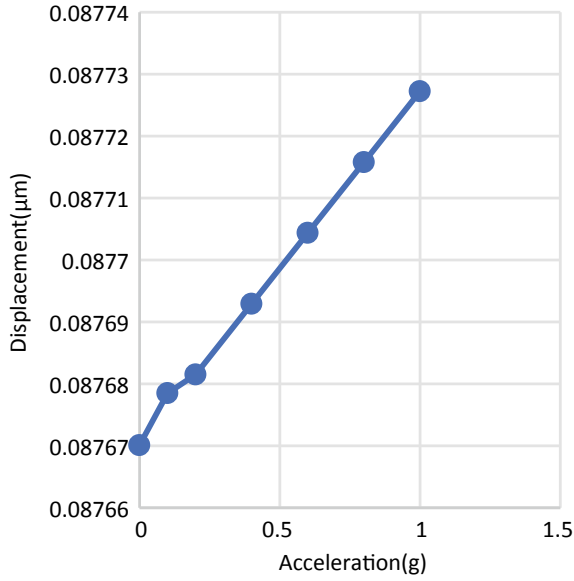
Fig. 19.10 Displacement versus acceleration
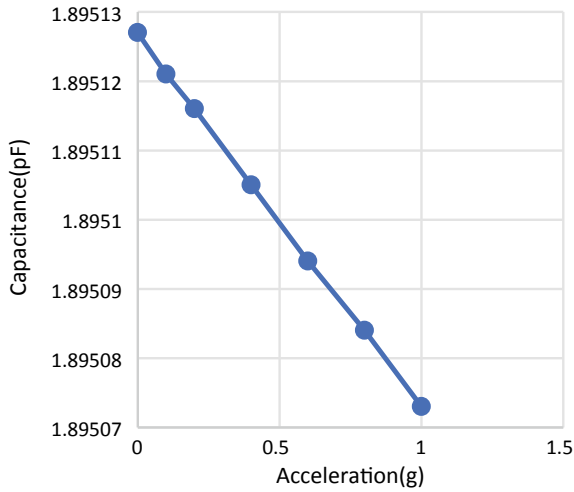
Fig. 19.11 Capacitance versus acceleration

Table 19.5 Comparison of displacement with DaCM and without DaCM

	Without DaCM	With DaCM
Maximum displacement for 1 g (mm)	4.8×10^{-2}	3.1×10^{-1}
Displacement in y-direction for 1 g (mm)	4.170842×10^{-2}	8.772723×10^{-2}

References

1. Pandey, K.P., Kumar, A.: Design and analysis of dual axis MEMS capacitive accelerometer. Int. J. Electron. Eng. Res. ISSN 0975-6450
2. Khan, S., Ananthasuresh, G.K.: A Micromachined Wide-Band In-plane Single-Axis Capacitive Accelerometer with a Displacement-Amplifying Compliant Mechanism. Taylor & Francis (2014)
3. Liu, C.: Foundations of MEMS. Pearson International Edition (2006). ISBN 0-13-199204-X
4. Mahalik, N.P.: MEMS, 3rd edn. Tata McGraw-Hill Publishers (2007). ISBN-13:978-0-07-063445-9

Chapter 20
Optimization of Neem Biodiesel Blend and Injection Pressure of CI Engine

C. Srinidhi, Sunil Panshetty, Madhusudhan and S. V. Channapattana

Abstract Current chapter focuses on the variation of injection of opening pressure at various engine loading conditions. The biodiesel chosen for experimentation was neem oil methyl ester, and it was blended with diesel at volumetric concentrations of 25, 50 and 75% to form B25, B50 and B75, respectively. The experimental results revealed that higher (280 bars) IOP leads to higher carbon dioxide emission and BTHE. The observations recorded were subjected to grey relation grade analysis for blend and injection pressure optimization. The GRG technique revealed that IOP of 280 bars and blend concentration of 25% is optimal.

Keywords Grey relation grade · NO_x · Blend of biodiesel · Injection opening pressure

20.1 Introduction

Compression ignition engines dictate the field of commercial transportation and agricultural machinery as they are known for their ease of operation and higher power competence to fuel consumption. Petroleum products or crude oil demand control the global economy as these are derived from fossil source. To this problem, many investigators have postulated fatty acid methyl esters (FAME) as possible alternate fuel for CI engines. This FAME commonly called as biodiesel bear similar thermophysical properties to that of biodiesel. Transesterification is the commonly inherited method for preparation of biodiesel from edible or non-edible oils [1–4].

C. Srinidhi (✉) · S. Panshetty
Department of Mechanical Engineering, Pune Vidyarthi Griha College of Engg and Technology, Pune, India
e-mail: srinidhi.campli@gmail.com

Madhusudhan
Department of Mechanical Engineering, Nitte Meenakshi Institute of Technology, Yelahanka, Bangalore, India

S. V. Channapattana
Department of Mechanical Engineering, D.Y. Patil College of Engineering, Ambi, Pune, India

Biodiesel is distinguished to three categories based on source of feedstock. If non-edible feedstock is used for preparation of biodiesel, then they are categorized as second-generation type and edible sources as first generation. Second-generation biodiesels are usually preferred as best possible feed stock as they do not raise fuel to food crises [5].

20.1.1   Experimental Analysis of Using Biodiesel

Researchers extensively worked on increasing usage of Biodiesel by altering various engine parameters like compression ratio (CR), fuel injection timing (FIP) and injection opening pressure (IOP) [6–8]. Looking at the current engine designs, diesel engine has fuel delivering systems which pressurize fuel to high pressures and later induce them in the combustion chamber. For such phenomenon, the current chapter focuses on the introduction of fuel injection pressure. For last few decades, research has been extensively carried out. But it is very much unclear that which blend of biodiesel and fuel injection pressure level suits best, which is yet to discovered. Studies indicate that incrementation of FIP has resulted in higher peak pressure and heat release rate [9–11]. Collaterally, the brake thermal efficiency also rises up making the NO_x emission to cross the threshold. [9–11] On the other hand, reducing the IOP leads to fall in BTHE and leads to higher CO and HC emissions [12, 13]. So, it is quite unclear that what should be the optimum injection opening pressure that has to set up for diesel engines to get better performance and lesser emissions [2].

20.1.2   Novelty

As there is no literature of actual optimal blend and IOP, current chapter provides an insight of optimization of parameters like blend percentage and injection opening pressure.

Experimental Methodology and Set-up: The current work is phased in two stages. In the first step, neem biodiesel is prepared by base catalytic transesterification process. KOH was used as a catalyst to reduce the operating temperature of the reaction [5]. In the next step, neem oil methyl ester (NOME) obtained is washed with demineralized water to remove extracts of excess KOH and methanol. The finally derived NOME is blended in volumetric proportions of 25, 50 and 75% with diesel. Finally, three test fuels are prepared which are ready to experimental test on CI engine. The experimentation was performed on a single-cylinder diesel engine. The engine standards are given in Table 20.1. The exhaust emissions were measured using a Naman-make analyser. The range and specifications are mentioned in Table 20.2

Table 20.1 Specifications of engine

Manufacture	Rocket Engg. Corpn. Ltd.
SFC	251 g/kWh
Rated power	4.8 kW @ 1500 RPM
Standard CR	17.5:1
Bore	87.5 mm
Stroke	110 mm
Injection timing	230 before TDC
Inlet valve open bTDC	4.5 bTDC
Exhaust valve open	35.5 bBDC
Inlet valve close	35.5 aBDC
Exhaust valve close	4.5 aTDC

Table 20.2 Device specifications and terminology

Device specification	Range	Accuracy	Uncertainties
Carbon monoxides (CO)	0–10.00%	$\pm 0.01\%$	± 0.1
Carbon dioxides (CO_2)	0–20.00%	$\pm 0.01\%$	± 0.15
Oxides of nitrogen (NO_x)	0–5000 ppm	± 1 ppm	± 0.2
Oxygen (O_2)	0–25.00%	$\pm 0.01\%$	± 0.1
Hydrocarbons (HC)	1–1500 ppm	± 1 ppm	± 0.2
Exhaust gas temp. (EGT)	0–500 °C	± 1 °C	± 0.1
Tachometer	0–10,000 rpm	± 10 rpm	± 0.2
Fuel flow metre	1–30 cc	± 0.1 cc	± 0.5
Pressure transducer	0–500 bar	± 1 bar	± 0.1

20.1.3   Design Factors and Response Variable

In design of experiment (DOE) technique, response fluctuations are unfamiliar function of the process variables, called as design factors. The three parameters considered for performance and emission study are braking torque, fuel blend percentage and injector pressure. The ranges implied are given in Table 20.3 (Table 20.4).

Table 20.3 Design factors and their levels

Design factor	Levels		
	1	2	3
Injector opening pressure (A)	200	240	280
Blend % (B)	25	50	75
Braking torque (C)	15	20	25

20.1.4 Results and Discussion

The test fuels were tested for their thermophysical properties and are given in Table 20.5. The procedure for testing these was as per ASTM standards.

20.1.5 Performance Characteristics

Brake Thermal Efficiency (BTHE): BTHE signifies the output power obtained to heat generated during combustion. Figure 20.1 plots the observations of BTHE at various IOPs and varying braking torques. It was observed that, as the IOP was incremented, the BTHE values also increased. The maximum BTHE value was recorded for B75 blend at engine parameter of 280 bar [4, 9–11, 14]. The calculation of S/N ratio was done on the basis of "higher the better". The regression equation obtained is (Table 20.6).

$$BTHE = 16.1 + 0.0174\,IOP + 0.398\,LOAD + 0.0257\,BLEND$$

Brake-Specific Fuel Consumption (BSFC): BSFC signifies the fuel consumed for a unit power derived. Also, for any alternative fuel, it would be desirous that the fuel consumption should be least. From figure, it was noted that the minimum and maximum BSFC values were recorded for B25 blend at 240 bars and B75 blend at 200 bar IOP, respectively [6, 7]. "Lesser the better" way was chosen for calculation S/N ratio of BSFC. The regression equation for the BSFC in regard to independent variables is (Fig. 20.2 and Table 20.7).

$$BSFC = 0.437 - 0.000183\,IOP + 0.000240\,BLEND - 0.00447\,LOAD$$

20.1.6 Emission Characteristics

Carbon Dioxide Emission (CO_2): Figure 20.3 illustrates the variation of CO_2 emission at various blends and IOPs. It was observed that as the blend concentration

Table 20.4 L9 orthogonal array containing experimental values as per Taguchi design

Expt. no	IOP	Blend	Load	O_2	CO_2	CO	HC	NO_x	BTHE	BSFC
1	200	25	15	14.8	8.27	0.1	102	66	26.032	0.343
2	200	50	20	11.8	10	0.3	135	89	29.46	0.312
3	200	75	25	7.06	8.93	0.2	141	101	31.594	0.306
4	240	25	20	13	10	0.1	110	95	30.328	0.295
5	240	50	25	12.6	14.3	0.1	115	121	30.283	0.304
6	240	75	15	17.4	9.56	0.1	119	81	26.79	0.361
7	280	25	25	12.4	12.6	0.1	103	132	30.778	0.29
8	280	50	15	17.4	8.64	0.1	86	79	27.884	0.33
9	280	75	20	21.5	7.73	0.1	102	114	32.607	0.297

Table 20.5 Properties of test fuels

Sr. no.	Properties	B100	B25	B50	B75
1	Density (kg/m^3)	912	831	856	891
2	Calorific value (MJ/kg)	36.72	40.3	39.16	37.21
3	Viscosity (cSt)	4.9	2.9	3.1	4.5
4	Flashpoint (°C)	182	91	118	149.25
5	Carbon residue	0.15	–	–	–
6	Cloud point (°C)	−1	–	–	–
7	Pour point (°C)	−8	–	–	–

Fig. 20.1 Variation of BTHE at various IOPs and torques

Table 20.6 Grey relation grade for BTHE

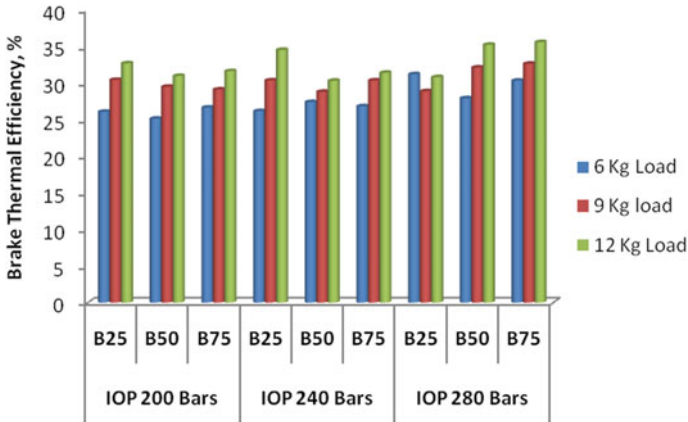| Sr. no.	Expt. readings of BTHE	Normalized S/N ratio of BTHE	Deviation sequences for BTHE	Grey relational coefficient BTHE	S/N ratio
1	26.0319	0	1	0.333333333	28.31011735
2	29.4596	0.549295373	0.450704627	0.525925704	29.38453691
3	31.5941	0.859921184	0.140078816	0.781153801	29.99211977
4	30.3283	0.678346981	0.321653019	0.608529377	29.63696135
5	30.2833	0.67175322	0.32824678	0.60368481	29.62406398
6	26.7901	0.127489701	0.872510299	0.364295991	28.55948669
7	30.7777	0.743668092	0.256331908	0.661085424	29.76472918
8	27.8843	0.305259653	0.694740347	0.418500975	28.90720402
9	32.6066	1	0	1	30.26611338
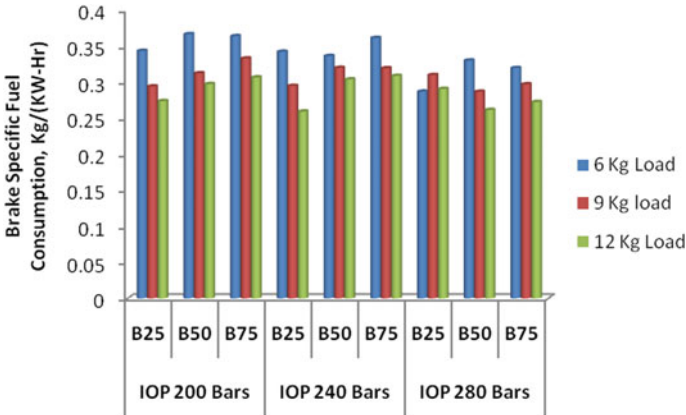
Fig. 20.2 Variation of BSFC at various IOPs and torques

Table 20.7 Grey relation grade for BSFC

Sr. no.	Expt. readings of BSFC	Normalized S/N ratio of BSFC	Deviation sequences for BSFC	Grey relational coefficient BSFC	S/N ratio
1	0.3431	0.7663	0.2336	0.6814	9.2901
2	0.312	0.3307	0.6692	0.4276	10.1169
3	0.3062	0.2455	0.7544	0.3985	10.2787
4	0.2945	0.0666	0.9333	0.3488	10.6182
5	0.3035	0.2054	0.7945	0.3862	10.3548
6	0.3611	1	0	1	8.8466
7	0.2902	0	1	0.3333	10.7447
8	0.3296	0.583	0.4169	0.5453	9.638
9	0.2967	0.1009	0.899	0.3573	10.5532

increased, the CO_2 percentage also increased. Also, the presence of incremental IOP evaluated the fact that IOP promotes better combustion of neem biodiesel-diesel blends. It is eminent that as biodiesel-diesel blends bear higher density and viscosity, it is better to inject these fuels at [15] higher IOP [11, 16]. The maximum CO_2 emissions were recorded for B75 blend at 280 bars. Also, "Higher the better" principle was used to calculate the S/N ratio of CO_2 emissions. The regression equation obtained is (Table 20.8)

$$CO_2 = 3.54 + 0.0074 \, \text{IOP} - 0.0310 \, \text{BLEND} + 0.312 \, \text{LOAD}$$

Carbon Monoxide Emission (CO): CO emission is regarded for any alternate fuel investigator as it highlights incomplete combustion of fuel. From Fig. 20.4, it was
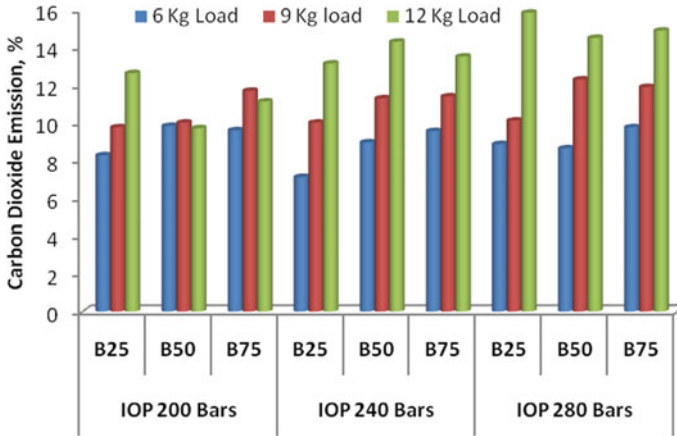
Fig. 20.3 Variation of carbon dioxide emission at various IOPs and torques

Table 20.8 Grey relation grade for carbon dioxide emission

Sr. no.	Expt. readings of CO_2	Normalized S/N ratio of CO_2	Deviation sequences for CO_2	Grey relational coefficient CO_2	S/N ratio of CO_2
1	8.27	0.890353697	0.109646303	0.820147678	18.35011019
2	8.96	0.580294157	0.419705843	0.543652086	20.00868155
3	7.87	0.765677364	0.234322636	0.680899615	19.01702918
4	10.01	0.580294157	0.419705843	0.543652086	20.00868155
5	8.77	0	1	0.333333333	23.11279268
6	11.7	0.654982614	0.345017386	0.591703802	19.60915785
7	11.13	0.201497538	0.798502462	0.385058954	22.03494148
8	10.45	0.819284292	0.180715708	0.734521026	18.73027485
9	13.52	1	0	1	17.76358988

observed that as the concentration of neem methyl ester increased, the percentage of CO emission also increased. This phenomenon leads to an understanding that neem biodiesel-diesel blends being denser and more viscous need better time for combustion [1, 12, 13]. Maximum CO emission was recorded for B75 blend at 240 bars of IOP and the least CO percentage at 240 bars for B25 blend [4]. "Smaller the better" principle was taken for calculation of S/N ratio. The regression equation for CO emission w.r.t. independent variables is (Table 20.9)

$$CO = 0.333 - 0.00125\,IOP + 0.00067\,BLEND + 0.00333\,LOAD$$
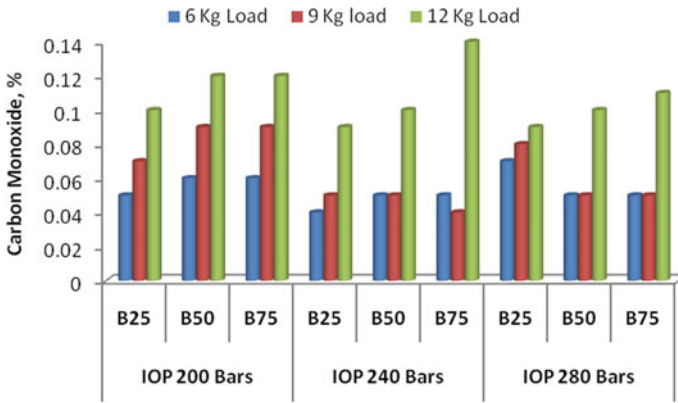
Fig. 20.4 Variation of CO emission at various IOPs and torques

Table 20.9 Grey relation grade table for CO emission

Sr. no.	Expt. readings of CO	Normalized S/N ratio of CO	Deviation sequences for CO	Grey relational coefficient CO	S/N ratio for CO
1	0.05	0	1	0.333333333	26.02059991
2	0.05	0.630929754	0.369070246	0.575327486	20
3	0.05	1	0	1	16.47817482
4	0.05	0	1	0.333333333	26.02059991
5	0.05	0.630929754	0.369070246	0.575327486	20
6	0.32	0	1	0.333333333	26.02059991
7	0.08	0.717684818	0.282315182	0.639128591	19.1721463
8	0.46	0	1	0.333333333	26.02059991
9	0.14	0	1	0.333333333	26.02059991

Unburnt Hydrocarbon Emission (HC): Emittents like HC coming out of engine exhaust signify the presence of incomplete burning of fuel [8, 17]. Figure 20.5 shows the variation of HC emission at various blend ratios and IOPs. It was noted that as the volumetric concentration of neem biodiesel in the blend increased, the amount of HC rose up. It shows that biodiesel combustion needs more time. Also, biodiesel-diesel blends have higher ignition lag which promotes the HC emission [1, 4, 12, 13]. Maximum HC emission was recorded for B75 blend at 240 bar and least HC for B25 blend at 200 bar. The presence of incrementation of IOP did not help in the reduction of HC. The regression equation for HC emission w.r.t. independent variables is (Table 20.10)

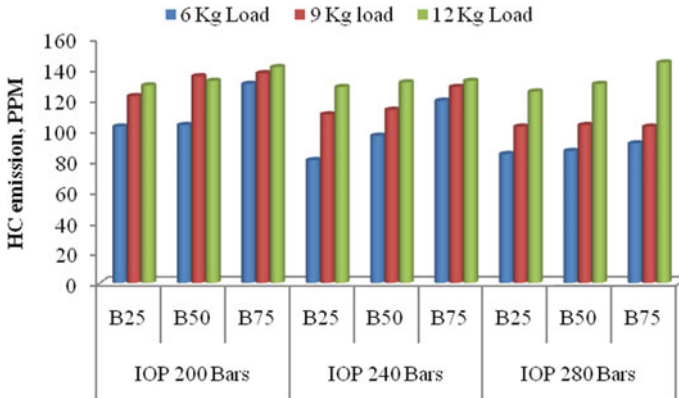$$HC = 149 - 0.363\,IOP + 0.313\,BLEND + 1.73\,LOAD$$

Fig. 20.5 Variation of HC emission at various IOPs and torques

Table 20.10 Grey relation grade for HC emission

Sr. no.	Expt. readings of HC	Normalized S/N ratio of HC	Deviation sequences for HC	Grey relational coefficient HC	S/N ratio for HC
1	102	0.654892454	0.345107546	0.591640676	40.17200344
2	96	0.087953083	0.912046917	0.354095883	42.60667537
3	91	0	1	0.333333333	42.98438225
4	110	0.502170712	0.497829288	0.501087717	40.8278537
5	86	0.41226248	0.58773752	0.459669719	41.21395681
6	137	0.34310695	0.65689305	0.432192068	41.51093923
7	100	0.635159593	0.364840407	0.57814135	40.25674449
8	140	1	0	1	38.68996902
9	119	0.654892454	0.345107546	0.591640676	40.17200344

Exhaust Oxygen (EO): Figure 20.6 demonstrates graphically the obtained exhaust oxygen at various loads and injection opening pressures. For biodiesel as fuel for combustion, the chemical structure itself contains embedded oxygen. The recording reveals that as the braking load increased, the amount of oxygen content decreased. Also, the amount of least oxygen was found for B50 blend at IOP of 200 bars. The presence of IOP helped in deriving higher EO. The presence of higher EO in exhaust signifies that the combustion occurring is complete in nature. This might be due to ignition delay. The amount of EO for B50 and B75 blends at IOPs 240 bars ad 280 bars almost showed the same trend. The regression equation obtained for EO with reference to independent variables is (Table 20.11)

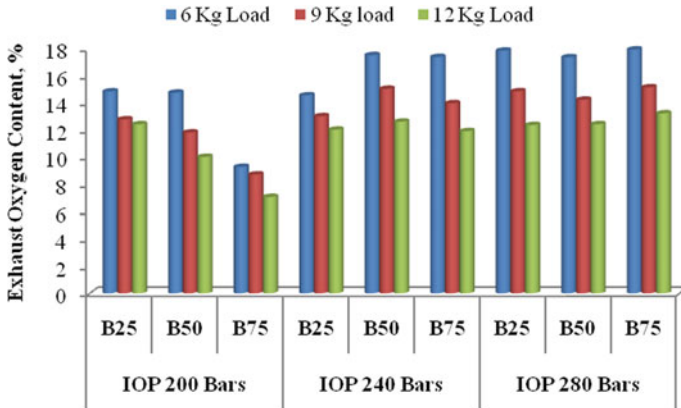$$EO = 6.54 + 0.0728\,IOP + 0.0380\,Blend - 0.585\,Load$$

Fig. 20.6 Variation of exhaust oxygen at various IOPs and torques

Table 20.11 Grey relation grade for exhaust oxygen

Sr. no	Expt. readings of O_2	Normalized S/N ratio of O_2	Deviation sequences for O_2	Grey relational coefficient O_2	S/N ratio of O_2
1	14.84	0.331788559	0.668211441	0.428004711	23.42867802
2	17.52	0.537212885	0.462787115	0.519325604	21.44499795
3	17.93	1	0	1	16.97609402
4	13	0.450859748	0.549140252	0.476580704	22.27886705
5	14.23	0.478257388	0.521742612	0.489360034	22.01430173
6	11.48	0.189675229	0.810324771	0.381584788	24.80099544
7	13.22	0.496269329	0.503730671	0.498141597	21.84036942
8	10.01	0.190710907	0.809289093	0.38188663	24.79099442
9	11.91	0	1	0.333333333	26.63259435

Oxides of Nitrogen (NO_x): Biodiesel-diesel blends possess higher molecular weight density due to when combusted leads to higher exhaust gas temperature resulting in higher peak pressures. Most investigators reported that higher NO_x emission results for higher volumetric concentration of biodiesel in the blend. Similar results were obtained for neem biodiesel-diesel blends at various braking torques and IOPs. Figure 20.7 recordings observed for B75 blend at 280 bar injection pressure showed the highest NO_x. The regression equation of NO_x is (Table 20.12)
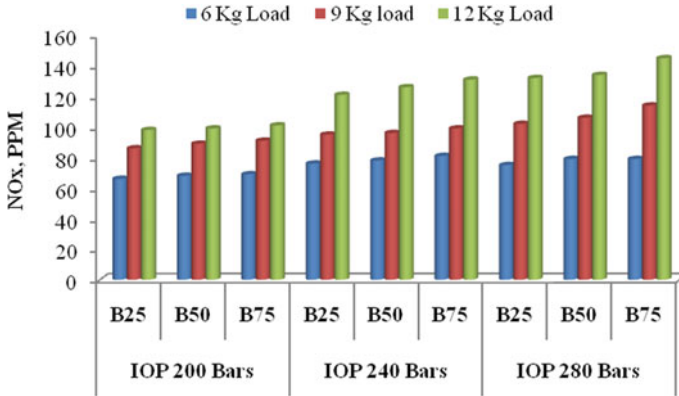
$$NO_x = 94.2 - 0.158\,IOP + 0.100\,BLEND + 0.200\,LOAD$$

Fig. 20.7 Variation of NO_x emission at various IOPs and torques

Table 20.12 Grey relation grade for NO_x

Sr. no.	Readings of NO_x	Normalized S/N ratio of NO_x	Deviation sequences for NO_x	Grey relational coefficient NO_x	S/N ratio of NO_x
1	66	0.371758779	0.628241221	0.443167641	36.39087871
2	89	0.070273983	0.929726017	0.349717354	37.38463439
3	101	0.216707107	0.783292893	0.389622668	36.9019608
4	95	0.852197627	0.147802373	0.771840334	34.80725379
5	121	0	1	0.333333333	37.61627185
6	81	0.070273983	0.929726017	0.349717354	37.38463439
7	132	0.622912366	0.377087634	0.570068464	35.56302501
8	79	0.622912366	0.377087634	0.570068464	35.56302501
9	114	1	0	1	34.32006687

20.2 Optimization Using Grey Relational Grade (GRG) Generation

In order to find the optimum combination of load, blend of fuel and injection pressure, its dependence on the output responses should be known. In the current work, dependent parameters like BTHE and CO_2 were given high weighting factor, and other parameters like CO, HC, NO_x and BSFC were highlighted as less weighting factor. By doing so, the grey relation grade (GRG) is achieved by which it is possible to compute the optimum combination of the engine design/operating parameters, i.e., load, blend of fuel and IOP. After getting the grey relation grade and with the weighting factor with the help of MINITAB® software, it is possible to analyse the Taguchi design of L9 orthogonal array. Higher GRG signifies the experimental result

which is closer to the ideally normalized value. In other words, optimization of the complicated multiple characteristics can be converted into optimization of a single grey relational grade. The grey relational grade is given in Table 20.13. Since the experimental design is orthogonal, it is then possible to separate out the effect of each parameter on thereby relational grade at different levels. Basically, the larger the value of relational grade, the better is the multiple performance characteristics (Fig. 20.8 and Table 20.14). Numbers in bold in Table 20.14 indicates best suitable levels in reference to better performance and lower emission.

Confirmation test: The confirmation test for the optimal parameters with its levels was conducted to evaluate quality characteristics. Table 20.15 shows the highest grey relational grade, indicating the process parameter set of A3B1C2 for the best multiple performance characteristics among the nine experiments. By using the A3B1C2 set-up, it confirms an experimental result as given in Table 20.15.

Table 20.13 Grey relation grades with corresponding S/N ratio and its order

Expt no.	IP	Blend	Load	Grey relational grades	Ranking
1	1	1	1	0.518732283	5
2	1	2	2	0.470811535	8
3	1	3	3	0.654796977	2
4	2	1	2	0.511979074	6
5	2	2	3	0.454418923	9
6	2	3	1	0.493261048	7
7	3	1	3	0.523565388	4
8	3	2	1	0.569088016	3
9	3	3	2	0.659382871	1

Fig. 20.8 Graph of grey relational grades versus experimental numbers

Table 20.14 Grey relation grades with corresponding S/N ratio and its order

Parameter	Level 1	Level 2	Level 3	Max–Min	Ranking
IOP (A)	0.5481136	0.486553	**0.584012**	0.097459	2
Blend (B)	**0.60248**	0.49810613	0.51809227	0.104374	1
Load (C)	0.5270271	**0.5473912**	0.54426	0.020364	3

Table 20.15 Results of confirmation test

	Initial parameter	Optimal process parameters	
		Predicted	Experimental
Levels	A1B1C1	A3B1C2	
O_2	14.84	20.468889	21.46
CO_2	8.27	7.211111	7.73
CO	0.05	0.045556	0.05
HC	102	94.88889	102
NO_x	66	58.88889	66
BTHE	26.0639	28.59839	32.60661148
BSFC	0.343156	0.34107	0.296713401

Predicted response formula is used to find the optimal level of combination in Table 20.15, and it can be calculated by using Minitab software

Predicted Response = Average A3 + Average B1 + Average C1 − 2 × mean response

20.3 Inferences

Based on the study conducted for multiple response parameters (engine performance and emission study) and its optimization on independent variables using grey relational analysis, the obtained optimized combination is found to be **A3B1C2 w**hich means that the blend percentage of 25% and IOP of 28 bars could be used as best suitable higher performance and lesser emission standards. The methodology adopted in this study can also be used to optimize other engine operating parameters like compression ratio and injection timing.

References

1. Sayin, C., Gumus, M.: Impact of compression ratio and injection parameters on the performance and emissions of a DI diesel engine fueled with biodiesel-blended diesel fuel. Appl. Therm. Eng. **31**, 3182–3188 (2011). http://dx.doi.org/10.1016/j.applthermaleng.2011.05.044

Chapter 21
Design and Manufacturing of Hand Injection Mold for Flip Badge—Analysis of Alternate Air Venting Patterns

Check for updates

Vijaykumar Kalwa and **Balaji Thottempudi**

Abstract The increased demand for plastic components and greater requirement in the market has created necessity for wider study and research in the area of plastic flow behavior for intricate profiles of core and cavity in mold. Polymers rapidly replaced other materials because of its chemical and physical characteristics. Best part of the polymer is being lighter in weight and functionally suitable to large amount of parts/components produced day to day. The influence of venting and the injection time on the mold impression filling were examined. It was observed that improper injection time and incorrect venting parameters lead to either short filling of the impression or flash on the component. Also, component profile has vital role in placing the venting region. The controlled injection time and optimum venting parameters found to have zero flash and 100% impression filling. The functionality/application of the produced part is also found to be satisfactory.

Keywords Flip badge · Air trap analysis · Shrinkage · Venting

21.1 Introduction

21.1.1 Background Theory

A hand mold is a simple mold used for low-quantity work. It is used in the injection molding for replicating components in large quantity. In injection molding, hand molds refer to simple molds that have no provision for heat, cooling, or ejection. They are usually only of a two- or three-plate design because of the simplicity of the parts. This research for hand mold comprises planning, detailed design, manufacturing,

V. Kalwa (✉)
Ramaiah University of Applied Sciences, Bangalore 560058, India
e-mail: vjkalva@gmail.com

B. Thottempudi
CreditAccess Grameen Limited, Bangalore 560058, India

227

machining non-identical vent profiles, costing, inspection, and trials of the component. The purpose of the examining over the distinct venting pattern is to make aware of true venting parameters, alternate vent profile pattern for unique component, flow analysis, and analysis of air venting method and manufacturing procedures theoretically as well as practically. This paper reveals the analysis of alternate venting pattern by considering component profile and important factors like design, manufacturing, and troubleshooting the online and offline occurred difficulties. Component selected for making hand injection mold is flip badge. A small object (such as tag) that is held up by a person so that it can be easily seen, that has writing and often a picture on it, represents the occasion or identity of person.

21.1.2 Objectives

1. To design a prototype hand mold for the given product (flip badge) and prove the molding.
2. To manufacture the mold by following all the procedures included in a production/multicavity molds.
3. To study in detail the total process involved like venting in mold making by practically doing it.
4. To never compromise on quality of the product and produce each and every element of the mold as per the given drawings and within the tolerance limits.
5. To understand the difficulties involved for filling the component caused by the entrapped air in the impression and troubleshoot the venting issues.

21.2 Experimental Work

Experimental work is designed to successfully reach the objectives set for the research work. It broadly consists of tool description, tool design, validation, tool fabrication, and testing of tool and analysis.

21.2.1 Tool Description

This section highlighted the parameters adopted for tool design. It consists of description of the component, geometrical details, material properties, and tool specifications [2, 3] (Table 21.1).

Table 21.1 Component specification

Particulars	Specifications
Component	Flip Badge
Area of the component	2431.64 mm^2
Area of the feed system	29.04 mm^2
Total projected area	2460.63 mm^2
Thickness of the component	2.5 mm
Mass of the component	5.6 grams
Material	Polypropylene
Shrinkage	1.50%
Melting temperature	160 °C
Density of material	946 kg/m^3

21.2.2 Shrinkage Calculation

The product quality of injection-molded plastic parts is the result of a complex combination of the material used, the part and mold designs, and the process conditions used to manufacture them. If plastics are processed by injection molding, deviation of the molding from the dimensions of the cavity cannot be avoided. These deviations from the nominal size are summarized under the term shrinkage [1]. In the injection-molding technique, shrinkage S, as explained by Eq. (21.1),

$$D = A + \left(A * \frac{S}{100} \right) \tag{21.1}$$

21.2.3 Detailed Design

In this paper, for analyzing the objectives, tool design was carried out in 2D drafting application (AutoCAD) which included plan view for core half and sectional front view. Also, 2D plan view is validated by modeling with same dimension as 2D in 3D environment with the help of Creo 2.0. It confines that dimensions applied were proper and no interference found between the parts of the mold (Fig. 21.1; Tables 21.2 and 21.3).

21.2.4 Tool Validation

The validation of the designed tool was carried out in SOLIDWORKS mold flow analysis package, especially for fill time and air trap analysis. In the obtained results,

Fig. 21.1 Prototype hand mold for flip badge
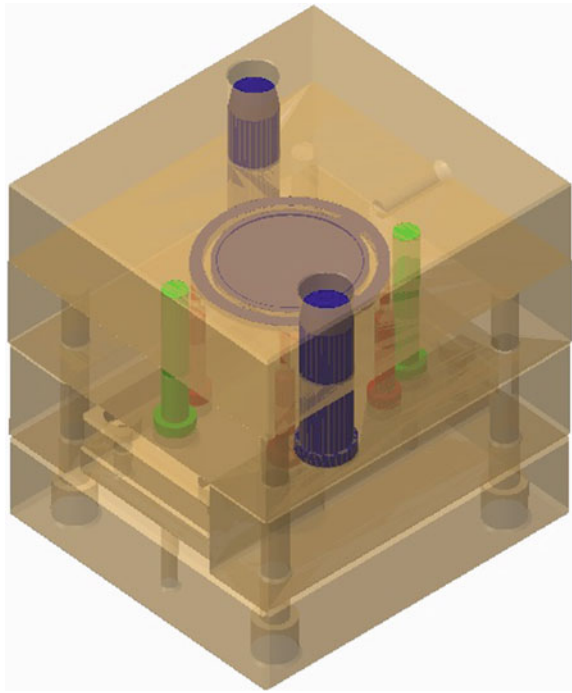
Table 21.2 Shrinkage calculation for core and cavity

S. No.	Actual dimension (mm)	Shrinkage calculation (achieved dimension, mm)
1	58	58.87
2	50	50.75
3	46	46.69
4	42	42.63
5	11	11.16
6	2.5	2.53

Shrinkage calculation for cavity

S. No.	Actual dimension (mm)	Shrinkage calculation (achieved dimension, mm)
1	42	42.63
2	0.5	0.50

expected errors were taken into consideration for troubleshooting by employing suitable machining parameters and methods. The below-mentioned result images prove that required fill time for selected component is 1.6 seconds and highlighted on image with dot marks for machining air vents (Figs. 21.2 and 21.3).

Table 21.3 Tool specification

Specifications	Description
No. of impressions	01
Type of mold	Two-plate mold
Type of runner	Round runner
Type of gate	Edge gate
Type of ejection	Pin ejection
Mold size	110 * 20 * 125 mm^3
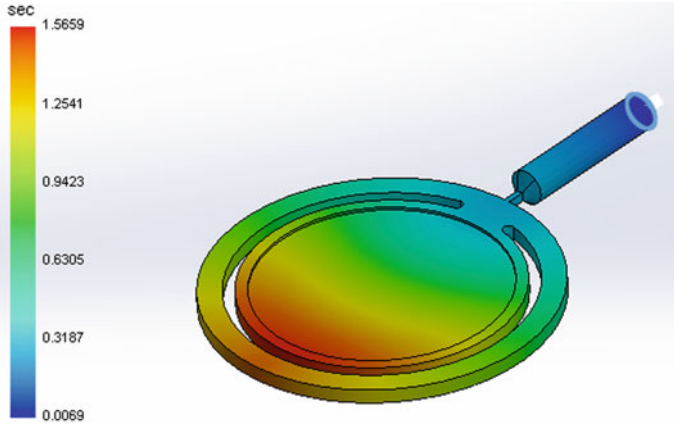
Fig. 21.2   Fill time analysis
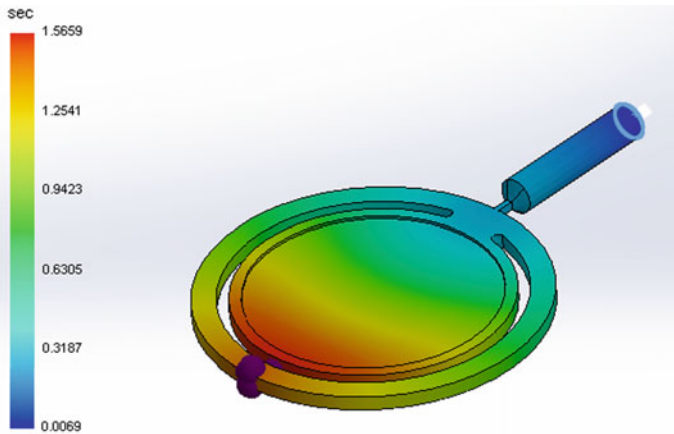
Fig. 21.3   Air trap analysis

Fig. 21.4 Photographic view of milling machine with rotary table attachment for investigation

Table 21.4 Parts' machining details

S. No.	Particulars	Material	Machines/tools
1	Core/cavity	D2 steel	CNC milling, spark EDM, conventional milling, co-ordinate drilling, grinding, lapping
2	Ejector plates and bottom plate	OHNS	Milling, grinding, co-ordinate drilling
3	Ejector pins/pushback pins/rest buttons	OHNS	Facing, turning, cylindrical grinding

21.2.5 Fabrication of the Tool

The parts for the hand mold were precisely machined by utilizing conventional and non-conventional machines. The critical parts of the mold like core/cavity are machined by CNC milling and spark EDM. Once after pre-machining, secondary operations were carried out for all the parts of the mold. As like design considerations, required tolerance on parts was maintained to maintain accurate assembly of the parts [4, 5]. In the below-mentioned table, fabrication details of the tool are briefly documented (Fig. 21.4; Table 21.4).

21.2.6 Surface Validation for Core and Cavity

Once after machining, core and cavity with required tolerance need to be checked for surface matching to ensure no gap between the plates. To ensure the proper mating of core and cavity, blue applied over both surfaces and assembled. On a assembled core and cavity plates, pressure applied to ensure even spreading of blue on both plate surfaces. After performing blue matching on core and cavity, both surfaces found to be flat (Fig. 21.5).

Fig. 21.5 Blue matching for core and cavity
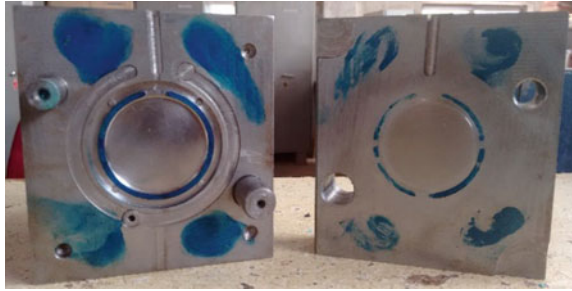
21.2.7 Air Vents' Machining

Standard dimensions preferred for venting slots are 0.05 and 3 mm deep with alternate shapes. To escape the entrapped air in the impression, air vents should be facilitated by machining. To ensure proper escaping of entrapped air in cavity, air vents to be machined on to the core plate of the mold in variety shapes and with different machining methods. In this experimentation, machining for air vents is carried out which is shown in below given photographs (Fig. 21.6; Tables 21.5 and 21.6).
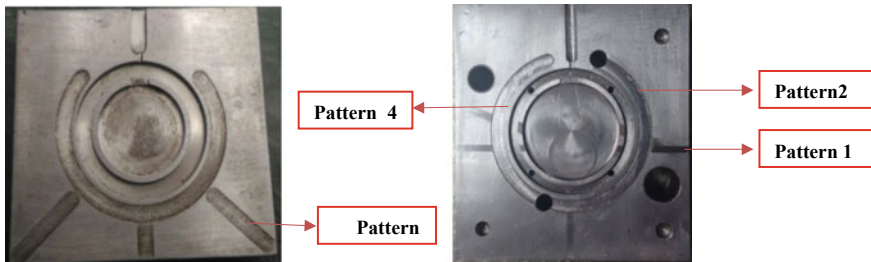
Fig. 21.6 Representation of alternate vent pattern machined

Table 21.5 Machining details for air vents

Vent pattern	Machining method	Parameters	Remarks
Pattern 1	Surface grinding	Linear cut (0.05 mm deep and 3 mm wide)	Component short filled
Pattern 2	Milling machine	Circular slot (dia. 8 and 0.2 mm deep)	Component short filled
Pattern 3	Milling machine	Diagonal cut to the impression (8 mm dia and 0.2 mm deep)	Component short filled
Pattern 4	Milling machine	Milling cut which connects from impression to the circular slot (0.2 mm deep)	Filled

Table 21.6 Characteristics of machines adopted for tool fabrication

S. No.	Characteristics	Specification	Machines/feed rate
1	Tool material	Copper, 1 mm diameter	Spark EDM
2	Spark gap	10–125 μm	
3	Spark frequency	210–450 kHz	
4	Peak voltage	40–250 V	
5	Dielectric fluid	Kerosene and water with Glycol	
9	Tool material	High carbon steel (face mill 5 teeth)	Vertical milling feed rate (0.02 mm/rev)
10	Cutter diameter	76 and 120 mm	
12	Tool material	High carbon steel	Turning/facing feed rate (0.1–0.2 mm/rev)
13	Cutting tool	Single-point cutting tool (right hand)	
15	Tool material	Abrasive wheel (aluminum oxide)	Surface grinding feed rate (0.6 mm/rev)

21.3 Discussion and Conclusions

21.3.1 Testing and Inspection

In this last stage, testing the fabricated tool by injecting molten plastic (polypropylene) was done by the plunger-type machine. Details of the trails are taken, and troubleshooting of occurred problems has done and briefed below (Fig. 21.7; Table 21.7).

Fig. 21.7 Component trails for tool validation

Table 21.7 Trails' observation

Trails	Status	Remark/issue
Trail 1	Short filled	Air vents/injection time
Trail 2	Short filled	Venting/Injection time
Trail 3	Short filled	Venting
Trail 4	Short filled	Venting
Trail 5	Filled	Break at weld line
Trail 6	Filled	Optimum injection time and proper venting provided

21.3.2 Observation

(I) Problems occurred during component trial

- Impression short filling.
- Flash on the component.

(II) Troubleshooting by

- Providing venting.
- Reducing injection time.

21.4 Conclusion

In this experimental process, the obtained component was inspected for its quality and application and found to be satisfactory. Due care was taken to manufacture the tooling following all the procedures, simulation results, and guidelines of a production mold. Summary of air vent patterns and troubleshooting of occurred errors noted in the paper understandably. The component could be practically used for its application. The objectives of research were successfully achieved, and the processes involved were clearly analyzed and summarized for further research work.

References

1. Ali, E.E., Balal, A.A., Abbas, R.A.: Shrinkage of plastic raw materials (a comparative study of mold). JECS **18**(3), 54–59 (2017)
2. DME Company (India) Ltd.: Mold Base Plastic Materials and Basic Assemblies Manual (2008)
3. Edutech NTTF IndiaPvt Ltd.: Mold Design Standards Manual. Training Centre Mumbai (2001)
4. Gerling, H., Heller, K.H.: All About Machine tools. New Age International Publishers, New Delhi (2009)
5. HajraChowdhary, S.K.: Workshop Technology. Media Promoters and Publishers (1971)

Chapter 22
Design and Optimization of Foot Locus Trajectory of Theo Jansen Mechanism

N. Prashanth, S. Karthik, G. R. Rahul and T. B. Sandarsh

Abstract The single degree of freedom legged robots are functional in terms of its simplicity and performance on both even and uneven terrains. The performance stability of these legged robots is determined by the trajectory of their foot locus. In the present work, Theo Jansen mechanism is used as locomotive drive mechanism for legged robot. The mechanism is designed and optimized using the Synthesis and Analysis of Mechanism (SAM) software during the conceptual design phase. The embodiment design was completed using CATIA. Simplex and evolutionary algorithms were utilized for optimization of foot locus to improve its step height and stride length. The influence of the link length and the input crank angle on the foot locus trajectory has been illustrated and compared for three different trials. The obtained results are compared with standard foot locus. Further, the results derived in this work can be utilized in selecting the link length for Theo Jansen mechanisms for various applications.

Keywords Planar mechanisms · Theo Jansen · Optimization · Synthesis · SAM · CATIA · Legged robot

22.1 Introduction

The legged locomotive drive mechanism for robots are advantageous compared to that of wheeled drive mechanisms because of their all-terrain capability. Legged robots employ a mechanism which can be broadly characterized as multi degrees of freedom or single degree of freedom. Multi degrees of freedom legged robot have high manoeuvrability and they require complex control schemes with multiple gaits. Multi degrees of freedom legged robots are complex in mechanical design, expensive and often results in poor reliability [1]. Single degree of freedom legged mechanisms have several advantages to their credit because of its simplicity and

N. Prashanth (✉) · S. Karthik · G. R. Rahul · T. B. Sandarsh
Department of Mechanical Engineering, Nitte Meenakshi Institute of Technology affiliated to
Visvesvaraya Technological University, Belagavi, India
e-mail: prashanth.n@nmit.ac.in

low cost. Single degree of freedom legged mechanisms adopt planar mechanisms which are predictable and require simple control schemes. The inherent nature of planar mechanisms ensures that they do not suffer from redundant mobility. Due to these advantages, they are widely used in several applications. The performance of legged robots can be analysed using various metrics such as stability margin, energy efficiency and foot locus trajectory. For single degree of freedom legged robot, foot locus trajectory influences the robot's ability to overcome obstacles and also the energy efficiency of the mechanism [2]. Foot locus is the path traced by the leg in one cycle of crank. The trajectory with which the foot of a walking mechanism comes in direct contact with the ground is very important. As the crank rotates, the foot traces out a cyclical path. The foot locus of the leg is defined by mainly four phases; stride/drive, lift, return and lower phases.

Theo Jansen mechanism is a single degree of freedom mechanism which is widely used as locomotive drive mechanisms for legged robots. The Theo Jansen's linkage is a planar leg mechanism designed by the kinetic sculptor Theo Jansen to simulate a smooth walking motion. Jansen's linkage bears artistic as well as mechanical merit for its simulation of organic walking motion using a simple rotary input [3]. The foot locus of single degree of freedom legged robot should be optimized and the trajectory of the foot locus should be controlled for stable locomotion of the robot. The step height and stride length of legged locomotion determine the terrain in which the robot can move and efficiency of the robot locomotion [4]. In the present work, the optimization and the performance analysis of Theo Jansen mechanisms are studied using Synthesis and Analysis of Mechanisms (SAM) software. SAM was developed by Artas Engineering software. SAM is an interactive PC-software package for design, analysis (motion and force) and optimization of arbitrary planar mechanisms. Mechanisms can either be generated via the design wizards or they can be assembled from basic components including beams, sliders, gears, belts, springs, dampers and friction elements [5]. CATIA was employed to design the basic structures of the robot and planar mechanism. Digital mock-up (DMU) kinematic analysis on the designed mechanism was performed to check the interference of linkages and structures of the robot.

22.2   Optimization of Mechanism

Figure 22.1 shows the method adopted for analysis and design of Theo Jansen mechanism. The standard link lengths of the Theo Jansen mechanism are obtained from the 11 holy numbers given by Jansen [6]. It is scaled down to the link lengths to our requirement by taking the ratios of the 11 holy numbers. The scaled link lengths were then utilized to construct the Theo Jansen mechanism in SAM and the corresponding foot locus was obtained. Table 22.1 shows the link lengths and the foot locus traced by the standard Theo Jansen mechanism. From the standard foot locus, optimization was performed based on the foot locus requirement for uneven terrains. The parameter of the foot locus is shown in Fig. 22.2.
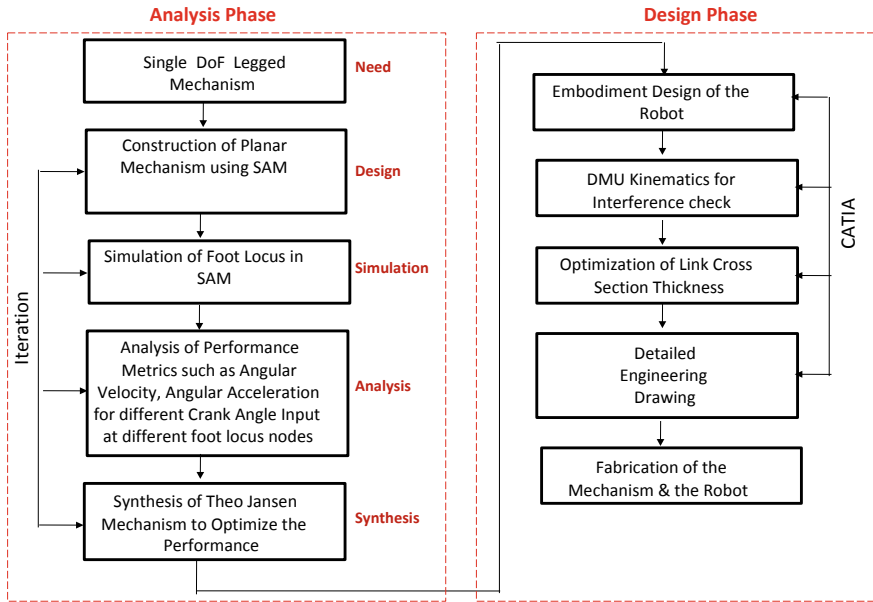
Fig. 22.1 Methodology

Table 22.1 Standard link length and foot locus of Theo Jansen mechanism
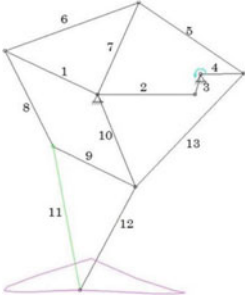
Links	Standard link length (mm)	Standard foot locus result (mm)
1	60.108	Step height: 23.074 mm
2	57.812	Stride length: 114.254 mm
3	12	
4	23.840	
5	78.698	
6	88.691	
7	63.281	
8	56.723	
9	56.143	
10	60.455	
11	101.825	
12	83.304	
13	93.595	

Fig. 22.2 Foot locus parameter [4]
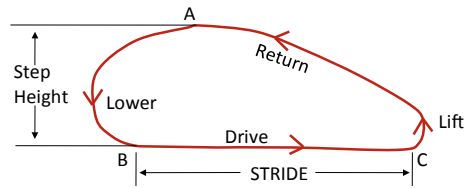
Fig. 22.3 Hodograph of Theo Jansen mechanism obtained from SAM
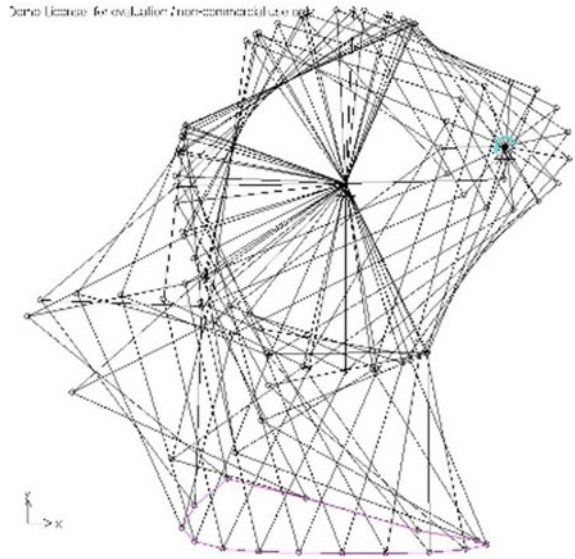
The hodograph obtained of Theo Jansen mechanism for one complete cycle is shown in Fig. 22.3.

The optimization of standard foot locus trajectory was performed by the following steps.

- **Modelling of Linkage Mechanism**: Standard Theo Jansen mechanism was constructed in SAM using the beam elements.
- **Configuring the Inputs (Actuators) and Constraints**: The input motion is given to the crank for the rotation of the crank.
- **Tracing Standard Foot Locus**: The standard foot loci for the standard link lengths were obtained. The coordinates of the standard foot locus were obtained.
- **Creating the Optimized Foot Locus Coordinates**: Based on the standard foot locus coordinates, a set of new target coordinates were derived to optimize the step height and stride length.
- **Input Target Coordinate for Synthesis of Links**: The coordinates for target path were selected in the software.
- **Define the Reference Frames**: The fixed supports of the mechanism are selected in the optimization process.
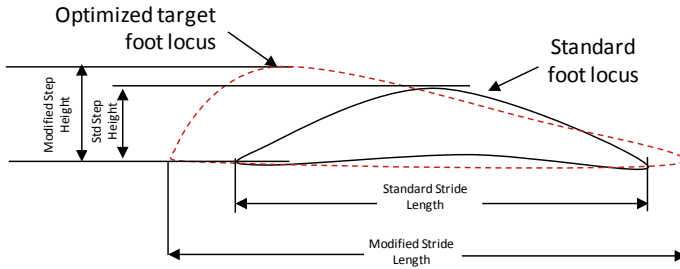
Fig. 22.4 Standard and optimized foot locus

- **Select the Optimization Algorithm**: In the optimization, one can choose between user-controlled modus and automatic modus. In the user-controlled mode, a global exploration of the parameter space is performed based on evolutionary algorithms leading to a set of solutions. The user can then select any of these solutions and further refine it via a local optimization, which can be either based on an evolutionary approach or on a simplex method. In the automatic mode, the best solution of the global search is automatically refined in a local optimization (again, either based on an evolutionary or a simplex approach). In the present work, the automatic modus is chosen as it gives the best solution.
- **Optimize**: After defining all the inputs, the optimization process is commenced; the software performs multiple iterations to obtain the target foot locus path obtained as shown in Fig. 22.4. During the process of optimization, the software will automatically synthesize the link length to obtain the desired foot locus.
- **Tabulation of New Link Lengths**: Once the desired foot locus was obtained through optimization, the updated link lengths were tabulated for CAD modelling.

As shown in Fig. 22.4, the target coordinates were entered as the reference file for the optimization process. The thick lines represent the standard foot locus and the dotted line represents the optimized foot locus. Using the above foot locus, several other foot loci were obtained by changing the link lengths to achieve longer stride length and higher step height.

Figure 22.5 shows the comparison of three different foot loci with that of the standard. First, the stride length and step height were compared with the standard foot locus and all the linkages. Percentage of increase or decrease of the link length was computed to identify the links which influenced the foot locus the most. These results were further tabulated as shown in Table 22.2. In the first trial, the stride length and step height are increased by 2.03% and 35.05%, respectively. This foot locus has higher step height and longer stride length when compared to all other trials; however, the main problem associated with this foot locus is the mechanism suffers from interference between the links during motion, the reason for interference is the increase in link length leading to higher step height, in order to overcome this problem, the cross-section thickness of link should be very small, however, reduction in cross-section thickness will further lead to poor leg strength, therefore, trial-1 was
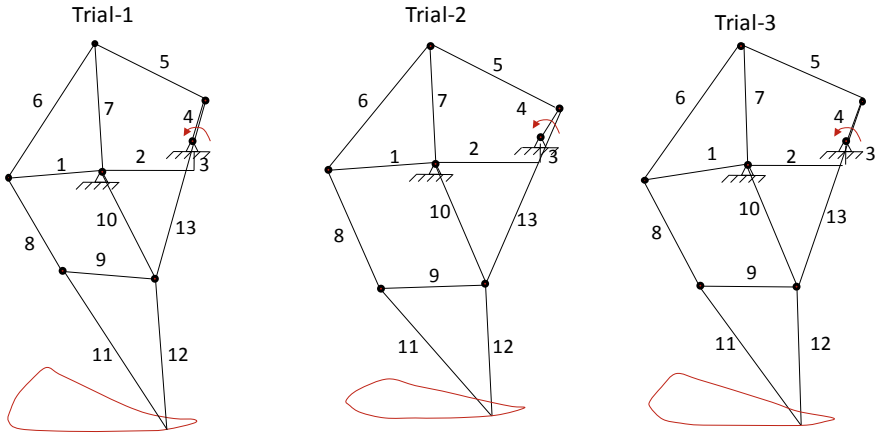
Fig. 22.5 Various foot loci in comparison with standard foot locus

Table 22.2 Nodes identified for the comparison of Theo Jansen foot locus

Link No.	Standard link length (mm)	Trial-1		Trial-2		Trial-3	
		Link length (mm)	% of change in link length (%)	Link length (mm)	% of change in link length (%)	Link length (mm)	% of change in link length (%)
1	60.108	60.108	0.00	60.32	0.35	61.832	2.87
2	57.812	57.812	0.00	57.812	0.00	57.812	0.00
3	12	12	0.00	12	0.00	12.12	1.00
4	23.84	25.153	5.51	20.96	−12.08	23.408	−1.81
5	78.698	72.952	−7.30	80.273	2.00	78.698	0.00
6	88.691	88.691	0.00	87.96	−0.82	91.419	3.08
7	63.281	63.281	0.00	63.281	0.00	63.281	0.00
8	56.723	58.317	2.81	69.57	22.65	64.089	12.99
9	56.143	56.679	0.95	58.8	4.73	58.601	4.38
10	60.455	63.01	4.23	71.57	18.39	68.92	14.00
11	101.825	102.1	0.27	91.813	−9.83	93.677	−8.00
12	83.304	76.1	−8.65	68.965	−17.21	72.902	−12.49
13	93.595	90.623	−3.18	105.627	12.86	103.7	10.80
Stride length	114.254	116.574	2.03	95.5	−16.41	102.6	−10.20
Step height	23.074	31.163	35.06	20.492	−11.19	27	17.01

not considered for further analysis. In the second trial, the stride length and step height were decreased to 16.41% and 11.19%, respectively. This type of foot locus will be more suitable for even terrains, since its step height is less compared to all other foot loci, and hence, this locus was not further considered for analysis. In the third trial, there is an increase in the step height by 17.01% which is suitable to overcome the obstacles of up to 27 mm and there is a decrease in the stride length by 10.2%. Due to the increased step height, it is inferred that foot locus obtained in trial-3 is suitable for both even and uneven terrains. From the above results, the foot locus obtained during trial-3 was chosen as the optimal and it was further considered for embodiment design.

22.3   Design of Legged Robot

Theo Jansen mechanism was designed using 3D CAD software CATIA V5. The legs of the robot were modelled using the link lengths obtained from SAM software. These links were then assembled to form the leg mechanism. Total of eight Theo Jansen mechanisms was modelled. The chassis for the robot was designed using sheet metal workbench. Pair of each leg was actuated by one geared DC servo motor, and gear drives were used to transmit power to the legs of the robot. Figure 22.6 shows the assembly of the legged robot.

To ascertain the interference between links and chassis in the robot, digital mock-up (DMU) kinematics analysis was performed in CATIA. Any interference in the
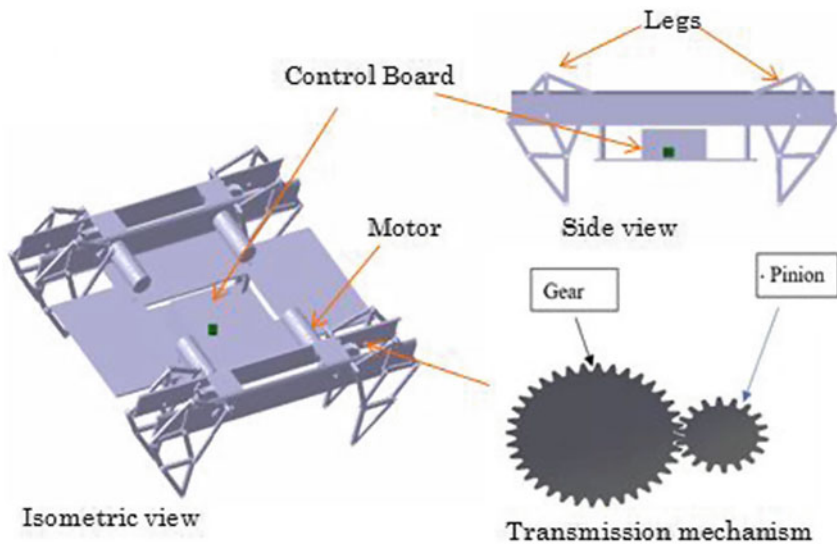
Fig. 22.6 Assembly of the legged robot

Fig. 22.7 Interference check in CATIA
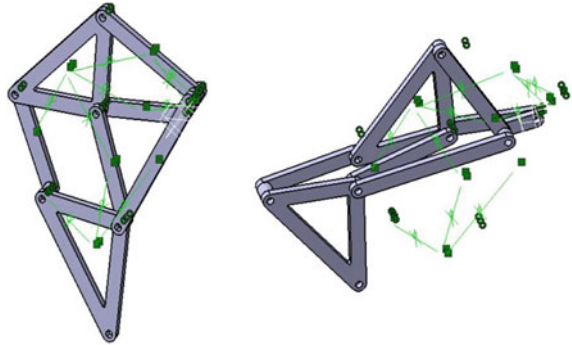
individual link lengths was overcome by optimizing the thickness of the links and also by creating the required stand-off distances between the links (Fig. 22.7).

22.4 Performance Analysis

In this section, the standard foot locus is compared with that of the three different loci obtained during optimization. The foot locus trajectory of Theo Jansen mechanisms is unique for each trial, and hence, they cannot be compared in terms of its path alone; therefore, critical nodes were identified along the foot locus which is common. These nodes are shown in Fig. 22.8.

Table 22.3 shows the influence of identified nodes on the foot locus generated by the Theo Jansen mechanism.

Table 22.4 shows the angular velocity and angular acceleration of the standard Theo Jansen robot leg (link which makes contact with the ground) as the crank rotates. Tables 22.5, 22.6 and 22.7 show the crank angle versus angular velocity and angular acceleration of the robot leg (link which makes contact with the ground) for the three trials, respectively. The analysis of angular acceleration of leg plays an important role, since the acceleration and frictional forces have interaction during

Fig. 22.8 Major points affecting the foot locus
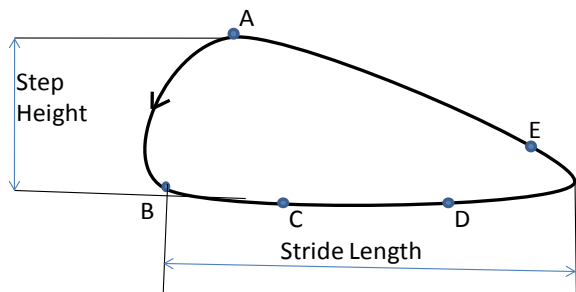
Table 22.3 Influence of nodes identified for the comparison of Theo Jansen foot locus

Nodes	Influence on mechanism
A	Step height determines the ability to overcome obstacles
B	Touchdown determines the point of contact with ground
C and D	Determines the stability during the stride length
E	Post lift-off retardation and approach towards maximum step height

Table 22.4 Performance parameters of Theo Jansen mechanism for standard link lengths

Nodes	Crank angle (rad)	Angular velocity (rad/s)	Angular acceleration (rad/s^2)
A	3.362	−4.696	−151
B	5.037	1.003	15.41
C	5.875	0.6952	11.6
D	6.713	2.194	9.959
E	4.2	−4.132	−35.16

Table 22.5 Performance parameters of Theo Jansen mechanism for trial-1

Nodes	Crank angle (rad)	Angular velocity (rad/s)	Angular acceleration (rad/s^2)
A	3.382	−2.09	−69.662
B	5.128	0.347	2.776
C	5.996	0.348	2.927
D	7.252	1.56	1.055
E	2.693	0.08	−10.114

Table 22.6 Performance parameters of Theo Jansen mechanism for trial-2

Nodes	Crank angle (rad)	Angular velocity (rad/s)	Angular acceleration (rad/s^2)
A	3.492	−3.771	−15.32
B	5.06	0.769	13.617
C	5.972	0.865	9.613
D	6.951	2.116	5.919
E	3.07	−1.856	−37.78

Table 22.7 Performance parameters of Theo Jansen mechanism for trial-3

Nodes	Crank angle (rad)	Angular velocity (rad/s)	Angular acceleration (rad/s^2)
A	3.58	−2.621	−64.04
B	4.837	1.363	15.63
C	5.675	0.380	10.96
D	6.512	1.773	10.6
E	3.161	−4.937	−98.36

the locomotion of the robot, and hence, it is imperative to understand the magnitude and directions of various parameters such as velocity and acceleration [7–9].

Figures 22.9 and 22.10 represent the crank angle versus angular velocity and crank angle versus angular acceleration, respectively, for the optimized foot locus, i.e. for trial-3. From the above graphs, one can observe that there is a rapid change in velocity from node A to B and Node D to E resulting in change of acceleration. The velocity from point B to D is almost uniform and therefore it results in minimum acceleration. The rapid change in velocity and acceleration happens during the lift and lower phase.

Figure 22.11 shows the comparison of angular acceleration between the standard Theo Jansen mechanism and the optimized foot loci. It can be observed that between nodes B, C and D, the variation of angular acceleration across the standard foot locus and optimized foot loci is negligible. However, at nodes A and E, the angular acceleration varies across all the foot loci. In the standard foot locus, at node A, the leg experiences maximum acceleration and its acceleration reduces as its approach
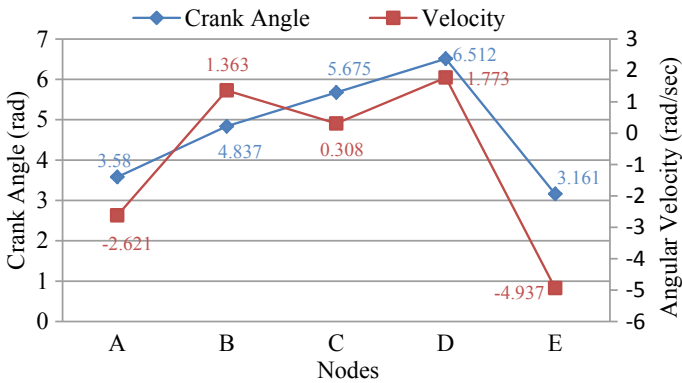
Fig. 22.9 Trial-3 crank angle versus angular velocity
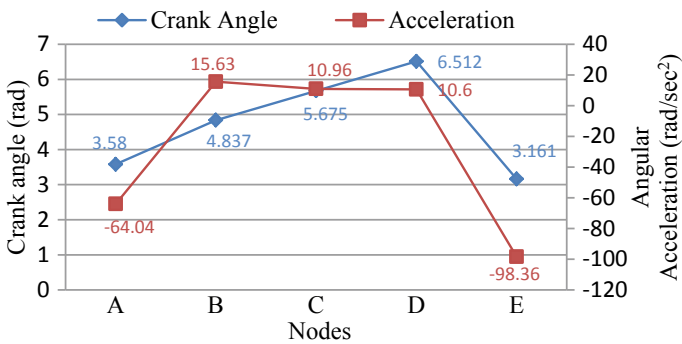
Fig. 22.10 Trial-3 crank angle versus angular acceleration
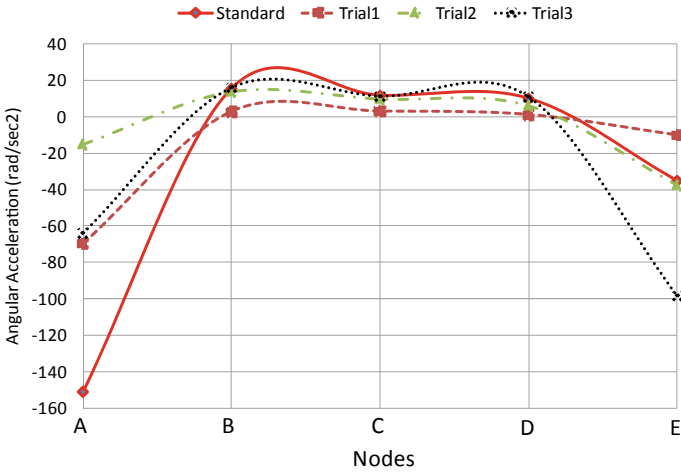
Fig. 22.11 Comparison of angular acceleration between standard and optimized foot loci

towards node B. In trial-3, it can be observed that the difference between angular acceleration between nodes A and E is considerably less than the standard foot locus.

22.5 Conclusions

While comparing the standard foot locus with that of the optimized foot loci, one can observe that in the standard link the maximum step height is achieved at the centre of the stride length, and hence, when the leg approaches the lower phase, it would not overcome the obstacle. In the optimized foot locus, the maximum step height is achieved during the lower phase and such foot loci are suitable for uneven terrains or overcome obstacle (obstacle size based on step height). Hence, it can be used in several applications. The results obtained in the present work can be further utilized to incorporate Theo Jansen mechanism for various applications. Further, the optimized mechanism will be fabricated and integrated with the robot to test its performance under real-world conditions such as different terrain, gaits and phase angles.

References

1. Tenreiro Machado, J.A., Silva, M.: An overview of legged robots. In: International Symposium on Mathematical Methods in Engineering, pp. 1–40 (2006)
2. Nansai, S., Rajesh Elara, M., Iwase, M.: Dynamic analysis and modeling of Jansen mechanism. Procedia Engineering **64**, 1562–1571 (2013)

3. Moldovan, F., Dolga, V.: Analysis of Jansen walking mechanism using CAD. In: Solid State Phenomena, vol. 166, pp. 297–302. Trans Tech Publications Ltd (2010)
4. Shigley, J.E.: The mechanics of walking vehicles. No. ATAC-LL71. ARMY TANK-AUTOMOTIVE CENTER WARREN MI (1960)
5. SAM-The Ultimate Mechanism Design Software. [Online]. https://www.artas.nl/en/sam/features/general
6. Jansen, T.: Theo Jansen's strandbeest (2011). Retrieved February 26, 2011
7. Ghassaei, A., Choi, P.P., Whitaker, D.: The Design and optimization of a crank-based leg mechanism. Pomona, USA (2011)
8. Mohsenizadeh, M., Zhou, J.: Kinematic analysis and simulation of Theo Jansen mechanism. Diss. Lamar University (2015)
9. Ingram, A.J.: Numerical kinematic and kinetic analysis of a new class of twelve bar linkage for walking machines. Diss. Rand Afrikaans University (2004)

Chapter 23
Performance Evaluation of Concentric and Eccentric Buckling Restrained Braces on the Dynamic Behaviour of RC Structures

H. J. Prajwal Shankar, Sunil Lamsal, Praveen Shrestha, Bharathi Ganesh and R. Prabhakara

Abstract Energy absorption and damage control are the two fundamental principles adopted in the earthquake resistant design of structures. This is possible through the usage of appropriate building materials, components, construction methodology and utilizing the advanced technology. Several lateral resisting systems were developed in order to enhance structural performance against earthquakes. Buckling restrained braces (BRBs) have been evolved as one of the promising lateral load resisting systems. The present study deals with the comparison of seismic performance of an RCC frame with BRBs over bare frame (BF) and shear wall (SW) lateral load resisting systems in a RC structure of 19 stories located in seismic Zone *V*, analyzed using an integrated structural analysis and design software ETABS version 16. 2. 0 using response spectrum method. It was observed with BRBs as lateral load resisting system performed better over BF and SW systems compared over several performance parameters.

Keywords Concentric buckling · Eccentric buckling · Buckling restrained braces · Energy absorption · Damage control

H. J. P. Shankar · S. Lamsal (✉) · P. Shrestha · B. Ganesh
Department of Civil Engineering, Nitte Meenaski Institute of Technology, BSF Campus
Yalahanka, Bangalore, Karnataka, India
e-mail: sunillamsal911@gmail.com

H. J. P. Shankar
e-mail: prajwal17shankar@gmail.com

P. Shrestha
e-mail: prav.stha@gmail.com

B. Ganesh
e-mail: bharathi.ganesh@nmit.ac.in

R. Prabhakara
Structural Engineering Division, PGS VTU, Belagavi, Karnataka 590018, India
e-mail: r.prabhakara@gmail.com

23.1 Introduction

The objective of seismic design of a structure is to limit the deformation within the permissible limits so as to ensure that the structures resist the earthquake of assumed intensity falling under the designated zone. The specified limit of serviceability is achieved by selecting an appropriate lateral load resisting systems such as moment-resisting frame (MRF), diagonal bracing (DB) and centre braced frame (CBR) [1]. However, these structures typically generate large inelastic deformation which can cause severe damage to the structure and subsequently increase the complexity of handling the damaged structure and cost of structural repair post-earthquake. It has been observed in the recent years, buckling restrained braces (BRBs) have become an attractive and feasible alternative to the conventional steel brace system, provided for dissipating earthquake energy [2]. BRB is an unbounded bracing member consisting of a steel core plate or a section encased in a concrete-filled steel tube over its length (Figs. 23.1 and 23.2) [3–5]. The former component resists axial force while the later component restrains the brace from buckling in compression.

The better seismic performances of BRBs have widely replaced the conventional steel braces in recent years. BRBs benefit from symmetric and stable hysteretic behaviour in compression with normal braces, and as a result, BRBs have higher energy absorption capacity. The energy dissipation in bracing is through yielding of brace in tension. In compression, the buckling before yielding results in less energy dissipation and causes instability of a structure [5]. This weakness of lateral bracings
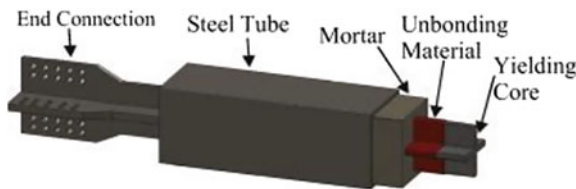
Fig. 23.1 Buckling restrained bracing [6]
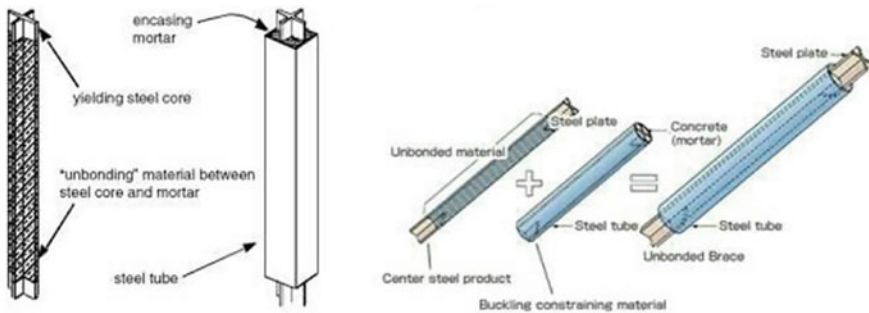
Fig. 23.2 Components of a BRB [7, 8]

is tried to overcome with a typical brace that can provide restrained against buckling in compression and named as buckling restrained brace which exhibits symmetric and stable cyclic behaviour and also high energy absorption [9, 10].

23.2   Present Study

The present study focuses on the analysis of a 19 storey RCC framed structure with concentric and eccentric BRBs to record the seismic performance in comparison with that of shear walled RCC framed structure. The geometric and material details of the structure are provided in Table 23.1. The plan of a live project building is selected for the study with minor modifications suitable to the present research study (Fig. 23.3). There are 16 bays in major direction and nine bays in the other direction. Different models considered for the analysis are the structure with bare frame, structure with

Table 23.1 RCC geometric and material details of framed structure

Type of building	Residential apartment
No of stories	19
Floor to floor height	3 m
Total height of building	57 m
Plan area	25.025 m × 52.75 m
Beam size	200 × 550 mm
Column size	450 × 750 mm
Slab thickness	125 mm, 150 mm
Concrete grades	M30, M40
Steel grades	Reinforcing: Fe 500, Fe 415 Structural: Fe 345
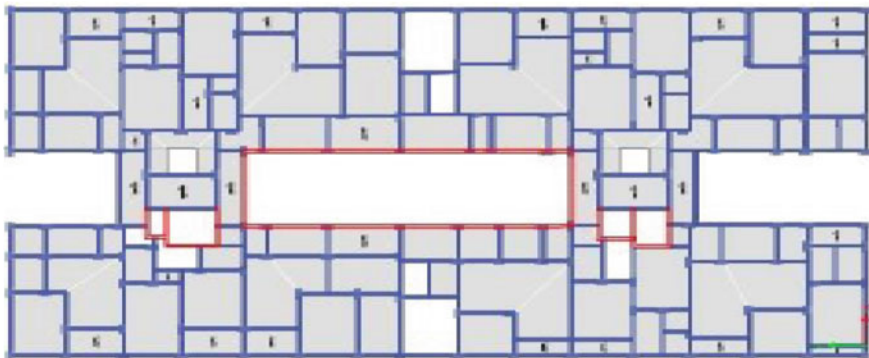
Fig. 23.3 Typical floor plan of the structure

shear wall and also the structure with concentric and eccentric BRBs as lateral load resisting systems [11–13].

23.3 Methodology

Following methodology is adopted while carrying out the analysis of the structure. ETABS ver 16.2.0 integrated software for analysis and design of structures is used to carry out linear dynamic analysis/response spectrum analysis. The geometric and material details of the structure are as follows (Table 23.1).

23.4 Various Models Considered for Analysis

RCC bare frame without lateral load resisting system, located in seismic Zone *V* is considered as a reference model. As per IS1893-2016, a Response Reduction Factor (RRF) of 3 corresponding to an ordinary moment resisting frame was used for the design. An RC wall 220 mm thick, made of M30 grade concrete, provided with shear wall type of lateral load resisting system is taken up for the analysis. A structure having RRF of 4.5 as per IS1893 (Part 1)-2016 provided with concentric and eccentric buckling restrained bracings (BRBs)—a combination of shear wall and steel bracings is considered for the analysis [14].

23.5 Procedure Followed in the Analysis

The procedure adopted for analyzing the structure is explained as follows.

a. Preparation of geometrical model for bare RCC frame.
b. Analyzing with and without shear wall for dynamic behaviour. Various types of live loads are considered as per IS 875: 2008 [15] as provided in Table 23.2. Defining the parameters of BRBs and applying calculated loads as per various load combinations as given in Table 23.3. Calculated loads are assigned on the respective floor areas in the model (Fig. 23.4).
c. Assigning the BRBs in predefined positions of bare RCC frame, in different patterns, both concentric and eccentric separately.
d. Carrying out seismic analysis of RC frame with concentric and eccentric BRB frames and records the results.
e. Comparing the seismic response of various types of model of RCC frame and draw a rational conclusion.
f. Comparing the results of software analysis with manual calculations.

Table 23.2 Area loading details

Sl. No.	Description	Loads in kN/m^2
1.	Corridors	3.0
2.	Staircase	3.0
3.	Rooms	2.0
4.	Toilet area (75 mm sunken)	1.5
5.	Terrace area (accessible)	2.0
6.	Utility (150 mm sunken)	3.0
7.	Balcony area (100 mm sunken slab)	2.0

Table 23.3 Load combinations (response spectrum analysis)

Sl. No	Factored load combinations
1	1.5TDL + 1.5TLL
2	1.5TDL + 1.5RS-X
3	1.5TDL + 1.5RS-Y
4	1.2TDL + 1.2TLL + 1.2RS-X
5	1.2TDL + 1.2TLL + 1.2RS-Y
6	0.9TDL + 1.5RS-X
7	0.9TDL + 1.5RS-Y
8	1.5TDL + 1.5WX
9	1.5TDL − 1.5WX
10	1.5TDL + 1.5WY
11	1.5TDL − 1.5WY
12	1.2TDL + 1.2TLL + 1.2WX
13	1.2TDL + 1.2TLL − 1.2WX
14	1.2TDL + 1.2TLL + 1.2WY
15	1.2TDL + 1.2TLL − 1.2WY
16	0.9TDL + 1.5WX
17	0.9TDL − 1.5WX
18	0.9TDL + 1.5WY
19	0.9TDL − 1.5WY

23.6 Design Using Conventional Method as Per Is456:2000

The design of BRBs was carried as per ASCE-7-05-Design Rule for Relative Strength in a tall BRBF [16]. The steel of Fe 345 grade was used for core and plane cement concrete of unit weight of 24 kN/m^3 for casing members. A design excel sheet was created to carry out the design with varying parameters and illustrated over the following steps.
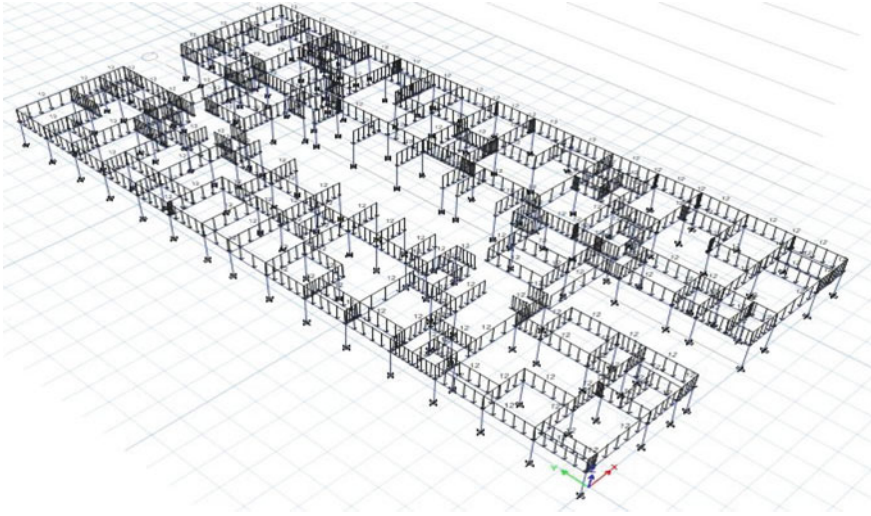
Fig. 23.4 Plan of a floor with load assignment

1. Calculation of the length of BRB (*L*) required in a bay by using trigonometric functions.
2. Assuming the length of non-yielding core by keeping the stiffness of BRB as an important parameter, (Reference publications) to achieve higher stiffness.
3. Defining the dimensions of non-yielding core such as width of core, thickness of core, outer core concrete thickness in both directions and the thickness of outer steel casing to achieve high strength and high stiffness as the main parameter.
4. Calculate the weight of non-yielding core.
5. Defining the dimensions of yielding core such as width of core, thickness of core, outer core concrete thickness in both *x* and *y* directions and the thickness of outer steel along with casing to achieve high strength and high stiffness as main parameters.
6. Calculation of the weight of yielding core (*W*).
7. Calculation of the total weight of BRB such as weight of yielding core and weight of non-yielding core.
8. Calculation of the total stiffness of BRB using the Eq. 23.1.

$$K = (AE/L) \cos 2\theta \tag{23.1}$$

where
   A = area of BRB core, E = young's modulus of steel used, 2.1×10^5 N/mm^2
   L = length of BRB, θ = angle of inclination of bracing.

23.7   Results

The present investigation was on the analysis of behaviour of 19 storey RC structures located in Zone *V*. Four types of models, namely bare frame, shear wall, concentric inverted *V* and eccentric inverted *V* BRBs, subjected to an earthquake force with *Z* = 0.36 are analyzed. The performances such as storey displacement, storey drifts, storey stiffness and storey shear of each model are tabulated Tables 23.4, 23.5, 23.6 and 23.7 and studied in comparison with the performances of bare framed model.

Table 23.4 Comparison of seismic responses for different cases considered

Sl No.	Model	Max. lateral displacement (mm)		Max. drift	
		x	*y*	*x*	*y*
1	Bare frame	140.8	80.7	0.003	0.002033
2	Shear walled	92.9	42.5	0.002025	0.000933
3	Concentric inverted *V* BRBF	84.3	48.1	0.001992	0.001221
4	Eccentric inverted *V* BRBF	84.6	49.6	0.001996	0.001267

Table 23.5 Comparison of seismic responses for different cases considered

Sl No.	Model	Max. storey stiffness (kN/m)		Max. storey shears (kN)	
		x	*y*	*x*	*y*
1	Bare frame	4780808.8	6956439.3	15739.7	19172.2
2	Shear walled	13066206	42877887	24989.4	46095.4
3	Concentric inverted *V* BRBF	5235352	8381545	11429.3	14612.2
4	Eccentric inverted *V* BRBF	5201813	8003786	11337.9	14212.5

Table 23.6 Normalized values of performance of the structure over the in terms of performance of bare frame model

Sl No.	Model	Max. lateral displacement (mm)		Max. drift	
		x	*y*	*x*	*y*
1	Bare frame	1	1	1	1
2	Shear walled	0.65	0.52	0.68	0.46
3	Concentric inverted *V* BRBF	0.59	0.60	0.66	0.60
4	Eccentric inverted *V* BRBF	0.60	0.61	0.67	0.62

Table 23.7 Normalized values of performance of the structure in terms of performance of bare frame model

Sl No	Model	Max. storey stiffness (kN/m)		Max. storey shears (kN)	
		x	y	x	y
1	Bare frame	1	1	1	1
2	Shear walled	2.73	6.16	2.73	6.16
3	Concentric inverted *V* BRBF	1.1	1.21	1.1	1.21
4	Eccentric inverted *V* BRBF	1.08	1.15	1.08	1.15

23.8 Conclusions

The conclusions from the above analysis are as follows.

1. The maximum storey displacement for bare frame model in *X* directions has exceeded the limit of displacement. This was directly proportional to the storey stiffness and shear wall exhibited higher stiffness compared over BF and BRBs models. However, storey shear was higher in the shear wall compared over other two.
2. Modal participating mass ratio for a bare frame model shows a value of more than 90% mass participation at the end of the twelfth mode.
3. Maximum storey displacement of shear walled model satisfies the upper limit of 114 mm ($H/500 = 57*1000/500$) for a nineteenth storeyed building. The maximum storey drift recorded is between storey 6 and storey 8 in *X* direction and is within the specified limit of drift as per IS1893:2016.
4. Variation in terms of storey displacements of BRBs was found to be 9.2% less than shear wall indicating that both concentric and eccentric BRBs patterns are equally better in resisting the earthquake forces.
5. Storey displacement of shear wall was 17.3% better and storey drift of shear walled model was better than that of BRBs along *Y* direction. The variation in terms of storey drift is minimal between concentric *X* BRBs eccentric inverted *V* models indicating that these patterns are equally good in resisting the earthquake force.
6. The storey stiffness of BRBF model is lesser by 81.33% than that of shear walled model. Since BRB system is more effective in resisting earthquake in Zone *V* than shear walled system, reduced stiffness may lead to cost optimization also.
7. The variation in terms of storey shear is minimal indicating both concentric and eccentric BRBF systems are equally good in resisting the earthquake force. The storey shear at different storeys of RC structure with BRBF model is 68.75% lesser than that of shear walled model signifying the use of BRBF in place of shear wall in resisting the earthquake in Zone *V*. Use of BRBF system may contribute to the optimization of mass of structure and hence cost also.

References

1. Medhekar, M.S., Kennedy, D.J.L.: Displacement-based seismic design of buildings—theory. Eng. Struct. **22**(3), 201–209 (2000)
2. Genna, F., Gelfi, P.: Analysis of the lateral thrust in bolted steel buckling-restrained braces. II: Engineering analytical estimates. J. Struct. Eng. **138**(10), 1244–1254 (2012)
3. Piedrafita, D., Cahis, X., Simon, E., Comas, J.: A new modular buckling restrained brace for seismic resistant buildings. Eng. Struct. **56**, 1967–1975 (2013)
4. Hosseini, A., Hassanipour, A.: Numerical modeling of BRB frame systems with and without concrete. J. Multidisc. Eng. Sci. Technol. **2**(8)
5. Sun, H., Jia, M., Zhang, S., Wang, Y.: Study of buckling-restrained braces with concrete infilled GFRP tubes. Thin Walled Struct. **136**, 16–33 (2019)
6. Piedrafita, D., Cahis, X., Simon, E., Comas, J.: A new perforated core buckling restrained brace. Eng. Struct. **85**, 118–126 (2015)
7. https://ascelibrary.org/doi/abs/10.1061/
8. https://www.sciencedirect.com/science/article/pii/S0141029613003805
9. Xie, Q., Zhou, Z., Huang, J.H., Meng, S.P.: Influence of tube length tolerance on seismic responses of multi-storey buildings with dual-tube self-centering buckling-restrained braces. Eng. Struct. **116**, 26–39 (2016)
10. Fahnestock, L.A., Sause, R., Ricles, J.M.: Seismic response and performance of buckling-restrained braced frames. J. Struct. Eng. **133**(9), 1195–1204 (2007)
11. Prinz, G.S., Richards, P.W.: Seismic performance of buckling-restrained braced frames with eccentric configurations. J. Struct. Eng. **138**(3), 345–353 (2011)
12. Della Corte, G., D'Aniello, M., Landolfo, R.: Field testing of all-steel buckling-restrained braces applied to a damaged reinforced concrete building. J. Struct. Eng. **141**(1), D4014004 (2014)
13. Skalomenos, K.A., Inamasu, H., Shimada, H., Nakashima, M.: Development of a steel brace with intentional eccentricity and experimental validation. J. Struct. Eng. **143**(8), 04017072 (2017)
14. IS 1893 (Part 1): 2016.: Criteria For earthquake resistant design of structures—general provisions and buildings
15. IS 875 (Part 1 & 2) 2008.: Code of practice for design loads (other than earthquake) for buildings and structures dead loads and imposed loads
16. Aukeman, L.J., Laursen, P.: Evaluation of the ASCE 7-05 standard for dual systems: Response history analysis of a tall buckling-restrained braced frame dual system. In: Structures Congress 2011, pp. 2707–2717 (2011)

Chapter 24
Analysis of Rotation Capacity of RC Beams Over Formation of Plastic Hinges

R. Prabhakara, B. Nambiyanna, R. Nakul and Bharathi Ganesh

Abstract Rotation capacity of a joint in a structural member under constant moment depends on the characteristics of the formation of plastic hinge. The rotation capacity and plastic hinge formation in RC member depends on many parameters and therefore makes it different over the formation of plastic hinge in steel structural members. It has been observed from the literature that the rotation capacity in RC structural member is influenced by several parameters such as mechanical properties of concrete and steel, geometry of the member, external load and boundary conditions, thus makes it to be an interesting structural behaviour which has to be explored very well. Parametric analysis on the rotation capacity and formation plastic hinge was carried out by collecting more than hundred data from the available literature. Relevant graphs were plotted to demonstrate the variation of plastic hinge length (lp) over the influencing parameters such as cross-sectional dimensions of the beams, grade of the concrete, tension reinforcement and span-to-depth ratio. The length of plastic hinge was calculated based on existing analytical models given by the researchers. Owing to the advancement in the analysis of nonlinear behaviour of structures using sophisticated software, the characterization of plastic hinges has to incorporated in the analysis. These analytical models are very useful and provided more knowledge

R. Prabhakara (✉)
Structural Engineering Division, PGS VTU, Belagavi, Karnataka, India
e-mail: r.prabhakara@gmail.com

B. Nambiyanna
Civil Engineering Department, Ramaiah Institute of Technology, Bangalore, Karnataka, India
e-mail: nambiyanna1@gmail.com

R. Nakul
Civil Engineering Department, Presidency University, Ittgalpura, Rajankunte, Bangalore, Karnataka, India
e-mail: nakul@presidencyuniversity.in

B. Ganesh
Department of Civil Engineering, Nitte Meenaski Institute of Technology, BSF Campus Yalahanka, Bangalore, Karnataka, India
e-mail: bharathi.ganesh@nmit.ac.in

on the behaviour of RC structures. In this study, existing analytical models are evaluated based on the different parameters. The plastic hinge length was determined by nonlinear regression analysis. It was found from the analysis that, large variation was found over the length of plastic hinge for the existing plastic hinge models and the proposed nonlinear regression analysis model yielded better results.

Notations

d	Effective depth of beam, mm
l	Effective length of the beam, mm
l_p	Plastic hinge length, mm
$l_{p.reg}$	Plastic hinge length by regression mm
z	Distance from critical section to point of contraflexure, mm
f'_c	Designed cylinder compressive strength in MPa
f_y	Specified yield strength of the reinforcement, MPa
ρ	Tension zone reinforcement in %
ρ	Compression zone reinforcement in %
θ_p	Plastic rotation (rad)

24.1   Introduction

Engineers are facing the challenging situation in the analysis of RC structures while providing safe and economical buildings to the society. Nonlinear analysis has become one of the important means of achieving the above goal. RC structures are made out of structural elements such as column, beam and slab; also their elastic and inelastic behaviour determines the load response behaviour of the structure. Rotation capacity and formation of plastic hinge in the structural members is one of the main issues in understanding the inelastic behaviour of the structure. More specifically in the earthquake design of structures, ductility plays a key role in the design criteria set by many countries' code provisions.

When the load applied is amplified, the hinge begins to form at locations where the moment is equal to the plastic moment, if further increase in the applied load then hinges transforming into plastic hinges and converting into mechanism followed with failure. Framed structures are designed to achieve the above by proportioning the beams and columns so that the majority of the plastic hinges are formed in the beams not in the column. For this reason, an important parameter is the plastic hinge, which controls the rotation capacity of the structural members. There are two different types of plastic hinges formed in RC structure, such as reversing plastic hinges and unidirectional plastic hinges. The reversing plastic hinge sustains both positive and negative inelastic rotations in the same region, and unidirectional plastic

hinge sustains both in different regions of the beam element during earthquake [1]. It was observed that plastic hinge length l_p in RC beams influenced by a number of parameters such as cross-sectional dimensions, yield and ultimate curvature, material characteristics, tension and compression reinforcement ratios, support type, intensity and nature of loading [2, 3].

The main objective of the present study is to propose a soft computing method that can estimate the rotation capacity and length of plastic hinge by using the available data from experimental studies conducted on RC beams [4–9]. The regression analysis was carried out to find out the influencing parameters on which the rotation capacity and plastic hinge length and also to demonstrate the relationship between the plastic hinge length and rotation capacity.

24.2   Rotation Capacity and Plastic Hinge Length

In the present investigation, the rotation capacity is defined as the rotation of critical section of a beam from yield stage to the ultimate stage, and the plastic hinge length is defined as the length of inelastic zone over which bending moment will be larger than or equal to yield moment over the length of the beam. It is generally agreed that the inelastic rotations are concentrated over a length called "plastic hinge length" where $M \geq M_y$ as shown in Fig. 24.1. The length of plastic hinge is dependent on many parameters, such as the shape of the ultimate bending moment diagram, and is also affected by the length between zero moment points and distance between support, reinforcement ratio, the characteristic strength of concrete and depth of section [2]. The corresponding plastic hinge length is determined with respect to integration of the curvature distribution for distinctive members.

The correlation between the cross section, ductility and the length of plastic hinge needs to be accurately determined. It has been observed there is a large variation in the plastic hinge length formulae proposed by the researchers as shown in Table 24.1. Sawyer, Corley and Mattock, for example, considered only the member's length and depth. Priestley and Park consider the length and diameter of reinforcement of the beam.

Fig. 24.1 Length of plastic hinge
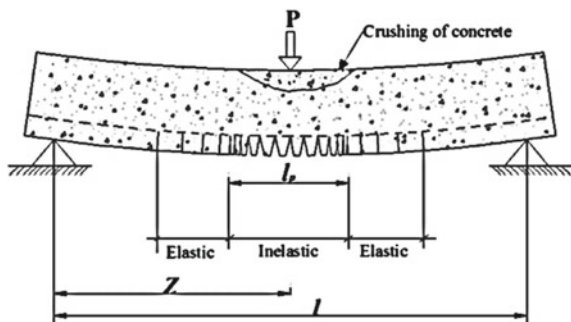
Table 24.1 Existing length of plastic hinge (l_p) models [8]

Reference	Length plastic hinge expression (l_p)
Baker (1956)	$k(z/d)^{1/4}\ d$
Sawyer (1964)	$0.25d + 0.075z$
Corley (1966)	$0.5d + 0.2\ \sqrt{d}\ (z/d)$
Mattock (1967)	$0.5d + 0.05z$
Priestley and Park (1987)	$0.08z + 6d_b$
Paulay and Priestley(1992)	$0.08z + 0.022d_b$
Sheikh and Khoury (1993)	$1.0\,h$
Coleman and Spacone (2001)	$G_f^c/[0.6f'_c(\varepsilon_{20} - \varepsilon_c + 0.8\ f'_c/E_c)]$
Panagiotakos and Fardis (2001)	$0.18z + 0.021d_b$
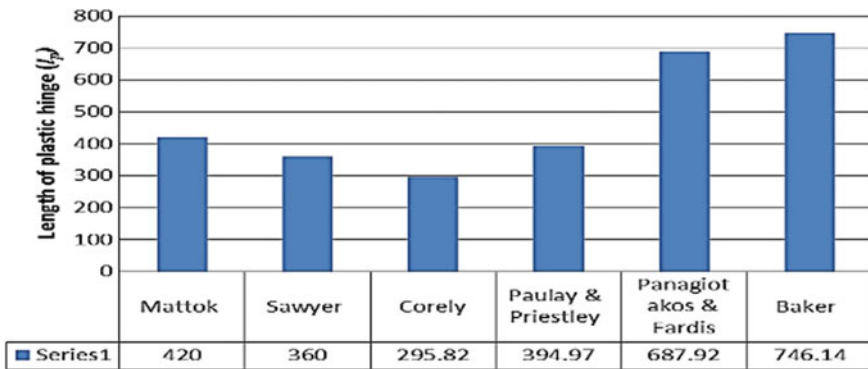
Fig. 24.2 Variation of plastic hinge length (l_p)

To be able to demonstrate the variations in the length of plastic hinge, the geometric and material properties were taken as an example from [6] $l = 6000$ mm, $b = 300$ mm, $d = 540$ mm, $f'_c = 30.9$ MPa, $z = 3000$ mm and $l/d = 11.1$. For the above data, plastic hinge lengths were obtained using the above equations and they are shown in Fig. 24.2. It was observed a large variation in the plastic hinge length which encouraged us to study on the parameters effect and regression analysis.

24.3 Parametric Study

In the present study, the central point loading configuration and different equivalent length of beams were selected from the literature [4–9]. The range of the parameters such as characteristics strength of concrete and steel, width and depth of beams,

Table 24.2 Range of parameters used

Parameters	Parameter range
f'_c (MPa)	20–129.1
f_y (MPa)	250–678
l (mm)	1000–12,000
b (mm)	50–500
d (mm)	90–950
z (mm)	500–6000
ρ (%)	0.13–6.45
ρ' (%)	0–4.84
l/d	4.17–21.82

tension and compression steel percentages and all other essential parameters that affect the beam behaviour under central point loading is shown in Table 24.2.

24.4 Determination of Length of Plastic Hinge

The length of the plastic hinge l_p was determined based on different parameters obtained from the previous studies. The beam plastic rotation (θ_p) was calculated from Eq. (1) [10].

$$\theta_p = \frac{0.004}{(x_u/d)} \tag{1}$$

The plastic hinge length l_p was calculated based on Eq. (2) [2], and curvature at yielding moment (φ_y) and the curvature at ultimate moment (φ_u) and plastic hinge length values were analytically calculated.

$$l_p = \frac{\theta_p}{(\varphi_u - \varphi_y)} = \frac{\theta_p}{\varphi_p} \tag{2}$$

Illustrative graphs have been plotted to observe the variation of l_p against the parameters which are shown in Fig. 24.3a–f.

It has been observed from Fig. 24.3a–f that the length of plastic hinge has not shown much variation with grade of concrete, and however, reduction in l_p was observed with increase in reinforcement ratio and further it was observed that l_p increased when the depth of the beam increased, l/d ratio, z and z/d ratio.
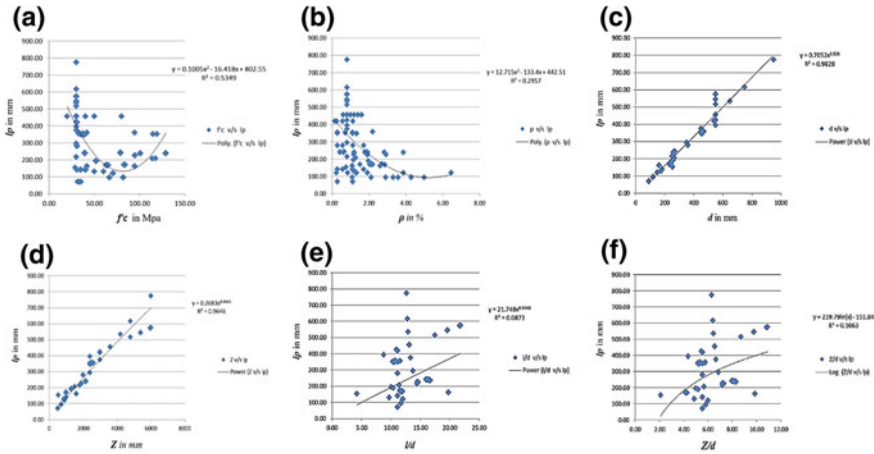
Fig. 24.3 Plastic hinge length (*l*p) versus various parameters

24.5 Nonlinear Regression Analysis

Nonlinear regression analysis is a method of mathematical modelling. In this study, cross-sectional dimensions, material characteristics, yielding and ultimate deflections, tension and compression reinforcement ratios were observed and parameters that affect on length of plastic hinge are analysed by using the nonlinear regression analysis. Formulated our regression equation for plastic hinge length (l_p) as follows.

$$l_p = 0.37 \times b^{0.00896} \times d^{0.667} \times f'c^{-0.0016} \times z^{0.3264} \times \rho^{-0.00207} \times \left(\frac{l}{d}\right)^{0.059266} \quad (3)$$

It has been observed from Fig. 24.4 that the comparison between regression plastic hinge length $l_{p\ reg}$ versus existing models l_p trend lines shows that the proposed model is predicted well with Mattock, Sawyer, Corely and Baker's models and R^2 values are almost equal to unity.

It has been observed from Fig. 24.5 that the comparison between regression plastic hinge length $l_{p\ reg}$ versus θ_p trend lines shows that there is no significant relationship between l_p and θ_p.

24.6 Conclusions

Based on the parametric study and proposed nonlinear regression analysis, the following conclusions are drawn.
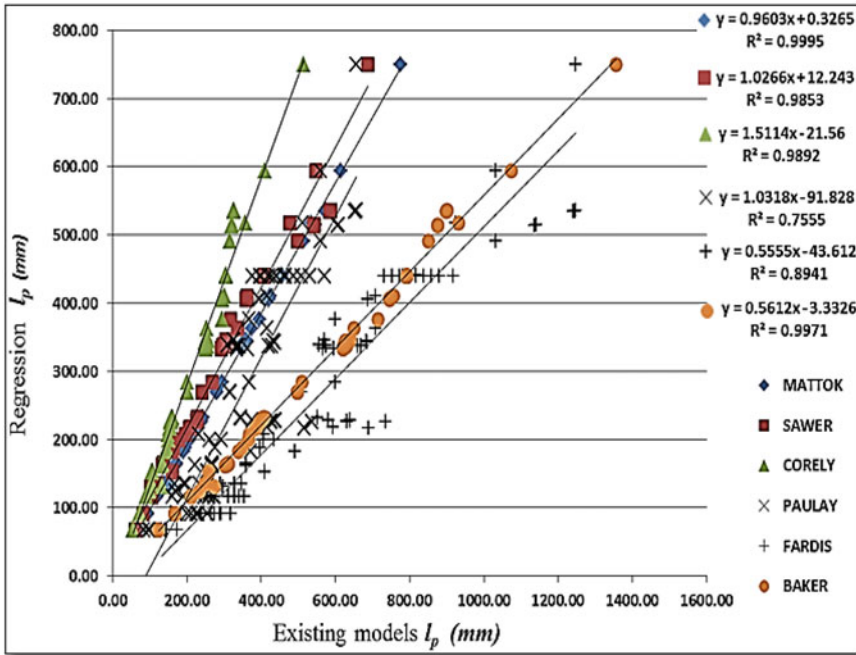
Fig. 24.4 Comparison between regression $l_{p\,reg}$ and existing models l_p

Fig. 24.5 Comparison between regression l_p and θ_p
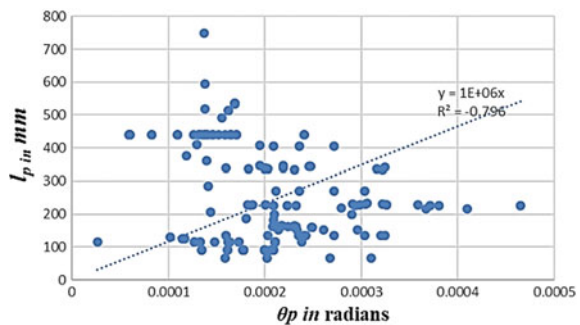
- The plastic hinge length results are obtained by using plastic rotation and curvatures at ultimate and yield load (vide Eqs. 1 and 2).
- Demonstrative graphs have been plotted to show the variation of influencing parameters. It was observed from Fig. 24.3 that the length of plastic hinge has not shown much variation with grade of concrete, and however, reduction in l_p was observed with increase in reinforcement ratio.
- Further, it was observed that l_p amplified with increase in depth, l/d ratio, z and z/d ratio.

- Analytical expressions given in the literature indicated that only the cross-sectional dimensions are under the bending effect of beam and other influencing parameters were not considered.
- The plastic hinge length (l_p) obtained by expressions given by the researchers gave different values and are not comparable (Fig. 24.2).
- It has been observed that analytical plastic hinge expression and proposed nonlinear regression expression yielded results that are comparable.
- Based on the comparison between l_p calculated by existing model and $l_{p.reg}$ calculated by nonlinear regression model, the results show that the nonlinear regression plastic hinge model ($l_{p.reg}$) is versatile and can be used all types RC beams.
- Based on comparison between rotation capacity and length of plastic hinge, there was no significant relation between them and hence, further investigation has to be done over large number of data.

References

1. Mendis, P.: Plastic hinge lengths of normal and high-strength concrete in flexure. Adv. Struct. Eng. **4**(4), 189–195 (2002)
2. Kheyroddin, A., Naderpour, H.: Plastic hinge rotation capacity of reinforced concrete beams. Int. J. Civil Eng. **5**(1), 30–47 (2007)
3. Gopinath, A., Nambiyanna, B., Nakul, R., Prabhakara, R.: Parametric study on rotation and plastic hinge formation in RC beams. J. Civil Eng. Tech. Res. **2**, 393–401 (2014)
4. Bigaj, A., Walraven, J.C.: Size effect on rotational capacity of plastic hinges in reinforced concrete beams. CEB Bull. Inf. **218**, 7–23 (1993)
5. Bosco, C., Debernardi, P.G.: Influence of some basic parameters on the plastic rotation of reinforced concrete elements. CEB Bull. Inf. **218**, 25–44 (1993)
6. Lopes, S.M.R., Bernardo, L.F.A.: Plastic rotation capacity of high-strength concrete beams. Mater. Struct. **36**(1), 22–31 (2003)
7. Fransson, H.: Rotation capacity of reinforced high strength concrete beams. Licentiate thesis. TRITA-BKN. Bulletin 32 (1997) ISSN 1103-4270 ISRN KTH/BKN/B--32—SE
8. Zhao, X., Wu, Y.F., Leung, A.Y., Lam, H.F.: Plastic hinge length in reinforced concrete flexural members. Procedia Eng. **14**, 1266–1274 (2011)
9. Manyoung Ko, M.Y., Kim, S.W., Kim, J.K.: Experimental study on the plastic rotation capacity of reinforced high strength concrete beams. Mater. Struct. **34**(5), 302–311 (2001)
10. Carpinteri, A., Corrado, M., Mancini, G., & Paggi, M.: Size-scale effects on plastic rotational capacity of reinforced concrete beams. ACI Struct. J. **106**(6)

Chapter 25
Influence of Metallurgical Parameters on Wear and Impact Characteristics in High Chromium Manganese Irons

G. J. Naveen, P. Sampathkumaran, S. Seetharamu, T. Pramod, Ashirwad Pandey and A. Sathyanarayanaswamy

Abstract Nickel chromium irons such as Ni-hard of different grades (high chromium iron) are being employed as wear-resistant materials in thermal power generation applications in view of their excellent inherent material characteristics. They are being deployed in bull ring segments, orifice, rolls, MPO, liners, etc., in thermal power plants and other engineering industries. But, these materials being brittle fail to withstand transient load. To overcome this problem, manganese is added to chromium iron to improve its impact characteristics apart from being wear resistant. In this context, the erosion and abrasion properties affected by metallurgical features are considered important from the point of enhancing its impact energy, without much sacrificing the wear resistance. Considering these aspects, high chromium manganese irons have been prepared in grey cast iron metal mould of section size of 24 mm, followed by heat treatment. The erosion, abrasion and impact energy have been studied using jet erosion, rubber wheel abrasion and drop weight impact test setup for varying manganese content in the range of 5, 10 and 15%. It is very much evident from the metallurgical investigations involving light microscopy that the least Mn

G. J. Naveen · P. Sampathkumaran · A. Pandey · A. Sathyanarayanaswamy
Department of Mechanical Engineering, Sambhram Institute of Technology,
Bengaluru 560097, India
e-mail: gj.naveenprakash@gmail.com

P. Sampathkumaran
e-mail: sampathkumaran53@gmail.com

A. Pandey
e-mail: ssp.ashirwad@gmail.com

A. Sathyanarayanaswamy
e-mail: asnsprabha2@gmail.com

S. Seetharamu
Department of Mechanical Engineering, Nitte Meenakshi Institute of Technology,
Bengaluru 560064, India
e-mail: ssramu278@gmail.com

T. Pramod (✉)
The Energy and Resources Institute, Bengaluru 560071, India
e-mail: tpramod5@yahoo.co.in

content sample (5% manganese content) shows the highest wear resistance, whereas on the other hand, the highest manganese addition of 15% exhibits highest impact energy. The hardness and the metallurgical features support these findings as one could visualize the phases and carbide morphological features getting transformed during the heat treatment process, thus favouring the abrasion, erosion and impact properties. These results have been compared and analysed with the results obtained from high chromium iron samples.

Keywords High chromium manganese iron · Erosion · Abrasion · Impact energy · Carbide size · Retained austenite

25.1 Introduction

The family of white irons including cast irons and nickel chromium irons have been investigated and reported [1, 2] extensively in the literature especially the high chromium irons, in view of its possessing good wear resistance property due to the presence of hard carbides in a hard and tempered martensitic matrix [3, 4]. But, there is one drawback with regard to its usage in power, mining, cement and other industries, and it is the brittle nature of it for not taking sudden load. Many researchers [5, 6] have made attempts on the development of wear-resistant high chromium cast iron material to withstand load under impact situations, through the addition of gamma forming elements such as manganese (Mn), copper (Cu) and nickel (Ni). Among them, Mn being cost-effective and productive has been tried up to about 5% by weight, beyond which the literature information is scanty. The influence of microstructure on the wear properties has been studied and reported in [7, 8]. Basak et al. [9] in their work have demonstrated the role of addition of Mn (4% by weight) in high chromium iron for enhanced impact energy but at the same time not sacrificing much on the wear resistance property. Thus, a trade-off between wear and impact characteristics is very much required at this stage. Keeping the literature points in view, the alloying element manganese is added in the range of 5–15% by weight to high chromium iron to improve the load-bearing capacity alongside wear property, as manganese is known to be a strong austenite-stabilizing element. In this work, the manganese concentration has been varied at 5, 10 and 15 weight percent to chromium (16–18 weight percent), and the castings are produced in a metal mould of section size 24 mm in an induction melting furnace, followed by heat treatment. The erosion and abrasion characteristics have been evaluated in a jet erosion and rubber wheel abrasion test rigs, respectively. The impact energy and hardness measurements are carried out using drop weight impact tester and Rockwell hardness tester. The results have been compared with high chromium iron without manganese addition in it. The light microscopy has been taken to examine and interpret the microstructures.

25.2 Materials and Methods

The materials chose are high chromium (16–18%)-alloyed iron and high chromium (16–18%) manganese-alloyed iron with manganese levels of 5, 10 and 15 weight percent. The castings are made by induction melting route by pouring liquid metal into the grey cast iron metal mould of section size 24 mm having the dimensions of $150 \times 100 \times 25$ mm^3. The test coupons are cut to a size of $75 \times 25 \times 6$ mm^3 using abrasive cutting machine from the casting as per the schematic diagram shown in Fig. 25.1 for erosion and abrasion tests and sample size of $55 \times 10 \times 10$ mm^3 for impact energy test.

The test samples are given heat treatment in a muffle furnace with an austenitization soak for 6 h at 950 °C followed by stress relieving treatment for 30 min at 200 °C. The erosion and abrasion tests were carried out in a jet erosion test rig and rubber wheel abrasion, respectively, as per the guidelines given in ASTM standard [10, 11]. The impact energy test is done in accordance with ASTM standard [12] guidelines using drop weight impact tester using an un-notched specimen. The hardness has been measured using Rockwell C hardness tester (conical indenter; with vertex angle 120°; hemispherical tip of radius 200 μm), at a test load of 150 kg. The metallographic procedure has been adopted to arrive at the microstructure and carbide volume using optical microscopy coupled with an image analyser. The retained austenite measurement has been carried out using X-ray stress analyser equipment with chromium as the target material. The details of characterization procedures are reported in [13, 14]. The chemical composition has been determined using optical emission spectroscopy.
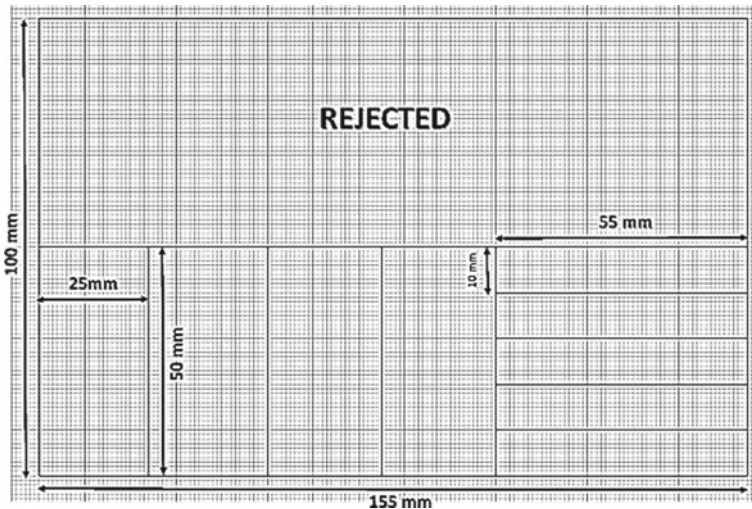

Fig. 25.1 Schematic diagram of casting made, showing the location of test samples for various tests

25.3 Results and Discussions

The sample designation along with its chemical composition is given in Table 25.1, and the hardness, retained austenite and carbide volume are given in Table 25.2, respectively. All the test data provided in this study are pertaining to the heat-treated conditions only.

25.3.1 Erosion and Abrasion

The erosion test conducted at 45° and 90° impact angles are shown in Fig. 25.2. It is very well seen from the erosion data that the maximum loss takes place at 45° impact angle and the least at 90° impact angle for HiCr5Mn, HiCr10Mn and HiCr15Mn samples. For HiCr iron sample, the highest erosion is noticed at 90° and the lowest at 45° impact angle. As per the theory [15], the highest erosion loss is reported at 45° for ductile materials and least erosion loss at 90° for brittle materials. In the present case also, the erosion loss of HiCr closely resembles with the data pertaining to the brittle material, and hence, it is exhibiting highest hardness and in turn low erosion resistance. This is on the expected lines as chromium carbide in HiCr which is having highest hardness as well as carbide volume (Table 25.2) and supports the erosion test data. In the case of HiCrMn iron samples, HiCr15Mn is showing the highest erosion loss compared to HiCr5Mn. Accordingly, the erosion data varies

Table 25.1 Chemical composition of HiCrMn iron samples

Sample identification	Composition (wt%)							
	C	Mn	Si	Cr	Ni	Mo	S	P
16–18% Cr (HiCr)	2.87	0.60	0.78	16.50	0.98	1.96	0.042	0.040
5% Mn 17–19% Cr (HiCr5Mn)	2.39	4.60	2.15	18.65	0.92	1.82	0.044	0.090
10% Mn 17–19% Cr (HiCr10Mn)	2.35	9.70	1.85	17.60	0.82	1.80	0.040	0.085
15% Mn 17–19% Cr (HiCr15Mn)	2.43	14.80	1.98	18.15	0.87	1.75	0.042	0.080

Table 25.2 Hardness, retained austenite and carbide volume of HiCrMn iron samples

Sample designation	Rockwell C hardness	Retained austenite (%)	Carbide volume (%)
HiCr	64.7	10	29.0
HiCr5Mn	61.0	50	27.5
HiCr10Mn	53.0	60	25.5
HiCr15Mn	50.9	64	24.0
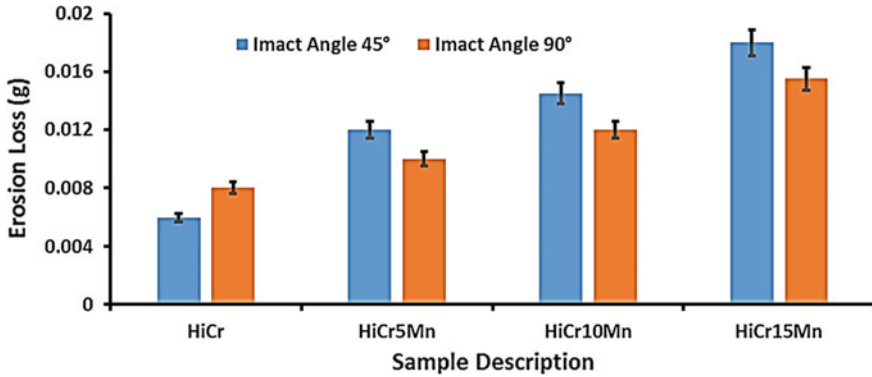
Fig. 25.2 Erosion loss at 45° and 90° impact angles
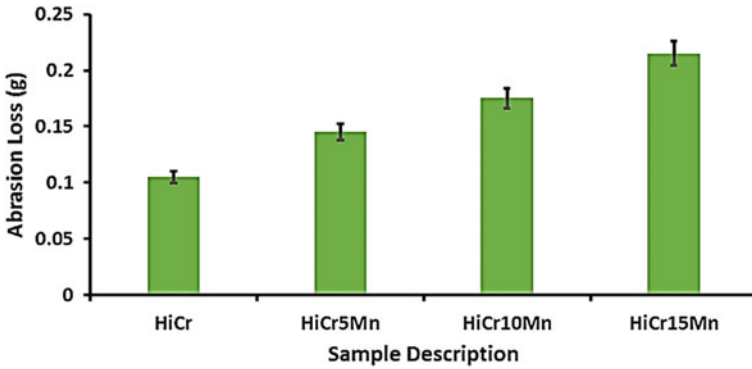
Fig. 25.3 Abrasion loss

with respect to hardness and carbide volume. Thus, it is seen that the addition of manganese content from 5 to 15% lowers the hardness and carbide volume and in turn increases the erosion loss.

The trend in abrasion loss (Fig. 25.3) remains the same like in the case of erosion loss with respect to the manganese addition. Higher the manganese level, higher the abrasion loss and vice versa. The highest abrasion loss is obtained for HiCr15Mn and least for HiCr5Mn as the hardness and carbide volume values support these trends (Table 25.2). The HiCr iron samples exhibit the least, as it is hard and brittle.

25.3.2 Impact Energy

It is very well known that higher is the austenite content, lower is the carbide volume and better is its toughness characteristics. In the present case also, higher manganese
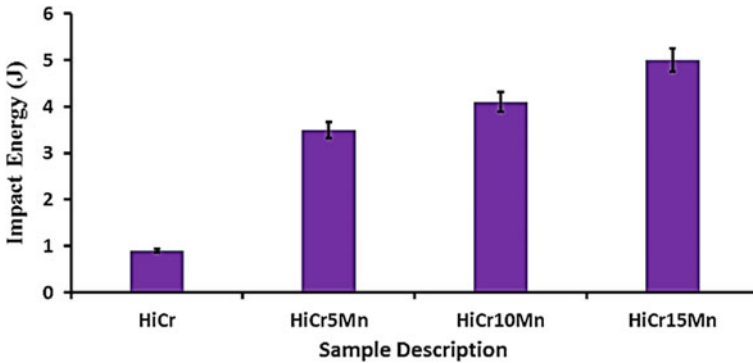
Fig. 25.4 Impact energy

content sample (HiCr15Mn) has yielded higher impact energy and vice versa as can be seen from Fig. 25.4. HiCr iron sample being brittle is showing very low impact energy, and hence, it cannot take any sudden shock. The retained austenite values also give credence to the data, i.e., retained austenite content of HiCr iron is about 10%, whereas HiCr15Mn sample is possessing retained austenite content in the range 50–64%. The results obtained are in line with the published reports [16–18], wherein with increase in manganese content, the wear resistance decreases. But, the impact energy increases due to the higher concentration of manganese present in it which acts as austenite-stabilizing agent. Hence, the reported data and the present results pertaining to the impact energy are in good agreement with each other. Thus, the main objective of obtaining higher impact energy in HiCr iron samples has been achieved by the addition of manganese to chromium iron at three levels. Further, it is envisaged that increase in manganese concentration beyond 15% would yield enhanced impact energy levels, which is not attempted in this work.

The impact energy value obtained in the present work is about 50% better than the value reported [9], whereas the wear property decreases by 20%. Thus, the use of HiCr15Mn seems to be beneficial to withstand the sudden load and at the same time not forgoing wear resistance.

25.3.3 Light Microscopic Features

The light micrographs of HiCr, HiCr5Mn and HiCr10Mn at a magnification of $500\times$ and $1000\times$ are shown in Figs. 25.5 and 25.6, respectively. The microstructure of HiCr iron reveals primarily eutectic carbides of different sizes in a matrix of predominantly martensite. Further, the carbides are distributed non-uniformly in the matrix. The retained austenite content obtained in this case is about 10%. The HiCr5Mn (Fig. 25.5b) shows fine carbides and is more or less uniformly distributed in the matrix of austenite. The occurrence of hexagonal carbides along with fine carbide

Fig. 25.5 Light microstructure of **a** HiCr, **b** HiCr5Mn and **c** HiCr10Mn samples at a magnification of 500×
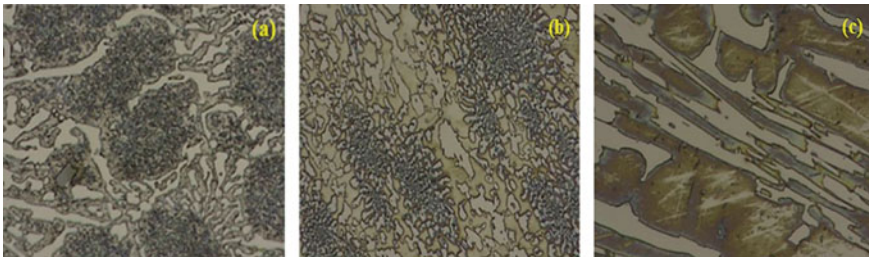
Fig. 25.6 Light microstructure of **a** HiCr, **b** HiCr5Mn and **c** HiCr10Mn samples at a magnification of 1000×

network is observed in the matrix. The addition of 10% manganese (HiCr10Mn) reveals long carbides with hyper-eutectic carbides in the matrix of austenite. Thus, all these micrographs help to discourse the erosion, abrasion and impact energy results in a meaningful way. It is quite logical about the fact that by considering the micrographs of HiCr iron, HiCr5Mn and HiCr10Mn, the carbide morphological features, i.e., size, its distribution and matrices decide its properties. In fact, microstructure dictates the characteristics of HiCr family. The literature reports [19–21] give more information on high chromium manganese irons regarding the impact energy aspects influenced by varied manganese levels, mould type, size as well as the heat treatment effect.

In summary, the results pertaining to the wear and impact properties of HiCr5Mn have yielded best wear resistance compared to HiCr10Mn and HiCr15Mn, whereas HiCr15Mn exhibited highest impact energy level compared to HiCr5Mn and HiCr10Mn. HiCr although has shown very poor impact energy, but its wear resistance is much superior compared to high chromium manganese iron samples. HiCr sample has exhibited brittle behaviour, i.e., the erosion loss is higher at 90° impact angle and lower at 45° impact angle which are in line with the reported predictions in the literature [15]. Thus, in the HiCrMn samples, wear resistance is in between brittle and ductile behaviour in view of the fact that for ductile samples, the wear is the lowest at normal impact angle (90°) and highest at shallow impact angles (30° and 45°)

as reported in [15]. Further, supporting experimental values, viz., hardness, retained austenite content, carbide volume and microstructures compiled, lend credence to the above findings.

Thus, the work may summarize that the dual objectives of obtaining best wear resistance and highest impact energy in high chromium manganese iron samples have been achieved based on different manganese concentrations in high chromium iron.

25.4 Conclusions

Based on the work carried out on HiCrMn iron samples, the following conclusions are drawn:

- HiCr sample shows the best erosion and abrasion resistance, but poor impact resistance in view of its material and metallurgical characteristics.
- HiCr5Mn iron samples exhibits the highest wear resistance compared to HiCr10Mn and Hicr15Mn samples.
- Impact energy of HiCr15Mn shows the highest among the high chromium manganese iron and high chromium iron samples investigated.
- A trade-off between wear and impact properties is desirable by choosing 10% Mn addition to HiCr in industries requiring good wear resistance property coupled with higher impact energy level.

All these test results have been substantiated with the supporting evidences such as hardness, retained austenite and carbide morphological features. It is inferred from this study that the addition of 15% of Mn to chromium iron is preferred for application involving impact load, whereas HiCr is best suited for erosion and abrasion resistance properties.

References

1. ELsawy, E.E.T., EL-Hebeary, M.R., EL-Mahallawi, I.S.E.: Effect of manganese, silicon and chromium additions on microstructure and wear characteristics of grey cast iron for sugar industries applications. Wear **390–391**, 113–124 (2017)
2. Jumaev, A.A.: Comparative study of the structure of casting from white wear resistant cast iron. Int. J. Adv. Res. Sci. Eng. Technol. **5**(12), 7575–7577 (2018)
3. Gundlach, R.B., Parks, J.L.: Influence of abrasive hardness on the wear resistance of high chromium irons. Wear **46**(1), 97–108 (1978)

4. Qui, B., Xing, S.M., Dong, Q., Liu, H.: Effect of impact energy on wear behaviour of high chromium white iron produced by liquid die forging. In: International Conference on Metal Material Processes and Manufacturing, MATEC Web of Conferences, vol. 207, 03011, pp. 1–5 (2018)
5. Tong, J.M., Zohu, Y.Z., Shen, T.Y., Deng, H.J.: The influence of retained austenite in high chromium cast iron on impact abrasive wear. Wear **135**(2), 217–226 (1990)
6. Patwardhan, A.K., Mehta, M.L., Sharma, C.P.: Manganese as an additive to chromium white iron for producing wear resistant microstructure. AFS Int. Cast Metal J. **6**, 3–9 (1981)
7. Laird, G.: Some comments on white cast iron microstructure and wear properties. AFS Trans. **128**, 497–504 (1993)
8. Kadhim, M.J., Abood, A.N., Yaseen, R.S.: The role of manganese on microstucture of high chromium white cast iron. Modern Appl. Sci. **5**(1), 179–1185 (2011) (Canadian Centre of Science and Education)
9. Basak, A., Penning, J., Dilewijns, J.: Effect of manganese on wear and impact strength of 12% chromium cast iron. AFS Int. Cast Metal J., vol. **6** (1981)
10. ASTM G76-18: Standard test method for conducting erosion tests by solid particle impingement using gas jets. ASTM International, West Conshohocken, PA (2018)
11. ASTM G65-04: Standard test method for measuring abrasion using the dry sand/rubber wheel apparatus. ASTM International, West Conshohocken, PA (2004)
12. ASTM E23-12: Standard test methods for notched bar impact testing of metallic materials. ASTM International, West Conshohocken, PA (2012)
13. Sampathkumaran, P., Ranganathaiah, C., Seetharamu, S., Kishore, : Effect of increased manganese addition and mould type on the slurry erosion characteristics of Cr-Mn iron systems. Bull. Mater. Sci. **31**(7), 1001–1006 (2008)
14. Sampathkumaran, P., Ranganathaiah, C., Seetharamu, S., Kishore, : Effect of manganese content and mould size on abrasion and slurry erosion behavior of chromium-manganese iron systems investigated by positron lifetime spectroscopy. Wear **267**(9 & 10), 1558–1565 (2009)
15. Raask, E: Erosion Wear in Coal Utilization. Book, Taylor & Francis Inc. Publication, pp. 1–621 (1988)
16. Guo, Z.H., Xiao, F., Lu, S., Li, H., Liao, B.: Effects of heat treatment on the microstructure and wear resistance of a high-chromium cast iron for rolls. Adv. Mater. Sci. Eng., pp. 1–7 (2016)
17. Hadji, A., Bouhamla, K., Mouche, H.: Improving wear properties of high chromium cast iron by manganese alloying. Int. J. Metal Cast. **10**(1), 43–55 (2015) (Springer Publications)
18. Kvon, S.V.S., Kulikov, V.Y., Filippova, T.S., Omarova, A.E.: Using high chromium iron as material for production of the equipping components of mine shafts. Metalurgija **55**(2), 206–208 (2016)
19. Krishnamoorthy, P.R., Seetharamu, S., Sampathkumaran, P.: Erosion wear in thermal power plants. 55th R & D Session, CBI & P (1989)
20. Agunsoye, J.O., Ochulor, E.F., Talabi, S.I., Olatunji, S.: Effect of manganese additions and wear parameter on the tribological behaviour of NFGrey (8) cast iron. Tribol. Ind. **34**(4), 239–246 (2012)
21. Sampathkumaran, P., Ranganathaiah, C., Seetharamu, S., Kishore.: Processes induced structural transformations and the impact properties of Cr-Mn iron systems. Mater. Manuf. Process. **23**, 320–325 (2008) (Tayler & Francis Publications)

Chapter 26
Simulation of High-Temperature Solid Particle Erosion of HVOF-Sprayed NiCrBSiFe and WC-Co/NiCrBSiFe-Coated Wall Using CFD

K. Raghavendra Naik, R. K. Kumar, V. Saravanan, S. Seetharamu and P. Sampathkumaran

Abstract The erosion characteristics of HVOF-sprayed NiCrBSiFe and WC-Co/NiCrBSiFe coatings made on SS347 grade steel have been investigated for high-temperature behaviour, especially in the boiler tubes used in thermal power generation. The computational fluid dynamic model has been adopted to study the influence of the impingement angle on the erosion properties of the coatings. The self-fluxing NiCrBSiFe alloys have shown the best erosion resistance of about two times at room temperature and about four times at 700 °C when compared with a composite powered coating of WC-Co/NiCrBSiFe. At 700 °C, The WC-Co/NiCrBSiFe undergoes thermal cracking between nickel rich and WC metallic phases due to low oxidation and thermal expansion mismatch between them leading to degradation of the coating; however, at this temperature, the self-fluxing alloy of NiCrBSiFe performed better when compared to WC-Co/NiCrBSiFe coating. The simulation is done with turbulence model, namely shear stress transport (SST) model with a base on user-defined function predicted from the experimental results. The computational fluid dynamic simulated data obtained from SST model and the experimental results were compared, and they are in good agreement with each other.

Keywords Erosion rate · Solid particle impact · Coatings · Computational fluid dynamics (CFD) · SST turbulence model

K. Raghavendra Naik (✉) · R. K. Kumar · V. Saravanan
Material Technology Division, Central Power Research Institute, Bengaluru 560080, India
e-mail: raghavendranaik454@gmail.com

S. Seetharamu
Department of Mechanical Engineering, Nitte Meenakshi Institute of Technology,
Bengaluru 560064, India

P. Sampathkumaran
Department of Mechanical Engineering, Sambhram Institute of Technology,
Bengaluru 560097, India

26.1 Introduction

Solid particle erosion is a serious problem in power plants, which reduces the service life of the mechanical components operating at high temperature due to impingement of coal and ash particles [1–3]. For instance, boiler tubes undergo severe degradation due to impaction of ash particles, containing quartz leading to the forced shutdown of the plant [4, 5]. The coating has been proven to be one of the advanced methods employed to set the best erosion resistance due to solid particle impact. There are several methods of deposition process known, and it is dependent on the type of application. For example, the coating processes such as weld overlay, thermal spray, diffusion, laser cladding, etc., adopted in thermal power plants face certain drawbacks such as very thin coatings are possible in the diffusion process, embrittlement taking place at the interface due to repeated welding and leading to crack formation in weld overly and very difficult to repair or refurbish at site. In view of the problem faced in this process, thermal spray coating gains momentum [6, 7] as they overcome them.

The factors like hardness, velocity, impingement angle, size and shape of the erodent need to be considered to study the erosion behaviour in detail both at room and elevated temperature among them; velocity and impact angle play a major role in selecting the coatings [8]. As per the theoretical predictions, ductile materials erode more rapidly at shallow impact angle (10°–30°); however, brittle material erodes more at normal impact angle (70°–90°) [9, 10]. The erosion rate at elevated temperatures is much higher at shallow as well as at normal impact angles compared to the room temperature erosion [11].

The high-velocity oxy-fuel (HVOF) process comes under the thermal spray, and it is being deployed in industries effectively from the point of erosion protection. The advantages of this spraying process are that it yields lower porosity levels, higher density, lower oxide content and superior bond strength compared to the conventional coatings [12].

Self-fluxing thermal spray coating like Ni-base will provide high erosive wear resistance at low and moderate temperature, and hence, it has received widespread applications [13]. The distributed hard WC particles in the Ni matrix will increase the hardness of the coating, thereby improving the erosion resistance at a higher temperature. The published information on 35% WC with NiCrBSiFe has shown superior wear resistance up to 500 °C in view of higher hardness and minimal porosity level achieved [14–16]. In the present study, an attempt has been made on the wear characteristics evaluation beyond 500 °C.

In recent trends, computational fluid dynamic (CFD) approach has become a useful tool to assess the erosion rate both at room and high temperature, and many works have been reported on this to account for the elevated temperature erosion behaviour of bulk material and coatings. The experimental data, therefore, serves as a validation tool to predict erosion behavior computationally. Thus, CFD is one of the advanced methods employed to predict the erosion phenomena for different flow conditions both at room temperature and high-temperature regimes. The CFD approach in conjunction with experimental data has been effectively used [17–21]

to study the wall thinning of pipes in the pulverised fuel system, slurry and silt erosion, ash erosion in pressure parts, etc., evolving amicable solutions to the critical problems faced in thermal power plants.

The published information on the topic (up to 800 °C) for plasma-sprayed coating with lower velocity of about 4 m/s indicates lower erosion of NiCrBSi and highest erosion of WC-CO/NiCrBSi. However, in the present work, the attempt has been made with HVOF self-fluxing alloy of NiCrBSiFe and the distributed hard 35% WC particles in the nickel matrix with high velocity up to 36 m/s, which simulating boiler environment and compared the erosion rate intensity through CFD modelling.

26.2   Experimentation

26.2.1   Materials and Methods

The SS-347 steel is the substrate material used as this finds extensive applications in a pulverised coal-fired thermal power plant. The coatings were made with a velocity of 680 m/s on the SS-347 base material of size $150 \times 150 \times 7$ mm^3. The test samples of size $15 \times 15 \times 7$ mm^3 were prepared using electro-discharge machining cutting process for testing and microstructural examination. The regular metallurgical procedure has been adopted for polishing and etching. The input conditions employed in the coating process and powder coating details are shown in Tables 26.1 and 26.2.

26.2.2   Erosion Test at Elevated Temperature

An erosion test set-up was designed and built to achieve the real service condition experienced in boiler involving high temperature as shown in Fig. 26.1. The morphology of erodent, namely silica sand, is shown in Fig. 26.2. The erosion test was

Table 26.1   HVOF spray parameter

Powder: Praxair 1350 VM size: −45 to +15 μm, JP5000HVOF		
1	Type of fuel: kerosene @170 PSIG, SCFH	5.8
2	The flow rate of oxygen @210 PSIG, SCFH	1850
3	Distance between nozzle to target, metre	0.381
4	Nitrogen as carrier gas @ 50 PSIG, SCFH	23
5	The velocity of particle pertaining to spray, m/s	680[a]
6	Per pass thickness of deposit formed	15
7	The feed rate of powder, kg/min	0.09

[a]Provided by the supplier of the coating

Table 26.2 Powder coating details

Code of sample	Chemical composition (weight percentage) of coating	Range of powder size (μm)
D1	NiCrBSiFe (14.7 Cr–3.21 B–4.35 Si–3.75 Fe–Bal–Ni)	−45 to +15
N1	35 WC-Co/65 NiCrBSiFe (30.6 W–4.2 Co–10.4 Cr–47.6 Ni–1.8 B–2.6 Si–2.8 Fe)	−45 to +15

1. Air Compressor
2. Air Filter
3. Pressure Gauge
4. Moisture controller
5. Digital Mass flow controller
6. Fluid Heater
7. Nozzle system
8. Particle Feeder
9. Specimen chamber
10. Test sample
11. Sample holder
12. Thermocouple
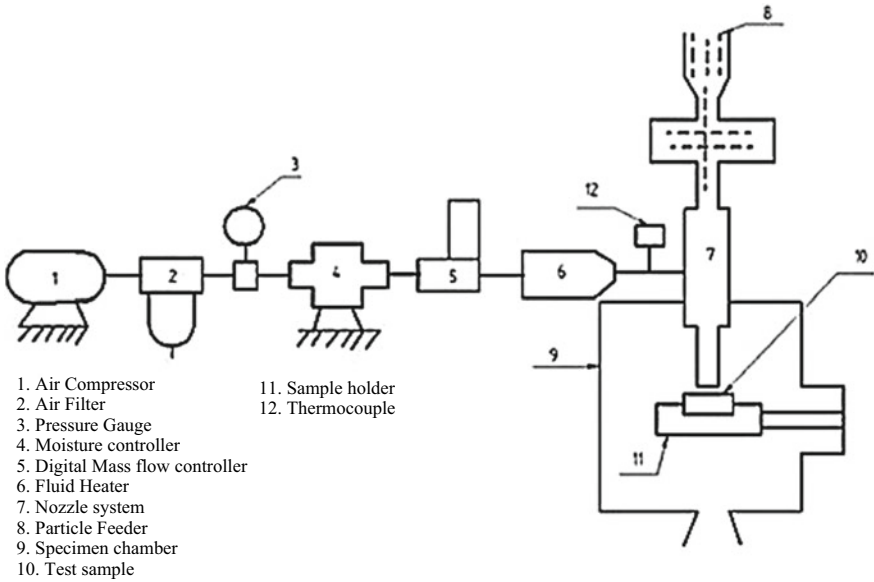
Fig. 26.1 High-temperature erosion test rig diagram
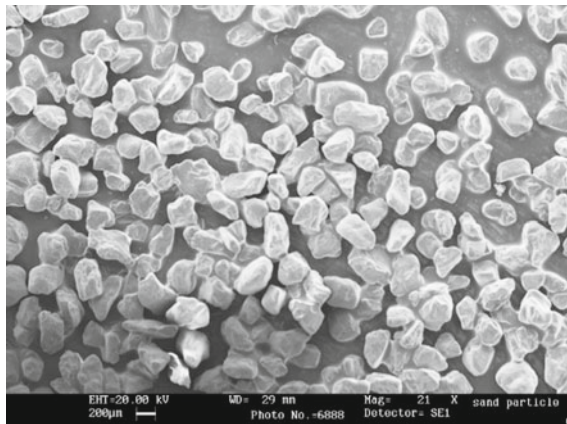
Fig. 26.2 Structure of erodent (silica sand)

conducted with the target sample fixed in a holder, which can be moved to set the desired impact angle of 15°, 30°, 45°, 75° and 90° which has been on the varying intensity levels of damage from the leading edge to the trailing edge. This is an accelerated test with the oil- and moisture-free dry air obtained from a compressor. Dry air is mixed with silica sand and then made to impinge on the sample to study the erosion behaviour both at room temperature and high temperature (700 °C). The particle velocity has been measured using double-disc device [22]. Table 26.3 gives the input parameters employed in this work.

26.2.3   Microstructure Observations

Figures 26.3 and 26.4 show the microstructure of the typical cross section of the

Table 26.3   Erosion test conditions

1	Abrasive type	Silica sand
2	Particle size	70 AFS
3	Particle velocity	36 m/s
4	Feed rate	142 g/min
5	Impingement angle	90° and 30°
6	Test temperature	Ambient temperature and high temperature (700 °C)
7	Test duration	7 min
8	Test specimen size	25 × 25 × 7 mm
9	Diameter of nozzle	5 mm
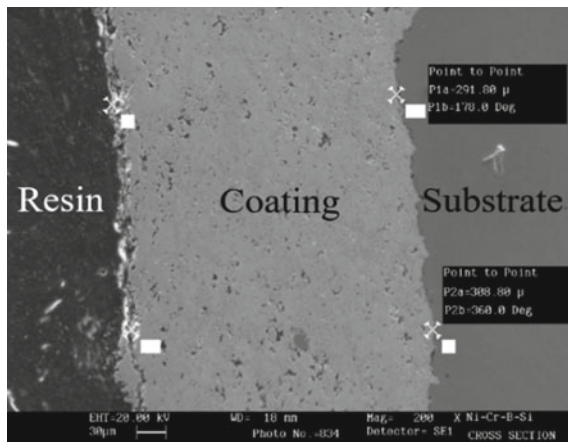
Fig. 26.3   Cross section of as-sprayed NiCrBSiFe

Fig. 26.4 Cross section of as-sprayed 35 WC-Co/NiCrBSiFe
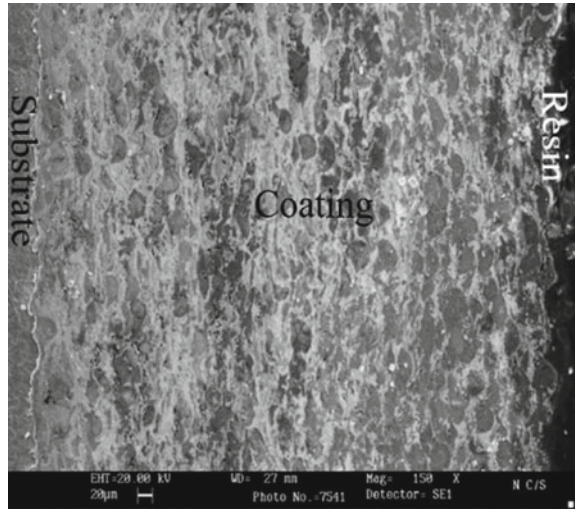
D1- and N1-sprayed HVOF sample. The purpose of adding WC to the matrix is to enhance the hardness level. The microhardness and the porosity were measured for both coatings. D1 coating shows the hardness and porosity level of about 750 $HV_{0.3}$ and 2.1%, for N1 coating, hardness of about 1050 $HV_{0.3}$ and 3.0% porosity, respectively.

The surface morphology of the D1 and N1 coatings is as shown in Figs. 26.5 and 26.6. From the surface morphology of the coating, it is observed that there is a higher porosity level in N1 coating. The dispersion of WC in the nickel-rich matrix in N1 coating increases the porosity level when compared to D1 coating, which may result in an increase in stress level around the pores. As the particle interact the surface, the cracks nucleate and propagate easily and cause the material to come off easily, thus resulting in higher erosion loss of the coating and also at 700 °C; the hardness

Fig. 26.5 SEM morphology of surface as-sprayed NiCrBSiFe
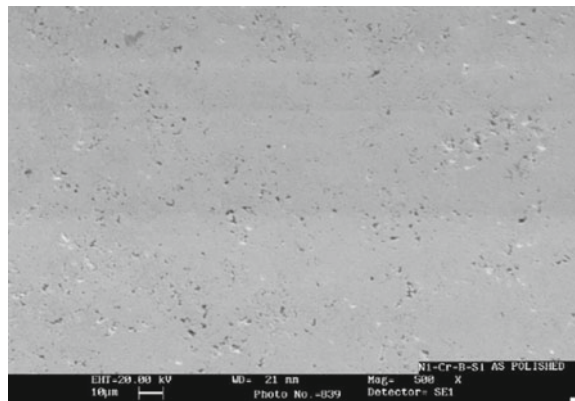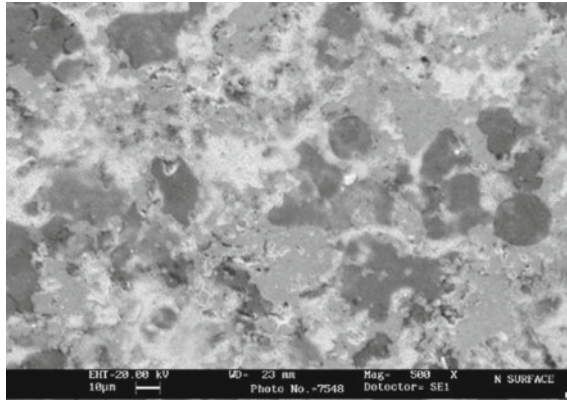
Fig. 26.6 SEM morphology of surface as-sprayed 35 WC-Co/NiCrBSiFe

decreases and hence results in higher erosion loss; similar observations have been made by other researchers reported [23, 24].

26.3   CFD Erosion Simulation

The CFD approach has been adopted to identify the critical erosion-prone regions obtaining low, mild and high erosion regions based on the varied flow conditions, flow trajectories, varied impact angles keeping the solid burden constant (gram loss per kg of abrasive used).

The individual model has been developed for five different impact angles of 15°, 30°, 45°, 75° and 90° to get particle trajectories and averaged particle impact velocity, but in this work, only the impact angles of 30° and 90° are considered for this study; following this, the simulation work has been done, and the data have been generated.

26.3.1   *Development of Erosion Model for Prediction of Erosion Rate*

In the erosion model, material removal takes place mainly by the impact of erodent particles on the target material due to the high kinetic energy possessed by the particle transforming it to potential energy. The erosion phenomena being complex in nature follow a particular sequence; the erosion loss governs the following equation.

$$E = K \cdot V_p^n \cdot (\alpha)^M \cdot \dot{m} \tag{26.1}$$

Table 26.4 Multiple nonlinear regression analysis data

Temperature (°C)	Materials	K	n	M
RT/Ambient	D1	3.01e−11	1.69	0.334
RT/Ambient	N1	8.76e−12	2.52	0.647
700	D1	1.911e−9	0.928	0.283
700	N1	2.586e−9	0.987	0.5547

where

V_P	particle impact velocity
K	constant reference velocity factor
α	impact angle in radian
n, M	velocity and angle exponent
$\dot{m}$	mass flow rate of erodent impacting
V_o	reference velocity
V_o	$(1/k\hat{}1/n)$
Erosion rate/$\dot{m}$	$(V_p/V_o)^n (\alpha)^M$

The impact angle is expressed in radians, and it is the angle between the approaching particle track and the wall. The experimental values with velocity, impact angle and temperature ranges are taken to MATLAB to solve multiple nonlinear regression analysis and the values of K, n and M are obtained by curve fit as shown in Table 26.4.

The above erosion Eq. (26.1) is implemented in Fortran code, with the help of Ansys CFX. Fortran subroutine is created in the form of user routine and finally source code Pt_erosion. F is called for solutions to the erosion equation for each of the material D1 and N1. A user-defined function is derived to solve the erosion equation which consists of velocity, impact angle, impact location and temperature of the target surface.

The sieve analysis is carried out to determine the particle size and its distribution, and for CFD analysis, the following assumptions have been made

1. The shape factor assumed to be 0.75
2. Particle impact is inelastic in nature
3. Perpendicular and parallel coefficient is considered as one

Also, three different velocities (20, 26 and 36 m/s) are considered in this, and the gap maintained between the jet and the test sample is 10 mm.

26.3.2 CFD Turbulence Model

Turbulence models are generally considered to predict the flow patterns. The shear stress transport model (SST) is nothing but two equations model which is more advanced than zero equation model [25]. The SST model is robust, and accuracy is

good when compared with the other models like k-ε, k-ω and SSG Reynolds stress model. In the present CFD work, SST model has been used in view of possessing a higher accuracy level.

26.3.2.1 SST (Shear Stress Transport) Model

The SST model is developed by Menter [26] and designed by Wilcox [27]. This model is a combination of the conventional k-epsilon and k-omega model.

$$\omega = \frac{k}{V_t}$$

In the SST model, turbulence viscosity V_t is defined as

$$V_t = \frac{a_1 k}{max\ (a_1 \omega,\ \Omega F_2)}$$

where a_1 is the 0.30 coefficient; the absolute value of the vorticity Ω is

$$F_2 = \tan h \left[\left[max \left(2\sqrt{k}/0.09\,\omega y,\ 500\,v/\omega y^2 \right) \right]^2 \right]$$

where y is the distance from the nearest wall, and v is the kinematic viscosity.

26.3.3 Model Description

There is a total mesh of 2,62,317 nodes and 2,80,666 elements. Ansys CFX15 is used to perform CFD analysis. Ansys-Pre was used to mesh 3D structures, as shown in Fig. 26.7a. The target surface and near-wall are used to have finer meshes with the dominant mesh of hexahedron. The hexahedron-based fluid mesh gives good results
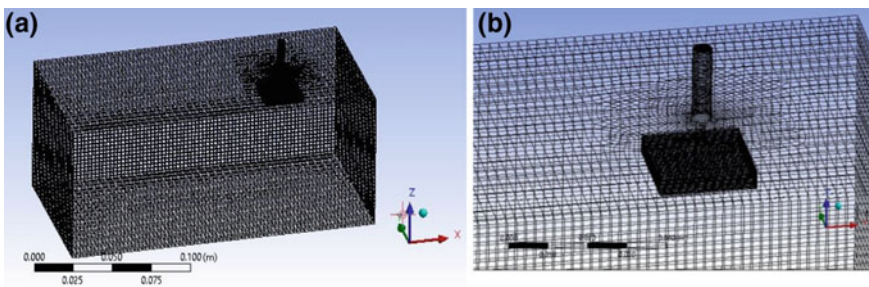
Fig. 26.7 Generation of mesh **a** domain of control volume **b** specimen to target surface
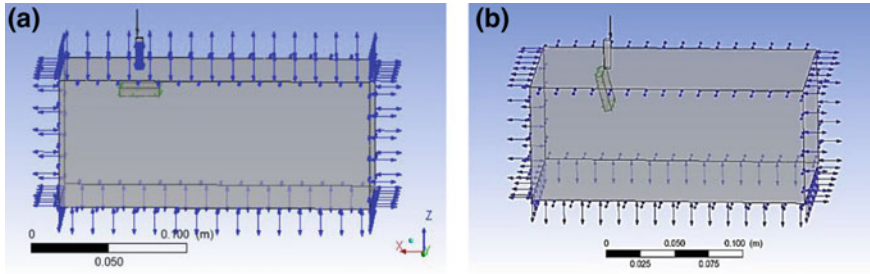
Fig. 26.8 Geometrical model set-up used for CFD study

Table 26.5 Boundary conditions adopted for CFD simulation study

Inflow condition	The mass flow rate of erodent and air velocity
Target surface	No-slip conditions
Roughness of wall	As-polished condition
Turbulence model	SST model standard
Outlet condition	Atmospheric pressure conditions with opening boundary

in analysing fluid flow near the target wall, as shown in Fig. 26.7b. The SST model involving steady state is used to simulate the flow conditions and codes developed using subroutine in the calculation part of erosion rate where the particle flow is in the opposite of the Z direction.

Figure 26.8 a and b shows the model with an impact angle of 90° and 30°. The boundary conditions adopted during CFD simulation are shown in Table 26.5.

26.4   Results and Discussion

26.4.1   CFD Simulation Results

The velocity of the particle to predict the erosion behaviour is 36 m/s and it is arrived at based on the experiments. The solid particle vectors contours is shown in Fig 26.9.

Figure 26.10 shows the distribution of erosion rate density of the sample of both D1 and N1 coatings at 30° and 90° impact angle using the SST turbulence model. The erosion scars from the CFD prediction replicate similar to the experimental test scar as shown in Fig. 26.11.
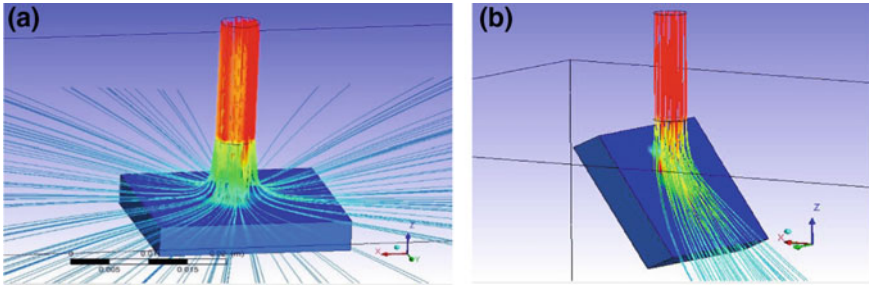
Fig. 26.9 Erosion rate density of contour **a** 90° **b** 30° impact angle
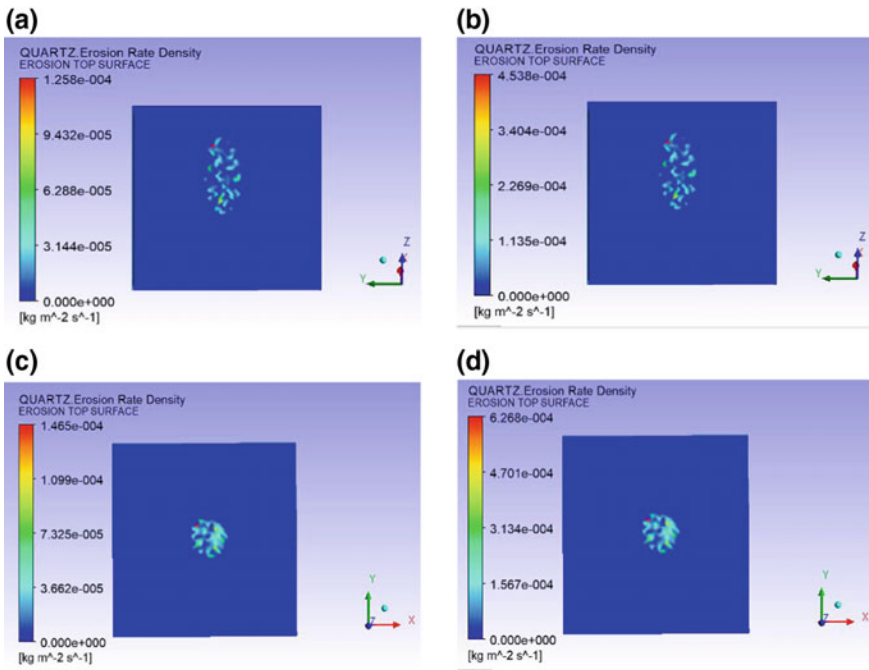
Fig. 26.10 Erosion rate density distribution on the target surface of the specimen **a** D1 **b** N1 at 30° impact angle and **c** D1 **d** N1 at 90° impact angle at a temperature of 700 °C

26.4.2   Discussion

Erosion Mechanism: The erosion rate of the self-fluxing alloy (single metallic coating) of D1 and N1 (two-phase materials) coatings with the impact angle of 30° and 90° for room and elevated temperature (700 °C) is shown in Fig. 26.12.

Figure 26.12 gives the erosion rate versus the impact angle. At room temperature, both coatings D1 and N1 show superior erosion resistance; however, at 90° impact,
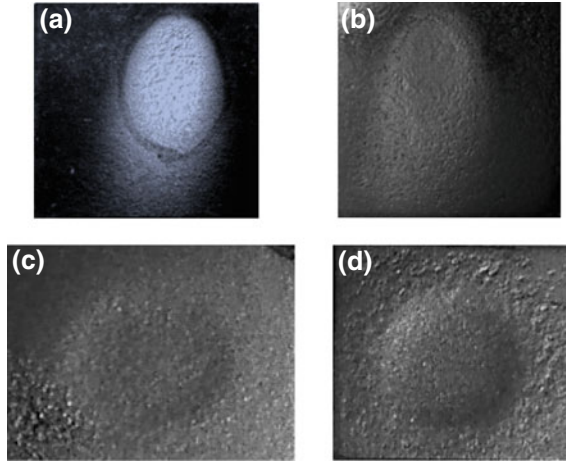
Fig. 26.11 Erosion rates on the target surface of specimen **a** D1 **b** N1 at 30° impact angle and **c** D1 **d** N1 at 90° impact angle at a temperature of 700 °C
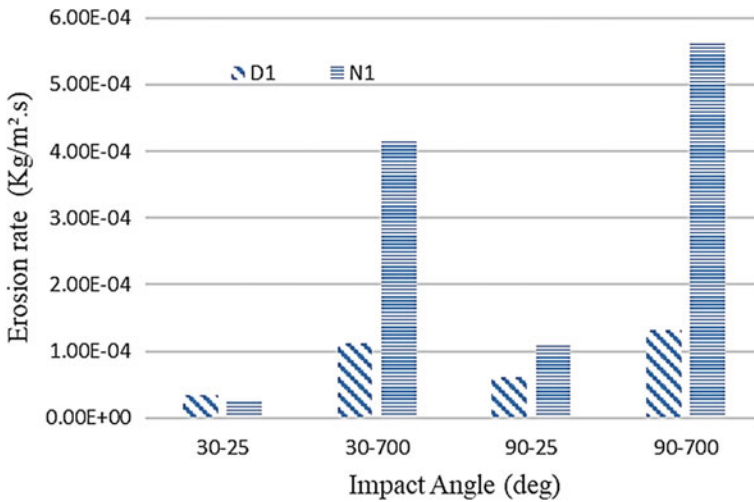
Fig. 26.12 Histogram illustrating the room and high-temperature erosion rate of D1 and N1 coatings at two different impact angles of 30° and 90°

the erosion is higher for both coatings; this may be due to brittle erosion nature at normal impact angle.

In the case of D1 coating at a higher temperature of 700 °C, the erosion rate is decreased at both the shallow and normal impact angle. At shallow impact angle coating will undergo plastic deformation as the material removal is by cutting and ploughing mechanisms, whereas at a higher angle of 90°, the erosion damage takes

place due to the repeated impact of the erodent. In this case, the erosion mechanism may be a combination of grooving, cratering and microcracking. The microstructure of the D1 coating has dense and layered structure and the microhardness of the coating measured is 780 HV. When the coating is exposed to higher temperatures, the hardness of the coating is reduced to half (430 HV) the value measured at room temperature. Even though the coating can withstand erosion at high temperatures, it is likely that there is an improvement in toughness due to the drop in hardness. It is well known that when the hardness decreases, the toughness increases [24].

In the case of N1 coating at a higher temperature of 700 °C, the rate of erosion is less at 30° impact and more at normal impact angle which is a characteristic behaviour of brittle materials. When the WC content in the coatings varies from 0 to 18%, the coating hardness increases gradually; however, with the increase of WC content, the porosity level also increases which leads to larger pores. When the WC content is more (35%), the brittleness as well as the pore size increases predominantly. These bigger sized pores may provide a path for the fracture and lead to the propagation of the crack. If the WC content is less than 25%, the pore sizes are smaller resulting in crack not getting formed as it absorbs a larger amount of impact energy. Further, a higher amount of WC (35%) with large pores undergoes the higher amount of plastic deformation with the formation of network cracks and gives rise to ease pathway by the crack propagation to occur. In the process, surface layer comes off following the delamination theory. The hardness of the coating by the addition of 35% WC was 1056 HV by exposing to a higher temperature of 700 °C; the hardness of the coating was reduced to 520 HV (almost half) which causes the highest erosion rate; lower hardness results in poor erosion resistance.

The erosion rate at an elevated temperature at normal impact angle was nearly 5–6 times higher for both the coating tested. Compared to stainless steel and other NiCr alloys, NiCrBSiFe coating has been proven to be very promising. WC agreements the greater wear resistance at room temperature; however, its poor resistance to oxidation and thermal expansion mismatch restricts its application to a temperature above 450–550 °C; similar kind of observation has been reported elsewhere [28–30], and the erosion loss governs Eq. (26.1) which is as per the literature [31].

26.4.3 Assessment of Simulation and Experimental Results

The erosion rate of D1 and N1 coatings for room and high temperature is shown in Table 26.6. The average erosion rate on the target surfaces of the specimen through experiments and computer simulation using the SST model is also shown. The SST model belongs to the family of eddy dissipation model and has been chosen because of its high accuracy and accurate prediction of flow separation from a smooth surface at the time of particle impact; similar kind of prediction is reported [25].

In this context, it is worth mentioning here that the work carried out by Kim et al. [21] has adopted the SST model for solid particle erosion prediction and compared it with the *k*-epsilon model and reported that the SST model is much better compared

Table 26.6 Comparison of experimental and simulation results on erosion

Sample	Impact angle (°)	Experimental data (kg/m^{2}s)	Numerical data (kg/m^{2}s)	% error
D1-25	30	3.50e−5	3.89e−5	11.13
N1-25	30	2.78e−5	3.16e−5	13.67
D1-700	30	1.12e−4	1.25e−4	11.60
N1-700	30	4.15e−4	4.54e−4	9.56
D1-25	90	6.09e−5	6.83e−5	12.11
N1-25	90	1.11e−4	1.21e−4	9.00
D1-700	90	1.32e−4	1.46e−4	10.98
N1-700	90	5.65e−4	6.28e−4	11.23

to the other models. Hence, in the present investigation, also SST model is used to the advantage of predicting the erosion rate in WC-nickel target material with minimum acceptable error. Further, it is seen that the % error (Table 26.6) obtained between the experiments and SST simulation lies in the range 9–14% which seems to be in the acceptable range. Thus, it is summarized both the experimental and simulated results are in close agreement with each other.

26.5 Conclusions

The experimental results pertaining to erosion characteristics at elevated temperate of self-fluxing NiCrBSiFe alloy and 35% WC-Co/NiCrBSiFe coatings made by HVOF technique have been investigated and compared with the CFD numerical simulation model. The CFD data closely match the experimental values obtained. The following are the important conclusions drawn.

- The HVOF-sprayed NiCrBSiFe-coated samples have shown higher erosion resistance both at room temperature and elevated temperature (700 °C) compared to 35% WC-Co/NiCrBSiFe HVOF-coated sample irrespective of the impact angle.
- It is desirable to adopt NiCrBSiFe coating for high-temperature erosion application as it does not seem to undergo oxidation.
- It is preferable to use WC-Co/NiCrBSiFe coating at a shallow angle (20°–30°) for erosion resistance application at room temperature, but at 90° impact angle, NiCrBSiFe is preferable.
- The percentage error obtained between the experimental results and CFD simulated data lies in the range 9% to 14%, which seems to be in the acceptable limits.
- The CFD application with the SST model seems to predict the erosion behaviour better using Ansys CFX module and the same study may be extended to higher temperature (greater than 700 °C) regimes.

References

1. Ramesh, C.S., Seshadri, S.K., Iyer, K.J.: A survey of aspects of wear of metals. Indian J. Technol. **29**(4), 179–185 (1991)
2. Archer, N.J., Yee, K.K.: Chemical vapour deposited tungsten carbide wear-resistant coatings formed at low temperatures. Wear **48**(2), 237–250 (1978)
3. Pawlowski, L.: The Science and Engineering of Thermal Spray Coatings. Wiley & Sons, 30 Apr 2008
4. Uusitalo, M.A., Vuoristo, P.M., Mäntylä, T.A.: High-temperature corrosion of coatings and boiler steels in the oxidizing chlorine-containing atmosphere. Mater. Sci. Eng. **346**(1–2), 168–177 (2003)
5. Stultz, S.C., Kitto, J.B. (eds.): Steam: Its Generation and Use. Babcock and Wilcox, Barberton, OH (1992)
6. Uusitalo, M.A., Vuoristo, P.M., Mäntylä, T.A.: High-temperature corrosion of coatings and boiler steels below chlorine-containing salt deposits. Corrosion Sci. **46**(6), 1311–1331 (2004)
7. Miguel, J.M., Guilemany, J.M., Vizcaino, S.: Tribological study of NiCrBSi coating obtained by different processes. Tribol. Int. **36**(3), 181–187 (2003)
8. Hutchings, I.M.: Wear by particulates. Chem. Eng. Sci. **42**(4), 869–878 (1987)
9. Sundararajan, G.: A comprehensive model for the solid particle erosion of ductile materials. Wear **149**(1–2), 111–127 (1991)
10. Finnie, I.: In: Nateson, K. (ed.) Corrosion-Erosion Behavior of Materials, p. 437. AIME, New York (1980)
11. Kulu, P., Hussainova, I., Veinthal, R.: Solid particle erosion of thermal sprayed coatings. Wear **258**(1–4), 488–496 (2005)
12. Mohanty, M., Smith, R.W., De Bonte, M., Celis, J.P., Lugscheider, E.: Sliding wear behaviour of thermally sprayed 75/25 Cr3C2/NiCr wear resistant coatings. Wear **198**(1–2), 251–266 (1996)
13. Kim, H.J., Hwang, S.Y., Lee, C.H., Juvanon, P.: Assessment of wear performance of flame sprayed and fused Ni-based coatings. Surf. Coat. Technol. **172**(2–3), 262–269 (2003)
14. Bell, G.R.: Eighth International Thermal Spraying Conference, Mimi, Florida, USA, pp. 396–406 (1976)
15. Ding, Z., Knight, R., Smith, R.W.: Thermal Spray: A United Forum for Scientific and Technological Advances, Materials Park, Ohio, USA, pp. 91–95 (1997)
16. Heath, G.R., Kamer, P.A.: Surface Modification Technology IX, Cleveland, Ohio, USA, pp. 109–113 (1995)
17. Parsi, M., Agrawal, M., Srinivasan, V., Vieira, R.E., Torres, C.F., McLaury, B.S., Shirazi, S.A.: CFD simulation of sand particle erosion in gas-dominant multiphase flow. J. Nat. Gas Sci. Eng. **27**, 706–718 (2015)
18. Duarte, C.A., de Souza, F.J., de Vasconcelos Salvo, R., dos Santos, V.F.: The role of inter-particle collisions on elbow erosion. Int. J. Multiph. Flow **89**, 1–22 (2017)
19. Zahedi, P., Zhang, J., Arabnejad, H., McLaury, B.S., Shirazi, S.A.: CFD simulation of multiphase flows and erosion predictions under annular flow and low liquid loading conditions. Wear **376**, 1260–1270 (2017)
20. Gandhi, M.B., Vuthaluru, R., Vuthaluru, H., French, D., Shah, K.: CFD based prediction of erosion rate in large scale wall-fired boiler. Appl. Therm. Eng. **42**, 90–100 (2012)
21. Kim, J.H., Joo, H.G., Lee, K.Y.: Simulation of solid particle erosion in WC-Ni coated wall using CFD. J. Mater. Process. Technol. **224**, 240–245 (2015)

22. Ruff, A.W., Ives, L.K.: Measurement of solid particle velocity in erosive wear. Wear **35**, 195–199 (1975)
23. Hidalgo, V.H., Varela, F.B., Menéndez, A.C., Martınez, S.P.: A comparative study of high-temperature erosion wear of plasma-sprayed NiCrBSiFe and WC–NiCrBSiFe coatings under simulated coal-fired boiler conditions. Tribol. Int. **34**(3), 161–169 (2001)
24. Tu, J.P., Liu, M.S., Mao, Z.Y.: Erosion resistance of Ni-WC self-fluxing alloy coating at high temperature. Wear **209**(1–2), 43–48 (1997)
25. Sklavounos, S., Rigas, F.: Validation of turbulence models in heavy gas dispersion over obstacles. J. Hazard. Mater. **108**(1–2), 9–20 (2004)
26. Menter, F.R.: Two-equation eddy-viscosity turbulence models for engineering applications. AIAA J. **40**(2), 254–266 (2002)
27. Wilcox, D.C.: Reassessment of the scale-determining equation for advanced turbulence models. AIAA J. **26**(11), 1299–1310 (1988)
28. Russo, L., Dorfman, M.: A structural evaluation of HVOF sprayed NiCr-Cr sub 3 C sub 2 coatings. Therm. Spray. Curr. Status Futur. Trends **2**, 681–686 (1995)
29. Berger, L.M., Hermel, W., Vuoristo, P., Mantyla, T., Lengauer, W., Ettmayer, P.: Structure, properties and potentials of WC–Co, Cr3C2–NiCr and TiC–Ni-based hard metal like coatings. In: Berndt, C.C. (ed.) Thermal Spray: Practical Solutions for Engineering Problems, pp. 89–98 (1996)
30. Berger, Z., Livshitz, M.: The structure and properties of hypervelocity oxy-fuel (HVOF) sprayed coatings. High-Temp. Mater. Process. **15**, 179–186 (1996)
31. Raask, E.: Mineral Impurities in Coal Combustion: Behaviour, Problems, and Remedial Measures. Taylor & Francis (1985)

Chapter 27
Optimization of Friction Stir Welding Parameters Using Taguchi Method for Aerospace Applications

K. Ramesha, P. D. Sudersanan, N. Santhosh, G. Ravichandran and N. Manjunath

Abstract The current research work investigated the optimization of the input parameters for the friction stir welding of AA3103 and AA7075 aluminum alloys for its applications in aerospace components. Friction stir welding is rapidly growing welding process which is being widely used in aerospace industries due to the added advantage of strong strengths without any residual stresses and minimal weld defects, in addition to its flexibility with respect to the position and direction of welding. Thus, the demand for this type of welding is very high; however, the welding of aluminum alloys is a key aspect for its use in aircraft components, particularly with respect to bracket mounting frames, braces and wing components. Henceforth in the current work, research is focused on optimization of welding of aluminum alloys, viz. AA 3103 and AA 7075; AA 3103 is a non-heat treatable alloy which is having good weldability, while AA 7075 is having higher strength. Therefore, the welding of these aluminum alloys will produce superior mechanical properties. The optimization of input parameters was accomplished in this work based on L9 orthogonal array designed in accordance with Taguchi method—using which the friction stir welding experiment was conducted. There were nine experimental runs in total after formulating the L9 orthogonal array table in Minitab software. The input parameters which were selected for optimization were—tool rotation speed, feed rate, tool pin profile. The output parameters which were optimized were hardness, tensile strength and impact strength. In addition, the microstructure of the fractured surfaces of the friction stir welded joint was analyzed. It was found from the optimization of the process parameters that strong friction stir welded joints for aerospace applications can

K. Ramesha · P. D. Sudersanan
Department of Mechanical Engineering, Dr. T. Thimmaiah Institute of Technology, Kolar Gold Fields, Karnataka, India

N. Santhosh (✉) · G. Ravichandran
Department of Mechanical and Automobile Engineering, CHRIST (Deemed to be University), Bengaluru, Karnataka, India
e-mail: santhoshnmitaero@gmail.com; santhosh.n@christuniversity.in

N. Manjunath
Department of Sciences and Humanities, CHRIST (Deemed to be University), Bengaluru, Karnataka, India

be produced at an optimized set of parameters of tool rotational speed of 1100 rpm, traverse speed of 15 mm/min with a FSW tool of triangular pin profile of H13 tool steel material.

Keywords AA3103 · AA7075 · Friction stir welding · H13 tool steel · Taguchi orthogonal array · Minitab · Aerospace · Components

27.1 Introduction

Friction stir welding is type of welding in which a non-consumable tool is being used in order to weld two workpieces. The welding of the workpiece occurs heating the working piece at its line of joint. The heat is generated due to the friction between the rotating tool and the workpiece, and as the tool is rotating, it intermixes both the workpiece materials. The mechanical intermixing of the workpiece material will be accomplished as the tool moves along the line of the joint, and subsequently the forging of hot and soft material is made by the means of mechanical pressure. The FSW tool serves two primary functions:

- Heating of the workpiece material.
- Mixing of two materials in a mushy state to produce the joint.

Friction stir welded aluminum alloys are widely used in aeronautical and aerospace industries for manufacturing airplanes both commercial and defense type, spacecraft, helicopters, etc. Among the different types of aluminum alloys, AA3103 is a non-heat treatable alloy and having superior strength, whereas the AA7075 is having higher strength. Thus, the weld obtained from these two alloys will be of superior quality. But AA7075 aluminum weld is quite expensive. In order to reduce the expense, the AA7075 aluminum alloy is welded with other grades of aluminum alloys. The AA3103 aluminum alloy has good weldability and is less expensive. Therefore, a weld produced from these two alloys will be showing the properties of both these alloys. For the weldment between AA2024-T365 and AA5083-H111, heat-treated H13 steel is used as the tool material; the tool is having a concave shoulder of 20 mm diameter and a pin diameter of 5 mm, and the height of pin is 4.7 mm.

The tool pin profiles used for welding are square, triangular and stepped. The welding parameters used for the experimentation are 900, 1120 and 1400 rpm for tool rotational speed and 16, 40 and 80 mm/min for feed rate [1]. The friction stir welding is conducted between two grades of aluminum alloys 5086 H116 and 5083 H321. Each workpiece plate is having a thickness of 6 mm, the AA 5086 is having dimensions of 100 * 95 * 6 mm, and the AA 5083 is of 100 * 70 * 6 mm dimensions. During the welding process, AA 5086 is taken as the advancing side (AS), while AA 5083 is the retracting side (RS), and this is because the advanced side material should be always a hard material. The tool used for welding is a chromium–molybdenum

tool which is made of H13 steel. The five different pin profiles used for the welding experiments are threaded, square, cylindrical, tapered and triangular [2]. The metallurgical characterization is carried out by SEM and EDS, and the mechanical properties are developed by tensile and hardness test. From this paper, they come out with the most efficient result that is of 710 rpm and 28 mm/min, and the tool design is cylindrical pin [3]. Fatigue behavior of friction stir welded Al–Mg joints exhibited wide scatter. The Al–Mg joints exhibited two distinct failure modes: kink crack and interfacial. Intermetallic compounds outside the weld likely led to fretting initiated fatigue. Insufficient material mixing resulted in underperforming joints [4]. The tool profiles are as follows: The shoulder shape is concave, pin shape is triangular, shoulder diameter is 12 mm, and pin diameter is 5.4 mm [5].

The tool used for friction stir welding is made up of carbon steel of diameter 20 mm with shoulder diameter 12 mm and with a cylindrical pin of diameter 5 mm. Eight joints were fabricated as per the design plan from the Taguchi method [6]. Microstructural suggested that there was no rigorous mixing, and there was a small change in the microhardness across the surface. The microelectron analysis test shows that there is a bonding at the atomic scale due to interfusion of the alloys in the nugget. Thus, the interdiffusion of alloying elements and attaining of similar orientation in the nugget have contributed good mechanical properties [7]. It is concluded that for AA5083–AA5083 similar material welding, the welding efficiency is 77% from base metal AA5083, and for the AA6061–AA5083 dissimilar material welding, the welding efficiency was 34 and 93% compared to AA5083 and AA6061 [8]. The tool used in this experiment is EN-31 with a shoulder diameter of 20 mm and pin diameter of 5 mm at the root and 5.75 mm pin length. The weld joints are cut as per ASTM dimensions for impact test [9, 10]. L8 orthogonal array is used by taking three process parameters and two levels for optimizing the process parameters for obtaining higher hardness and tensile strength of the welded region [11, 12].

From the literature review, it is seen that the friction stir welding of aluminum components has great scope, and studies can be carried out on the process since friction stir welding depends on the parameters selected, which facilitates the need to optimize these input parameters so that we could find out how it affects the resulting weld and the output parameters like strength and quality of weld. To do so, there are many input parameters, so by going through the findings, it is finalized that three parameters which are speed, feed rate and tool profile are considered, and each parameter has to be selected. These values will be then optimized in order to obtain the perfect combination of the input parameter value so that high quality weld will be obtained.

27.2   Materials and Methods

The current section gives an overview of the materials used for fabrication of the plates that are friction stir welded by optimizing the parameters.

27.2.1 Selection of Materials

AA 7075 and AA 3103 are the aluminum alloys which are chosen as the two work-piece materials having dimensions of 103 * 50 * 6 mm, for friction stir welding in this experiment. The chemical composition of the workpiece is presented in Tables 27.1 and 27.2.

27.2.2 Selection of Tool

The welding tool is made up of H13 tool steel. The weld tool is manufactured by casting process and then heat treated. Right after the heat treatment, the tool is kept in oil bath (for three days). This is done in order to improve the strength of the weld tool.

27.2.3 Selection of Welding Parameters and Levels

The three main parameters selected for this welding operation are tool rotational speed, feed rate of tool and tool pin profile. The selection of the welding parameter values was based on the knowledge obtained from the literature survey. Table 27.3 gives the values selected for the welding parameters and their levels.

27.2.4 Experimental Setup

The entire experiment is carried out in a vertical CNC machine. Both the workpieces are placed on a rig with AA3103 specimen placed on the advancing side. The rig for holding the workpiece rigidly is installed on the CNC worktable. The friction stir welding is carried out based on the combination of input parameter values, obtained using Minitab software. Computer numerical control (CNC) machining is a machining process in which the machining tools and traverse path of the cutting tool are controlled by means of a computer. In this machining process, pre-programmed computer software will control all the movements of the tool. When a CNC machine is activated, the desired operations required to be done will be programmed into the software in the form of G codes and M codes, and these programs shall then dictate the tool for the corresponding motions to perform the operations. The current experiment is carried out in a high quality CNC milling machine without using coolant and with a maximum speed of 1200 rpm. The maximum feed rate used in our project is 25 mm/min, and the electric drive used is a 25-kw drive motor. The fixture is used to hold the workpiece tight and in perfect position without any vibration while

Table 27.1 Chemical composition of AA 3103 (weight %)

Elements	Mn	Fe	Cu	Mg	Si	Zn	Cr	Ti + Zr	Al
Percentage composition	1.5	0.7	0.1	0.3	0.5	0.2	0.1	0.1	Balance

Table 27.2 Chemical composition of AA 7075 (weight %)

Elements	Al	Zn	Mg	Cu	Cr
Percentage composition	90	5.6	2.5	1.6	0.23

Table 27.3 Welding parameters and their levels

Parameters	Unit	Symbol	Level 1	Level 2	Level 3
Tool rotational speed	rpm	A	1000	1100	1200
Feed rate	mm/min	B	15	20	25
Tool pin profile	Shape	C	Square	Circle	Triangle

Table 27.4 Design of experiments matrix with input values

Experimental trial No.	Speed of rotation (rpm)	Feed rate (mm/min)	Tool pin profile
1	1000	15	Circular
2	1000	20	Square
3	1000	25	Triangle
4	1100	15	Square
5	1100	20	Triangle
6	1100	25	Circular
7	1200	15	Triangle
8	1200	20	Circular
9	1200	25	Square

welding. The fixture consists of a main plate and above that four supporting sides each containing a M12 hole, where the tightening screws are inserted to adjust the position of the workpiece. The experimental trails were carried out based on Taguchi's L9 orthogonal array. The values of the input parameters were selected based on the literature survey. A nine run, three factors, three-level orthogonal array was designed by following Taguchi's design of experiments, which is given in Table 27.4.

27.2.5 CNC Programming

Since the friction stir welding of the workpieces was carried out in a CNC machine, a program was required to run the welding experimentation. The CNC program used for the friction stir welding considered the various aspects of tool rotational speed, feed rate and depth with preparatory functions (G codes) and miscellaneous functions (M codes).

27.3   Results and Discussions

A nine trial run experiment was conducted in the vertical CNC milling machine by giving the input parameters varied at three levels of input parameters. The output parameters selected for the experiment are tensile strength, hardness and impact strength, and each of them determined using UTM, Brinell hardness testing machine and Charpy testing machine, respectively. Further, the microstructure of the fractured surfaces of the friction stir welded joints is **analyzed** using a Hitachi make SU 3500 scanning electron microscope. Initially, the specimens of 10 mm * 10 mm * 5 mm thickness from the fractured surfaces of the friction stir welded joints are cut and prepared suitably for microscopic observations in SEM at various resolutions and magnifications to analyze the fractography and evaluate the fracture mechanics behind the weld joints, which is presented in this section. Table 27.5 gives the values of the different properties characterized for the given set of parameters selected for the experimental trials carried out as per the design of experiments formulated in accordance with Taguchi's L9 orthogonal array.

The obtained results are the entered into the L9 orthogonal array with the input parameter values and analyzed in the Minitab software. As a result of the statistical approach, the software will optimize and compare both input and output parameters and provide combinations of input parameters which will produce the best and high quality weld.

Table 27.5   Resultant values from the experimental trials

Sl. No.	Speed (rpm)	Feed rate (mm/min)	Type of pin profile	Brinell hardness (HBW * 10/1000)	Tensile strength (N/mm^2)	Impact energy (J)
1	1000	15	Circular	90.7	89.9	4
2	1000	20	Square	92.3	96.1	2
3	1000	25	Triangle	96.7	81.2	4
4	1100	15	Square	90.2	97.1	10
5	1100	20	Triangle	98.3	95.4	6
6	1100	25	Circular	96.6	84.4	4
7	1200	15	Triangle	89.6	102.8	12
8	1200	20	Circular	92.3	98.7	4
9	1200	25	Square	92.8	87.7	4

27.3.1 Analysis of Tensile Strength

The tensile strength of the weldment characterized using an Intron make UTM of 1 k N capacity is tabulated and analyzed for the optimization of the values. Figures 27.1 and 27.2 show main effects plot for signal-to-noise (*SN*) ratios and for means. For the main effects plot for the *SN* ratios, the *x*-axis represents the input parameters, whereas the *y*-axis shows the *SN* ratios. For the main effects plot for means, the *x*-axis represents the input parameters, whereas the *y*-axis represents means. The Taguchi analysis has given validation for the *SN* ratio with the critical aspect considering the "larger is better" formulations that eventually gives the optimized values for the parameters; it is seen from the graph for *SN* ratio and main effects plot for means of tensile test results that the tensile strength of the weld joint will be maximum for a tool rotational speed of 1200 rpm, feed rate of 20 mm/min with a tool of square profile.

$$S/N = -10 * \log(\Sigma(1/Y^2)/n) \tag{27.1}$$

The empirical formula for "larger is better" is given in Eq. 27.1. The analysis of variance (ANOVA) was carried out in the Qualitek-4 software to find out the percentage influence of input parameters on the output parameters. The percentage influence of input parameters on tensile strength is given in Table 27.6. The feed rate of the tool is having more influence on tensile strength of the weld.
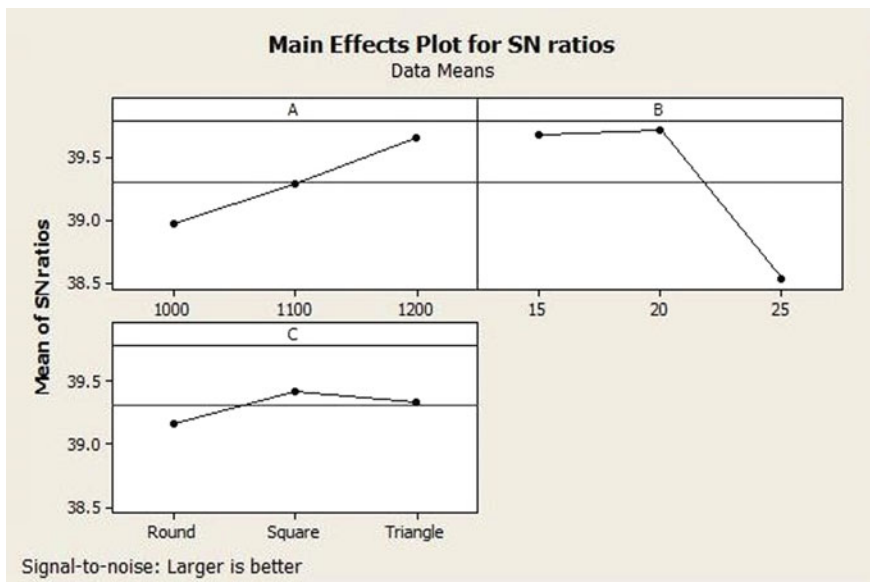

Fig. 27.1 Main effects plot for signal-to-noise ratios of tensile test results
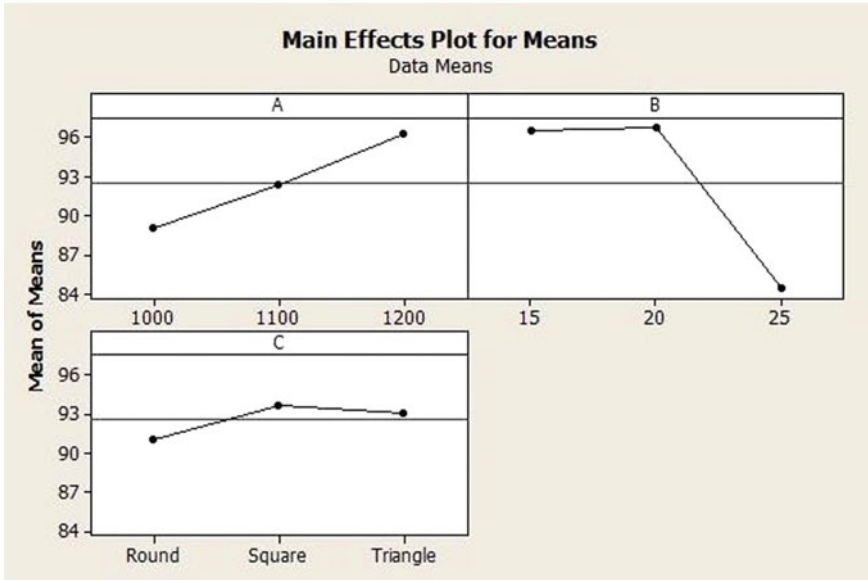
Fig. 27.2   Main effect plot for means of tensile test results

Table 27.6   Significant percentage of input parameters on tensile strength

Factor	Percentage P (%)
Speed	15.591
Feed	69.436
Profile	0
Other error	14.973
Total	100.00

27.3.2   Analysis of Hardness

The hardness of the weld was measured in Brinell hardness testing machine, and a load of 1000 kg was applied on the weld specimen while testing. Figs. 27.3 and 27.4 show main effects plot for *SN* ratios and for means. For the main effects plot for the *SN* ratios, the *x*-axis represents the input parameters, whereas the *y*-axis gives the *SN* ratios. For the main effects plot for means, the *x*-axis represents the input parameters, whereas the *y*-axis represents means.

The *SN* ratios are validated for "larger is better" condition, and it is herewith seen from the graph that the Brinell hardness of the weld joint is maximum for tool rotation speed of 1100 rpm, feed rate of 25 mm/min, friction stir welded with triangle tool insert. The percentage influence of input parameters on Brinell hardness is shown in Table 27.7. The table shows the feed rate of the tool is having more influence on
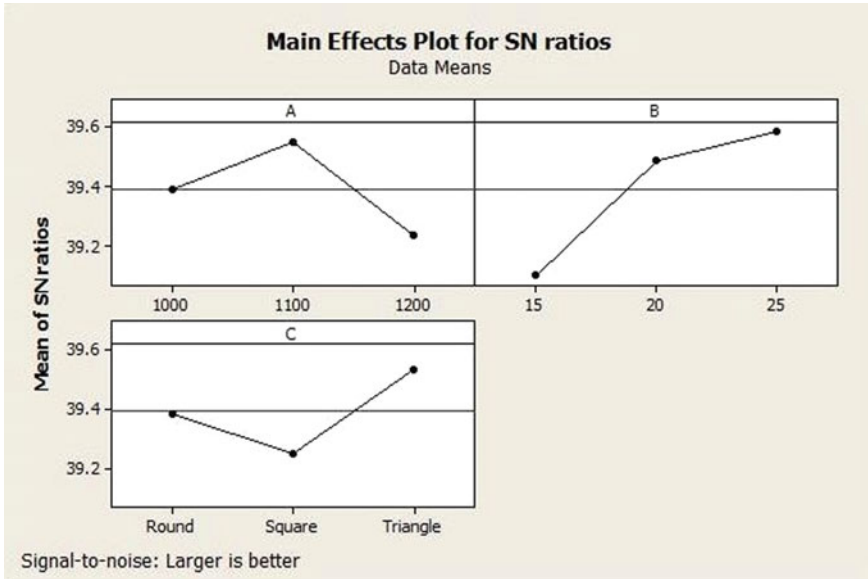
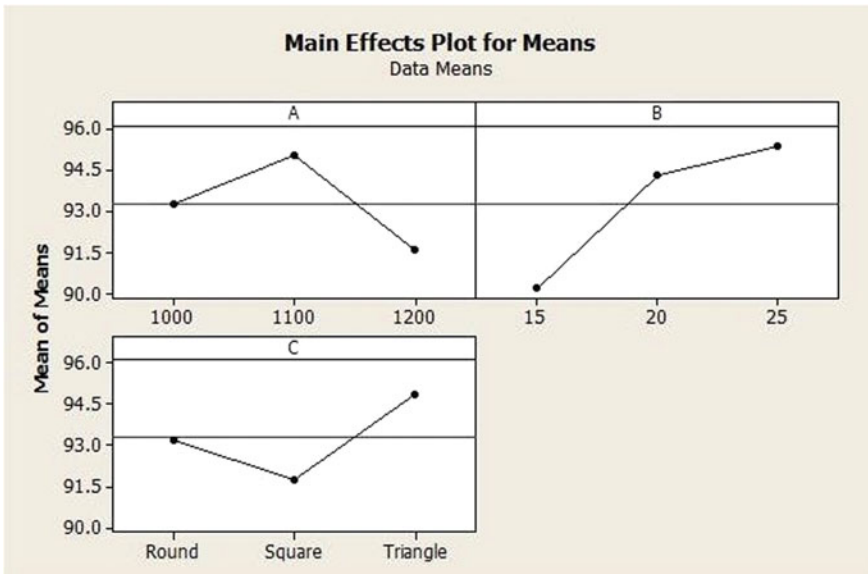**Fig. 27.3** Mean effect plot for signal-to-noise ratios of Brinell hardness test results

Fig. 27.4 Mean effect plot for means of Brinell hardness test results

Table 27.7 Significance percentage of input parameters on hardness

Factors	Percentage P (%)
Speed	20.093
Feed	54.225
Profile	15.572
Other error	10.11
Total	100.00

Brinell hardness of the weld.

27.3.3 Analysis of Impact Strength

The impact strength of the weld specimen was determined by a typical Charpy test. Figs. 27.5 and 27.6 show main effects plot for *SN* ratios and means, respectively. For the main effects plot for the *SN* ratios, the *x*-axis represents the input parameters, whereas the *y*-axis gives the *SN* ratios. For the main effects plot for means, the *x*-axis represents the input parameters, whereas the *y*-axis represents means. The main effects plot is analyzed for *SN* ratio considered to be better for larger values.

The percentage influence of input parameters on impact strength is given in Table 27.8. The table shows that the feed rate of the tool is having more influence on
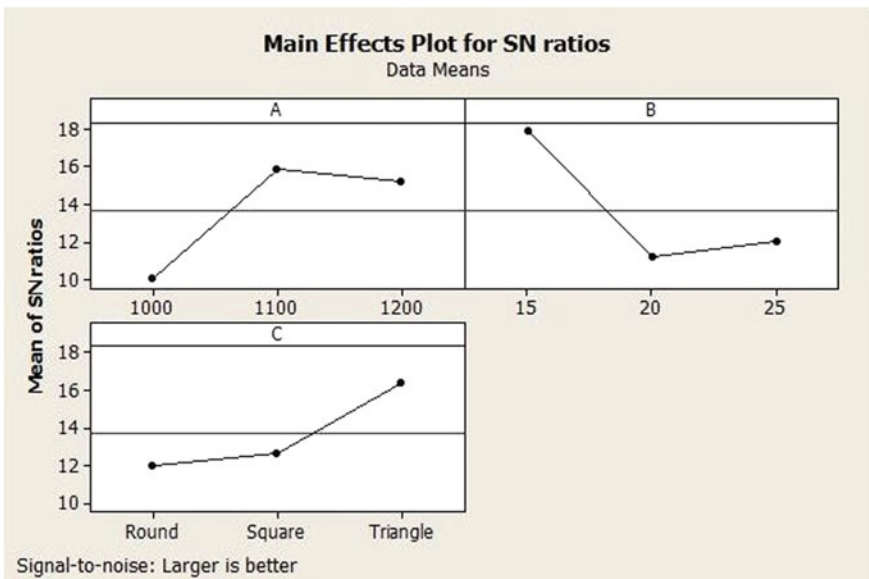

Fig. 27.5 Mean effect plot for signal-to-noise ratios of impact test results
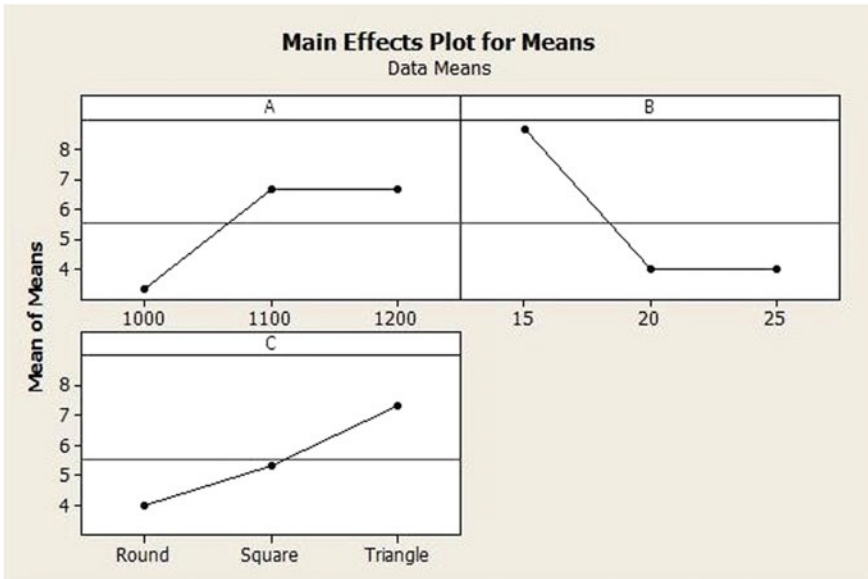
Fig. 27.6 Mean effect plot for means of impact test results

Table 27.8 Significance percentage of input parameters on impact strength

Factor	Percentage P (%)
Speed	21.649
Feed	46.391
Profile	15.463
Other error	16.497
Total	100.00

impact strength of the weld.

27.3.4 Fractography of the Weld Joint

The fractography of the weld joint of the aluminum AA 3103 and AA 7075 specimens is given in Fig. 27.7, and it is clearly evident that the fractured surfaces show a distinct coarse structure with twinned interfaces and striated surfaces rather than slip bands, thereby validating the fact that the residual stresses are minimal in friction stir weld joints; however, striations and luder bands can be observed, thus providing a proof for plastic deformation that has occurred under tensile loads before fracture. Further, the SEM image captured under a voltage of 20 k V at a magnification of 500× gives an account of the striated bands all around the periphery of the atoms inter-dwindled
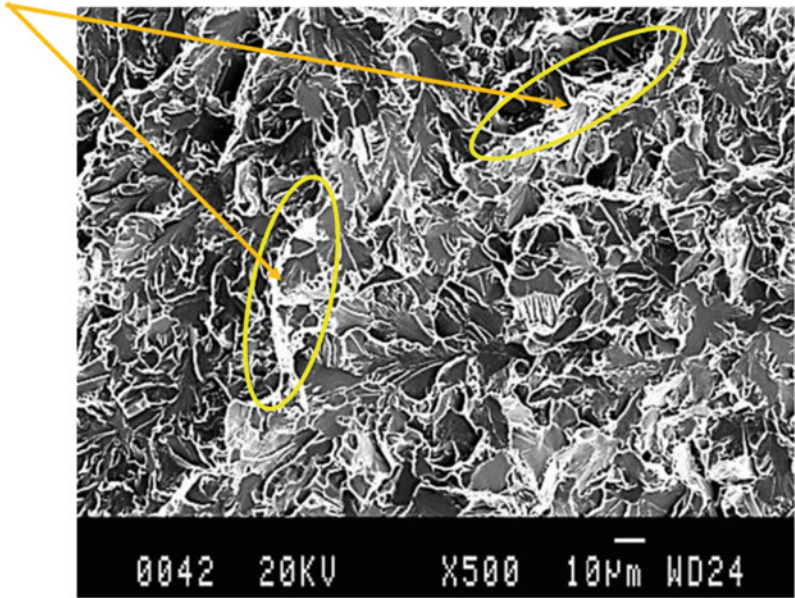
LUDER BANDS

Fig. 27.7 Mean effect plot for means of impact test results

in the FSW weld structure due to the interatomic forces and coherent bonding that result in a strong joint.

27.4   Conclusions

After the analysis of the output parameters, it has been found out that if the friction stir welding is conducted at 1100 rpm tool rotational speed, 15 mm/min feed rate and using tool of triangular pin profile, an effective weld of AA3103 and AA7075 could be produced. Further, it has been observed that welds produced at higher tool rotational speed and lower feed rate give higher output values. Out of all the three types of tool profile, the weld produced by using triangular pin profile tool gave the best output. Also, the fractography of the friction stir welded specimens validates the fact that the friction stir welding of the aluminum alloys reduces the stress accumulation, distortions and other thermal effects as is evident in other welding processes. Hence, friction stir welding process can be employed for joints of aerospace components, in particular bracket mounting frames, braces and wing components, which require high degree of structural integrity.

References

1. Santhosh, N., Mahamad, M.: Thermomechanical modeling and experimental evaluation of friction stir welds of aluminium AA6061 alloy. Int. J. Eng. Res. Technol. (IJERT) **2**(8), 1494–1499 (2013)
2. El-Hafez, H.A., El-Megharbel, A.: Friction stir welding of dissimilar aluminum alloys. World J. Eng. Technol. **6**, 408–419 (2018)
3. Kundu, Jitender, Singh, Hari: Friction stir welding of dissimilar AL alloys: effect of process parameters on mechanical properties. Eng. Solid Mech. **4**, 125–132 (2016)
4. Sadesh, P., Kannan, M.V., Rajkumar, V., Avinash, P.: Studies on friction stir welding of AA2024 and AA6061 dissimilar metals. Procedia Eng. **75**, 145–149 (2014)
5. Rao, H.M.: Effect of process parameters on mechanical properties of friction stir spot welded magnesium to aluminum alloys. Mater. Des. **15**, 1–34 (2015)
6. Rao, H.M.: Effect of process parameters on mechanical properties of friction stir spot welded magnesium to aluminum alloy. Mater. Des. 235–245 (2015)
7. Varma, R.R., Ibrahim, A.B.: Mechanical properties of the friction stir welded dissimilar aluminium alloy joints. Int. J. Mech. Prod. Eng. **2**, 1–5 (2014)
8. Kumbhar, N.T., Bhanumrthy, K.: Friction stir welding of Al 5052 with Al 6061 alloys. J. Metall. **2012**, 1–7 (2012)
9. Selamat, N.F.M., Baghadi, A.H., Sajuri, Z.: Friction stir welding of similar and dissimilar aluminum alloys for automotive application. Int. J. Automot. Mech. Eng. **13**, 3401–3412 (2016)
10. Shahabuddin, Dwivedi, V.K.: Effect of tool geometry of friction stir welding on mechanical properties of AA-7075 aluminum alloy. Int. J. Mech. Eng. Technol. **9**, 625–633 (2018)
11. Ramakrishna, M.V.A., Mahender, T.: Investigation of friction stir welding parameters of 5083 aluminum alloy by Taguchi method. Int. J. Eng. Technol. Sci. Res. **4**, 1078–1082 (2017)
12. Santhosh, N., Ramesha, K.: Mechanical and thermal characterization of friction stir weld joints of Al–Mg alloy. Int. J. Res. Aeronaut. Mech. Eng. (2017, December 22–23)

Chapter 28
Assessment of the Shear Strength of Fly Ash-Based Geopolymer Concrete

S. Kumar, S. Rajendra and K. S. Sreekeshava

Abstract Analytical approaches determine the shear strength of geopolymer concrete on experimentally evaluated parameters of strength such as compressive strength, tensile strength and flexural strength. The analytical approach has been introduced by using the equations of the correlated stress functions to evaluate the shear strength. The new approach has been introduced over traditional Mohr's failure envelope to assess the shear strength. The shear stress evaluated under these approaches is compared with the solution by the equation suggested by ACI-318-95. The variation of results from these approaches varied a maximum of 40% with results by the equation (ACI-318-95). The validation of each approach would be subjected to further discussion with previous research significance under the same context.

28.1 Introduction

There are several research works carried on geopolymers as binder or inorganic polymer but some intensive research works carried on Geopolymer concrete under the context of structural applications. Numerous studies by experimentations were recorded and still continuing on material properties. There are some effective works which incorporate the classical theories and experimental investigations to elucidate the material properties under structural applications. Some of the analytical and experimental approaches are explicated by traditional methods which are being used for conventional concrete.

S. Kumar (✉) · K. S. Sreekeshava
Jyothy Institute of Technology, Bengaluru, Affiliated to Visvesvaraya Technological University, Belagavi, India
e-mail: s.kumar@jyothyit.ac.in

S. Rajendra
Vijaya Vittala Institute of Technology, Bengaluru, Affiliated to Visvesvaraya Technological University, Belagavi, India

Several researchers have considered concrete as an isotropic material which has the same material properties along with all directions. In reality, it is a mixture of sands and gravels and it is not an isotropic material. Its tensile stress is near 1/10 of the compressive stress in the perpendicular direction measured on an experimental specimen. It is important to notice that mixtures have the same properties like orthotropic or anisotropic materials but they are considered as homogeneous materials. So they do not have the same E1 and E2 and others.

Several experimental investigations have been conducted to study the shear strength of concrete and predicted the results as a function of the compressive strength. The shear strength of concrete generally varies with the several associated factors such as internal frictions due to aggregate interlocking, the strength of cement paste and aggregates. In this study, the shear strength of concrete is discussed and predicted by the general strength of concrete as a whole without assessing the properties of individual materials by which is made up of.

28.1.1   Research Significance

Most of the experimental investigations on the mechanical properties of geopolymer concrete were compared with the code recommendations. Some of the expressions on the correlation of strength parameters of the conventional concrete are highlighted to compare with the present investigation. The correlation of split tensile strength to compressive strength is expressed as $f_t = 0.59 f_{ck}^{0.5}$, $f_t = 0.30 f_{ck}^{0.5}$, $f_t = 0.23 f_{ck}^{0.5}$ by ACI-318-99, CIB FIB and Neville, respectively [1]. The correlation of flexural strength to compressive strength of conventional concrete is expressed as $f_r = 0.7 f_{ck}^{0.5}$, $f_r = 0.62 f_{ck}^{0.5}$, $f_r = 0.60 f_{ck}^{0.5}$ by IS 456-2000, ACI-318 and BS 8110, respectively [2].

28.2   Basic Materials and Mix Proportion

The geopolymer is prepared by using fly ash, aggregates and alkaline solutions ($NaOH + Na_2SiO_3 + H_2O$). The fly ash and aggregates used for mix are conforming to IS: 3812 [3] IS: 383 [4], respectively. The geopolymer concrete is prepared with different mix proportions. The basic material testing and mix proportions are discussed elsewhere [5]. Same molarity (14 Molar) of alkaline solutions is used for all the mix. The detail of mix used for this work is shown in Table 28.1.

Table 28.1 Selected mix details of GPC

Mixture	Fly ash (%)	Fly ash (Kg/m^3)	Coarse aggregate (Kg/m^3)	Fine aggregate (Kg/m^3)	NaOH (Kg/m^3)	Na_2SiO_3 (Kg/m^3)	Plasticizer (Kg/m^3)
FGC-M6	25	521.44	876.02	688.30	89.76	224.4	4.8

Table 28.2 Test results of the strength parameters of concrete

Mixtures	Compressive strength (f_{ck}) MPa	Split tensile strength (f_t) MPa	Fexural strength (f_r) MPa
FGC-M1	13.35	1.88	2.52
FGC-M2	15.69	2.13	2.87
FGC-M3	18.56	2.44	3.13
FGC-M4	22.75	3.08	3.68
FGC-M5	26.35	3.52	4.28
FGC-M6	28.56	3.67	4.53
FGC-M7	31.98	4.12	4.98
FGC-M8	33.69	4.33	5.1
FGC-M9	35.58	4.53	5.32
FGC-M10	37.64	4.65	5.77
FGC-M11	40.23	5.14	6.05
FGC-M12	41.54	5.33	6.34

28.2.1 Testing of Concrete

Compressive strength split tensile strength and flexural strength tests of concrete are conducted as per IS: 516-1959 [6] and presented in Table 28.2.

28.2.2 Correlation of Strength Parameters

Graphically representing correlations of split tensile strength to compressive strength and flexural strength to compressive strength as shown in Figs. 28.1 and 28.2 respectively.

The correlation of corresponding strength parameters (f_s) by regression analysis are presented in the power function in the form $f_s = f(f_{ck}) = k(f_{ck})^n$ and are given in Eqs. (28.1) and (28.2).
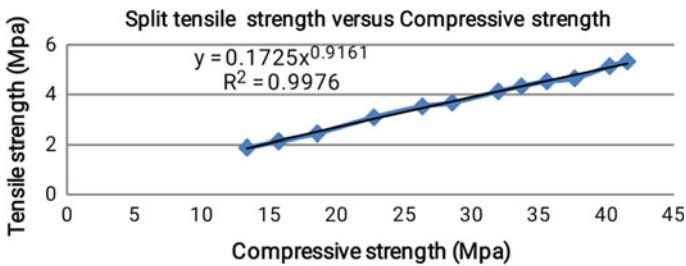

Fig. 28.1 Correlation of compressive strength to split tensile strength
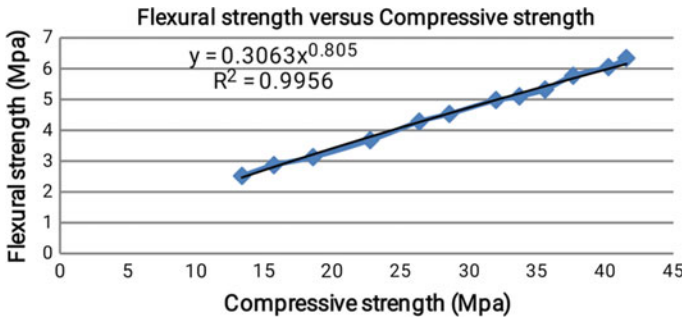
Fig. 28.2 Correlation of compressive strength to flexural strength

$$f_t = f(f_{ck}) = 0.1725(f_{ck})^{0.9161} \tag{28.1}$$

$$f_r = f(f_{ck}) = 0.3063(f_{ck})^{0.805} \tag{28.2}$$

28.3 Assessment of Shear Strength

28.3.1 Assessment of Shear Strength by Split Tensile Strength

The shear stress is analysed under classical theories of mechanics by considering cylindrical specimen subjected to split tensile test as shown in the Fig. 28.3a, b and c. The shear mechanism is explicated in Eqs. 28.3–28.5. The direct tensile strength of conventional concrete is expected to be 90% of split tensile strength [7]. Due to non-availability of the proper experimental evidences on direct tensile strength of geopolymer concrete, the direct tensile strength of concrete is considered as equal to split tensile strength to compute principal tensile strength. The relevant multiplication factor on direct to split tensile strength can be incorporated based on experimental investigation.
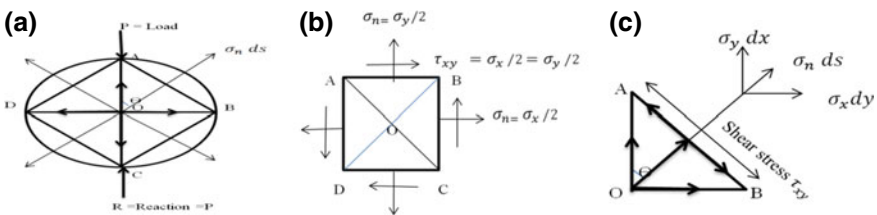

Fig. 28.3 Shear mechanisms by split tensile strength test

AO $=$ OB $= d/2$ (where d is the diameter)

$$\frac{f_t}{2} = \tau_{xy} = \tau_c = \frac{4P}{\pi dl} \tag{28.3}$$

Principal stress (σ_1, σ_2)

$$\sigma_1, \sigma_2 = \frac{\sigma_x + \sigma_y}{2} \pm \sqrt{\left(\frac{\sigma_x - \sigma_y}{2}\right)^2 + \tau_{xy}^2} \tag{28.4}$$

$$\sigma_1 = \sigma_x = \frac{f_t}{2}, \sigma_2 = 0$$

$$\tau_c = f(f_t) = \frac{f_t}{2} \tag{28.5}$$

28.3.2 Assessment of Shear Strength by Flexural Strength

The Shear strength of concrete is analysed by considering the shear stress of prism without reinforcement subjected to flexure test under two points load placed at a shear span of "a" as shown in Fig. 28.4. The flexural strength of the beam f_r is assessed from simplified bending equation of two points loading. The shear strength of the concrete is arrived through Eqs. 28.6–28.13.

$$f_{cr} = \frac{3Pa}{bD^2} \tag{28.6}$$

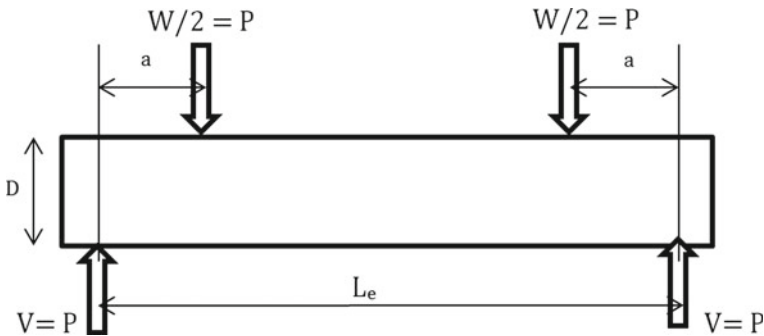$$f_{cr} = \frac{3P}{bD}\left(\frac{a}{D}\right) \tag{28.7}$$

Fig. 28.4 Flexural strength by two points loading

$$\text{Shear force } V = \frac{P}{2} \tag{28.8}$$

$$V = \frac{f_r}{6}\left(\frac{D}{a}\right)bD \tag{28.9}$$

$$V = \frac{f_r}{6}\left(\frac{D}{a}\right)bD \tag{28.10}$$

$$\frac{V}{bD} = \tau_v = \frac{f_r}{6}\left(\frac{D}{a}\right) \tag{28.11}$$

$$\tau_v = 0.167 \times \left(\frac{D}{a}\right) \times f_r \tag{28.12}$$

Experimental investigations shows that maximum shear arrived at section when $\left(\frac{D}{a}\right) = 1$ (when $\theta = 45°$) hence the Eq. (28.4) become

$$\tau_v = 0.167 f_r \tag{28.13}$$

Shear strength of prism τ_v is equated to the shear strength of concrete τ_c, and from Eq. 28.2, the shear strength of concrete is assessed and explicated in Eqs. 28.14 and 28.15.

$$f_r = f(f_{ck}) = 0.3063(f_{ck})^{0.805}$$

$$\tau_c = \tau_v = 0.0511 \times f_{ck}^{0.8063} \tag{28.14}$$

$$\tau_c = \tau_v = f(f_r(f_{ck})) = 0.0511 \times f_{ck}^{0.805} \tag{28.15}$$

From Eq. 28.1, the compressive strength of concrete is explicated through Eq. (28.16)

$$f_t = f(f_{ck}) = 0.1725(f_{ck})^{0.9161}$$

$$f_{ck} = 6.8(f_t)^{1.09} \tag{28.16}$$

From Eqs. (28.15) and (28.16), the shear strength of concrete as a function of tensile strength is given in Eq. (28.17)

$$\tau_c = \tau_v = f(f_r(f_{ck}(f_t))) = 0.0511 \times (6.8(f_t)^{1.09})^{0.805}$$

$$\tau_v = f(f_r(f_{ck}(f_t))) = 0.0511 \times 4.679(f_t)^{0.87}$$

$$\tau_v = f(f_r(f_{ck}(f_t))) = 0.23 \times (f_t)^{0.87} \tag{28.17}$$

28.4   Failure Envelopes

Generally in triaxial shear test, the specimen is subjected to like stresses (compressive stresses) in mutually perpendicular axis and the shear stress is assessed as the function of compressive stress but the tensile strength of the materials is not considered.

Mohr's theory of failure provides acceptable strength prediction of concrete. The parabolic and straight line envelope has been suggested for the family of Mohr's circle representing the failure condition. The research works on mechanism of shear transfer were referred in ASCE-ACI-426 [8], and this shows the failure envelope drawn on the corresponding circles of stresses to assess the shear strength.

The principal stresses are graphically represented by drawing the Mohr's circles. The principal compressive stress is drawn in a positive quadrant, and principal tensile stress is in negative quadrant of the axis. The Mohr's failure envelope is drawn as the function of principal compressive and tensile stresses. The value of shear stress is the function of principal stresses measured between the points of intersection of the tangent of the circles on y-axis to the origin.

$$\text{When } \tau_c = f(\sigma_1, \sigma_2)$$

$$\text{Graphically } \tau_c = ED$$

$$\tau_c = \frac{\sigma_1}{2}; \quad \text{When } \sigma_2 = 0$$

$$\tau_c \neq 0; \quad \text{Even if } \sigma_2 = 0$$

The value of τ_c is existed even when the principal tensile stress is zero. The concrete is generally weak in tension and can be considered as critical strength parameter rather than compressive stress parameter. The concrete structure will fail even though it has good compressive strength when the principal tensile stress is reached to its maximum limit. Under this condition, the shear strength of the concrete could be considered on the tensile strength of the concrete. A new approach is introduced here over modified failure envelope by drawing the triangle AO1O2 with angle Φ as shown in Fig. 28.5.

In this approach, the shear strength of the material is zero when the tensile strength of material tends to zero. The shear strength from the modified approach can be assessed as explained below.
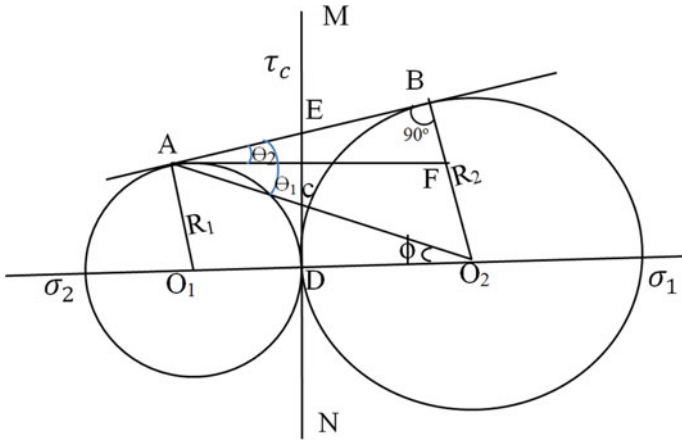
Fig. 28.5 Modified failure envelope

τ_c is the modified function (f_m) of σ_1, σ_2 and ϕ

$$\sigma_1 = f_{ck}; \quad \sigma_2 = f_t$$

$$\tau_c = f_m(\sigma_1, \sigma_2, \phi)$$

Graphically, $\tau_c = CD$

When $\sigma_2 = 0$ then $\phi = 0$ and $\tau_c = 0$; the shear strength CD is given in Eq. (28.23), derived through Eqs. (28.18)–(28.22)

$$\tan \theta_1 = \frac{R_2}{2\sqrt{(R_1 R_2)}} \tag{28.18}$$

$$\tan \theta_2 = \frac{R_2 - R_1}{2\sqrt{(R_1 R_2)}} \tag{28.19}$$

$$R_2 = \frac{\sigma_1}{2} \tag{28.20}$$

$$R_1 = \frac{\sigma_2}{2} \tag{28.21}$$

$$\Phi = \theta_1 - \theta_2 \tag{28.22}$$

$$\tau_c = CD = \frac{\sigma_1}{2} \tan \Phi \tag{28.23}$$

The shear strength of geopolymer concrete is compared with the empirical equation suggested by ACI-318-08 [9] as shown below in Eq. (28.24)

$$\tau_c = \frac{1}{6}\sqrt{f_c'} \tag{28.24}$$

Codes are suggesting certain material properties in the absence of experimental results. Here, ACI-318 suggesting the shear strength is based on the compressive strength of the concrete. The results of series of shear strength from the respective equation are shown in Table 28.4 and graphically represented in Fig. 28.6.

Table 28.4 Assessment of shear strength

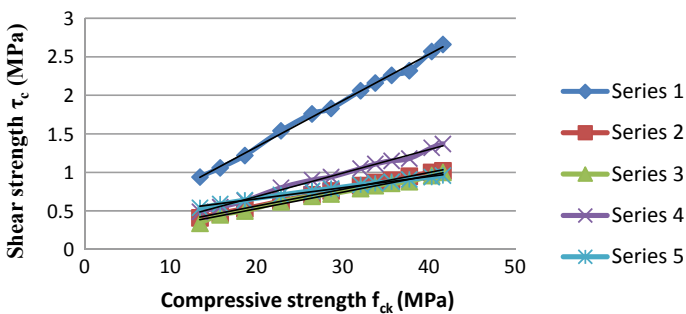| Mixtures	$\tau_c = f(f_t)$ MPa (Eq. 28.5) (Series1)	$\tau_c = f(f_r(f_{ck}))$ MPa (Eq. 28.15) (Series 2)	$\tau_c = f(f_r(f_{ck}(f_t)))$ MPa (Eq. 28.17) (Series 3)	$\tau_c = f_m(\sigma_1, \sigma_2, \phi)$ MPa (Eq. 28.23) (Series 4)	τ_c (ACI 318-95) MPa (Eq. 28.24) (Series 5)
FGC-M1	0.94	0.41	0.34	0.49	0.54
FGC-M2	1.06	0.47	0.45	0.55	0.59
FGC-M3	1.22	0.53	0.50	0.63	0.64
FGC-M4	1.54	0.63	0.62	0.80	0.71
FGC-M5	1.76	0.71	0.69	0.90	0.76
FGC-M6	1.83	0.76	0.72	0.94	0.79
FGC-M7	2.06	0.83	0.79	1.05	0.84
FGC-M8	2.16	0.87	0.83	1.11	0.86
FGC-M9	2.26	0.90	0.86	1.15	0.88
FGC-M10	2.32	0.95	0.88	1.18	0.91
FGC-M11	2.57	1.00	0.96	1.32	0.94
FGC-M12	2.66	1.02	1.00	1.37	0.96

Fig. 28.6 Comparison of results

28.5   Conclusions

The experimental analysis of shear strength is concluded by comparing the results with the solution by the equation suggested by ACI-318-08 for conventional concrete which is taken as reference.

1. The shear strength of the concrete evaluated as a function of tensile stress only (Series 1) shows a higher value. The concrete fails when the maximum tensile strength is equal to principal tensile strength. This solution can be considered as the upper bound solution for the maximum shear strength of plain concrete.
2. The shear strength computed on the flexural strength as a function of compressive strength $f(f_r(f_{ck}))$ varied with range maximum of 24% and the minimum of 6% with the result of reference equation (ACI-318-08).
3. The shear strength based on the tensile stress which is the function of compressive and flexure strength $f(f_r(f_{ck}(f_t)))$ shows the maximum of 38% and minimum of -4% of variations.
4. The shear strength on modified function of principal stresses $f_m(\sigma_1, \sigma_2, \phi)$ shows the maximum of $+40\%$ and minimum of 10% variation.
5. The new approach on modified failure envelope provides consistent solution of average 13% with the reference equation up to the concrete strength equal to M-25 grade.
6. The shear strength of the concrete mix grade higher than M-25 showed comparatively higher shear strength by modified failure envelope in comparison of other series of solutions. The shear strength of concrete will be significantly more for higher grade concrete. The general equation on shear strength could not be justifiable for high-grade concrete unless modifying the equation or experimental formulation on the range of strength of concrete. The validation of these approaches is limited with one reference and could be considered for further discussion with other previous research significance.
7. The geopolymer concrete shows comparatively equal shear strength with conventional concrete and validates with the equations suggested for conventional concrete. The relationship between the strength parameters can be justifiable with conventional concrete.

References

1. Lavanya, G., Jagan, J.: Evaluation of the relationship between split tensile strength and compressive strength for geopolymer concrete of varying grades and molarity. Int. J. Appl. Eng. Res. **10**(15), 35523–35527 (2015). ISSN 0973-4562
2. Yusuf, I.T., Jimoh, Y.A., Salami, W.A.: An appropriate relationship between flexural strength and compressive strength of palm kernel shell concrete. Alexandria Eng. J. **55**, 1553–1562 (2016)
3. IS: 3812.: Specification for pulverised fuel ash" Part-2, Bureau Of Indian Standard, New Delhi (2003)

4. IS: 383.: Specification for coarse and fine aggregates" Bureau Of Indian Standard, New Delhi (1970)
5. Kumar, S., Pradeepa, J., Ravindra, P.M.: Experimental investigations on optimal strength parameters of fly ash based geopolymer concrete. Int. J. Struct. Civil Eng. Res. **2**(2), 143–152 (2013)
6. IS: 516-1956.: Methods of tests for strength of concrete" Bureau Of Indian Standard (1956)
7. Al-Sahawneh, E.I. A new approach for the determination of tensile and shear strengths of normal weight concrete. IOSR J. Eng. **05**(08), 38–48 (2015). ISSN (e): 2250-3021, ISSN (p): 2278-8719
8. ASCE-ACI Committee 426.: Shear strength of reinforced concrete members. ASCE Proc. **99**(6), 1091–1188 (1973)
9. AC1: 318-2008.: "Building Code Requirements for Structural Concrete", and Commentary Report (AC1 318-08), ACI Committee (2008)